University of Southampton

Optical sensors for the location of buried optical cables and disturbances acting on extended lengths of optical fibre

by

Stuart John Russell BSc

A thesis submitted for the degree of PhD

Faculty of Applied Science and Engineering

The Optoelectronics Research Centre

September 2000

UNIVERSITY OF SOUTHAMPTON

ABSTRACT

FACULTY OF APPLIED SCIENCE AND ENGINEERING

Optoelectronics Research Centre

Doctor of Philosophy

OPTICAL SENSORS FOR THE LOCATION OF BURIED OPTICAL CABLES AND DISTURBANCES ACTING ON EXTENDED LENGTHS OF OPTICAL FIBRE

By Stuart John Russell

The work presented in this thesis, investigating two novel optical fibre sensor systems, was carried out as part of industrially sponsored (Radiodetection Ltd) and supported applied research project. The first sensor determines the longitudinal position of acoustic disturbances acting on an extended length of optical fibre cable and the second system locates the lateral position of a buried dielectrically-sheathed fibre cable.

The first system uses a new optical architecture, based on a well-known reciprocal interferometer known as the Sagnac. For the first time, a 40km long Sagnac optical architecture has been constructed and investigated. This novel network exhibits a loss 9dB lower than previously constructed systems, and has added benefits arising from the use of a single, high power (4mW) Erbium-doped fibre super-luminescent source (SLS) and a single detector. Positional results showing a resolution of ±20m have been observed in laboratory conditions and a new model to predict optical cross-talk effects has been developed.

The second system is believed to be the first optically-based sensor for the location of buried fibre optic cables. An RF electromagnetic field, emitted from above the cable, radiates through the ground and modulates the polarisation state of the light guided by the optical fibre, via the Faraday effect. The lateral position of the buried cable can then be inferred by observing the peak in the amplitude of modulation as the locator is traversed across the buried position of the fibre allowing, for the first time, dielectrically-sheathed optical cables to be located non-intrusively.

Acknowledgements

I would like to thank everybody involved in this project for their continued help throughout this work and I would like to especially thank Dr John Dakin for his supervision of my work over the past three years. Special thanks go to my sponsors, although now more like friends, Andrew, Bob and Barry, who without which none of this work would have been possible. I would also like to say thankyou to everyone in the ORC for the pleasant working environment and especially my office mates, Corin, Sally, Ed and Arshad. Finally I would like to thank my parents for their support throughout my PhD and for their help in getting me here in the first place.

CONTENTS

Publication List

1) "Location of time-varying strain disturbances over a 40km fibre section, using a dual-Sagnac interferometer with a single source and detector", S.Russell, J.P.Dakin, Conference Presenation. OFS 13, Kyonju, Korea, April 17 1999.

2) "Sensor Network for Structural Strain and High Hydraulic Pressure, Using Optical Fiber Grating Pairs, Interrogated in the Coherence Domain", J.P.Dakin, V.Foufelle, S.Russell,O.Hadeler. OFS 13, Kyonju, Korea, April 17 1999.

3) "Real-time location of multiple time-varying strain disturbances, acting over a 40km fiber section, using a novel dual-Sagnac interferometer", S.J.Russell, K.R.C.Brady, J.P.Dakin, Journal of Lightwave Technology, publication accepted and pending print.

4) "An improved 40km dual-wavelength, dual-Sagnac sensor, with enhanced signal processing, allowing real-time location of multiple time-varying strain disturbances", S.J.Russell, K.R.C.Brady, OFS 14, Venice, Italy, October 2000.

5) UK Patent Application "Locating time varying strain disturbances using a novel dual wavelength Sagnac interferometer", Patent application No. GB9821956.1,GB9903166

6) UK Patent Application "Locating buried fibre cables using a propagating EM wave generated by an electric dipole or other suitable antenna", Patent application No. GB9820535.4, prior art: EP 0390341, US 5576871, EP 0513381.

Chapter 1 Introduction

The work presented in this thesis has been carried out as part of an industrially sponsored and supported applied research project. The focus of this work has been the design and development of two separate fibre-optic sensing systems. The first system is based on a new architecture capable of locating time-varying strain perturbations, over a 40km length of optical fibre and the second is a novel cable location system for detecting the buried location of dielectrically sheathed cable bundles. Although not directly related, these systems find a common application and complement each other in the protection and management of a telecommunications network.

1.1 Overview

Optical fibres have recently found extensive use in the telecommunications industry. Fibre optic technology is ideal for this application, because, when compared to their electronic equivalents, fibre-optic systems allow low noise, high-bandwidth data transmission with extremely low loss and dispersion [1.1-1.3]. It is also relatively simple to design systems which are immune to electromagnetic interference (EMI). In addition, multiplexing of data onto fibre-optic channels, using both TDM (time division multiplexing) and WDM (wavelength division multiplexing) techniques, allows many conventional high bandwidth lines to be combined. This reduces the number of separate fibres necessary and hence the cost of any network. So successful have fibre optics been, that fibre cable links now form the backbone of most major communications systems.

Another important, although far more diverse, application of fibre optic technology is in optical sensors [1.4-1.7]. Optical sensors are generally compact, lightweight and as with data networks can be designed to be immune to EM interference and are relatively easy to multiplex. They also offer the advantage that no electrical power supply is required at the transducer element of the sensor, making them preferable in situations involving electrical safety or remote access. However, despite these advantages, optical fibre sensors have at times found it difficult to compete with more conventional, established, devices. This is partly due to the fact that conventional sensors often perform adequately, mainly due to

their existing mature state of development. As a result they are also normally less expensive and, of course, are more familiar to the end user.

Despite this fact, optical fibre sensors have made an impact in certain niche markets. Some of their marked successes include underwater acoustic sensing (hydrophones and hydrophone arrays) [1.8], where their superior sensitivity and the ease with which they can be multiplexed make them advantageous. Further successes have been in strain [1.9,1.10], temperature [1.11,1.12], chemical [1.13,1.14] sensing and in the measurement of rotation (gyroscopes)[1.15,1.16]. In recent years, fibre sensors have also found uses in the space industry, (where weight is an important factor), for example integral temperature and strain monitoring of the fuel tanks and aircraft skin in the new experimental space shuttle replacement X-33.

1.2 Optical Fibre sensors

A fibre optic sensor may be defined as a device or system in which a change in a measurand field such as temperature, pressure or strain induces a change in a measurable property of the light guided by a fibre or fibre network [1.17 Chapter 1]. Such properties may include the following aspect of optical propagation, i.e. the

1) Phase
2) Polarisation state
3) Intensity
4) Spectral content
5) Optical scattering

of the light guided by the fibre.

In this way, by suitable choice of optical configuration and / or fibre, a desired property of the light may be directly measured and the value of the associated measurand field can be inferred. There are many different forms of optical sensor, but they may all be subdivided into two groups, *extrinsic* and *intrinsic* sensors.

1.2.1 Extrinsic optical fibre sensors

An *extrinsic* fibre optic sensor [1.18] may be defined as an instrument in which the value of the measurand field is recovered by examining the properties of light transmitted through, or scattered from, a remote measurement region, external to the fibre. The fibre is used only to guide light to, and / or from, this remote measurement region. Information related to the measurand field is imparted to the light via some change external to the fibre and not to the fibre itself.

Extrinsic sensors were some of the first conceived. The majority of these took the form of intensity based systems, usually employing multi-mode fibres. Fig 1.1 shows a simple fluid level meter[1.19]. A large diameter multi-mode optical fibre is given a 90° wedge shaped end, such that when surrounded in air, light transmitted down the fibre is totally internally reflected. This reflected light is then guided back down the fibre to an optical detector, where its intensity can be measured. However, when the fluid level rises to immerse the wedged end of the fibre, the external refractive index change causes the majority of the light to be coupled into the liquid. This causes the returned optical signal to virtually vanish.

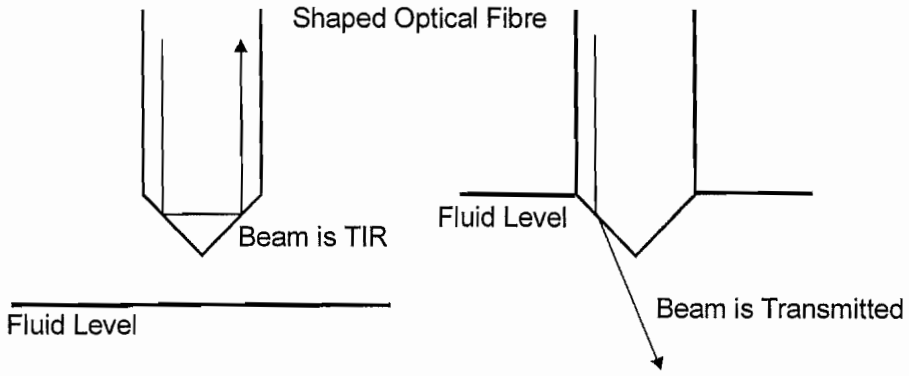

Figure 1.1 An extrinsic fluid level meter. *Light transmitted down the fibre is totally internally reflected if the fluid level is below the fibre tip. However, when the level rises, the change in refractive index causes the light to be coupled out of the fibre into the fluid.*

A second example of an intensity based extrinsic sensor is a simple arrangement shown in Fig 1.2. Light transmitted along the first optical fibre is emitted in a cone with an angle dependent on the difference between the fibre's cladding and core refractive indices. This emitted light cone is incident on a second optical fibre held in close proximity, a distance, d, away. The amount of light captured by this second fibre is directly related to the fibre

separation. Any vibration or acoustic disturbance that changes this separation is revealed in the intensity fluctuations of the captured light[1.20].

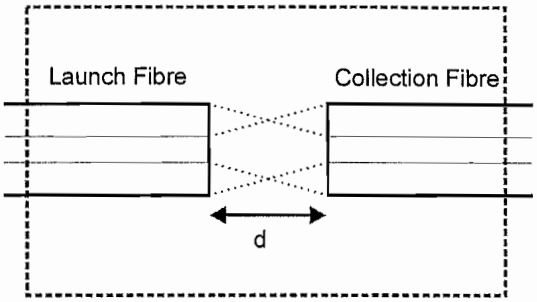

Figure 1.2 An extrinsic vibration sensor. *The light captured by the second fibre is directly related to the fibre separation. Any vibration or acoustic disturbance is revealed by observing the intensity fluctuations of the gathered light.*

Not all extrinsic optical fibre sensors, however, are intensity based devices. One of the first optical temperature sensors built [1.21] was a simple device using an optical fibre to gather light emitted by a blackbody. As the temperature of the blackbody rises, it begins to behave as a light source, and emit radiation, with a temperature-dependent spectral shape. The profile of the spectrum was then measured by passing this gathered light through several filters and measuring the intensity after each. Temperature resolutions of a few degrees were achieved, but initially the uses of such sensors were limited to temperatures greater than 500K, mainly due to the 0.4-1.1μm spectral response of the silicon detectors used.

A final example of an extrinsic sensor is the laser velocimeter [1.18] as shown in Fig 1.3. This system exploits fibre technology to guide light to, and receive light from, a remote object. The Doppler shifted scattered light is captured by the same fibre and combined with a reference beam, producing a beat signal, the frequency of which related to the velocity of the receding (or approaching) object.

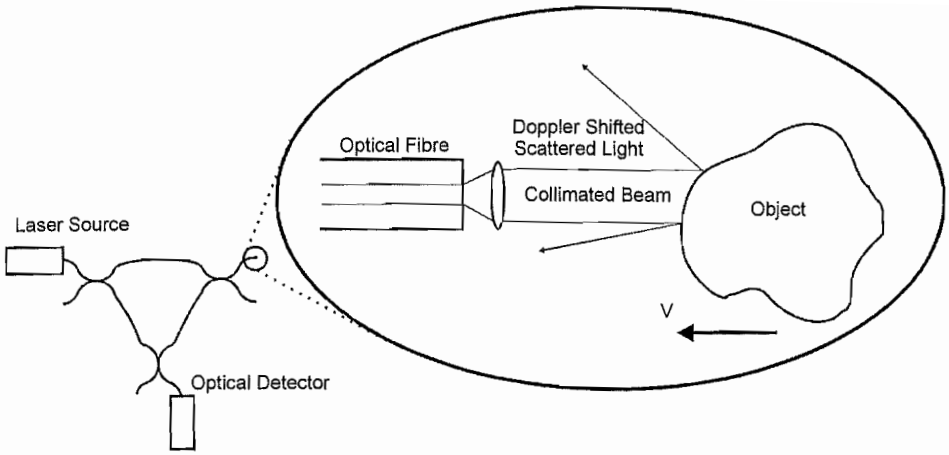

Figure 1.3. The Homodyne laser velocimeter. *Light is projected onto an approaching / receding object. The Doppler shifted scattered light is then captured by the same fibre and mixed with a reference, producing a signal whose frequency is proportional to the velocity of the object relative to the sensor.*

1.2.2 Intrinsic optical fibre sensors

The second of the two groups are the *intrinsic* fibre optic sensors [1.17] and their development has dominated the research field for the past 25 years. In sensors of this type the light is completely contained within the waveguide itself. The measurand field then directly affects the properties of the waveguide, in turn affecting the propagation of the guided light. This change can then be measured and the associated measurand determined. I.e. information about the measurand is imparted to the guided light by changes in the fibre itself.

1.2.2.1 Intensity-based intrinsic fibre sensors

The first intrinsic fibre optic sensors were conceived in the late 1960's and, as with extrinsic sensors, some of the first were intensity-based devices. However, the vast majority of sensors under research and in use today are based on other principles. Fig 1.4 shows a simple intrinsic fibre optic pressure sensor [1.22], formed by running a mono-mode fibre between two rigid plates, each with a periodic array of rods bonded to them. As pressure is applied to the upper plate, the fibre is deformed by the rods causing microbend loss. The pressure applied to the top plate can then be quantified by observing the intensity of light transmitted to the far end of the fibre. The important factor with this sensor is that

a physical change is the waveguide itself is responsible for imparting measurand information to the light.

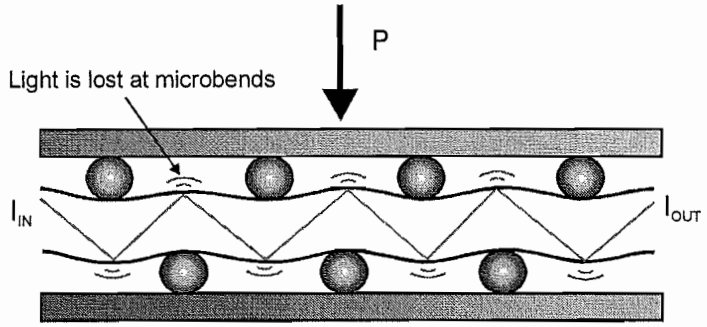

Figure 1.4 Intrinsic pressure sensor. *As pressure is applied to the upper plate, the fibre is deformed causing micro-bend loss. The intensity of the guided light then allows the pressure on the plate to be inferred.*

Herga Ltd used this principle to form a commercial pressure sensor. A polymer fibre was spirally wound around a central monomode optical fibre and sheathed in a deformable polymer tube. Pressure exerted on the tube would then, in a similar way to that previously described, cause microbend loss on the central optical fibre.

1.2.2.2 Spectrally-encoded Intrinsic Sensors

By far the most important spectrally-encoded intrinsic sensor technology is the in-fibre Bragg grating. Research into sensors of this nature has dominated the sensor field in recent times, with novel developments being made in strain and temperature sensing and the use of active devices as sensors [1.23].

As shown in Fig 1.5, an in-fibre Bragg-grating is formed by a spatially-periodic modulation in the refractive index of the fibre core. The action of such a device is to act as a narrow band reflective filter, its centre wavelength being related to the effective spatial-period of the refractive index modulation and its spectral reflectance profile determined by the refractive index modulation amplitude profile along the fibre. When such devices are strained, or undergo a temperature change, their period and hence the peak reflected wavelength is altered, both via physical length changes and via index changes (induced by the photo-elastic effect). There have been far too many techniques developed to determine the reflected wavelength to mention in this summary, but, for a more in-depth review of this technology I refer you to an article by Dakin and Volanthen [1.24].

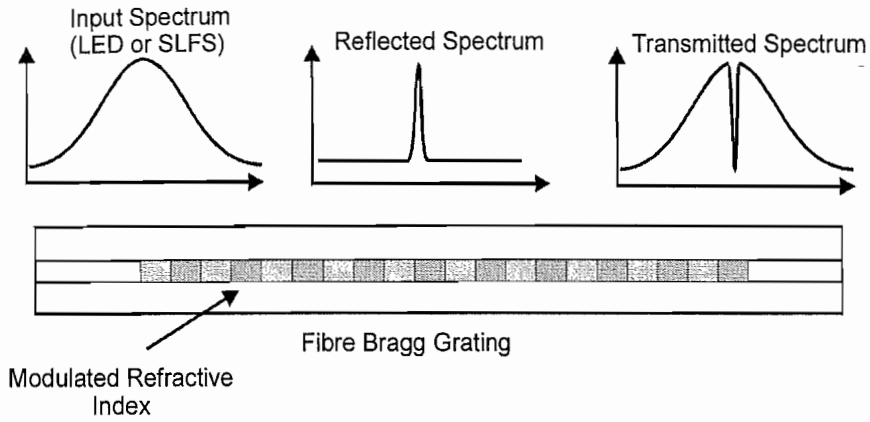

Figure 1.5 The in-fibre Bragg grating. *An in-fibre Bragg grating is formed by a periodic modulation of the core refractive index. Such a device acts as a narrow-band reflective filter, with a peak reflected wavelength directly related both to the fibre strain and its temperature.*

1.2.2.3 Interferometric sensors

Interferometric sensors form a large subgroup of optical fibre sensors and are generally considered one of the best ways of detecting small perturbations, for example acoustic or seismic disturbance, strain and temperature. One of the most extensively researched areas of interferometric sensors has been that of fibre gyroscopes.

As in classical optics, there are many forms of fibre interferometer. The Mach-Zehnder, Michelson, Fabry-Perot and Sagnac are the most common, but to describe each in detail would be outside the scope of this review. However, to summarise, dual-path interferometers first split light from a common source into two arms. One of the arms acts as a reference, whilst the other is exposed and modulated by the measurand field. The light from both arms is then brought together and the interference pattern detected as resulting amplitude changes in the output of a "square law" optical detector. For example, an acoustic disturbance changes the phase of the light guided by the measuring arm, by both altering the length of the optical path and by changing its refractive index, via the photoelastic effect. This is then revealed in the intensity of the detected light after the light from both arms is brought together.

Interferometric techniques do, however, suffer from the general disadvantage of having a non-linear (eg, $1+\cos\theta$, in the case of the two path sensor) response to the measurand field. As will be described in detail later, (Chapter 1.1), several different biasing and

demodulation techniques [1.25] have been developed to improve upon the interferometer's natural response, processing the signal to give a linear response and driving the sensor to a point of high sensitivity. A final note on the application of interferometric techniques is their use in multiplexing of discrete sensors, i.e. white light interferometry [1.26], which brings us to the final section of sensing.

1.2.3 Distributed sensing

So far we have assumed the use of point sensors, i.e. devices that either monitor the measurand field at a single point, or give a line-integrated average response to the measurand field over a short interaction length. Probably the greatest advantage of optical fibres is their ability to be easily multiplexed, or with correct processing, to determine the positional variation of the measurand field along the interaction length. This technique is known as distributed sensing [1.27].

Positional information is most commonly recovered from time-of-flight information, i.e. by measuring the propagation delay between emitted and received radiation. The greatest difference in propagation delay occurs when emitted and received radiation travel in opposite directions. With radio-waves this has been extensively used in RADAR (RAdio Detection And Ranging). In the case of optical fibre sensors, the positional information is recovered by measuring the time delay between an emitted optical pulse and its received back-scattered signal. In this way, knowing the velocity of the light guided by the fibre, the distance to the interaction point may be determined. This generic method forms the basis for numerous distributed sensors. When used in the free space, it is termed LIDAR (LIght Detection And Ranging) and when used in fibres, OTDR (Optical Time Domain Reflectometry) [1.28].

Intensity based sensors can be formed by measuring the back-scattered intensity of Rayleigh (elastically scattered light) or Fresnel (reflected light) light giving information about the distributed position of discontinuities and loss along the fibre. One of the earliest OTDR sensors reported [1.29] monitored the state of polarisation of light scattered from a polarised pulse as it propagated along a standard single mode fibre. In this way, by observing the change in the polarisation state of scattered light, information about a host of measurand fields, having an effect on polarisation (e.g. strain, magnetic field, electric

field), could be recovered. With appropriate filtering and / or detection methods, spectrally-encoded sensors can be realised, utilising inelastically scattered light e.g. Raman [1.30] or Brillouin [1.31] radiation, finding application in the fields of distributed strain and temperature sensing. A high intensity pump signal launched along a single mode fibre causes fluorescence of the fibre in a wavelength band around the pump. In glass, Raman fluorescence takes the form of a relatively broad continuum around the pump, the shorter wavelength anti-Stokes emission having higher amplitude than the longer wavelength Stokes. The amplitude of the anti-Stokes component is particularly temperature dependent. Brillouin scattering is different, in that light is emitted in two relatively narrow bands spaced approximately 10-12GHz away from the pump signal. With knowledge of the ratio of the amplitude of the Brillouin signal to the Rayleigh, combined with the spacing between the Brillouin emission and the pump, both the strain acting on the fibre and the temperature can be recovered. The first of these methods has been employed by York Sensors Ltd in their distributed Raman based temperature sensor.

Position dependent measurand information can also be recovered in certain types of interferometer. An interferometer known as the Sagnac[1.32] is particularly useful. This form of sensor has already found application in the areas of magnetic field sensing, hydrophones, and perhaps their most extensively researched application, gyroscopes. However, in this work it is the application of distributed sensing of time varying strain or other transient disturbances which is of interest.

1.3 Novel Work Presented in this Thesis

We now present a summary of the work presented in this thesis, our own novel contribution to the field of fibre optic sensors. This work has been part of a directly funded industrial research project, designed to develop an optical sensor system aimed at solving practical problems faced by the telecommunications industry. The problems are apparent if you consider the following situations.

1.3.1 Telecoms Network Operation Problems

1) Fibre optics have become an integral part of the telecommunications industry. The ease with which data channels can be multiplexed leads to the inevitable situation where a single fibre optic cable may be carrying several million phone-calls simultaneously. The loss of such a cable will inevitably cost the network operator substantial revenue, and although these system are designed with some degree of redundancy, may even lead to the situation where communications are disrupted. The protection of these services, therefore becomes an important factor in the day to day operation of the network. When construction and other companies wish to dig near their cables, they run the risk of accidentally damaging the fibre. Although this happens infrequently the loss in revenue is substantial enough to warrant substantial expenditure in order to prevent accidents of this nature.

2) A second problem is accurately marking the buried position of the cable, so that other companies operating near to the service may avoid damaging it. Also the speed with which the fibre can be repaired and returned to service, e.g. if an alarm system were to fail and the cable be partially damaged, is also an important factor. In order for the cable to be repaired, it is normally necessary to first find its buried location without damaging surrounding fibres or services. Typically, steel reinforced cables are used when laying an optical fibre network. Cable location systems in use today take advantage of this steel sheath in order to locate their buried position. Unfortunately, in addition to accidental damage, steel cables are vulnerable to damage caused by lightning strikes and corrosion. Non-conducting dielectric sheathed cables, such as Kevlar, would make ideal substitutes as they are invulnerable to these forms of damage. As yet, however, network operators have been reluctant to use them, due to the fact that they are difficult to locate once buried, as they render the present location technology, which relies on a conducting sheath, ineffective. A cable location system, capable of locating the position of a buried fibre, independent of its protective sheath, would be a valuable asset for these companies. It is assumed that such a system would require at least one of the optical fibres in the bundle to be continuous, even after the bundle has been damaged. This is true also for previous systems which require not the fibre to be intact, but the sheath. If the cable is cut clean in half, neither system can locate its buried position. However, in extreme cases such as these, with a distance-to-fault measurement using an OTDR, the operator can visually

inspect the cable route for damage and find the position where the route has been disturbed.

1.3.2 Aims of project

The first aim of this project was to design and develop an optical sensor system capable of monitoring the threat to an optical cable bundle.

The second aim was to develop a cable location method which would be effective, regardless of how the cable bundle was sheathed.

Two novel systems have been developed in an attempt to tackle these highlighted problems. In order to describe the research path taken in the development of each of these sensors, this thesis is divided into two separate sections, each of which dealing with each sensor in turn.

1.3.2.1 FTAS (Fibre threat analysis system) SECTION 1

The first section of this thesis presents a novel Sagnac architecture for the detection and location of time-varying disturbances over an extended 40km length. The Sagnac is a reciprocal loop interferometer. Light from a single source is split and routed in opposite directions around a shared optical path before being recombined on a detector, where the interference pattern created can be observed. Normally, if both paths are equal, light beams returning in each direction will arrive in phase. Consider what happens when this loop is disturbed. A disturbance acting at the centre of the loop has no effect, due to the fact that light travelling in opposite directions encounters the disturbance at the same time and therefore incurs the same perturbation, i.e. the symmetry of the loop is unbroken. However, when a disturbance acts at a point away from the loop centre, light travelling in one direction encounters the disturbance a short time before light travelling in the other. If this disturbance is time varying, then it is easy to see that a relation between the position of the disturbance and the resulting relative phase of light beams (and hence the signal generated by the Sagnac) can be found.

Although Sagnac interferometers have been considered for time-varying strain measurements before, we present a new structure. This has far lower optical loss than previously developed systems, and the added advantages of simpler signal processing and the need for only one high-powered source and one detector. The loop length of this new Sagnac architecture is no less than 50 times longer than any other previously reported system.

Although we have presented this system as a solution to specific problems faced by the telecoms industry, we beleive this sensor could also find application in many other fields. For example, if a fibre were laid in the same duct as a gas or water main, the sensor would still be able to monitor the service route for disturbances and could raise an alarm if the gas or water main were to begin to leak, disturbing the fibre. Similarly it may also be able to pre-empt a leak by detecting a slow temperature change, as the pipe weakens. This system could also be used for applications as wide ranging as vehicle positioning (i.e. trains on tracks, or aircraft on runways) and intruder alarms. A final example of the use of this sensor could be in the detection and monitoring of structural health of a building or other civil engineering structure, (eg bridges, dams etc).

Chapter 1.1 introduces the basic Sagnac interferometer and the conditions that must be met for reliable operation of this type of sensor. Previously researched similar optical architectures are then discussed and the advantages / disadvantages of each highlighted. Chapter 1.2 then concentrates on our new optical architecture, presenting its novel features. The theoretical response of the system is derived and the complications and advantages arising from optical crosstalk are modelled and a new theory of operation discussed. Chapter 1.3 focuses on computer simulations of the dual-Sagnac in the presence of noise and multiple disturbances acting simultaneously on its sensor loop. Chapter 1.4 presents in detail the experimental apparatus built, and presents the first location of tone disturbances acting on a 40km section of fibre using a Sagnac interferometer. The simultaneous location of multiple disturbances is discussed and the first ever experimental results presented. Chapter 1.5 summarises the progress made in the research of this sensor and indicates how it could be improved for future trials.

1.3.2.2 EMO (Electro-magnetic / Optical cable location system) SECTION 2

Section 2 presents a novel cable location system, with which it is hoped to be able to locate buried dielectric cables. This system utilises changes in the state of polarisation of the light guided by the fibre to locate the buried position of the dielectric cable. A magnetic field, applied from above ground, in proximity to the cable, propagates through the soil to interact with the buried optical fibre. This field modulates the polarisation state of the guided light, via the Faraday effect, producing changes which can be observed by narrowband detection at the far end of the fibre. These results are then relayed to the operator of the magnetic field generator. The buried position of the fibre can then be inferred by observing the relative response as the field generator is traversed laterally across the buried fibre. To our knowledge this is the first time the Faraday effect has been used in this manner to locate buried cables.

Chapter 2.1 introduces the basic concept of the cable location system and discusses the initial complications that arise. These include electro-magnetic field generation and Faraday effect quenching. Initial experimental laboratory and field trials of a system designed to test the feasibility of such a system are presented in Chapter 2.2. Improvements to the optics arrangement and improved signal processing electronics are then introduced in Chapter 2.3. Finally, Chapter 2.4 deals with further work that could be undertaken to carry this research forward.

References Chapter 1

[1.1] J.M.Senior, "Optical fiber communications", 2nd Edition, Prentice Hall, 1992

[1.2] P.Russer, "Introduction to optical communication", Ed M.J.Howes, D.V.Morgan, John Wiley, 1980.

[1.3] R.M.Gagliodi, S.Karp, "Optical communications", John Wiley, 1976.

[1.4] A.D.Kersey "A Review Of Recent Developments In Fibre Optic Sensor Technology" *Optical Fibre Technology Vol 2 Pg 291-317 (1996)*

[1.5] Editor E.Udd "Fibre Optic Sensors" *SPIE Critical reviews, Vol CR44, (1992).*

[1.6] E.Udd, "Fiber Optic Smart Structures", Proceedings of the IEEE, pg 884-894, Vol 84, No 6, June 1996.

[1.7] T.G.Giallorenzi, J.A.Bucaro, A.Dandridge, G.H.Siegel JR, J.H. Cole, S.C. Rashleigh, R.G.Preist, "Optical fiber sensor technology", IEEE Journal of Quantum Electronics, pg 626-662, Vol 18, No 4, April, 1982

[1.8] S.Knudsen, K.Bløtekjær, "An ultrasonic fiber-optic hydrophone incorporating a push-pull transducer in a Sagnac interferometer". IEEE Journal of Lightwave Technology, pg 1696-1700, Vol 12, No 9, 1994.

[1.9] D.Inaud, S.Vurpillot, E.Udd, "Long gauge structural monitoring for civil structures", Proceedings of SPIE, Vol 3489, pg 93, 1998.

[1.10] D.R.Huston, P.L.Fuhr, "Fiber optic smart civil structures", Fiber optic smart structures, Ed E.Udd, Wiley, 1995.

[1.11] J.P.Dakin, D.J.Pratt, "Distributed optical fibre Raman temperature sensor using a semiconductor light source and detector", Electronics letters, Vol 21, No 13, June, 1985.

[1.12] W.W.Morey, G. Meltz, W.H.Glenn, "Bragg-grating temperature and strain sensors", Proceedings of Optical fiber sensors 89, pg 526, Berlin, 1989.

[1.13] M.Brenci, F.Baldini, "Fiber optic optrodes for chemical sensing", proceedings OFS-8, pg 313, 1992.

[1.14] G.Boisde, A.Harmer, "Chemical and biochemical sensing with optical fibers and waveguides", Artech House, Boston, London, 1996. ISBN 0-89006-737-6.

[1.15] T.Kumagai, H.Kajioka, W.Ohnuki, M.Akiyama, S.Saito, "Industrial applications of FOG", proceedings OFS-13, pg 64-67, Korea, 1999.

[1.16] W.K.Burns, "Optical fiber rotation sensing", Academic press, San Diego, 1994.

[1.17] Editors B.Culshaw , J.P.Dakin "Optical Fiber Sensors, Principles and Components" Vol 1 Pub Artech House, London, Boston 1989 ISBN 0-89006-317-6

[1.18] Editors B.Culshaw, J.P.Dakin "Optical Fiber Sensors, Systems and Applications" Vol 2 Pub Artech House, London, Boston 1989 ISBN 0-890006-376-1

[1.19] J.W.Snow, "A fiber optic fluid level sensor: practical considerations", Proceedings of SPIE, Vol 986, pg 164, 1988.

[1.20] E.Udd, P.M.Turek, "Single mode fiber optic vibration sensor", Proceedings of SPIE, Vol 566, pg 135, 1985.

[1.21] E.Udd, "Fiber optic smart structures", Proceedings of the IEEE, Vol 84, No 6,June 1996.

[1.22] J.N.Fields, J.H.Coles, "Fibre microbend acoustic sensor", Applied Optics, pg 3265-3267, Vol 19, 1980.

[1.23] O.Hadeler, E.Ronnenkliev, M.Ibsen, R.I.Laming, "Polarimetric distributed feedback fibre laser sensor for simultaneous strain and temperature measurements", Applied Optics, pg 1953-1958, Vol 38, No 10, 1999.

[1.24] J.P.Dakin, M.Volanthen, "Distributed and multiplexed fibre grating sensors, including discussion of problem areas" IEICE Transactions On Electronics, pg 391-399 Vol E83C, No.3, 2000.

[1.25] A.Dandridge,A.B.Tveten, T.G.Giallorenzi, "Homodyne Demodulation Scheme for Fibre Optic Sensors Using Phase Generated Carrier", IEEE Transactions on Microwave Theory and Techniques, pg 1635-1641, Vol MTT-30, No 10, 1982.

[1.26] J.Brooks, R.H.Wentworth, R.C.Youngquist, M.Tur, B.Y.Kim, H.J.Shaw, "Coherence multiplexing of Fibre-Optic Interferometric Sensors", IEEE Journal of Lightwave Technology, pg 1062-1071, Vol LT-3, No 5, 1985.

[1.27] J.P.Dakin "Distributed Optical Fibre Sensors" in E.Udd "Fibre Optic Sensors" *SPIE Critical reviews, Vol CR44, (1992).*

[1.28] P.Healy, "Review of Long Wavelength Single-Mode Optical Fibre Reflectometry Techniques", IEEE Journal of Lightwave Technology, pg 876-886, Vol LT-3, No 4, 1985.

[1.29] A.Rogers, "Polarisation Optical Time Domain Reflectometer", Electronics Letters, pg 489-490, Vol 16, No 13, 1980.

[1.30] J.P.Dakin, D.J.Pratt, "Distributed optical fibre Raman temperature sensor using a semiconductor light source and detector", Electronics letters, Vol 21, No 13, June, 1985.

[1.31] V.Lecoeuche, D.J.Webb, C.N.Pannel, D.A.Jackson, "16km Distributed Temperature Sensor Based on Coherent Detection of Spontaneous Brillouin Scattering Using a Brillouin Laser", Proceedings OFS-13, pg 345, Kyonju, Korea, 1999.

[1.32] E.Udd, "Sagnac Distributed Sensor Concepts", Proceedings Distributed and Multiplexed Fiber Optic Sensors, pg 46-52, Vol 1586, 1991.

SECTION 1 : (FTAS)

Fibre Threat Analysis System

An Optical Sensor For The Location Of Time-Varying Strain Perturbations

Chapter 1.1 The Sagnac Interferometer

This chapter introduces the Sagnac interferometer. The basic Sagnac ring, as constructed from fibre optic components, is firstly presented and the conditions which must be met for reliable operation discussed. The response of the interferometer is then derived and the principle upon which disturbances can be located is discussed. Previous optical architectures for this application are then presented, highlighting both the advantages and disadvantages of each of the previously researched systems. Finally, the concept of phase biasing and signal recovery using active dual-sideband demodulation, to improve the sensitivity of the interferometer is introduced.

1.1.1 The Basic Sagnac Interferometer

1.1.1.1 Construction of a Sagnac interferometer

The first of the optical sensor systems presented in this thesis is based on the use and understanding of a reciprocal path interferometer, known as the Sagnac. In its simplest form, the Sagnac interferometer consists of optical components which first split light into two beams and then route each of these beams in opposite directions around a common optical path. After propagating around the optical path, both beams are recombined on a detector, (or screen) where the resulting interference pattern can be observed. Fig 1.1.1 shows a simple bulk-optical configuration forming a Sagnac interferometer.

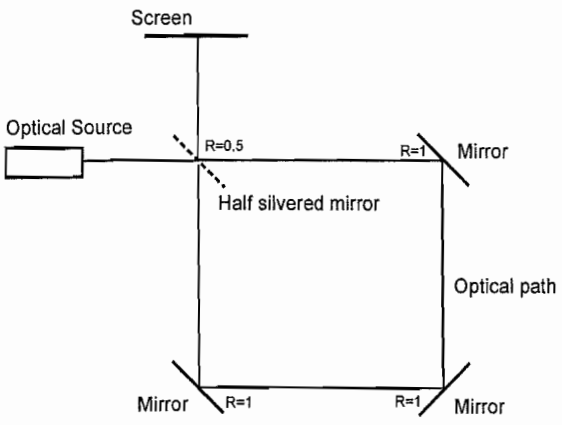

Figure 1.1.1 The Sagnac interferometer. *The basic Sagnac interferometer consists of optical components which route light in opposite directions around a commonly shared path before recombining it on a screen (or detector) where the interference pattern can be observed.*

Light from a source is split using a half silvered mirror. 100% reflecting mirrors are then used to route the transmitted and reflected beams around a common free-space optical path before they are again incident on the half silvered mirror. This in turn combines the two beams on a screen allowing the interference pattern to be observed. Optical structures similar to this formed some of the first Sagnac interferometers.

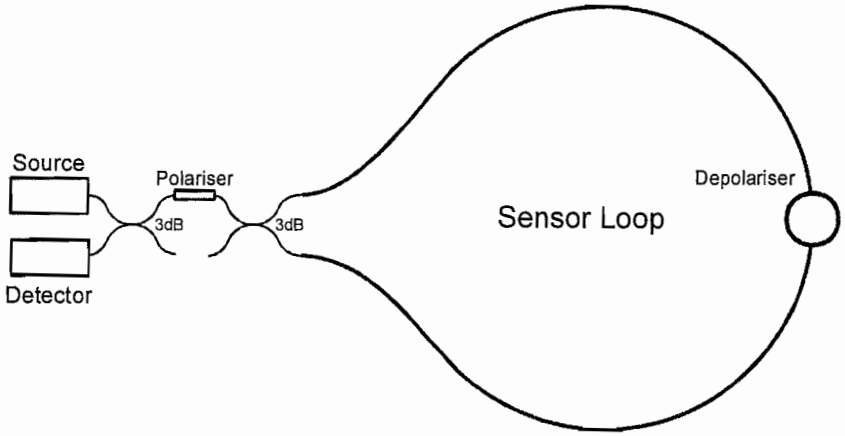

Figure 1.1.2 The Sagnac interferometer as constructed from fibre optic components. *Schematic of the Sagnac interferometer, realised from fibre optic components. A broadband, low-coherence, source is used to reduce the effects of interference from back-scattered light, arising from Rayleigh and Fresnel scattering. Reciprocal operation is ensured by plane polarising the launched light in the configuration shown. Using a Lyot depolariser, the state of polarisation is effectively randomised in the wavelength domain, hence reducing polarisation fading effects by averaging over the source bandwidth.*

Fibre optic components, however, offer convenient, alternative ways to form an interferometer of this type. The biconically-fused fibre coupler [1.1.1] is a commonly used device that couples incident light into each of two output ports, whilst presenting very low insertion and polarisation dependent loss. The fraction of light coupled to each of the output arms need not necessarily be equal but, for the Sagnac, 50/50 (or 3dB) couplers are usually used. Consider what happens in the optical configuration shown in Fig 1.1.2. Light emitted by a broadband source is divided by the first 3dB coupler. Since one output arm of this first coupler is unused, 50% of the light is lost. The light in the other output arm however, is then plane polarised by propagation through a fibre-based polariser. This plane polarised light then encounters a second 3dB coupler and is again split equally into two wavetrains, one propagating clockwise and the other counter-clockwise around a loop of fibre defining an optical path. After propagating around the loop, the two wave-trains are recombined by the same 3dB coupler, through which they were launched into the loop. The combined light again passes through the polariser and is incident on a detector where

the intensity of the interference signals may be observed, (again incurring a 50% loss into the source arm). Comparing this structure with the initially presented bulk-optics architecture, we see that the second 3dB coupler performs the function of the half-silvered mirror and that the first simply allows the interference pattern to be observed on a detector. The mirrors have now been replaced with a coil of single mode optical fibre, which can be bent into a loop to define the optical path taken by counter-propagating beams.

1.1.1.2 Operating conditions for the Sagnac interferometer

In order for a Sagnac interferometer to operate correctly, two conditions must be satisfied.

1) The optical paths for clockwise (CW) and counter-clockwise (CCW) propagating light must be reciprocal. This means that the physical path length and the propagation velocity for counter propagating light must be equal, typically to 1 part in 10^{12}. The first condition, that of equal path length, is met simply by the physical symmetry of the system. The second, however, is a little more complicated. If more than one polarisation mode were permitted to propagate around the loop, then, due to both residual and strain-induced birefringence in the fibre, the propagation velocity for each may be different. This would violate the first condition. The solution, as shown in Fig 1.1.2, is to filter a single plane polarised optical mode, ensuring that the path taken by propagating and counter-propagating wave-trains are of equal length [1.1.2]
2) The light source used in the construction of such an interferometer should ideally be broadband. This ensures a short coherence length, thus reducing the effects of interference from back-scattered light, which could arise from either Rayleigh [1.1.3] scattering in the fibre or Fresnel reflections at joints.

Another important, additional device for reliable operation of the Sagnac interferometer is the Lyot depolariser [1.1.4]. The polarisation state of the light may be altered as it propagates around the sensor loop by any intrinsic, or strain induced, birefringence in the fibre. It is possible that, when the two wave-trains arrive back at the detector, their polarisation states could change or even be orthogonal. If the latter were the case, they would not visibly interfere, and a fringe pattern would not be observed. This effect is called "polarisation fading" [1.1.5] and can be a serious problem in interferometers of this kind. A perfect depolariser would depolarise the light, so that its state of polarisation

becomes completely scrambled, i.e. depolarised. Depolarised light would have a random polarisation state, such that no change would be observed in the intensity of the light after propagation through a plane polarisation analyser, as the analyser is rotated through any angle. A perfect depolariser does not exist, but fortunately practical depolarisers like the Lyot depolariser [1.1.4] can be realised under certain conditions. By passing light through two highly birefringent fibres, joined with their polarisation axes orientated at 45 degrees to each other, a device can be constructed that effectively randomises the polarisation state of the input light, by averaging the output state in the wavelength domain. When broadband light is incident on such a device, assuming correct choice of fibre length and birefringence, an output with an average state of polarisation of virtually zero, over the wavelength range of interest, can be achieved. This ensures interference will always occur at some wavelength and fading effects will be minimised. The Lyot depolariser is discussed fully in appendix 1.

1.1.1.3 Phase response of the Sagnac interferometer

In order to understand the use of the Sagnac in sensing applications it is necessary to derive its phase / intensity response. Consider the optical architecture shown in Fig 1.1.2. Defining the instantaneous amplitude, $E(\omega,t,\phi)$, of the electric field of the radiation emitted by the source at a time t to be given by:-

$$E(\omega,t,\phi) = E_0 e^{i(\omega t+\phi)} \qquad [1.1.1]$$

where, ω, is the optical frequency and, ϕ, its phase, we may proceed to derive the change in detected optical intensity as a function of the phase difference between counter-propagating wavetrains. We shall assume that the couplers have an intensity coupling fraction f. Then if light of intensity $E^2/2$ were incident on the device, each output would show an intensity $fE^2/2$ and $(1-f)E^2/2$ respectively. Following this around the loop, we may show that the clockwise propagating wave arrives at the detector with an electric field amplitude given by [1.1.2]. Likewise, for the counter-clockwise wave, we arrive at [1.1.3].

$$E_{clockwise} = E_0 f(1-f) i^2 e^{i(\omega t+\phi_1)} \qquad [1.1.2]$$

$$E_{counter\_clockwise} = E_0 f(1-f) i^2 e^{i(\omega t+\phi_2)} \qquad [1.1.3]$$

The total electric field, E_T, incident on the detector is the sum of [1.1.2] and [1.1.3] and the intensity, I, of the light incident on the detector is then simple to calculate, as shown in [1.1.4].

$$I = \frac{1}{2}\left\langle E_T \cdot E_T^{*} \right\rangle = \frac{1}{2} E_0^{\,2} f^2 (1-f)^2 \left\langle \left| e^{i(\omega t+\phi_1)} + e^{i(\omega t+\phi_2)} \right|^2 \right\rangle \qquad [1.1.4]$$

This then simplifies to [1.1.5],

$$I = 2 I_0 f^2 (1-f)^2 (1+\cos(\Delta\phi)) \quad \Delta\phi = \phi_1 - \phi_2 \qquad [1.1.5]$$

I is the intensity of the light arriving at the detector, I_0 is the peak intensity of the emitted radiation and ϕ_1 and ϕ_2 are the relative phase offsets for CW and CCW-propagating wave-trains, respectively. As expected, the Sagnac interferometer has the usual raised cosine response expected for a dual beam interferometer. This is shown in Fig 1.1.3.

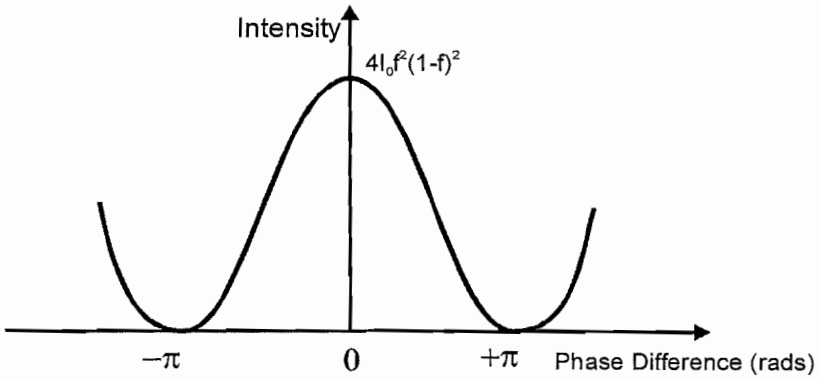

Figure 1.1.3 Phase response of an unbiased Sagnac interferometer. *As expected with a balanced dual beam interferometer, the response is a raised cosine. Giving a maximum intensity response when optical paths are balanced and a minimum when the optical paths are unbalanced by π radians.*

1.1.2 Positioning of a time varying strain disturbance

For our current application, the most interesting characteristic of the Sagnac interferometer is its ability to measure the position at which a time-varying disturbance acts on the sensor loop. Such an influence results in a time varying relative phase shift between counter-propagating wave-trains.

For simplicity, consider the situation shown in Fig 1.1.4. A single time-varying strain disturbance, $\varepsilon(t)$, acting at a distance, z, away from one end of the sensor loop, perturbs the propagation of light around the Sagnac interferometer. As one wave-train propagates around the sensor loop, it will encounter the disturbance at a time t_1. The fibre will, at this time, be under a strain, ε_1, imposed by the disturbance. This strain will phase shift the light, as shown in equation 1.1.6:-

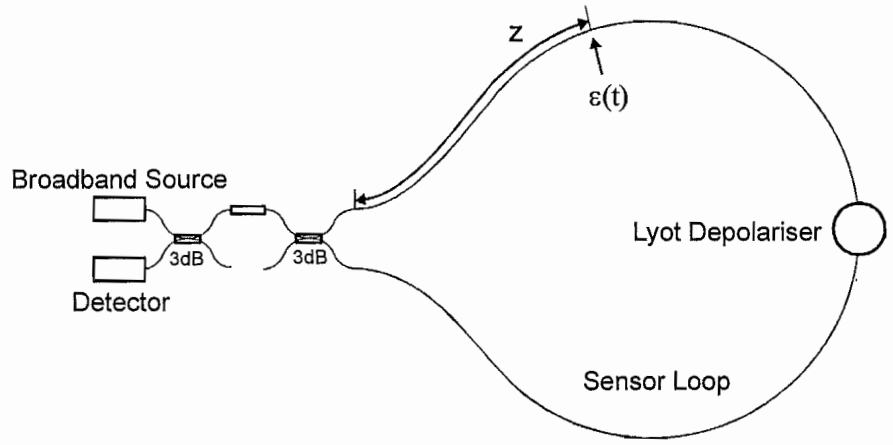

Figure 1.1.4 The Perturbed Sagnac Interferometer. *Shown above is the Sagnac interferometer, realised from fibre optic components. A disturbance, acting at a distance z from the CW propagating input end of the sensor loop generates a phase shift in the counter-propagating wavetrains.*

$$\frac{d\phi}{d\varepsilon} = \frac{2\pi}{\lambda}\left(n\frac{\partial l}{\partial \varepsilon} + l\frac{\partial n}{\partial \varepsilon}\right) \qquad [1.1.6]$$

where ∂l is the imposed length change, ∂n is the induced refractive index change and λ is the wavelength of the optical source. The propagating wave-train will incur a phase shift ϕ_1. The counter propagating wave-train encounters the disturbance a short time later, at a time t_2. However, now the strain imposed by the disturbance will generally have changed compared to that at time, t_1, and thus the phase shift induced in the counter propagating wave-train will have a different value, ϕ_2. There will therefore be a net phase shift, $\Delta\phi(t)$, between the propagating and counter propagating wave-trains as they arrive back at the detector, where:-

$$\Delta\phi(t) = \phi(t_1) - \phi(t_2) \qquad [1.1.7]$$

However, since the propagation velocity of the light and the sensor loop length are known, then t_1 and t_2 may be expressed in terms of the position of the disturbance.

$$\Delta\phi(t) = \phi\left(t - \frac{z}{V}\right) - \phi\left(t - \frac{L-z}{V}\right) \qquad [1.1.8]$$

where, V is the propagation velocity of the light through the fibre (given by $V = c / n$),c is the speed of light in a vacuum, n is the refractive index of the fibre, L is the length of the sensor loop and $\phi(t)$ is the phase shift introduced by the disturbance at a time t.

It may be shown that, if $2z / V << 1$ and if $\Delta\phi(t) << 1$, then Taylor expansion may be used to simplify the expression. Neglecting higher order terms, this yields an approximation:-

$$\Delta\phi(t) = \frac{L-2z}{V} \cdot \frac{d\phi}{dt} \qquad [1.1.9]$$

This yields a small signal approximation, showing that under these conditions the Sagnac interferometer has a response to a disturbance, proportional to the disturbance's distance from the loop centre and to its rate of change.

1.1.3 Phase biasing of the interferometer response

1.1.3.1 Principle of active-phase biasing

As previously stated, the phase response of the Sagnac interferometer is of the usual raised cosine shape, i.e. $I = 1 + \cos(\Delta\phi)$, shown in Fig 1.1.3. Without additional components, a small change in the relative phase offset between counter-propagating wave-trains therefore produces only a small change in the observed intensity at the output of the interferometer, making any sensor relatively insensitive to small disturbances. Active phase biasing, as presented by Dandridge et al [1.1.6], is a method by which the sensitivity of interferometers of this kind can be increased. The sensor loop of the interferometer is deliberately perturbed with a sinusoidal bias modulation at a frequency f. This is usually accomplished by either stretching the fibre using a piezoelectric cylinder, or, when faster

modulations are required, by using an electro-optic lithium niobate phase modulator. However, the latter generally suffer from high insertion loss and have a high polarisation sensitivity. The amplitude of this modulation is controlled such that the interferometer is driven sinusoidally between points corresponding to the positive and negative quadrature points of its phase response. As shown in Fig 1.1.5, this has the effect of biasing the system to the point in its response where the gradient of the response to additional phase modulation is approximately linear.

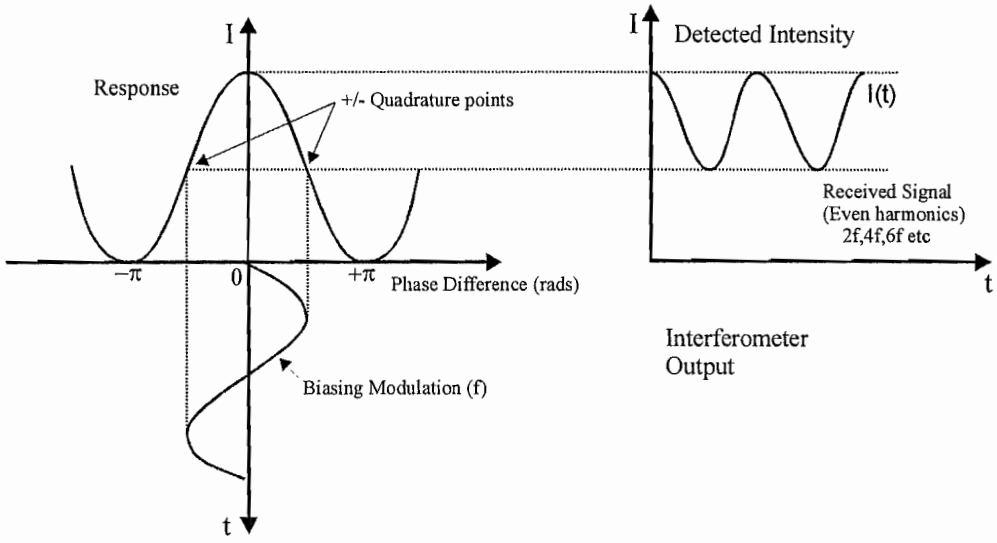

Figure 1.1.5 Response to phase bias in an unperturbed reciprocal interferometer. *A reciprocal interferometer gives a "raised-cosine" intensity versus phase response. A sinusoidal biasing modulation of frequency f drives the response of the interferometer between the positive and negative quadrature points. The output of the interferometer in turn contains only even harmonics of the biasing modulation.*

If there is no other cause of optical phase shift in the Sagnac loop (i.e. $\Delta\phi(t,z) = 0$), then the signal at the detector consists only of even harmonics of the biasing modulation frequency, as is shown in Fig 1.1.6. Since the interferometer is now biased on the relatively linear section of its response, a small change in the relative phase offset between counter-propagating wave-trains now induces a much larger change in the output intensity than if the interferometer were unbiased.

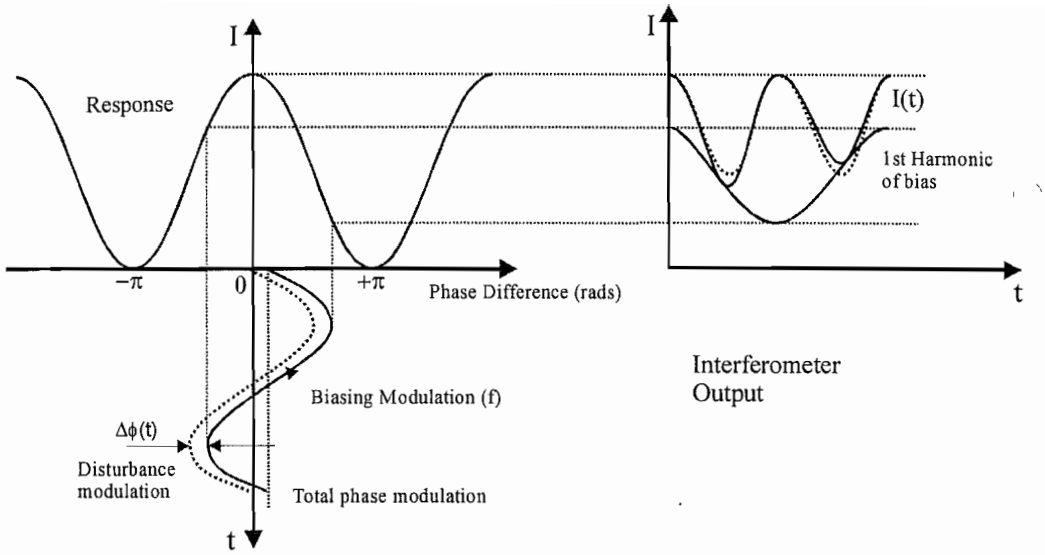

Figure 1.1.6 Biased response of perturbed reciprocal interferometer. *When the sensor loop of a biased interferometer is disturbed by a separate time dependent phase modulation, $\Delta\phi(t)$. This disturbance shifts the biasing modulation away from the origin, producing an anti-symmetric bias, which in turn, in addition to the even harmonics, produces odd harmonics of the biasing modulation frequency.*

Any disturbance acting on a biased reciprocal interferometer sensor loop creates an additional phase offset, $\Delta\phi(t,z)$, which adds to the bias modulation. This has the effect of amplitude modulating the bias modulation, producing a phase modulation between points on the interferometer response curve which are no longer symmetric to each other. As can be seen diagramatically in Fig 1.1.6, modulating the relative phase shift in this manner has the effect of introducing odd harmonics of the biasing modulation frequency to the signal received at the output of the interferometer.

The response of a phase biased Sagnac interferometer can therefore be expressed as shown in equation 1.1.10. A cosinusoidal modulation is applied at the very start of the sensor loop (i.e. $z = 0$) resulting in a phase modulation of frequency, ω, and amplitude A, controlled such that the interferometer is biased to quadrature.

$$I = 1 + \cos\left(A\left(\cos(\omega t) - \cos\left(\omega\left(t - \frac{n}{c} L \right)\right)\right) + \Delta\phi(t,z)\right) \qquad [1.1.10]$$

Fig 1.1.7 shows the frequency spectra for both an unperturbed phase biased Sagnac interferometer and a phase-biased Sagnac perturbed by a 1kHz tone disturbance creating a phase modulation 0.1radians in amplitude.

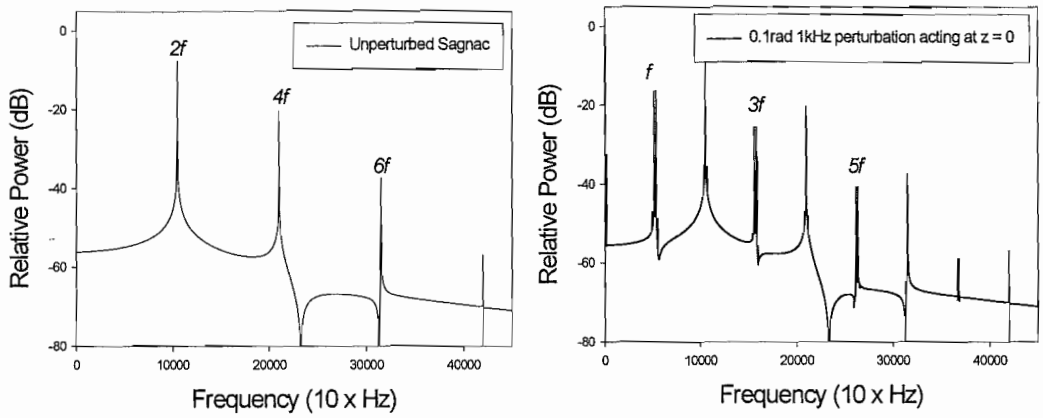

Figure 1.1.7 Theoretical intensity frequency spectra for a Sagnac interferometer. *Plotted above are the theoretical frequency spectra for a Sagnac interferometer phase biased with a sinusoidal modulation of $\pi/4$ amplitude. The spectra for an undisturbed sensor loop and for a loop perturbed by a 1kHz tone creating a phase modulation 0.1 radians in depth are shown.*

1.1.3.2 Signal recovery (active-dual side-band demodulation)

As shown in Fig 1.1.7, baseband information about the sensor loop perturbation, i.e. knowledge of $\Delta\phi(t,z)$ is no longer directly observable from the intensity output of a phase-biased interferometer. Instead, information related to the sensor loop perturbation reveals itself in side-bands, centred around the odd harmonics of the bias modulation frequency. These occur at frequencies of $(2m-1)\omega \pm \omega_{dist}$, where, m, is an integer, ω, is the bias modulation frequency and, ω_{dist}, the perturbation frequency.

In order to recover information about the perturbation, the signal must be demodulated. This can be accomplished using active dual-sideband demodulation. The detected signal is simply multiplied by a square wave of frequency equal to that of the applied bias modulation signal. This has the effect of "rectifying" all the components of the detected signal at frequencies corresponding to the odd harmonics of the bias modulation. The

perturbation signal is then recovered by low pass filtering this rectified waveform, to remove the residual high frequency components. Similarly, by multiplying the detected signal by a square wave with a frequency double that of the bias modulation frequency and low pass filtering, a DC level is obtained (related to the amplitude of the modulation carrier) which can be used as a normalisation constant, correcting for optical loss in the Sagnac and polarisation fading effects.

The process of dual-sideband demodulation can be mathematically expressed by expanding equation 1.1.10 into a series of terms containing each frequency component. This is accomplished using the Jacobian expansion [1.1.7], defined in equation 1.1.11 and 1.1.12 below.

The Jacobian expansion

$$\cos(x\sin\omega) = J_0(x) + 2\sum_{n=1}^{\infty} J_{2n}(x)\cos(2n\omega) \qquad [1.1.11]$$

$$\sin(x\sin\omega) = 2\sum_{n=1}^{\infty} J_{2n-1}(x)\sin((2n-1)\omega) \qquad [1.1.12]$$

where J_n is the n^{th} Bessel function, and x and ω are arbitrary functions
Using this expansion, equation 1.1.10 can therefore be expressed as;

$$\begin{aligned} I = 1 &+ J_0(A.a_1)\cos\Delta\phi(t,z) + \\ &+ 2J_2(Aa_1)\cos(2\psi_1)\cos\Delta\phi(t,z) \\ &+ 2J_4(Aa_1)\cos(4\psi_1)\cos\Delta\phi(t,z) \\ &+ 2J_6(Aa_1)\cos(6\psi_1)\cos\Delta\phi(t,z) + ..O(\cos(8\psi_1)) \\ &+ 2J_1(Aa_1)\sin(\psi_1)\sin\Delta\phi(t,z) \\ &+ 2J_3(Aa_1)\sin(3\psi_1)\sin\Delta\phi(t,z) \\ &+ 2J_5(Aa_1)\sin(5\psi_1)\sin\Delta\phi(t,z) + ..O(\cos(7\psi_1)) \end{aligned} \qquad [1.1.13]$$

where, a_1, and, ψ_1, are constants which depend on the modulation frequency, and sensor loop length. This now shows all of the frequency components as previously displayed in Fig 1.1.7. The final point to note is that Fig 1.1.7 used a small signal approximation for the amplitude of the sensor loop perturbation. This being the case, $cos\Delta\phi(t,z) \approx 1$ and $sin\Delta\phi(t,z) \approx \Delta\phi(t,z)$.

1.1.4 Configurations for disturbance location

It was previously noted that the Sagnac interferometer was potentially capable of locating the position of a time varying strain disturbance [1.1.8]. However, the response of the Sagnac interferometer to a disturbance, as shown in equation 1.1.9, still presents us with a problem. We have two unknowns, i.e. the position of the disturbance and its rate of change. The following section outlines previously published work, carried out in order to solve this problem and hence locate the disturbance.

1.1.4.1 The Mach-Zehnder Sagnac interferometer

Many schemes have been proposed, in order to solve the location problem presented by the Sagnac response, shown in equation [1.1.9]. The first method to be reported was carried out by Dakin [1.1.9] et al, at Plessey research. In this approach, the phase shift introduced by the disturbance acting on the sensor loop was directly measured by combining signals from the Sagnac interferometer with the processed output of a separate Mach-Zehnder interferometer, Fig 1.1.8.

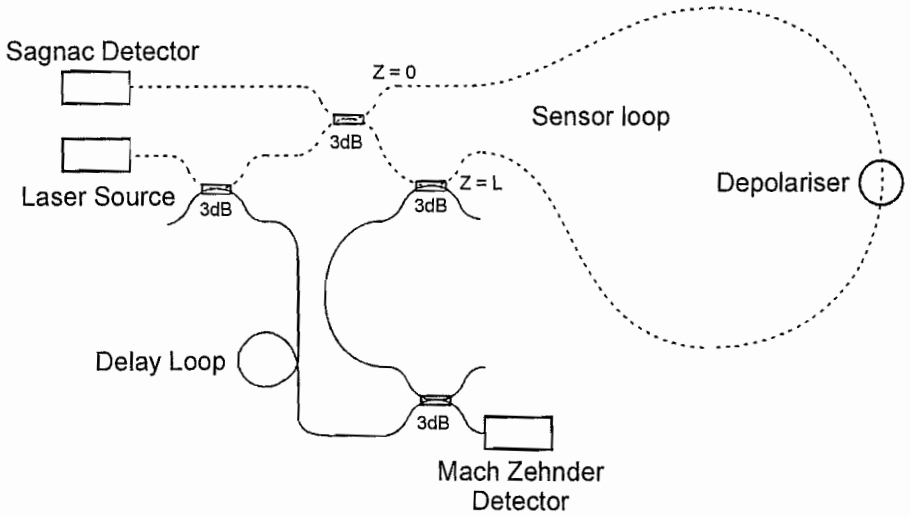

Figure 1.1.8 The combined Mach-Zehnder, Sagnac interferometer. *A Sagnac is formed by a 200m sensor loop, a laser source and a separate detector (highlighted by a dotted line). The Mach-Zehnder is formed by splitting light from one end of the Sagnac sensor loop and from the source and balancing the paths from source and sensor loop to a second detector where the two optical signals are combined.*

In this original method the Sagnac interferometer was formed by a laser source, a 200m long sensing loop of single mode fibre and a detector. The Sagnac is shown as a dotted line in Fig 1.1.8. As previously described, when the sensing loop is disturbed by a time varying phase modulation, the Sagnac detector receives a signal which is proportional to the position at which the disturbance acts and also to the rate of change of this imposed phase modulation.

$$\Delta\phi(t)_{Sagnac} \propto z \cdot \frac{d\phi(t)}{dt} \qquad [1.1.14]$$

The Mach-Zehnder interferometer is formed by coupling light from the source via a delay path (solid line) and combining it with light emerging from one end of the Sagnac sensor loop by means of a delay loop in the reference arm of the Mach-Zehnder interferometer. These two arms of the Mach-Zehnder are balanced to within the coherence length of the source, (it is the need for coherence length balancing, without the need for excessive accuracy in balancing the paths that dictated the use of a laser source). This delay loop is by necessity approximately of the same length as the sensor loop. With appropriate quadrature phase biasing the Mach-Zehnder detector generates a signal proportional to the actual phase modulation induced in the sensing loop.

$$\Delta\phi(t)_{Mach-Zehnder} \propto \phi(t) \qquad [1.1.15]$$

It is easy to differentiate this signal with respect to time, to derive $d\phi/dt$. The rate of change of the phase shift induced by the time varying disturbance is then known, allowing the Sagnac response, equation [1.1.9], to be decoded and the position found.

This method is a simple solution to the problem presented by the Sagnac response. However, as is often the case with the first work in an area, there are several disadvantages. In order for the sensor to operate, the two arms of the Mach-Zehnder interferometer must be balanced to within the coherence length of the light source. The Sagnac interferometer, however, performs better with a short coherence-length source, which would make it extremely difficult to balance the optical paths of the Mach-Zehnder. A compromise must therefore be achieved between the sensor loop length, and the

coherence length of the source. There is also the added difficulty that there is a need for a length of fibre of approximately equal length to the sensor loop, on a single reel or drum at the interrogation end of the optics structure making it highly susceptible to "pick-up" environmental acoustic noise, which would increase the phase noise in the system. As reported, a sensor loop length of 200m was realised. However, for our application we require a sensor loop length of several tens of kilometres. Using this architecture, this would prove difficult. An added disadvantage also arises from the compromise necessary in choosing the coherence length of the source, as the source would have a longer coherence length than that used for a Sagnac alone and hence a narrower line width. Polarisation fading effects would therefore be more difficult to reduce using the Lyot depolariser as previously discussed, as this would require a long length of HI-BI fibre making it impractical and, as previously stated, a long coherence length source would increase noise from Rayleigh backscatter and Fresnel reflections. A further disadvantage with this optical system is its high intrinsic optical loss. This is 6dB above the theoretical minimum for the Sagnac loop and also 6dB higher for the Mach-Zehnder.

1.1.4.2 The Michelson / Sagnac interferometer

The phase shift induced by the time varying disturbance may also be measured by other forms of interferometer. Spammer et al [1.1.10-1.1.11] reported the investigation of a combined Sagnac-Michelson interferometer, shown in Fig 1.1.9. This was achieved by using wavelength division technology to define two separate interferometers. The Sagnac interferometer was formed in the usual manner: a light source, of wavelength λ_1, is coupled into two wavetrains, which then counter-propagate around a length of single mode fibre, forming a loop. The interference pattern produced by the Sagnac interferometer is then observed by coupling the light in a narrow band around λ_1 onto a detector by using WDM technology.

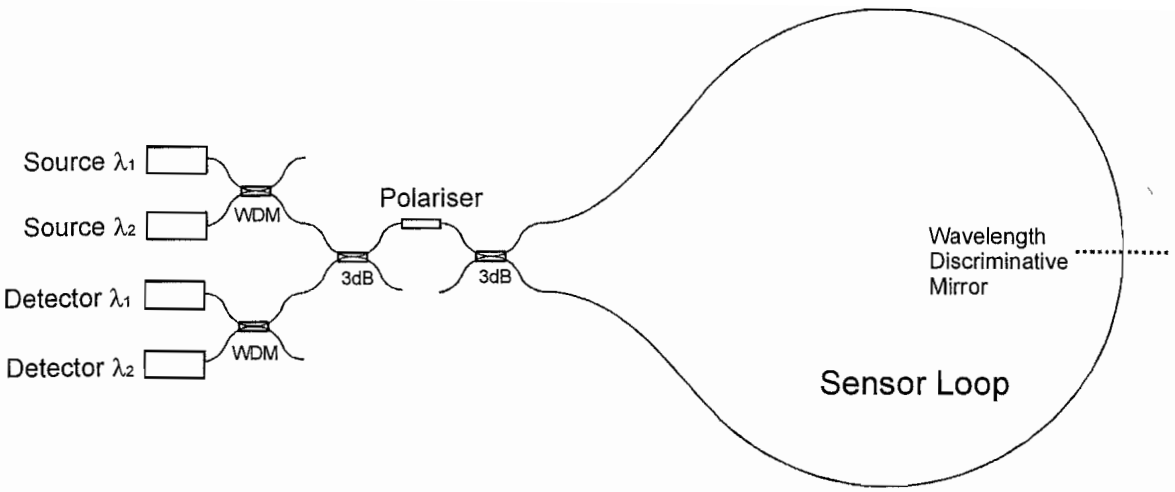

Figure 1.1.9 The combined Sagnac-Michelson Interferometer. *Two optical sources are routed around a sensing loop of fibre before each is incident on its own optical detector. The Sagnac is formed is the same way as previously presented whilst the Michelson is formed using a wavelength discriminating mirror positioned at the centre of the sensing loop of fibre.*

The Michelson interferometer in this architecture is formed by coupling light from a second light source, with a wavelength of λ_2, into two wavetrains counter-propagating around the same sensor loop. However, approximately at the centre of the sensor loop is a wavelength discriminative mirror (for example a fibre Bragg grating or Dichroic mirror), which reflects the two wavetrains at λ_2. The reflected wavetrains then propagate back to the start of the sensor loop, where they interfere. Light in a narrow band around λ_2 is then coupled onto a second detector, where the Michelson interference pattern can be observed.

This method again suffers from the disadvantage of having to balance the two arms of the Michelson interferometer to within the coherence length of the source, which necessitates a source of narrower line-width than would ideally be used in a Sagnac. An additional disadvantage is that this method requires two separate optical sources, each of different wavelengths and two optical detectors. However, since a delay coil is no longer needed to balance the optical paths of the Michelson, it does offer the advantage that there would not be a large length of fibre acting as a microphone near the interrogation end of the sensor. It also presents a further advantage of having no additional intrinsic loss. Additional optical loss would of course arise from the use of non-ideal optical components.

1.1.4.3 The dual-path Sagnac interferometer

A second way of locating a time varying strain disturbance acting on the sensor loop of a Sagnac based sensor, is to configure two separate Sagnac interferometers such that they share a common part of the loop. This was first presented by Udd [1.1.8]. A simple architecture of such a sensor is shown in (Fig 1.1.10). In order for each of the Sagnacs to give independent responses, the position at which the disturbance acts on each of the sensors must be different. This is achieved by offsetting each of the Sagnac interferometers by including delay coils of known lengths into the optical paths, either before or after the sensor loop, depending on the interferometer path.

The two separate Sagnac interferometers are formed by the following components:-

Sagnac 1: Consists of the source, detector 1, a delay coil of length L1 and the sensor loop. (Shown by a dotted line).

Sagnac 2: Consists of the source, detector 2, a delay coil of length L2 and the sensor loop.

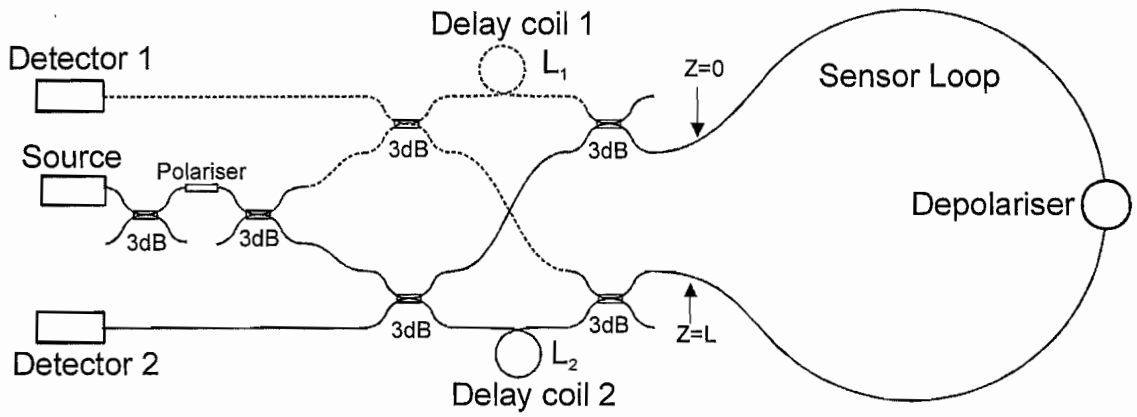

Figure 1.1.10 The dual path Sagnac interferometer. *Two Sagnac interferometers are formed by routing using 3dB couplers. This allows them to share the same sensor transducer but are offset relative to each other by delay coils of known lengths L1 and L2.*

As was shown in equation 1.1.8, there will be a net phase difference induced between the counter-propagating wave-trains in each of the two Sagnac interferometers.

The first Sagnac incurs a net phase shift of:-

$$\Delta\phi_1(t) = \phi\left(t - \frac{z}{v}\right) - \phi\left(t - \frac{L + L1 - z}{v}\right) \qquad [1.1.16]$$

The difference seen between this response and that of the single Sagnac is that the CW propagating wave-train for the first Sagnac has now to first pass through a delay coil of length, *L1*, before passing through the sensor loop. This introduces a time delay of, *L1/v*, to the phase term on the RHS of equation 1.1.16. The second Sagnac gives a similar response, but now it is the CCW propagating wave-train that is delayed by an amount *L2/v*:-

$$\Delta\phi_2(t) = \phi\left(t - \frac{z + L2}{v}\right) - \phi\left(t - \frac{L - z}{v}\right) \qquad [1.1.17]$$

Again using Taylor expansion, these phase terms may be expressed as follows.

$$\Delta\phi_1(t) \approx \frac{d\phi}{dt}\frac{L - L1 - 2z}{v} \qquad [1.1.18]$$

$$\Delta\phi_2(t) \approx \frac{d\phi}{dt}\frac{L + L2 - 2z}{v} \qquad [1.1.19]$$

The two Sagnacs yield two independent equations, each a different function of the disturbance position and rate of change. Solving simultaneously allows the position and the rate of change of the strain disturbance to be found.

An adaptation of this structure was investigated by Rønnekleiv et al [1.1.13]. However, to ensure operation of the interferometer at its sensitive quadrature point, the first two 50/50 couplers were replaced by three port devices. In this way, it is ensured that at least one of the outputs would be biased at a sensitive operating point. The phase modulation induced by the disturbance is then determined by observing the intensity on the two optical detectors. The disturbance position may then be determined, as shown in equations 1.1.18 and 1.1.19. This dual-Sagnac method has several advantages over previously discussed methods. The first is that, due to the perfectly balanced nature of the Sagnac, a low coherence source may now be used, reducing the phase noise inherent to interferometers. Additionally, due to the fact that the response of each interferometer is of the same nature, it is not necessary to differentiate the output from one of the interferometers in order to be able to locate the disturbance. (I.e. they are both proportional to the rate of change of the disturbance acting on the sensor loop). The location of the disturbance may be directly

related to the ratio of the signals obtained from each of the Sagnacs, simplifying the signal processing. A sensor loop length of 100m was achieved, with a delay length of a further 100m. The positional sensitivity reported was ±0.3m. There are, however, problems with this architecture. Dual detectors make the system complicated, due to the need to balance the gain of each channel. Also, delay coils are required at the interrogation end of the structure. This is not as much of a problem as in previous structures, since the delay length is no longer required to be of the same length as the sensor loop and can be as little as 10% of the total loop length. Although the sensor loop length was far shorter than that required by our application, there should be fewer problems involved in increasing the length of the sensor loop, using this architecture.

Fang [1.1.14] reported the investigation of a second dual-path Sagnac interferometer. Active phase biasing, as presented earlier, was used to ensure operation at the quadrature point. This method has the advantage that the two signals, from each of the Sagnac interferometers, are detected by a single detector. They are then separated by band-pass filtering around the biasing frequency followed by phase sensitive detection. Again, a relatively short sensor loop length of 800m was achieved, far shorter than that required by the application of interest to the current project. Also the intrinsic loss of dual-path Sagnac interferometers is usually at least 12dB higher than a single Sagnac.

1.1.4.4 The dual-wavelength dual-Sagnac interferometer

Another way of defining two Sagnac interferometers, as first suggested by Udd [1.1.12], is to use wavelength-division multiplexing. In such a case, two separate Sagnac interferometers may be defined by routing light from two separate sources, such that they travel different paths before sharing a common sensor loop, in much the same way as was done for the dual-path Sagnac. There is, however, a minor complication. Since each of the Sagnacs are operated at different wavelengths, then the rate of change of phase, as seen by each of the interferometers, will be marginally different. They can, however, be related through equation 1.1.20.

$$\frac{d\phi}{dt} = \frac{\partial\phi}{\partial\varepsilon}\frac{\partial\varepsilon}{\partial t} \qquad [1.1.20]$$

where, ϕ, is the optical phase, ε, is the imposed strain and, t, is the time. Since the rate of change of the induced strain is equal for each of the interferometers, then we may, through equation 1.1.6, show that the phase change induced by the imposed strain is inversely proportional to the optical wavelength. The phase response for each of the interferometers may then be shown to be proportional to:-

Sagnac 1: $$\Delta\phi_1 \propto \frac{2\pi}{\lambda_1}\frac{\partial\varepsilon}{\partial t}\frac{L - L_1 - 2z}{v}$$

Sagnac 2: $$\Delta\phi_2 \propto \frac{2\pi}{\lambda_2}\frac{\partial\varepsilon}{\partial t}\frac{L + L_2 - 2z}{v}$$

Spammer et al [1.1.15] presented a dual-wavelength, dual-Sagnac of this nature using separate sources at 1300nm and 1550nm respectively. The response for each Sagnac was then detected using separate detectors for each. However, as with all previously published sensors, the sensing element of the loop was only of the order of a few hundred metres. As a final note, there has also been work published on multiplexing Sagnac interferometers, allowing discrimination between multiple sensor loops [1.1.16].

1.1.5 Summary and conclusions

This chapter has introduced the fibre optic Sagnac interferometer, with emphasis on its use as a distributed disturbance sensor. It has been shown that, although care has to be taken and extensive optoelectronic engineering performed when constructing such a device, it should be relatively simple to construct a sensor which would suit our application, i.e. time-varying strain monitoring of a fibre optic service. Although relatively insensitive to external perturbation, methods of active-phase biasing have been introduced as a solution to increasing the acoustic sensitivity of the Sagnac, employing active dual-sideband demodulation as a signal recovery method.

Several previously researched fibre optic architectures have been discussed and the advantages and disadvantages for each brought to light. We believe that a dual-Sagnac optical architecture can be realised which would incorporate the advantages exhibited by the previously researched systems, whilst avoiding the disadvantages. In this way, as

presented in detail in the next chapter, we have conceived a dual-wavelength, dual-Sagnac optical architecture with advantages in its use of:-

1) An extended 40km long sensor loop.
2) Use of a single broadband high-power optical source.
3) Use of a single optical detector.
4) Low intrinsic optical loss.

References Chapter 1.1

[1.1.1] V.J. Tejippe, "Passive fibre optic components made by fused biconical taper process." Proceedings of SPIE, Optical fibres and their applications, Vol 1085, 1989.

[1.1.2] W.K.Burns, R.P.Moeller, C.A.Villarruel, M.Abebe, "An all fibre gyroscope with polarisation maintianing fibre", Optics letters, Vol 9, No 12, 1989.

[1.1.3] C.Cutter, S.A.Newton, H.J.Shaw, "Limitation of rotation sensing by scattering", Optics letters, Vol 5, pp-488-490, 1980.

[1.1.4] P.R.Cooper, "All-fibre Lyot depolariser." Optics and laser technology, Vol 18, No 2, 1986.

[1.1.5] N.J.Frigo, A.Dandbridge, A.B.Tveten, "Technique for elimination of polarisation fading in fibre interferometers." Electronics letters, Vol 20, No 8, pp 319-320, April 12, 1984

[1.1.6] A.Dandridge, A.B.Tveten, G.H.Siegel, E.J.West, T.G.Giallorenzi, Electronic letters, Vol 16, No 11, pp-408-409, 1980.

[1.1.7] N.W.McLachlan, "Bessel functions for engineers", Publisher Oxford University Press, 1946.

[1.1.8] D.M.Shupe, Applied Optics, Vol 19, No 5, pp 654-655, 1980.

[1.1.9] J.P.Dakin, D.A.J.Pearce, C.A.Strong, C.A.Wade, "A novel distributed optical fibre sensing system, enabling location of disturbances in a Sagnac loop interferometer". Proceedings of sixth EFOC/LAN, p. 276-279,1988.

[1.1.10] S.J.Spammer, P.L.Swart, A.Boosen, "Interferometric distributed fibre optic sensor", Applied optics, Aug 1st, Vol 35, No 22, pp 4522-4523, 1996.

[1.1.11] S.J.Spammer, A.A. Chtcherbakov, P.L.Swart, "Dual-wavelength Saganc-Michelson distributed optical fibre sensor", Proceedings SPIE, pp 2838-34, Aug, 1996.

[1.1.12] E.Udd, "Sagnac distributed sensor concepts", proceedings of SPIE, Vol 1586, pp 46-52, 1991.

[1.1.13] E.Rønnekleiv, K. Bløtekjær, K. Kràkenes, "Distributed fibre sensor for location of disturbances", Proceedings of 9th Optical fibre sensors Conference (National Research Council of Italy, Florence, 1993), postdeadline paper PD7.

[1.1.14] X.Fang. "A Variable loop Sagnac interferometer for distributed impact sensing" *Optics letters*, Vol 21, No 6, March 15th, 1996.

[1.1.15] S.J.Spammer, A.A.Chtcherbakov, P.L.Swart, "Distributed dual wavelength Sagnac impact sensor", microwave and optical technology letters, Feb 20, Vol 17, No 3, pp 170-173, 1998.

[1.1.16] B.J.Vakov, M.J.F.Digonnett, G.S.Kino, "A novel fibre optic sensor array based on the Sagnac interferometer", Journal of lightwave technology, Vol 17, No 11 pp-2316-2326, 1999.

Chapter 1.2 The Dual-Wavelength Dual-Sagnac Interferometer, Theoretical Analysis.

This chapter presents details of our novel dual-wavelength, dual-Sagnac interferometer configuration. The reader is advised that this chapter deals extensively with the theoretical background upon which this sensor is based. The complete system and its use as a disturbance sensor is dealt with in chapter 1.4. Firstly, the architecture of the system will be presented and the principle of operation upon which it is based will be detailed. Unlike other dual Sagnac's, there is the possibility for optical cross-talk [1.2.1] to occur between the two optical channels if the WDM components used are imperfect. The analytical response of the novel dual-wavelength Sagnac is derived, and the effects of optical crosstalk are modelled. The complications that this creates are then discussed, and a method for reducing these unwanted effects is presented. Signal recovery, using an active dual-sideband demodulation scheme [1.2.2] is then introduced and the relevant expressions that model this are derived, allowing a calibrated disturbance positioning algorithm to be coded.

1.2.1 Architecture of the dual-wavelength dual-Sagnac interferometer

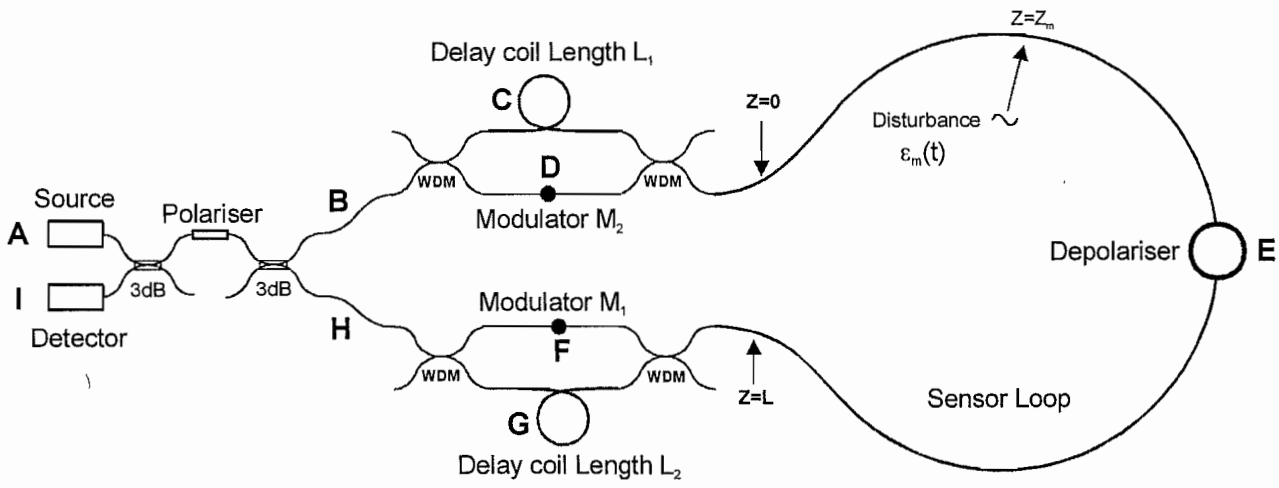

Figure 1.2.1 The dual-wavelength dual-Sagnac Interferometer. *Each Sagnac interferometer is formed by paths defined by the WDMs. The two Sagnac interferometers formed are phase biased by piezoelectric modulators, M_1 and M_2 . The sensor loop for each interferometer is also offset by delay loops of lengths, L_1 and L_2,, respectively.*

1.2.1.1 Principle of operation

The optics structure proposed above would ideally operate as follows. Light from a single broadband, low coherence source would be spectrally sliced into two wavelength bands using wavelength-division-multiplexers (WDM's). These would route the light along two essentially independent Sagnac interferometer loops, one for each wavelength band. The first Sagnac loop is defined by the bi-directional path, ABCEFHI (Path 1), read clockwise around the sensor architecture. This circuit includes a fibre delay coil, C, a sensing fibre length, E, and a piezoelectric phase modulator, F. Similarly, the second Sagnac interferometer is defined by routing light bi-directionally around a path labelled ABDEGHI (Path 2). This again includes a piezoelectric modulator, D, a common sensing fibre length, E, and a fibre delay coil, G. The effective centres of each of the sensor loops are offset (in opposite directions) by half of the path length of the delay coils labelled, C, and, G. This should ensure that each Sagnac interferometer gives a different response to a common perturbation, despite sharing a common fibre section, allowing simultaneous evaluation of the position of the disturbance, its amplitude and its rate of change.

Each Sagnac interferometer is sinusoidally phase-biased at different frequencies, (f_1 and f_2). The bias frequencies, (f_1 and f_2), were chosen such that the magnitude of their difference frequency, $|f_1-f_2|$, was above the frequency range of the expected disturbance signals (i.e. the base-bandwidth of the sensor output). This phase bias should allow both of the interferometers to share a common optical detector, as it provides amplitude-modulated carriers of a different frequency for each signal generated by each Sagnac interferometer. As described in the previous chapter, due to the non-linear nature of the Sagnac phase response when unperturbed, only even harmonics of the bias modulation are expected on the detected signal (although, in practice, the detection system will be band limited to respond only up to the 2^{nd} harmonic). However, when a disturbance acts on the loop, odd harmonics of the bias frequency are expected to appear.

After detection, the output from each Sagnac is recovered using a dual, active dual-sideband electronic demodulation technique. Each lock-in (Phase sensitive detection system) monitors components, f_1, f_2, $2f_1$ and $2f_2$ of the bias frequencies in the detected signal, by multiplying the detected signal by the corresponding frequency, before low-pass

filtering the output. This generates four demodulated outputs, df_1, $d2f_1$, df_2, and $d2f_2$, which may then be processed in the usual manner, as described in section 1.1.4 to give a position-dependent result. If we assume the system stays within a small signal approximation, this results is a ratio which is independent of the rate of change or amplitude of the perturbation. Figure 1.2.2 shows the position error that would result using this approximation versus the amplitude of the disturbance. As can be seen below levels of 0.1 radians the approximation creates very small errors of the order of 100m.

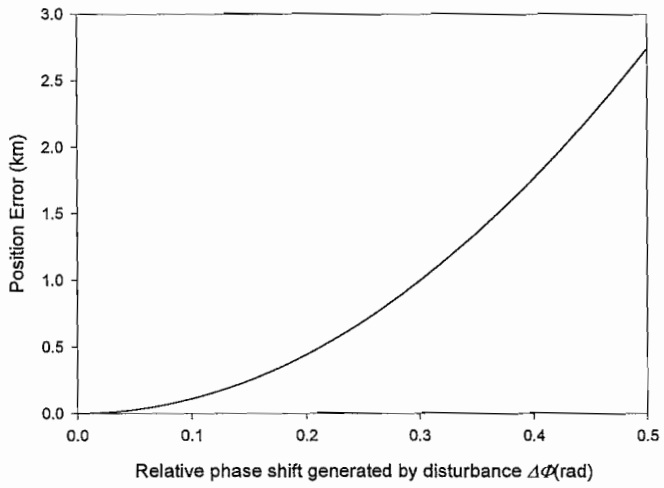

Figure 1.2.2 Position error that results from using small signal approximation versus the disturbance amplitude at the end of a 40km long Sagnac interferometer. Plotted is the amplitude of the relative phase shift generated at the interferometer output versus the positional error generated using this small signal approximation.

Unfortunately, for a real system, the situation is not quite as simple. Due to non-ideal optical WDM components, there will inevitably be a certain amount of residual optical crosstalk, such that a further two optical paths become weakly allowed. These new paths are labelled ABCEGHI (Path 00) and ABDEFHI (Path 11). The first allows light to travel around the sensor loop without incurring a phase-bias modulation. This allows a disturbance to create a base-band signal on the detector when the sensor loop is perturbed. Fortunately, as detailed later, this component is removed by electronic signal recovery. The second crosstalk path is potentially more serious, as it allows light to be phase-biased by both frequencies corresponding to each Sagnac, resulting in an error in the calibration of the sensor after signal recovery. As will be shown shortly, this fortunately is a predictable effect which can be corrected for after calibration.

1.2.1.2 Advantages of our novel dual-wavelength dual-Sagnac

Our new optical architecture presents many advantages over previously researched Sagnac architectures:-

1) Use of a single high-power broadband optical source. A superluminescent Erbium doped source is used, which is spectrally sliced into two bands, routed to form two Sagnac interferometers, reducing the optoelectronics required for the sensor. Previous dual-wavelength systems have used independent sources, making the cost and complexity of the system unnecessarily high.

2) Use of a single optical detector. By phase biasing each of the Sagnacs at different frequencies, the signals generated by each are multiplexed onto a single, high-gain, optical detector. They are then separated using lock-in amplifiers. Previous dual-Sagnac systems have used separate optical detectors, requiring the gain and frequency response of each to be carefully balanced. Our approach also offers the advantage of recovering each frequency component separately, allowing self normalisation of each optical channel, hence correcting for polarisation fading effects and imbalanced loss in each Sagnac.

3) An extended sensor loop length of 40km. Previously devised systems have used lengths far shorter than this novel sensor. To our knowledge, the longest reported experimental sensor used a sensor loop length of 800m; approximately 50 times shorter.

4) A low intrinsic optical loss, due to inherent architectural design losses. Using ideal components the basic Sagnac as described in chapter 1.1, Fig 1.1.2. has an excessive optical loss of only 6dB. Previously researched dual-path Sagnac interferometers have, in general, had a loss of 15dB, whereas our new dual-wavelength Sagnac has an intrinsic optical loss of only 9dB. The additional 3dB arising from the requirement for spectral slicing of the single source.

1.2.2 Analytical Response of a Dual-Wavelength Sagnac Interferometer

1.2.2.1 Derivation of intensity at the detector

Due to the complications created by optical crosstalk, we shall now analyse the system response, including any contributions arising due to cross-talk. Previous optical architectures have used two separate sources [1.2.3,1.2.4], making the response for each of the interferometers simpler to calculate. This new optical architecture employs spectral slicing [1.2.5] to define the two Sagnac interferometers and so it is necessary to consider, independently, the effect on each element of the source spectra. We shall define the amplitude of the electric field, $E(t,\lambda)$, of an element of received radiation to be :-

$$E(t,\lambda) = E_0(t,\lambda)\exp\left(j\cdot\left(\frac{2\pi c}{n\lambda}t + \phi(t)\right)\right) \qquad [1.2.1]$$

where $E_0(t,\lambda)$ is the peak amplitude of the electric field of the received radiation at a time t, with a wavelength, λ, n is the refractive index of the fibre, c is the speed of light in a vacuum and, $\phi(t)$, is the time-dependent optical phase modulation, induced as the optical wavetrain propagates through a phase modulator. Here, $\phi(t)$ may be caused by either a strain perturbation on the sensor loop, or by one of the piezoelectric bias modulators.

In order to calculate the theoretical intensity of light at the optical detector, we must consider the contributions for light travelling in both directions around each of the four previously defined optical paths. We shall assume that the first two wavelength-independent couplers in the system have an intensity coupling fraction, f, and that the WDM's have spectral intensity transmission functions, $T_1(\lambda)$, and, $T_2(\lambda)$, for each of their output arms, respectively. Considering the general case, where we have m separate strain disturbances, $\varepsilon_m(t)$, acting at positions, z_m, around the sensor loop, each creating a phase perturbation, $\phi_m(t)$, we obtain expressions for the amplitude components for light travelling around the allowed optical paths, as shown in equations (1.2.2-1.2.9).

Electric field components, for CW propagating light along the optical route labelled in Fig. 1.2.1. Where the subscript denotes optical path, i.e. CW1=Path 1

$$E_{CW1} = f(1-f)T_1^2(\lambda)E_0\left(t-\frac{n}{c}(L+L_1),\lambda\right)\exp\left(j\cdot\beta_1(\lambda)\cos(\omega_1 t)+j\cdot\sum_m\phi\left(\lambda,t-\frac{n}{c}(L-z_m)\right)\right) \quad [1.2.2]$$

$$E_{CW2} = f(1-f)T_2^2(\lambda)E_0\left(t-\frac{n}{c}(L+L_2),\lambda\right)\exp\left(j\cdot\beta_2(\lambda)\cos\left(\omega_2\left(t-\frac{n}{c}(L+L_2)\right)\right)+j\cdot\sum_m\phi\left(\lambda,t-\frac{n}{c}(L+L_2-z_m)\right)\right) \quad [1.2.3]$$

$$E_{CW00} = -f(1-f)T_1(\lambda)T_2(\lambda)E_0\left(t-\frac{n}{c}(L+L_1+L_2),\lambda\right)\exp\left(j\cdot\sum_m\phi\left(\lambda,t-\frac{n}{c}(L+L_2-z_m)\right)\right) \quad [1.2.4]$$

$$E_{CW11} = -f(1-f)T_1(\lambda)T_2(\lambda)E_0\left(t-\frac{n}{c}L,\lambda\right)\exp\left(j\cdot\beta_1(\lambda)\cos(\omega_1 t)+j\cdot\beta_2(\lambda)\cos\left(\omega_2\left(t-\frac{n}{c}L\right)\right)+j\cdot\sum_m\phi\left(\lambda,t-\frac{n}{c}(L-z_m)\right)\right) \quad [1.2.5]$$

Electric field components, for CCW propagating light along the optical route labelled in Fig. 1.2.1. Where the subscript denotes optical path i.e. CWW1=Path 1

$$E_{CCW1} = f(1-f)T_1^2(\lambda)E_0\left(t-\frac{n}{c}(L+L_1),\lambda\right)\exp\left(j\cdot\beta_1(\lambda)\cos\left(\omega_1\left(t-\frac{n}{c}(L+L_1)\right)\right)+j\cdot\sum_m\phi\left(\lambda,t-\frac{n}{c}z_m\right)\right) \quad [1.2.6]$$

$$E_{CCW2} = f(1-f)T_2^2(\lambda)E_0\left(t-\frac{n}{c}(L+L_2),\lambda\right)\exp\left(j\cdot\beta_2(\lambda)\cos(\omega_2 t)+j\cdot\sum_m\phi\left(\lambda,t-\frac{n}{c}(L+z_m)\right)\right) \quad [1.2.7]$$

$$E_{CCW00} = -f(1-f)T_1(\lambda)T_2(\lambda)E_0\left(t-\frac{n}{c}(L+L_1+L_2),\lambda\right)\exp\left(j\cdot\sum_m\phi\left(\lambda,t-\frac{n}{c}(L_1+z_m)\right)\right) \quad [1.2.8]$$

$$E_{CCW11} = -f(1-f)T_1(\lambda)T_2(\lambda)E_0\left(t-\frac{n}{c}L,\lambda\right)\exp\left(j\cdot\beta_1(\lambda)\cos\left(\omega_1\left(t-\frac{n}{c}L\right)\right)+j\cdot\beta_2(\lambda)\cos(\omega_2 t)+j\cdot\sum_m\phi\left(\lambda,t-\frac{n}{c}z_m\right)\right) \quad [1.2.9]$$

Where $\beta_1(\lambda)$ and $\beta_2(\lambda)$ are the wavelength-dependent modulation depths for each of the piezoelectric modulators, respectively. Note also that the optical frequency term, shown previously in equation 1.2.1, has now been omitted, as it is common to all equations. The total complex amplitude of the electric field incident on the detector can now be expressed simply as the sum of these eight terms. The intensity of light at the detector may then be found by multiplying the electric field term with its own complex conjugate and taking its time average (Eq. 1.2.10).

$$I(t,\lambda) = \left\langle E(t,\lambda)\cdot E^*(t,\lambda)\right\rangle \quad [1.2.10]$$

Due to the low coherence length of the broadband source, only light travelling around optical paths of equal length can interfere and hence give a contribution to the terms in the derived intensity function (assuming that the delay coils, of lengths L_1 and L_2, have a

length difference significantly greater than the coherence length of the source). It should be noted that, for our system, the source coherence length $L_c = 120\mu m$ and L_1-L_2 is 500m. The remaining terms yield an expression for the intensity at the detector, as shown in equation (1.2.11). Five distinct terms arise from this equation, the first of which has only DC components, whereas the other four are time varying.

$$I(t,\lambda) = 2f^2(1-f)^2 I_0^2(\lambda)[DC + Term1 + Term2 + Term3 + Term4] \qquad [1.2.11]$$

$$DC = T_1^4(\lambda) + T_2^4(\lambda) + 2T_1^2(\lambda)T_2^2(\lambda)$$

$$Term1 = T_1^2(\lambda)T_2^2(\lambda)\sum_m \Delta\phi_{m00}(t,z,\lambda)$$

$$Term2 = T_1^4(\lambda)\cos\left[\beta_1(\lambda)\left(\cos\omega_1 t - \cos\left(\omega_1\left(t - \frac{n}{c}(L+L_1)\right)\right)\right) + \sum_m \Delta\phi_{m1}(t,z,\lambda)\right]$$

$$Term3 = T_2^4(\lambda)\cos\left[\beta_2(\lambda)\left(\cos\omega_2\left(t - \frac{n}{c}(L+L_2)\right) - \cos\omega_2 t\right) + \sum_m \Delta\phi_{m2}(t,z,\lambda)\right]$$

$$Term4 = T_1^2(\lambda)T_2^2(\lambda)\cos\left[\beta_1(\lambda)\left(\cos\omega_1 t - \cos\omega_1\left(t - \frac{n}{c}L\right) + \beta_2(\lambda)\left(\cos\left(\omega_2\left(t - \frac{n}{c}L\right)\right) - \cos\omega_2 t\right)\right) + \sum_m \Delta\phi_{m11}(t,z,\lambda)\right]$$

Term 1 (from path 00, ABCEGHI) is generated by the first cross-talk path. Light travels around the optical network without being phase biased. For a small perturbation, a base-band signal is seen by the detector due to the non-linear response of the unbiased Sagnac, this appears at double the frequency of a phase disturbance acting on the loop.

Term 2 (from path 1, ABCEFHI) is generated by the first (wavelength-defined) Sagnac interferometer. Light propagates around the loop, incurring a phase bias of frequency, ω_1, and a time delay of $-nL_1/c$. This is a desired signal and is processed in the usual manner.

Term 3 (from path 2, ABDFGHI) is generated by the second (wavelength-defined) Sagnac interferometer. Light propagates around the loop incurring a phase bias of frequency, ω_2, and a time delay of nL_2/c. Again this is a desired signal.

Term 4 (from path 11, ABDEFHI) is generated by the second cross-talk path. Light propagates around a path, incurring a phase bias at both modulator frequencies, ω_1 and ω_2. It does not acquire any additional delay, as it passes only through the sensor loop and bypasses both delay coils. It will be shown that this generates small error signals.

The signal observed by the optical detector can finally be calculated by integrating equation 1.2.11 over the wavelength range covered by the source, in our case from 1500nm to 1600nm, Eq [1.2.12]. This was accomplished using a computer mathematical package, Mathcad 8.0 plus and lead us to realise several important properties exhibited by this new optical architecture.

$$I(t) = \int_{1500}^{1600} I(\lambda, t) d\lambda \qquad [1.2.12]$$

1.2.2.2 Properties of the dual-wavelength phase biased Sagnac interferometer

The properties of a single Sagnac interferometer with phase-bias processing have been described. It was explained how a sinusoidal phase bias increases the response slope, and hence the inherent sensitivity of the interferometer, by moving the response to the quadrature point. If the biasing modulation is at a frequency *f*, then, when unperturbed, the output of the interferometer consists only of even harmonics of the biasing frequency i.e. *2f*, *4f* etc. When two Sagnac interferometers are multiplexed together, as they are in our dual-wavelength Sagnac interferometer, then there are additional effects which have to be considered. If the first Sagnac interferometer is biased at a frequency f_1 and the second at a frequency f_2, then, in the case when there is zero optical cross-talk, then as expected the two interferometers behave as if they were entirely separate. However, when the optical cross-talk has a non-zero value, the two biasing frequencies have the potential to beat together, thereby producing a set of potentially undesirable frequencies corresponding to the sums and differences of the two intended biasing frequencies. i.e. $|\pm pf1 \pm qf2|$, where p and q are integers. This may become a problem if one of these difference frequencies were to co-inside with one of the modulation frequency harmonics. This may be shown graphically by converting the signal described by equation 1.2.12 to the frequency domain. This has been done numerically using a computer maths package, "Mathcad 8.0 Plus Professional" and the result is shown, for different levels of cross-talk, in Figs 1.2.3-1.2.5. In the case where we have zero optical cross-talk and no disturbance acting on the sensor loop, we observe the following theoretical power spectrum at the detector, Fig 1.2.3:-

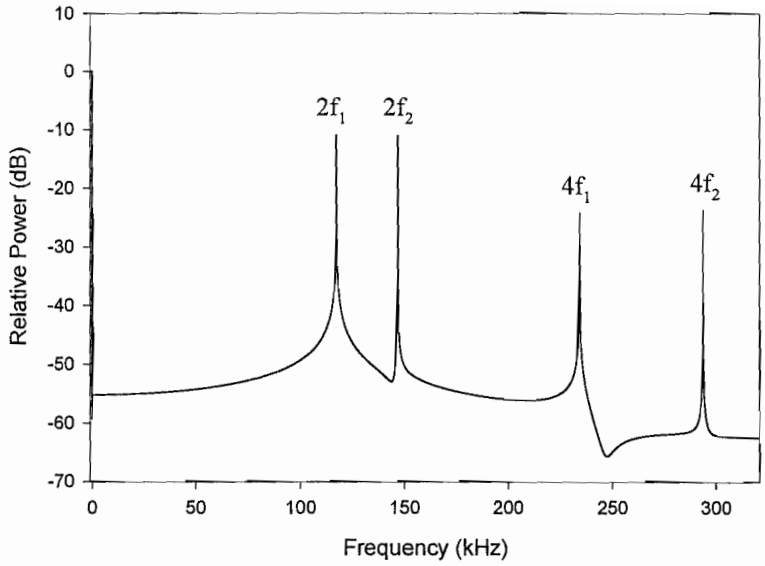

Figure 1.2.3 Theoretical frequency spectrum of an unperturbed dual-wavelength Sagnac interferometer phase-biased to the quadrature point. *The first two even harmonics of the biasing frequencies are shown above. Note only even-harmonic frequencies $2f_1, 4f_1$ etc and $2f_2, 4f_2$ etc are present and no sums or difference frequencies are observable.*

As expected, there are only even harmonics of the biasing modulation frequencies present. For simplicity, only the second and fourth harmonics are shown on this graph, but in practice higher harmonics will generally be present, as was previously explained in chapter 1.1.2. When a disturbance acts on the sensor loop, it causes the odd harmonics to appear, and these form the desirable signal component, which is determined by the processing electronics. Shown in Fig 1.2.4 is the expected frequency spectrum for the dual-wavelength dual-Sagnac interferometer when a single disturbance of frequency 1 kHz acts on the sensor loop. As can be seen, the disturbance creates much stronger side-bands around the odd harmonics of the biasing frequencies.

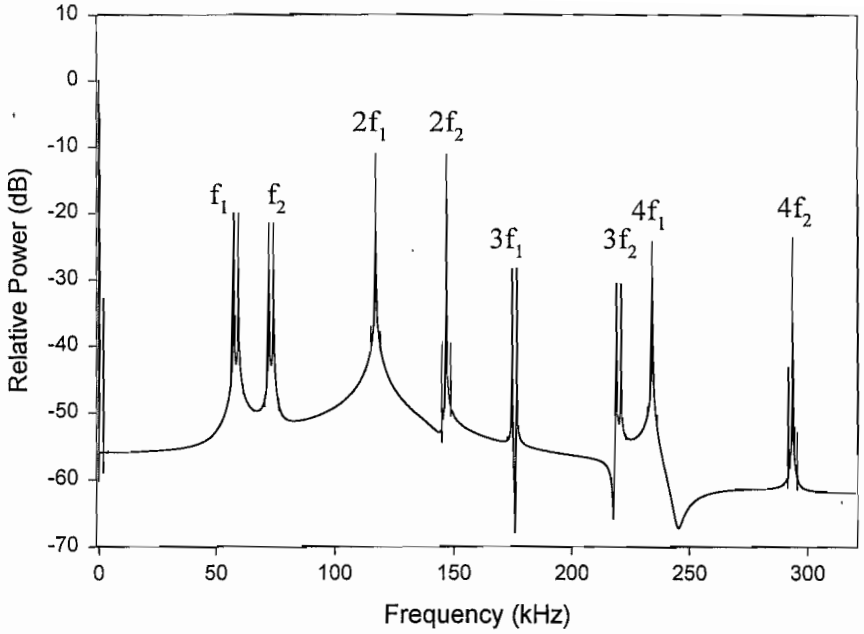

Figure 1.2.4 Theoretical frequency spectrum of the dual-wavelength biased Sagnac interferometer with no optical cross-talk and a 1 kHz disturbance acting on the sensor loop. *Note that side-bands of the odd harmonics of the biasing modulation frequency appear. I.e. frequency components* $f \pm f_{disturbance}$ *are produced.*

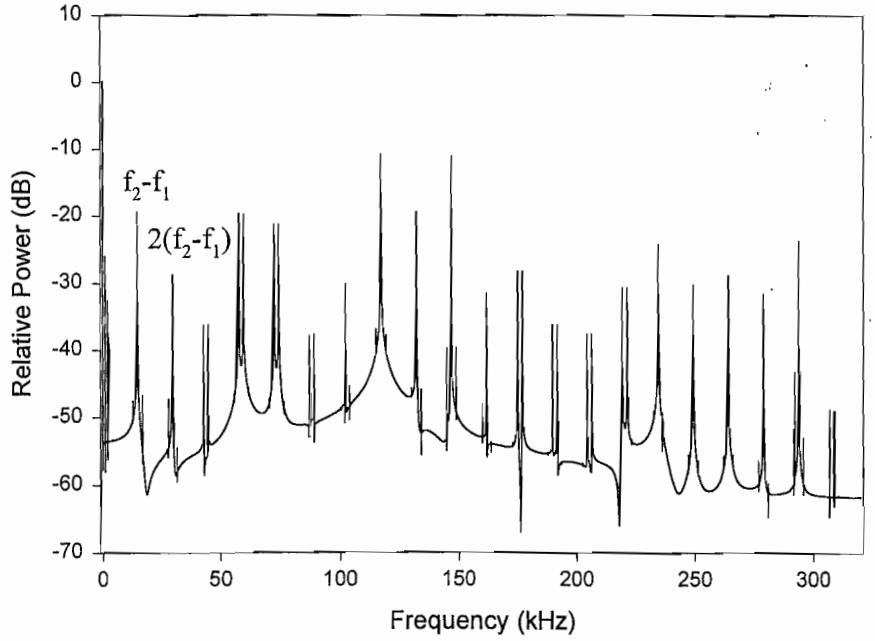

Figure 1.2.5 Theoretical frequency Spectrum of dual wavelength Sagnac interferometer with –8.7dB optical cross-talk, 1kHz disturbance frequency. *As can be seen above, additional sum and difference frequencies appear when the optical cross-talk is non zero. The relative intensity of the beat frequency decreases with frequency*

When optical cross-talk is taken into account, harmonics of the biasing frequencies beat together, producing additional sum and difference frequencies. Shown in Fig 1.2.5, is the frequency spectrum predicted for the dual-wavelength dual-Sagnac interferometer with a -8.7dB optical cross-talk level and a single disturbance of 1 kHz acting on the sensor loop.

As predicted, additional sum and difference frequencies, each obeying the relation pf1± qf2 appear, where p and q are integers. The first difference or beat frequency between the first and second harmonics of the two biasing frequencies are easily observed and are labelled in Fig 1.2.5. It should be possible, however, to choose modulation frequencies that create inter-modulations, which do not coincide with the desired signal frequency components.

1.2.3 Signal Recovery

As presented in the previous chapter, the signal generated by a disturbance acting on the sensor loop can be recovered using an active dual-sideband demodulation scheme [1.2.2]. In order to locate the position at which the disturbance acts, it is necessary to quantitatively determine the signals produced by dual-sideband demodulation. This was done in the previous chapter for a simple Sagnac interferometer. The complications arising from optical crosstalk, however, create an additional term, which is dependent on both the phase-bias frequencies. The following section derives expressions which model the action of dual-sideband demodulation of the received signal generated by a dual-Sagnac, dual-wavelength interferometer.

1.2.3.1 Recovery of signal terms

The terms which describe the desirable contribution from each of the wavelength defined Sagnac paths have been previously defined in Eq 1.2.12 are as follows.

Signal 1

$$T_1^4(\lambda)\cos\left[\beta_1(\lambda)\left(\cos\omega_1 t-\cos\left(\omega_1\left(t-\frac{n}{c}(L+L_1)\right)\right)\right)+\sum_m\Delta\phi_{m1}(\lambda,t)\right]$$

Signal 2

$$T_2^4(\lambda)\cos\left[\beta_2(\lambda)\left(\cos\left(\omega_2\left(t-\frac{n}{c}(L+L_2)\right)\right)-\cos\omega_2 t\right)+\sum_m\Delta\phi_{m2}(\lambda,t)\right] \qquad [1.2.14]$$

The form of the above expression is well known as simply that for AM modulation and it is relatively simple to rearrange them into a form where they may undergo Jacobian expansion, as described in section 1.1.3.2.

Using trigonometric identities, it may be shown that the above terms take the following form, i.e.

Signal 1 $T_1^4(\lambda)\cdot\left[\cos(\beta_1(\lambda)a_1\sin\psi_1)\cos\left(\sum_m\Delta\phi_{m1}(\lambda,t)\right)-\sin(\beta_1(\lambda)a_1\sin\psi_1)\sin\left(\sum_m\Delta\phi_{m1}(\lambda,t)\right)\right]$ [1.2.14]

Signal 2 $T_2^4(\lambda)\cdot\left[\cos(\beta_2(\lambda)a_2\sin\psi_2)\cos\left(\sum_m\Delta\phi_{m2}(\lambda,t)\right)-\sin(\beta_2(\lambda)a_2\sin\psi_2)\sin\left(\sum_m\Delta\phi_{m2}(\lambda,t)\right)\right]$

Where $a_1=-2\sin\left(\omega_1\cdot\frac{(T_1+T_L)}{2}\right)$, $\theta_1=\frac{\omega_1}{2}\cdot(T_L+T_1)$, $\psi_1=\omega_1\cdot t-\theta_1$

Also $a_2=2\sin\left(\omega_2\cdot\frac{(T_2+T_L)}{2}\right)$, $\theta_2=\frac{\omega_2}{2}\cdot(T_L+T_2)$, $\psi_{21}=\omega_2\cdot t-\theta_2$

The above equations are now of a form which may undergo Jacobian expansion.
The first and second harmonics of the above signal can therefore be shown to be given by;

1st Harmonic demodulated signal; $df_1 = -2T_1^4(\lambda)\cdot J_1(\beta_1(\lambda)a_1)\sin\left(\sum_m\Delta\phi_{m1}(\lambda,t)\right)$ [1.2.15]

2nd Harmonic demodulated signal $d2f_1 = 2T_1^4(\lambda)\cdot J_2(\beta_1(\lambda)a_1)\cos\left(\sum_m\Delta\phi_{m1}(\lambda,t)\right)$ [1.2.16]

Similarly, for the second signal term it may be shown that the demodulated signals may be modelled by the following expressions;

1st Harmonic demodulated signal $df_2 = -2T_2^4(\lambda)\cdot J_1(\beta_2(\lambda)a_2)\cdot\sin\left(\sum_m\Delta\phi_{m2}(\lambda,t)\right)$ [1.2.17]

2nd Harmonic demodulated signal $2f_2 = 2T_2^4(\lambda)\cdot J_2(\beta_2(\lambda)a_2)\cdot\cos\left(\sum_m\Delta\phi_{m2}(\lambda,t)\right)$ [1.2.18]

1.2.3.2 Recovery of optical crosstalk term

The response of the perfect dual-wavelength, dual-Sagnac interferometer may now be modelled. However, in an imperfect Sagnac, the dual-modulated cross-talk term needs to be included. The dual modulated cross-talk term is as follows.

Cross-talk term

$$T_1^2(\lambda)T_2^2(\lambda)\cos\left[\beta_1(\lambda)\left(\cos\omega_1 t-\cos\omega_1\left(t-\frac{n}{c}L\right)\right)+\beta_2(\lambda)\left(\cos\left(\omega_2\left(t-\frac{n}{c}L\right)\right)-\cos\omega_2 t\right)+\sum_m\Delta\phi_{m11}\right] \quad [1.2.19]$$

Using trigonometric identities, this may be rearranged to the following;

$$T_1^2(\lambda)T_2^2(\lambda)\begin{bmatrix}\cos(a_{1c}\beta_1(\lambda)\sin\psi_{1c})\cos(a_{2c}\beta_2(\lambda)\sin\psi_{2c})\cos\left(\sum_m\Delta\phi_{m11}(t)\right)-\sin(a_{1c}\beta_1(\lambda)\sin\psi_{1c})\sin(a_{2c}\beta_2(\lambda)\sin\psi_{2c})\cos\left(\sum_m\Delta\phi_{m11}(t)\right)\\-\sin(a_{1c}\beta_1(\lambda)\sin\psi_{1c})\cos(a_{2c}\beta_2(\lambda)\sin\psi_{2c})\sin\left(\sum_m\Delta\phi_{m11}(t)\right)+\cos(a_{1c}\beta_1(\lambda)\sin\psi_{1c})\sin(a_{2c}\beta_2(\lambda)\sin\psi_{2c})\sin\left(\sum_m\Delta\phi_{m11}(t)\right)\end{bmatrix}$$

[1.2.20]

Again this may be expanded using the Jacobian expansion. However, in the case of the dual-modulated cross-talk term, the expansion is the multiple of two Jacobian expansions. Similarly, with the signal terms we define the following constants;

$$a_{1c}=-\sin\left(\omega_1\frac{T_L}{2}\right),\quad \theta_{1c}=\omega_1\frac{T_L}{2},\quad \psi_{1c}=\omega_1 t-\theta_{1c}.$$

$$a_{2c}=-\sin\left(\omega_2\frac{T_L}{2}\right),\quad \theta_{2c}=\omega_2\frac{T_L}{2},\quad \psi_{2c}=\omega_2 t-\theta_{2c}$$

The contributions to the demodulated signals from the dual modulated cross-talk terms are as follows;

df_1: $$-2T_1^2(\lambda)T_2^2(\lambda)J_0(a_{2c}\beta_{m2}(\lambda))J_1(a_{1c}\beta_{m1}(\lambda))\sin\left(\sum_m\Delta\phi_{m11}(t)\right) \quad [1.2.21]$$

$d2f_1$: $$2T_1^2(\lambda)T_2^2(\lambda)J_0(a_{2c}\beta_{m2}(\lambda))J_2(a_{1c}\beta_{m1}(\lambda))\cos\left(\sum_m\Delta\phi_{m11}(t)\right) \quad [1.2.22]$$

df_2: $$-2T_1^2(\lambda)T_2^2(\lambda)J_0(a_{1c}\beta_{m1}(\lambda))J_1(a_{2c}\beta_{m2}(\lambda))\sin\left(\sum_m\Delta\phi_{m11}(t)\right) \quad [1.2.23]$$

$2f_2$: $$2T_1^2(\lambda)T_2{}^2(\lambda)J_0(a_{1c}\beta_{m1}(\lambda))J_2(a_{2c}\beta_{m2}(\lambda))\cos\left(\sum_m\Delta\phi_{m11}(t)\right) \quad [1.2.24]$$

The total demodulated signal is the sum of the contributions from both the demodulated cross-talk and the demodulated Sagnac path signals.

The final demodulated terms are therefore the sum of the contributions from each of the three previously expanded terms;

$$df_1 = -2T_1^4(\lambda)\cdot J_1(\beta_1(\lambda)a_1)\sin\left(\sum_n \Delta\phi_{m1}(\lambda,t)\right) - 2T_1^2(\lambda)T_2^2(\lambda)J_0(a_{2c}\beta_2(\lambda))J_1(a_{1c}\beta_1(\lambda))\sin\left(\sum_n \Delta\phi_{m11}(\lambda,t)\right)$$

$$d2f_1 = 2T_1^4(\lambda)\cdot J_2(\beta_1(\lambda)a_1)\cos\left(\sum_n \Delta\phi_{m1}(\lambda,t)\right) + 2T_1^2(\lambda)T_2^2(\lambda)J_0(a_{2c}\beta_2(\lambda))J_2(a_{1c}\beta_1(\lambda))\cos\left(\sum_n \Delta\phi_{m11}(\lambda,t)\right)$$

$$df_2 = -2T_2^4(\lambda)\cdot J_1(\beta_2(\lambda)a_2)\cdot\sin\left(\sum_n \Delta\phi_{m2}(\lambda,t)\right) - 2T_1^2(\lambda)T_2^2(\lambda)J_0(a_{1c}\beta_1(\lambda))J_1(a_{2c}\beta_2(\lambda))\sin\left(\sum_n \Delta\phi_{m11}(\lambda,t)\right)$$

$$d2f_2 = 2T_2^4(\lambda)\cdot J_2(\beta_2(\lambda)a_2)\cdot\cos\left(\sum_n \Delta\phi_{m2}(\lambda,t)\right) + 2T_1^2(\lambda)T_2^2(\lambda)J_0(a_{1c}\beta_1(\lambda))J_2(a_{2c}\beta_2(\lambda))\cos\left(\sum_n \Delta\phi_{m11}(\lambda,t)\right)$$

[1.2.25]

As shown by the expressions derived above, not only does optical crosstalk create additional frequency components, but the amplitudes of the demodulated signals are also modified. This effect would alter the calculated position of a disturbance if it were not taken into account.

1.2.3.3 Properties of demodulated signals

The optical crosstalk level for a dual-wavelength, dual-Sagnac interferometer using simple sinusoidal WDM components was calculated to be of the order of –10dB. We therefore expect that the contribution from paths 1 and 2 will be dominant over the contribution from the crosstalked paths. The second order Bessel function, $J_2(xa_1)$, which determines the demodulated amplitude corresponding to the second harmonic of the phase bias frequency, is a maximum with arguments of $\pm\pi$ radians. However, a_1 can take values only between *-2* and *2* radians. Upon examination, it can be seen that a_1 is maximised when the modulation frequency is chosen such that the argument of the sine that determines a_1 is $n\pi/2$ where n is an integer. These specific frequencies are eigenfrequencies of the Sagnac loop length and are part of a set shown by equation 1.2.26.

$$\omega_{Eigen} = \frac{2(p+1)\pi c}{nL} \qquad [1.2.26]$$

where p is an integer. In this way, by maximising the second harmonic, one may set the optimum phase biasing modulation frequency.

However, the demodulated signal corresponding to the second harmonic of the biasing frequency carries no information about the disturbance acting on the sensor loop. It may be shown that the first harmonics of the modulation frequencies are maximised at modulation depths of $x = \pi/4$ radians, i.e. at the quadrature point and it is this point to which each Sagnac should ideally be phase-biased.

1.2.3.4 Eliminating the effects of optical crosstalk

A very important result, observed from the theoretical examination of the dual-wavelength dual-Sagnac interferometer, is that, under certain conditions, the effects created by optical cross-talk, may be completely nulled. This is due to the fact that the wanted Sagnac path and the unwanted crosstalk paths differ in length by an amount equal to the delay coil length. This in turn creates a relative phase shift between the phase-bias imposed on the wanted Sagnac signal and the unwanted crosstalk term. Examining the expressions defined in equation 1.2.25 it can be observed that the amplitude of the cross-talk dependant parts of the demodulation terms are, for a particular Sagnac, related to the value taken by the zeroth order Bessel functions $J_0(a_{1c}x)$, or $J_0(a_{2c}x)$, for each Sagnac respectively. When this Bessel function vanishes the cross-talk dependant term vanishes with it.

The constant a_{1c} is defined previously as, $a_{1c} = -\sin\left(\omega_1 \frac{T_L}{2}\right)$.

Therefore, when the modulation frequency is such that the argument of the sine that defines, a_{1c}, is, $p\pi$, then the cross-talk effect vanishes, where p is an integer. Therefore cross-talk effects may be ignored if the following condition is true.

$$\omega = \frac{2n\pi}{T_L} \qquad [1.2.27]$$

This condition is easily met in practice and is therefore a desirable operating point for each of the two Sagnacs to operate when cross-talk is significant.

1.2.4 Noise considerations for a 40km long Sagnac interferometer

Previously investigated Sagnac interferometers have used sensor loop fibre lengths far shorter than the proposed 40km length of our novel sensor architecture. We have assumed, thus far, that, due to the inherent low loss of our novel optics structure, the problems involved in increasing the fibre sensing length would be negligible. However, recent research has brought to light a fundamental noise source which may limit the performance of the sensor as the loop length increases. There are several noise sources which need to be considered. The first is a fundamental noise source in the detection system. Thermally-induced phase noise in the optical fibre is then dealt with and finally noise sources related to the choice of optical source used are analysed.

1.2.4.1 Optical detection noise sources

We shall consider the case where we have a photodiode with a responsivity of R_s, (typically 0.9A/W at 1550nm), and a transimpedance amplifier with a transfer function of G ohms. In this case there are two fundamental noise sources which are of concern.

1) Shot noise (photon noise), due to the photocurrent and dark current generated by the photodiode. In a semiconductor diode it is well known that there is a shot noise current as shown by [Eq, 1.2.29].

$$i^2_{shot\_noise} = 2qPR_s + 2qi_{dark\_current} \quad A^2Hz^{-1} \qquad [1.2.29]$$

where q is the charge of an electron, P is the incident optical power and, $i_{dark\_current}$, is the current generated by thermal processes within the photodiode, without incident light. The dark current is usually of the order of a few pico-amps, and can therefore be ignored compared to the signal current, which is of the order of a few micro amps.

2) Thermal noise of the diodes and the amplifiers resistance.

Thermal or Johnson noise [1.2.6]: Thermal processes within an electrical resistor cause a current to flow within a resistor, without a voltage being applied. This current may be expressed as follows;

$$i^2_{Johnson\_noise} = \frac{4k_BT}{G} + \frac{4k_BT}{R_{diode}} \quad A^2Hz^{-1} \qquad [1.2.28]$$

where, $i_{Johnson\_noise}$ is the Johnson noise current, k_B is Boltzmanns constant, T is the absolute temperature, G is the transimpedance gain and R_{diode} is the resistance of the photodiode. However, the thermal noise contribution from the photodiode is usually several orders of magnitude lower than that of the transimpedance amplifier and can therefore be ignored.

As can be seen, the photon noise is proportional to the root of the incident power, whereas the thermal noise is constant with changing optical power. It is desirable therefore to design a system limited by the fundamental photon noise component. This is simply achieved by increasing the incident optical power above a value of P_{snl}, (Eq 1.2.30) plotted in Fig 1.2.6, where:-

$$P_{snl} = \frac{2k_BT}{qGR_s} \qquad [1.2.30]$$

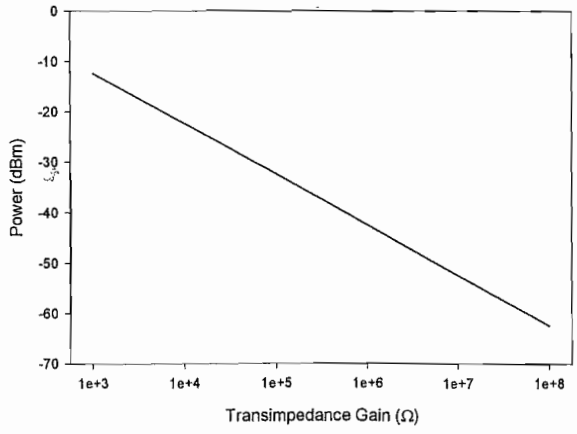

Figure 1.2.6. Graph showing optical power required for shot noise limit Vs detector transimpedance gain.

It was previously assumed that the shot noise was the dominant fundamental noise mechanism in interferometric sensors. It is therefore informative to plot the shot noise as a phase equivalent. For a biased Sagnac of length L_T, the RMS AC component of the signal generated, when a sinusoidally varying strain disturbance with an amplitude of A radians and frequency ω acts on the sensor loop, can be given by:-

$$V_{ACrms} = \frac{\sqrt{2}}{2} \cdot J_1\left(\frac{\pi}{2}\right) APR_s G\omega\left(\frac{L_T - 2z}{v}\right) \qquad [1.2.31]$$

where z is the position at which the disturbance acts, v the velocity of light in the fibre and P is the incident peak optical power transmitted around the path defining the Sagnac of interest, that is incident on the detector.

The RMS shot noise can similarly be expressed as:-

$$V_{Nrms} = G\sqrt{2 \cdot 0.757 \cdot qR_s 2P} \qquad [1.2.32]$$

where the $0.757P$ is the RMS value of the intensity of light incident on the detector when the Sagnac is sinusoidally phase biased. Also an additional factor of $2^{-1/2}$ arises, due to the dual Sagnac configuration, assuming each Sagnac has equal optical power.

Since the sensitivity of the Sagnac interferometer is dependent on where the disturbance acts we shall assume that the disturbance acts at a point where the sensitivity is that of the average of the sensor, i.e. at $z = L_T/4$. This leads to an expression for the noise-equivalent phase [1.2.33] for a perturbed phase-biased Sagnac, plotted in Fig 1.2.7, for three different optical powers.

$$\phi_{noise} = 8.7 \cdot \frac{v\sqrt{q}}{\omega L_T \sqrt{PR_s}} \qquad [1.2.33]$$

where ω is the frequency of the disturbance.

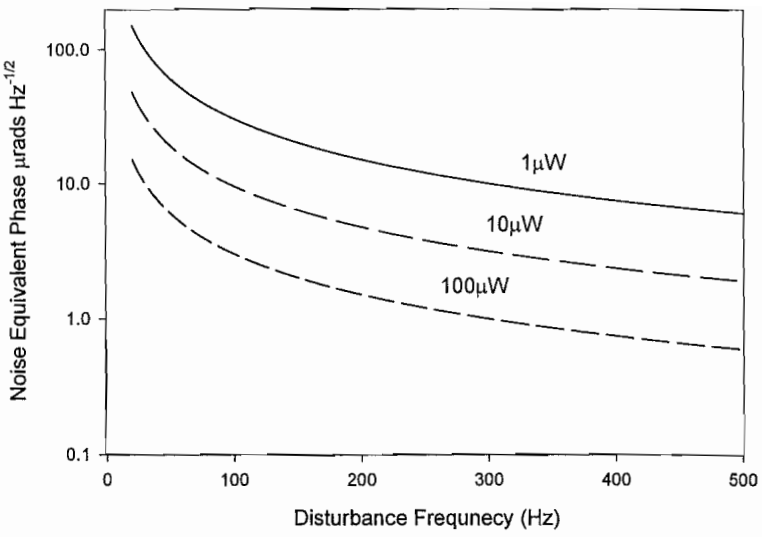

Figure 1.2.7 Shot noise equivalent RMS phase amplitude. *Plotted above is the shot noise equivalent RMS phase amplitude for a phase-biased dual-Sagnac interferometer, perturbed at $L_T/4$ with a disturbance of frequency f. Three separate optical power levels are shown 1µW, 10µW, and 100µW.*

If shot noise were the limiting noise in our system, then it is easy to see that noise-limited RMS phase amplitude detection levels of the order of a few µ radians, per root Hertz are achievable, even with modest (few µW) detected optical intensities. However, since the amplitude of the noise equivalent disturbance would vary both as a function of its frequency and position on the sensor loop, it is more practical to plot the detector shot noise as a noise equivalent phase difference, $\Delta\phi_{shot\_noise\_equivalent}$, generated at the output of the Sagnac. It may be shown that this noise equivalent, relative phase difference, can be given by;

$$\Delta\phi_{shot\_noise\_equivalent} = \frac{\sqrt{0.757 \cdot q}}{J_1(\pi/2) \cdot \sqrt{P \cdot R_s}} \qquad [1.2.34]$$

Figure 1.2.8 shows the noise equivalent relative phase for various received optical intensities. As can be seen, relative phase noises of the order of 0.1µrads $Hz^{-1/2}$ can be achieved with reasonable levels of received optical intensities.

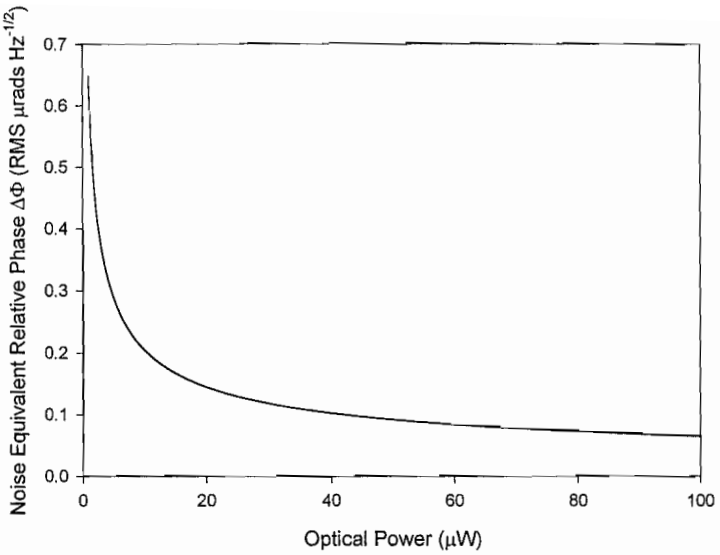

Figure 1.2.8 Noise equivalent relative phase. *Plotted above is the shot-noise equivalent relative phase difference, $\Delta\phi$, generated at the output of a Sagnac interferometer. (Quadrature biased Sagnac interferometer).*

1.2.4.2 Thermal phase noise in optical fibres

Until fairly recently, this noise source although theoretically expected has been largely ignored due to lack of experimental evidence. Wanser et al [1.2.8] was one of the first to seriously consider this noise source as the absolute fundamental limit for interferometer sensitivity. Thermodynamic processes within the fibre modulate the refractive index, which creates a phase modulation of the light as it propagates along the fibre. There are two contributions to this refractive index modulation, the first involves temperature fluctuations along the fibre and the second, density fluctuations. The latter dominates at frequencies above about 1MHz.

Kråkenes et al [1.2.9] presented a model for this thermally-induced phase noise, which was later experimentally confirmed by Knudsen et al [1.2.10]. The phase shift induced by a randomly varying refractive index in a Sagnac interferometer can be expressed by, [Eq 1.2.35].

$$\Delta\phi_s = \frac{2\pi}{\lambda}\int_0^{L_T}\left\{\Delta n\left(x, t-\frac{L_T-x}{v}\right)-\Delta n\left(x, t-\frac{x}{v}\right)\right\} \qquad [1.2.35]$$

where $\Delta n(x,t)$ is the fluctuating term in the refractive index at a position x and time t. The phase-noise spectral density of the thermal phase modulation was then found by

calculating the time autocorrelation function of the above and then transforming to the Fourier domain. This leads to an expression for the phase-noise spectral density, $S_{\Delta\phi s}(\omega)$, shown in equation [1.2.36].

$$S_{\Delta\phi_s}(\omega)=\left(\frac{2\pi}{\lambda}\right)^2 S_{\Delta n}(\omega)\cdot 2L_T\left[1-\sin c\left(\frac{\omega L_T}{v}\right)\right] \qquad [1.2.36]$$

where $S_{\Delta n}(\omega)$ is the Fourier transform of $\Delta x(\tau)R_{\Delta n}(\tau)$ and $R_{\Delta n}(\tau)$ is the spatial auto-correlation function of the density fluctuations.

Fortunately, it is not necessary to calculate this, as the phase-noise spectral density can be found by comparing the result with that for the Mach-Zehnder and that previously derived by Wanser et al [1.2.8]. This leads to an expression for the phase noise spectral density, as shown in equation [1.2.37].

$$S_{\Delta\phi_s}(\omega)=\frac{k_B T^2 L_t}{\kappa\lambda^2}\left(\frac{dn}{dt}+n\alpha\right)^2 \ln\left(\frac{k_{\max}^4+(\omega/D)^2}{k_{\min}^4+(\omega/D)^2}\right)\left[1-\sin c(\omega L_T/v)\right] \qquad [1.3.37]$$

where k_B is Boltzmanns constant, T is the absolute temperature, D is the thermal diffusivity of the fibre, α is the linear expansion coefficient of the fibre and κ is the thermal conductivity of the fibre. Also, k_{min} and k_{max} are related to the mode field radius and outer cladding radius, $2.405/a_f$ and $2/w_0$ respectively, where a_f is the mode field radius and w_0 is the cladding radius. The resulting phase noise is plotted as a function of frequency in (Fig 1.2.9) for a 40km phase biased Sagnac.

Property	Value
k_B	1.38×10^{-23} J/K
T	300 K
κ	1.37 W/(mK)
a_f	4×10^{-6} m
W_0	65×10^{-6} m
α	5.5×10^{-7} /K
D	0.82×10^{-6} m^2/s
λ	1550nm

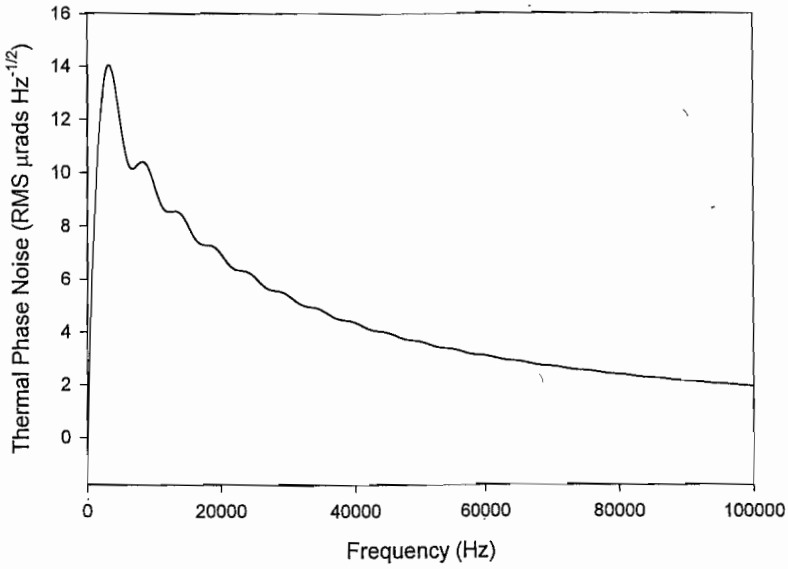

Figure 1.2.9 Theoretical thermal phase-noise versus frequency for 40km of single mode fibre.

For frequencies less than the natural frequency of the loop, the noise effectively tends to cancel itself. This is due to the natural correlation between counter-propagating waves in a reciprocal loop, an effect not seen in other forms of interferometer. Thermal phase noise peaks at a frequency of the order of the fundamental loop eigenfrequency and gradually falls off as the frequency increases. This leads to an excess phase noise of the order of a few µrad $Hz^{-1/2}$ at approximately 50kHz, the frequency of the phase bias. At very low frequencies, and for moderate incident optical powers, (i.e. <50Hz and <10µW), the noise is shot noise limited. Fig 1.2.10 shows the total noise equivalent phase, i.e. where;

$$i_{Total}^2 = i_{Shot}^2 + i_{Thermal}^2 \qquad [1.3.38]$$

The difference now being that the signal / noise ratio cannot be arbitrarily increased by simply increasing the received power. However, we may now assume that the dominant noise source in the system arises from thermal phase contributions from the fibre itself.

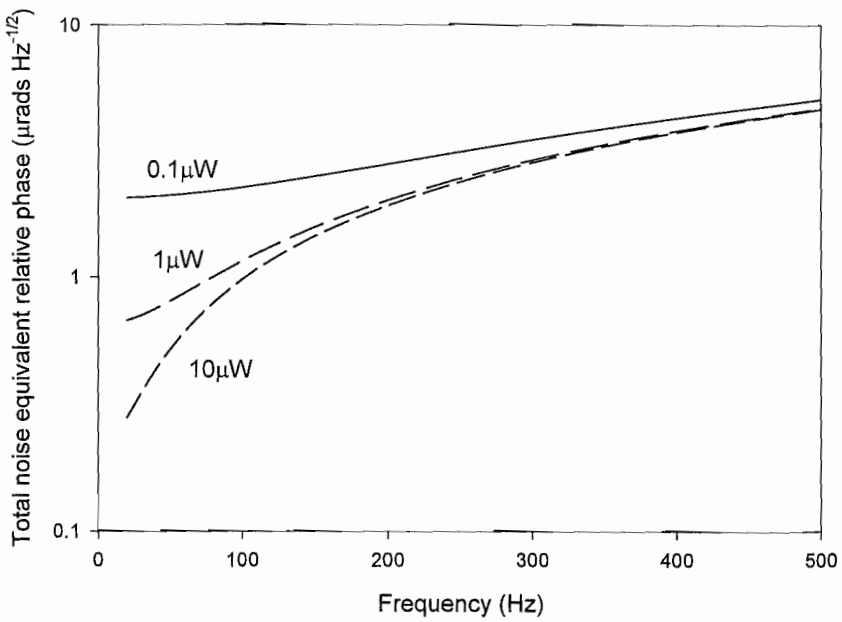

Figure 1.2.10 Total noise equivalent phase for a 40km long Sagnac interferometer constructed from 1550nm single mode fibre.

We have therefore shown that fibre phase noise largely dominates and limits the fundamental sensitivity of the Sagnac interferometer. However, a theoretical phase-noise of the order of a few μrad $Hz^{-1/2}$ is still readily available.

1.2.4.3 Optical Source Noise

An additional potential source of noise is the optical source. The source required for the dual-Sagnac system is required to be broadband and have a minimum intensity of the order of a few mW. There are two possible sources for this application,

1) Edge light emitting diodes, (ELEDs). Low radiance versions of these sources give a relatively clean Gaussian profile spectrum with bandwidths of the order of 50nm and centre wavelengths of 1550nm or 1300nm. However, at the time at which this research was undertaken these devices were limited in power to 100μW. This made them difficult to work with, as high gain receivers would have been required, limiting the bandwidth of the detection system. More recently, super-luminescent diodes have become available with optical powers in the mW range. These would now be a more suitable source and are a possible improvement to the system, as they would greatly

reduce the cost and complexity of the sensor. However, the very high radiance versions of these sources have narrower linewidths and can exhibit "less-clean" spectra due to intra-cavity reflections.

2) Super-luminescent Source. Erbium-doped fibre is pumped via a WDM with either a 980nm or 1480nm diode pump. The pump is absorbed by the Erbium ions which re-emit spontaneously in a broadband around 1550nm. The spontaneously emitted photons are then amplified via stimulated emission as they propagate thorugh the population inverted Erbium fibre. This process is termed amplified spontaneous emission (ASE) and can be used to produce a broadband source with an optical output power of several mW's. The source spectrum and output power however, can be effected by many factors. These include,

a) The doping concentration of Erbium ions
b) The length of Erbium doped fibre
c) The pump power
d) and the temperature

As presented later in the thesis, a source with an optical power of 4mW and a 40nm bandwidth was constructed with a spectrum having only a small 4dB dip at 1540nm.

In order to model the noise generated by this source, we can use a erbium doped fibre amplifier, (EDFA), model presented by Desurvire [1.2.11], in the regime where we have no input signal. There are several noise contributions in an optical amplifier system.

ASE-shot noise
Signal-ASE beat noise
And ASE-ASE beat noise.

In a typical amplifier configuration, the ASE surrounding the signal is an unwanted component and so the shot noise generated by this was treated separately. However, the ASE itself is used as our source and so is the required component. Single-ASE nosie and ASE-ASE noise can be considered classically to be the heterodyne noise created by optical components within the optical bandwidth beating together. Since there is no

amplified optical signal, the signal-ASE beat contribution is not present. However, the remaining noise source, ASE-ASE beat noise must be considered in case it has a significant impact on the total signal to noise of the system.

If we consider the situation shown in (Fig 1.2.11), where we have an optical amplifier, emitting broadband ASE into an optical system, (In this case, the system is our Sagnac sensor), exhibiting an optical loss T_{opt}, before the light is detected by a pin-diode and transimpedance amplifier.

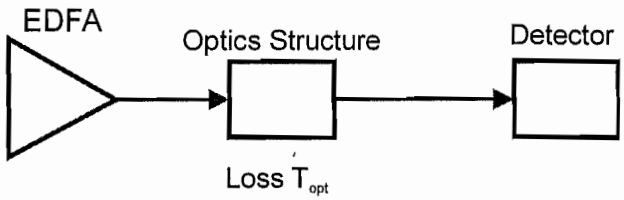

Figure 1.2.11 Optical configuration for EDFA noise model.

It may be shown that the ASE-shot noise and the ASE-ASE beat noise components can be given by the following expressions.

$$i^2_{ASE-Shot} = q^2 R_s^2 G_0 T_{opt} F B_o \quad Hz^{-1} \qquad [1.3.39]$$

$$i^2_{ASE-ASE} = q^2 R_s^2 F^2 G_0{}^2 T^2_{opt} B_o \quad Hz^{-1} \qquad [1.3.40]$$

Where B_o is the optical filter bandwidth (20nm = 2500GHz) in each Sagnac, q is the charge on an electron, R_s is the responsivity of the detector, G_o is the optical small signal gain for the amplifier and T_{opt} is the transmission loss of the optics. F is the noise figure of the amplifier, given by $F = (1+ 2n_{sp}(G_o+1))/G_o$ where n_{sp} is the spontaneous emission factor (The value of this is 1 for a completely inverted medium).

Since we have already modelled the shot noise contribution to the performance of the Sagnac system, we now need to compare the ASE-ASE component to find out when it dominants the shot noise. An added complication is that the EDFA was not originally engineered as an amplifier but as a source. The length of Erbium fibre used was therefore much longer than would be required for an optimised amplifier. The spontaneous emission factor will therefore be higher than 1. Also, if used as an amplifier the gain, of the EDFA

would be far from optimal. We shall therefore use a gain of 15dB and a spontaneous emission factor of 3 when comparing these noise sources [1.2.11].

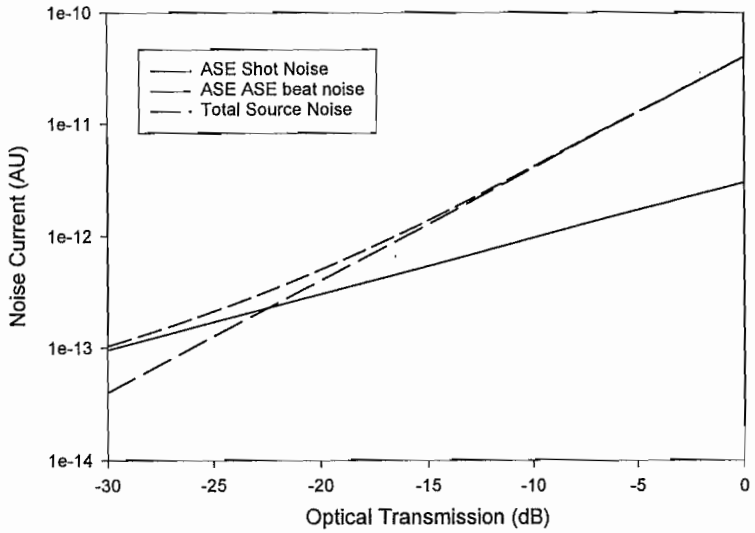

Figure 1.2.12 Plot of source noise components, ASE-ASE beat noise and ASE-Shot noise. *Plotted above are the noise components generated by the optical source. As is easily observed the ASE-ASE noise contribution dominants at high optical powers and ASE-Shot noise at low optical powers < 20μW.*

As shown in, (Fig 1.2.12), shot noise becomes the dominant noise source when the transmission loss of the optics system increases past 23dB. Assuming a 4mW source this corresponds to an optical power of 20μW. Referring to, (Fig 1.2.10), this corresponds to a noise equivalent relative phase of approximately 0.1 μrads per root Hertz. As the optical source power is increased the ASE-ASE beat noise contribution will limit the minimum achievable detection system noise. For our system, however, this limit is far lower than the thermal noise contribution and can therefore be ignored. However, when shorter loop lengths are used this ASE-ASE beat noise contribution will become relevant. Fig 1.2.13 shows the theoretical ASE-ASE beat noise limit.

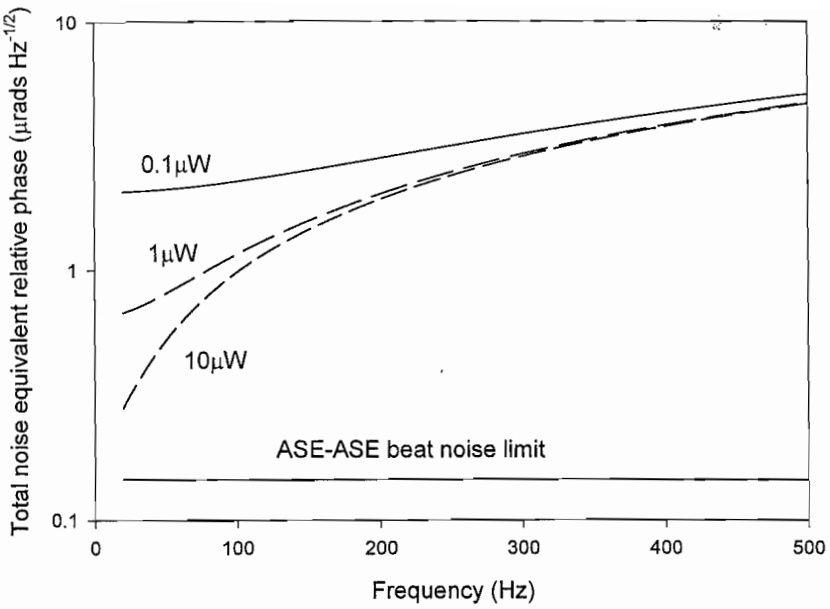

Figure 1.2.13 ASE-ASE beat noise limitation. This graph shows the maximum achievable noise equivalent phase using a 4mW ASE source.

1.2.5 Summary and conclusions

This chapter has dealt with the theory of a dual-wavelength, dual-Sagnac interferometer. The response of the system to an arbitrary phase disturbance was derived and the effects of optical crosstalk were modelled. It was found that crosstalk creates undesirable frequency components in the signal received at the output of the sensor, which in turn affect the amplitudes of the demodulated signals. The process of dual-sideband demodulation was modelled and it was found that if biased at correct frequencies the signals corresponding to the crosstalk components were not demodulated and could therefore be ignored. The noise of the system was then modelled and it was found that there are three noise sources of concern. The first, shot noise was found to limit in cases where low optical powers are received (<0.1μW). However, as the received power is increased thermal phase noise in the fibre itself becomes the dominant factor. The noise of the system was also found to be dependent on the optical source used. Our solution, to use an ASE source was found to suffer from the disadvantage of ASE-ASE beat noise. This noise source, as it is proportional to the received optical power becomes relevant in situations involving high received power or short sensor loop lengths. The optimal situation was found to be when we receive optical powers in the range 1-20μW leading to phase noises of a the order of 0.5-3μrads $Hz^{-1/2}$. Since we expect signals in the range of

0.1rads this still allows an easily achievable signal / noise ratio of between 60-70dB in a sampling time of 1 second.

References Chapter 1.2

[1.2.1] A.M.Hill, D.B.Payne, "Linear crosstalk in wavelength-division-multiplexed optical-fibre transmission systems", Journal of lightwave technology, Vol 3, pp 643-650

[1.2.2] A.Dandridge, A.B.Tveten, G.H.Siegel, E.J.West, T.G.Giallorenzi, Electronic letters, Vol 16, No 11, pp-408-409, 1980.

[1.2.3] S.J.Spammer, A.A. Chtcherbakov, P.L.Swart, "Dual wavelength Saganc-Michelson distributed optical fibre sensor", Proceedings SPIE pp 2838-34 Aug 1996.

[1.2.4] S.J.Spammer, A.A.Chtcherbakov, P.L.Swart, "Distributed dual wavelength Sagnac impact sensor", microwave and optical technology letters, Feb 20, Vol 17, No 3, pp 170-173, 1998.

[1.2.5] J.M.Senior, S.E.Moss, S.D.Cusworth, "Optical crosstalk in LED spectral slicing", International Journal of Optoelectronics, Vol 11, No 1, pp 47-52.

[1.2.6] P.Horowitz, W. Hill, "The art of electronics-second edition," (Cambridge University Press), Ch 7, pp 453, 1996.

[1.2.7] P.Horowitz, W. Hill, "The art of electronics-second edition," (Cambridge University Press), Ch 7, pp 450, 1996.

[1.2.8] K.H.Wanser, "Fundamental phase noise limit in optical fibres due to temperature flucuations", electronics letters, Jan 2, Vol 28, No 1, pp 53-54, 1992.

[1.2.9] K Krakenes, K Blotekjaer, "Comparison of fibre-optic Sagnac and Mach-Zehnder interferometers with respect to thermal processes in the fibre", Journal of lightwave technology, Vol 13, No 4, Apr, 1995.

[1.2.10] S Knudsun, A B Tventen, A Dandridge, "Measurements of fundamental thermal induced phase fluctuations in the fibre of a Sagnac interferometer", IEEE photonics technology letters, Vol 7, No 1, Jan, 1995.

[1.2.11] E Desurvire, "Erbium-doped fiber amplifiers," (John Wiley & Sons), Ch 3, 1994.

Chapter 1.3 Distributed Disturbance Sensing, Numerical Modelling.

In the previous chapter, the analytical response expected from the dual-wavelength, dual-Sagnac interferometer was modelled. Expressions for the signals obtained by dual-sideband demodulation of the first two harmonics of the biasing frequencies were derived. These expressions were given in terms of the relative phase shifts between counter-propagating wave-trains, induced when an arbitrary phase disturbance acted on the sensor loop. The following chapter now describes how a sensor of this type may be used to locate the position at which a time dependant disturbance acts. The effects of multiple disturbances and acoustic noise are also investigated.

1.3.1 Strain induced phase shifts

Before further analysis can be undertaken, the relative phase shift induced for light travelling around the four separate paths previously defined, must be derived. Consider the effect a strain disturbance has on the light travelling around the sensor loop of a dual-wavelength, dual-Sagnac interferometer. As previously presented in chapter 1.1 the relative phase shift between counter-propagating wave-trains, induced by a time varying strain disturbance, is related to the rate of change of the induced phase shift induced and the position, relative to the loop centre, at which the disturbance acts. In the same way as the intensity term, (Eq 1.2.11), was derived we may derive the following expressions for the relative phase shifts induced for the four possible optical paths that are present in the dual-wavelength, dual-Sagnac (Fig 1.2.1).

Unbiased, path 00 ; $$\Delta\phi_{00}(\lambda,t,z)=\phi\left(\lambda,t-\frac{n}{c}(L_1+z)\right)-\phi\left(\lambda,t-\frac{n}{c}(L+L_2-z)\right) \quad [1.3.1]$$

Sagnac 1, path 1; $$\Delta\phi_1(\lambda,t,z)=\phi\left(\lambda,t-\frac{n}{c}z\right)-\phi\left(\lambda,t-\frac{n}{c}(L+L_1-z)\right) \quad [1.3.2]$$

Sagnac 2, path 2; $$\Delta\phi_2(\lambda,t,z)=\phi\left(\lambda,t-\frac{n}{c}(L_2+z)\right)-\phi\left(\lambda,t-\frac{n}{c}(L-z)\right) \quad [1.3.3]$$

Dual-biased, path 11; $$\Delta\phi_{11}(\lambda,t,z)=\phi\left(\lambda,t-\frac{n}{c}z\right)-\phi\left(\lambda,t-\frac{n}{c}(L-z)\right) \quad [1.3.4]$$

Where L is the sensor loop length, L_1 and L_2 are the delay coil lengths and z has been defined as the distance from the start of the sensor loop at which the disturbance acts. If the induced phase modulation is small, then we may apply the Taylor expansion, and neglecting higher order terms, obtain the following approximations for the strain induced phase shifts. For the higher order terms to be ignored, we require that the disturbance frequency be much smaller than the natural sensor loop frequency, i.e. $\omega L/v < 1$. Where, ω, is the disturbance frequency, L, is the sensor loop length and, v, is the phase velocity of the light.

Small signal approximated relative phase shifts.

Non-biased, path 00; $$\Delta\phi_{00} = \frac{d\phi(\lambda,t)}{dt}\frac{n}{c}(L - L_1 + L_2 - 2z) \quad [1.3.5]$$

Sagnac 1, path 1; $$\Delta\phi_1 = \frac{d\phi(\lambda,t)}{dt}\frac{n}{c}(L + L_1 - 2z) \quad [1.3.6]$$

Sagnac 2, path 2; $$\Delta\phi_2 = \frac{d\phi(\lambda,t)}{dt}\frac{n}{c}(L - L_2 - 2z) \quad [1.3.7]$$

Dual modulated, path 11; $$\Delta\phi_{11} = \frac{d\phi(\lambda,t)}{dt}\frac{n}{c}(L - 2z) \quad [1.3.8]$$

The relative phase shift induced by a time varying strain disturbance can now be seen to be proportional to the rate of change of the disturbance acting on the sensor loop. However, the amplitude of the relative phase difference is also complicated by dual-wavelength operation. As described in chapter 1.1, we may define the phase shifts in terms of the strain imposed on the fibre.

Non-biased, path 00; $$\Delta\phi_{00} = \frac{d\varepsilon(t)}{dt}\frac{2\pi}{\lambda}\frac{n}{c}(L - L_1 + L_2 - 2z) \quad [1.3.9]$$

Sagnac 1, path 1; $$\Delta\phi_1 = \frac{d\varepsilon(t)}{dt}\frac{n}{c}\frac{2\pi}{\lambda}(L + L_1 - 2z) \quad [1.3.10]$$

Sagnac 2, path 2; $$\Delta\phi_2 = \frac{d\varepsilon(t)}{dt}\frac{n}{c}\frac{2\pi}{\lambda}(L - L_2 - 2z) \quad [1.3.11]$$

Dual modulated, path 11; $$\Delta\phi_{11} = \frac{d\varepsilon(t)}{dt}\frac{n}{c}\frac{2\pi}{\lambda}(L - 2z) \quad [1.3.12]$$

In this way, each term contains a common term $d\varepsilon/dt$, which does not vary with optical wavelength. Each term can now be shown to be inversely proportional to the wavelength of the light.

1.3.2 Signal processing methods

As expected, the signal recovered from the phase-biased dual-wavelength, dual-Sagnac interferometer by dual-sideband demodulation show's the same raised cosine response as for the unbiased interferometer, but biased to its relatively linear quadrature point. This makes an analytical solution for the disturbance position more difficult, due to the non-linear nature of the sensor response. There is however, a way to simplify matters, for applications where background acoustic noise levels are relatively low (i.e. $\Delta\phi_{noise} \approx 50\mu rads\ Hz^{-1/2}$, *this figure assumes a 30dB (100m) signal / noise for a disturbance generating a 25mRad phase shift*). In such applications, the disturbance to be recovered and located is often of an unknown nature. (I.e. of unknown frequency, amplitude and phase) and in addition may only appear transiently. However, the amplitude of the disturbance can normally be assumed to be small, ($\Delta\phi_{signal} < 0.1 rads$).

We may therefore make the assumption that the disturbance does not create a sufficiently large relative phase shift between counter-propagating wave-trains to drive the biased interferometer beyond its relatively linear response range. (i.e. $\Delta\phi < 0.1$ *rads*).

This being the case, we may make the following approximations $sin(\Delta\phi) \approx \Delta\phi$, and $cos(\Delta\phi) \approx 1$. The demodulation terms for the first and second harmonics of the biasing frequency for each of the two Sagnac's then simplify to the following;

$$df_1(\lambda) = -2\cdot T_1^4(\lambda)\cdot J_1(\beta_1(\lambda)a_1)\sum_n\left(\frac{d\varepsilon_n(t)}{dt}\frac{n}{c}\frac{2\pi}{\lambda}(L+L_1-2z_n)\right) - 2\cdot T_1^2(\lambda)T_2^2(\lambda)J_0(a_{2c}\beta_2(\lambda))J_1(a_{1c}\beta_1(\lambda))\sum_n\left(\frac{d\varepsilon_n(t)}{dt}\frac{n}{c}\frac{2\pi}{\lambda}(L-2z_n)\right)$$

$$d2f_1(\lambda) = 2\cdot T_1^4(\lambda)\cdot J_2(\beta_1(\lambda)a_1) + 2T_1^2(\lambda)T_2^2(\lambda)J_0(a_{2c}\beta_2(\lambda))J_2(a_{1c}\beta_1(\lambda))$$

$$df_2(\lambda) = -2\cdot T_2^4(\lambda)\cdot J_1(\beta_2(\lambda)a_2)\sum_n\left(\frac{d\varepsilon_n(t)}{dt}\frac{n}{c}\frac{2\pi}{\lambda}(L-L_2-2z_n)\right) - 2\cdot T_1^2(\lambda)T_2^2(\lambda)J_0(a_{1c}\beta_1(\lambda))J_1(a_{2c}\beta_2(\lambda))\sum_n\left(\frac{d\varepsilon_n(t)}{dt}\frac{n}{c}\frac{2\pi}{\lambda}(L-2z_n)\right)$$

$$d2f_2(\lambda) = 2\cdot T_2^4(\lambda)\cdot J_2(\beta_2(\lambda)a_2) + 2\cdot T_1^2(\lambda)T_2^2(\lambda)J_0(a_{1c}\beta_1(\lambda))J_2(a_{2c}\beta_2(\lambda)) \qquad [1.3.13]$$

For the analysis in the following chapter, it will be assumed that we have a signal recovery method which simultaneously samples the values corresponding to the demodulated signals, df_1, $d2f_1$, df_2, $d2f_2$, at a rate far higher than the frequency of the disturbance signal we are attempting to recover (i.e. $f_{sample} >> 500Hz$). In this way, we may generate a result, (the estimate ratio), which is the ratio of the four demodulated signals, i.e. $df_1 d2f_2 / df_2 d2f_1$. If we examine the theoretical expressions that model these demodulated signals, [Eq 1.3.13], we can easily see that this estimate ratio is dependant only on the position of the disturbance and that the term $d\varepsilon/dt$ cancels, (assuming a single disturbance).

For the simplified case of zero crosstalk, the estimate ratio maybe shown to be given by;

$$\frac{df_1 d2f_2}{d2f_1 df_2} = \frac{J_1(\beta_1(\lambda)a_1)\cdot J_2(\beta_2(\lambda)a_2)\cdot(L+L_1-2z)}{J_1(\beta_2(\lambda)a_2)\cdot J_2(\beta_1(\lambda)a_1)\cdot(L-L_2-2z)} \qquad [1.3.14]$$

Further more it can be shown that when biased at eigen-frequnecies and to quadrature, that $J_1(\beta_1(\lambda)a_1) = J_1(\beta_2(\lambda)a_2)$ and $J_2(\beta_2(\lambda)a_2) = J_2(\beta_1(\lambda)a_1)$. The estimate ratio therefore reduces to;

$$estimate\_ratio = \frac{(L+L_1-2z)}{(L-L_2-2z)} \qquad [1.3.15]$$

The position may then be found by re-arranging this equation [1.3.15].

1.3.3 Positioning a single point tone disturbance

The following section investigates the response of the dual-wavelength dual-Sagnac interferometer to a variety of strain disturbances acting on the sensor loop. Firstly, the ideal case is investigated, i.e. a disturbance of constant known frequency, acting continuously at a single discrete point. However, in any real application of such a sensor, it is unlikely that any disturbance would act as a true point source. Due to the nature of the most practical applications of a sensor of this type, there will normally be no direct contact between the sensor transducer and the source of the acoustic disturbance. The acoustic wave generated by the disturbance will travel through the intermediate medium (e.g. soil, road, fibre sheath) and therefore affect a significant section of the sensor loop simultaneously, (several meters). However, over lengths of this order the disturbance can

be assumed to be constant and therefore this will not effect the nature of the induced phase shift.

Consider first the ideal case of a point acoustic disturbance. The strain modulation of the fibre may be expressed as,

$$\varepsilon(t) = x_d \cos(\omega_d t + \alpha_d) \qquad [1.3.16]$$

where, x_d is the modulation depth of the tone disturbance, (remember that this is assumed to be within the linear approximation, i.e. $x_d < 0.1$), ω_d is the angular frequency of the tone disturbance and ,α_d, is the relative phase of the disturbance. The rate of change of this disturbance is therefore,

$$\frac{d\varepsilon(t)}{dt} = -x_d \omega_d \sin(\omega_d t + \alpha_d) \qquad [1.3.17]$$

When substituted into the above expressions for the demodulation terms, [1.3.13] then it may be shown that the time dependence of the terms df_1 and df_2 are directly related to the time derivative of the disturbance acting on the sensor loop of the Sagnac interferometer. The other terms, $d2f_1$, and $d2f_2$ are simply DC levels, invariant with time. The magnitude of these DC levels are a direct measure of the AM carrier or bias magnitude. Effects such as polarisation fading may effectively decrease the carrier amplitude. However, since the amplitude of the first and second harmonic demodulation terms will be attenuated by the same amount, then effects of this nature may be corrected for by taking the ratio of the demodulation terms for a particular Sagnac. I.e. the corrected ratio $df_1/d2f_1$ should have an amplitude which is a function of both the disturbance's position and its modulation depth, but which is independent of both the optical power and the magnitude of the polarisation fading. Obviously complete fading should be avoided as it will still drastically affect the signal / noise of the resulting ratio.

Figure 1.3.1 shows a simulation of the expected demodulated waveforms generated by a tone point disturbance of 0.1 radians amplitude and of 100Hz, acting at the start of the sensor loop (z = 0), of a dual-wavelength, dual-Sagnac. It is assumed the Sagnac is biased

at the 11th and 14th Eigen-frequencies, and has a sensor loop length of 40km and delay coil length of 4.0km. This corresponds to Eigen-frequencies 48.5kHz and 62.5kHz respectively.

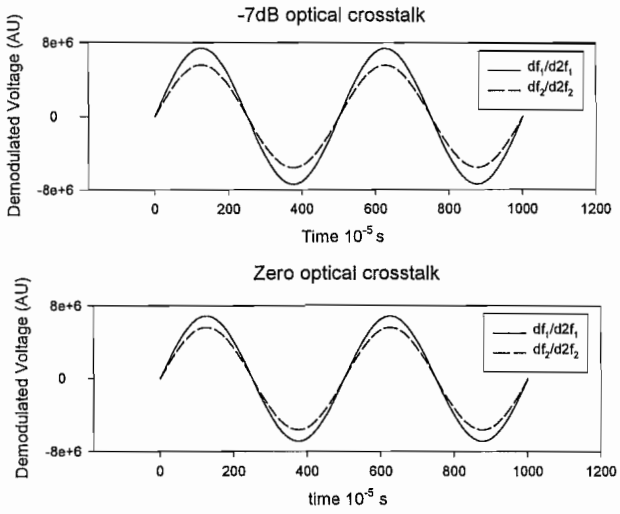

Figure 1.3.1 Theoretical time dependence of the demodulated corrected ratio df/d2f for each of the Sagnacs in a dual-Sagnac interferometer. *The response for each of the Sagnac 's forming the dual-wavelength dual-Sagnac interferometer are shown. The ideal case, (i.e. of zero optical cross-talk), is shown in the lower plot and the case for –7dB optical cross-talk in the upper plot.*

The lower of the two plots shown in (Fig 1.3.1) shows the expected response for the zero optical crosstalk scenario. The upper plot shows the case for an optical cross-talk level of –7dB. The effect of cross-talk on the demodulation terms can now be seen graphically and as previously discussed. There is a slight difference in the demodulated amplitudes for the case of zero and non zero cross-talk. The polarity of the change in amplitude is dependent on the phase biasing frequency and the relative phase of the demodulating reference. It is quite difficult to see in these figures as it is a relatively small change, however, if we look at the spacing between the response for each of the Sagnacs, i.e. at time 170 $\times 10^{-5}$s we see that this gap between the two sinusoidal waveforms is larger in the upper plot.

Figure 1.3.2 shows the variation of the amplitude of the corrected ratio's $df_1/d2f_1$ and $df_2/d2f_2$ as a function of the disturbance position at an instant in time. As expected the response is linear. In the ideal case, both of the Sagnacs exhibit the same position / demodulated amplitude gradient but the response for each is offset along the disturbance position axis by the delay coil length of 4km. The effect of optical crosstalk is to

preferentially alter the gradient of this response. Again, as shown in equation 1.3.9, the biasing frequency has a direct effect on the extent to which this occurs.

For example figure 1.3.2 shows the simulated results for a dual-Sagnac, (40km sensor loop, 4km delay), biased at 48.5kHz and 62.5kHz respectively. The effect of cross-talk on the Sagnac biased at 48.5kHz is virtually non detectable, however, the effect on the Sagnac biased at 62.5kHz is easily observed, in the upper plot.

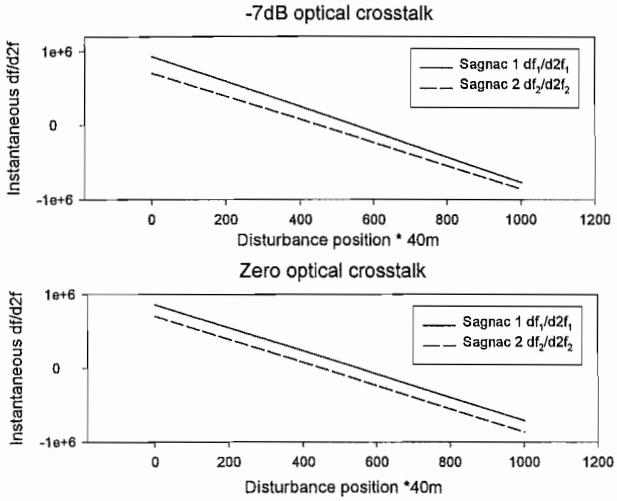

Figure 1.3.2 Theoretical instantaneous demodulated amplitude variation with disturbance position. *Both the case for zero cross-talk and –7dB cross-talk are plotted.*

As previously explained the time dependence of the demodulated signals $df_1/d2f_1$ and $df_2/d2f_2$ may be eliminated by dividing them, yielding a result, "the estimate ratio", which is a function of the disturbance's position, but independent of its rate of change. There is, however, a disadvantage to this approach. As the denominator of the position dependant ratio tends to zero the ratio tends to infinity making location difficult. However, since the acoustic sensitivity of the loop falls to zero at its centre, disturbances acting near the loop centre will inevitably be difficult to locate. Figure 1.3.3 shows the positional variation of this estimate ratio, $df_1\ d2f_2\ /\ df_2\ d2f_1$, with the disturbance position. In contrast the ratio changes slowly with distance towards the ends of the sensor loop, increasing the error in the position result.

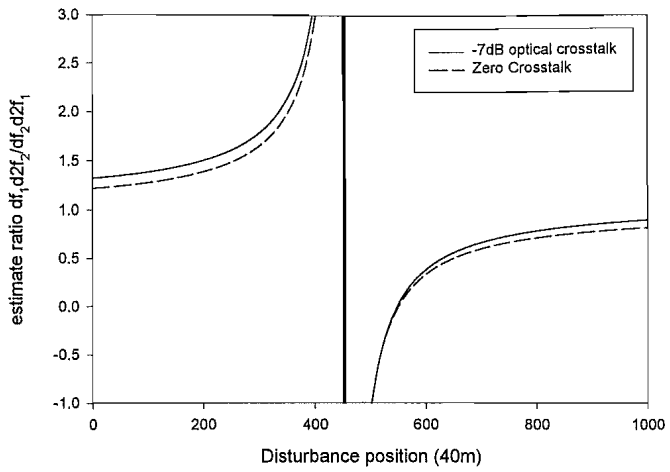

Figure 1.3.3 Theoretical variation of estimate ratio with disturbance position. *Shown above is the positional variation of the linear regime response of a dual-wavelength, dual-Sagnac interferometer phase biased at Eigen-frequencies of the loop length to a modulation depth of π/4 radians. Both 0 and –7dB optical cross-talk levels are shown.*

1.3.3.1 Computer simulations

Using "Mathcad 8.0 Plus Professional" from Mathsoft, a computer worksheet was written to simulate the operation of the dual-wavelength, dual-Sagnac interferometer and the signal recovery electronics. The full listing for the Mathcad worksheet is given in appendix 3. The theoretical intensity of radiation incident on the detector of a biased dual-wavelength, dual-Sagnac interferometer was plotted as a function of time. This theoretical intensity trace was then sampled into a data set at a rate of 24MHz over a simulated sample time of 0.1 seconds. This meant that we had a data set consisting of 240000 data points. The dual-sideband demodulation of this data set was then simulated by numerically multiplying the expected intensity trace by a square wave at the bias modulation, "carrier" frequency. The square wave alternates between +/- 1, which has the effect of rectifying the carrier. The AM modulation may then be recovered by numerical simulation of a low pass filter. This was realised by converting the simulated data to the Fourier domain using a Fast-Fourier-Transform, (FFT), and then multiplying the data with a filter characterisation function. The data set was then converted back to the time domain by applying the inverse transform (iFFT), generating the simulated demodulated signals. This was done at

frequencies, f_1, f_2, $2f_1$ and $2f_2$, producing the four demodulated terms, previously discussed.

The ideal situation was simulated, (i.e. zero crosstalk). A point tone disturbance of 0.1 radians amplitude and 100Hz frequency acting at a distance z from the start of the sensor loop was considered. The estimate ratio was then calculated for each of the data points in the set and the corresponding disturbance position was found. The results were plotted in a histogram form showing the calculated disturbance position versus the number of simulated results that fall within each position bin. The bin width was set to 100m.

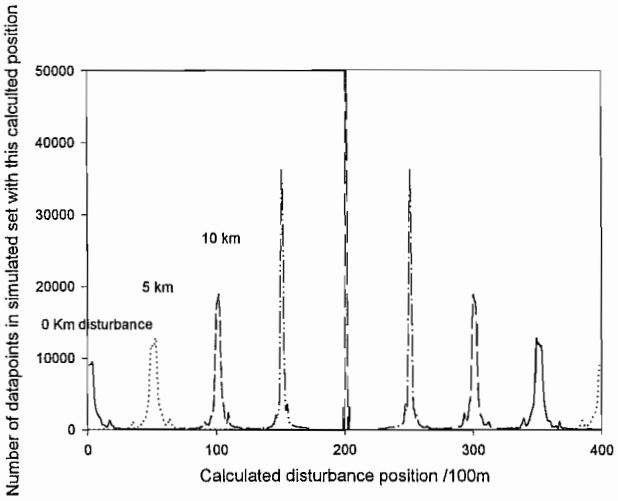

Figure 1.3.4 Theoretical histogram of calculated position Vs Number of counts. *(Simulated Results) Disturbance 100Hz, 0.2 radians amplitude acting at z = 0,5,10,15,20,25,30,35,40Km respectively.*

Figure 1.3.4 shows the combined results for several simulations. Each simulation moved the disturbance a further 5km along the sensor loop. The number of sample points for each of the simulations was constant at 240000. The height of the histogram peak as shown in, (Fig 1.3.4), is therefore related to the standard deviation of the calculated position, which decreases towards the loop centre and increases as the ends of the loop are approached. These results show correct positioning of the tone disturbance with a positional error of ±100m at the centre of the sensor loop increasing to ±1000m towards the ends of the sensor loop.

1.3.3.2 Discussion

The previous section presented the simulated results for a tone, point-disturbance acting at a position, *z*, along a sensor loop of a dual-wavelength, dual-Sagnac interferometer. The results showed that the simulated demodulation of the intensity trace for such an interferometer yielded a position dependant "estimate ratio" that behaved as predicted by the analytical expressions defined by equation 1.3.9. However, the simulation was assumed to be a perfect case scenario, i.e. that only a single disturbance acted on the sensor loop in an environment, absent of noise. The variance of the positional result generated by these simulations was however, dependent on the disturbance position. This was due to the fact that when an analogue signal is sampled, information is lost. This creates what is known as digitisation noise. This slight noise in the sampled signal then revealed itself as an uncertainty in the calculated position, which due to the shallow gradient in the positional response of the estimate ratio, becomes significant towards the loop ends, (Fig 1.3.3).

We shall now consider the effects of statistical noise on the positional sensitivity of the dual-wavelength, dual-Sagnac interferometer. The effects of statistical noise (noise in detection system, not the acoustic background noise) are explained by considering the effect noise has on the positional variation of the corrected ratio, *df/d2f*, for each of the Sagnac interferometers. As shown in, (Fig 1.3.2), the positional variation of the corrected ratios for each of the Sagnacs vary linearly with respect to the disturbance position at any given instant in time. The effect of statistical noise is to "blur" this linear response. Consider the case where a single point disturbance acts near the centre of the sensor loop. Due to the relatively small difference in propagation delay for counter-propagating wave-trains, the sensor is less acoustically sensitive towards the centre of the loop, the corrected ratios will therefore have a small value. The signal to noise ratio of the recovered disturbance signal will therefore be small and the resulting error in the estimate ratio will be large. One might assume that this would lead to a large error in the position result. However, due to the steep gradient of the estimate ratio response in this region of the sensor loop (Fig 1.3.3), the error in the position result is negligible.

In contrast when a tone point disturbance acts towards the ends of the sensor loop the corrected ratios take a large value. The signal to noise ratio of the disturbance signal

obtained is large. However, due to the shallow gradient of the estimate ratio response it takes only a very small change in this ratio to incorrectly position the disturbance. The effect of statistical noise on a system of this sort is to broaden the position results towards the ends of the sensor loop. Figure 1.3.5 shows the results obtained from the simulation of a tone point disturbance acting 5km into a 40km sensor loop. The two plots show the results for

1) (upper trace) A noiseless simulation
2) (lower trace) added Gaussian noise with an amplitude approximately $1/10^{th}$ that of the disturbance amplitude.

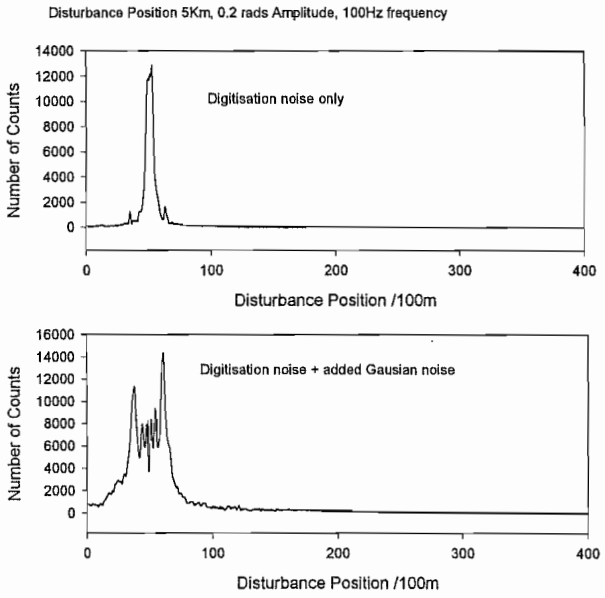

Figure 1.3.5 Simulation of statistical noise. *Top trace shows results obtained when no noise added. Bottom trace shows results when Gaussian noise is added to demodulated waveforms (Equivalent to approximately 0.01radians).*

1.3.4 Effects of multiple disturbances and acoustic noise

Until now the simulations carried out have been assumed to apply to an ideal situation, i.e. the disturbance excites only a single point on the sensor loop and that within the time period that the data is sampled, there is only a single disturbance acting on the loop.

In any real situation, this may not be the case. Such a sensor may be employed in an uncontrolled environment. The nature and magnitude of disturbances acting on the sensor loop may therefore not always be predictable and there is a definite possibility that several disturbances may act on the loop simultaneously.

1.3.4.1 Multiple disturbances of the same frequency

In order to gain an understanding of the effects of multiple disturbances on the positional capabilities of the dual-wavelength, dual-Sagnac interferometer, it is useful to consider certain simplified situations. The first of these simplified situations to consider is where two disturbances of equal amplitude and at the same frequency, acting in phase disturb the loop, but at two different positions on the sensor loop.

As before the following simulation assumes that the disturbance frequency is small compared to the natural frequency of the loop and that the disturbance generates only a small relative phase shift at the interferometer output. If for simplicity we assume that we have two small disturbances acting at either end of the sensor loop of a dual-Sagnac interferometer, but where each Sagnac has not been offset by a delay coil. The first disturbance, a distance z_1 from the loop centre will generate a positive relative phase shift between counter propagating wave-trains. The second however, since it is on the opposite side, also a distance z_1 from the sensor loop centre, will induce a relative phase shift of the same amplitude as the first but in the opposite direction. The resulting combined phase shift will therefore be zero and no signal will be observed. However, in our situation each Sagnac is offset in opposite directions, relative to the other by a delay coil. The resulting combined net phase shift between counter-propagating wave-trains in this situation will therefore be non-zero. Further more the relative phase shift observed by each Sagnac will be equal but opposite in sign. This will accordingly give an "estimate ratio" of 1 and be positioned at the loop centre. It may further be shown that in a general case where we have two disturbances of the same frequency, amplitude and phase, acting at distances z_1 and z_2 from the start of the sensor loop, then the sensor will accordingly locate a single false disturbance acting midway between the two actual disturbances, i.e. at $(z_1 + z_2)/2$. Since the relative phase shift, $\Delta\phi$, induced by a disturbance is proportional to its amplitude, then this average must also be weighted with respect to each of the disturbance amplitudes. So

finally, if we have two disturbances of the same frequency and phase, acting at positions z_1 and z_2 with amplitudes A_1 and A_2 then the sensor will locate a single disturbance acting at $(A_1z_1+A_2z_2)/(A_1+A_2)$.

Figure 1.3.6 shows the positional histogram obtained by simulating responses to different pairs of disturbances, each pair having equal frequency, amplitude and phase. The first graph shows the result for two disturbances acting at 10km and 25km respectively and the second shows the result for two disturbances acting at 0km and 40km. The averaging effect can now easily be seen. (Note due to the histogram bin width of 100m the x axis scale is calibrated in increments of 100m, therefore 400 on this axis corresponds to 40km).

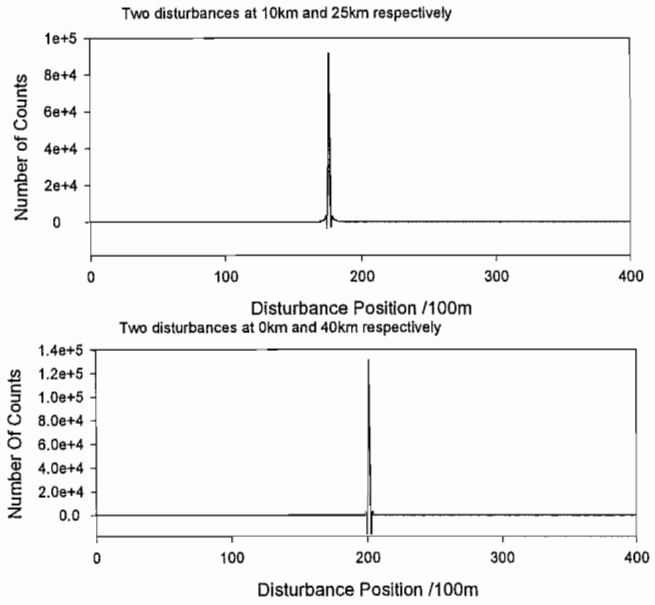

Figure 1.3.6 Results from simulation of multiple, point disturbances of the same frequency and amplitude. *Upper plot shows results for two disturbances acting at 10km and 25km. Lower plot shows results for disturbances acting at 0km and 40km. As can be seen, as expected the calculated disturbance position is the average of the two disturbance positions.*

The above situation assumed that the two disturbances acting on the sensor loop were acting in phase. However, in a real situation, the disturbances acting on the sensor loop are highly unlikely to be in phase, (the only likely correlated source of acoustic disturbance would be 50Hz electrical power vibration, e.g. electrical substation or pylons). The situation where two disturbances act out of phase is more complicated. When the disturbances act in phase the corrected ratios may be assumed to be time independent, i.e. each disturbance is at the same point in its sinusoidal response. In the case where the

disturbances act out of phase the corrected ratios can no longer be assumed to be time independent.

For example consider two general sinusoidal tone disturbances of the same frequency defined as;

Disturbance 1. $\varepsilon_1(t) = x_{d_1} \cos(\omega_d t + \alpha_{d_1})$ acting at z_1

Disturbance 2. $\varepsilon_2(t) = x_{d_2} \cos(\omega_d t + \alpha_{d_2})$ acting at z_2

Where, x_d, is the disturbance amplitude, ω_d, is the disturbance frequency and, α_d, is the relative phase of the disturbance. This results in a phase shift between the sinusoidal corrected ratios, $df_1/d2f$, and, $df_2/d2f_2$, obtained for each of the Sagnac interferometers. Therefore the resulting estimate ratio $df_1 d2f_2 / df_2 d2f_1$ is no longer time invariant and varies with the form of a tangent function. The point of inflexion of the tangential curve is at the value expected for the amplitude-weighted average position of the two disturbances acting on the sensor loop. The histogram plotted therefore is broadened around the amplitude-weighted average disturbance position. The amount to which the peak is broadened is dependent on the relative phase of the two disturbances. When each disturbance acts in phase the peak is not broadened. As the relative phase offset increases the peak becomes broader until eventually at 180° information of the disturbance position is lost. As the relative phase offset moves beyond the 180° mark the peak begins to narrow again and eventually reaches the 360° situation, when the two disturbances act in phase once more.

Figure 1.3.7 shows the results from several simulations of two disturbances, acting at positions 5km and 15km on a biased, dual-wavelength, dual-Sagnac sensor loop. The relative phase shift between the two disturbances is shown on the graph.

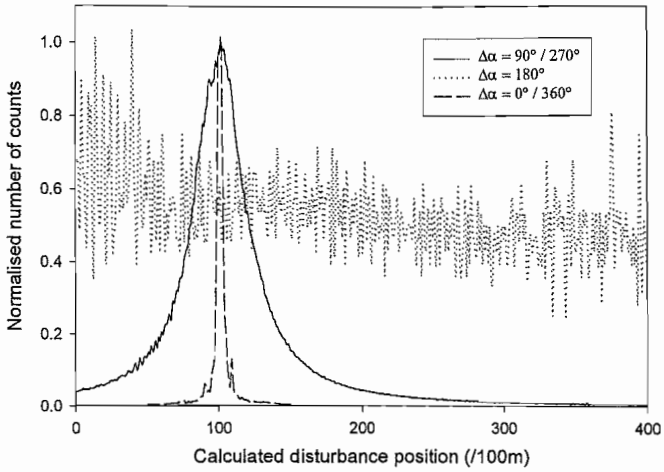

Figure 1.3.7 Position Histogram, Twin disturbances at 5km and 15km respectively. Relative phase shift α.

1.3.4.2 Disturbances of different frequencies

In any realistic application of the dual-wavelength, dual-Sagnac interferometer the disturbances that act on the sensor loop will not be tone disturbances but arbitrary functions, uncorrelated or even random in nature. The principle of Fourier analysis relies on the fact that any arbitrary periodic function may be expanded into a series of sine and cosine components. This does not, however, effect the positioning algorithm, since each frequency component of the arbitrary disturbance function acts at the same position. The principle of superposition, (assuming we stay within linear response regime of the interferometer), therefore implies that each frequency component can, in principle be positioned separately. However, when we have two disturbances of different frequencies acting at different locations the situation is more complex. If the first disturbance is of a frequency f_{dist1} and the second is of a frequency f_{dist2} then the two disturbances can be thought to beating together, periodically reinforcing and cancelling each other. The positional histogram should therefore be a broadened distribution with a mean equal to the average position of the two disturbances. The amplitude of the response generated by each of the disturbances, however, is proportional to the rate of change of the phase shift induced by the disturbance. This implies that for disturbances of the same amplitude then the higher frequency disturbance will be dominant. For example figure 1.3.8 shows the positional results for two disturbances acting at 5km and 15km respectively. The first

disturbance is of 0.1 radians amplitude and 100Hz in frequency. The second, however, is 0.2 radians in amplitude and 50Hz in frequency. The distribution is as expected. Since the amplitude of the higher frequency component is lower that that of the lower frequency disturbance the sensor locates a single disturbance midway between the two disturbances however, the peak in the histogram plot is also broadened, as expected.

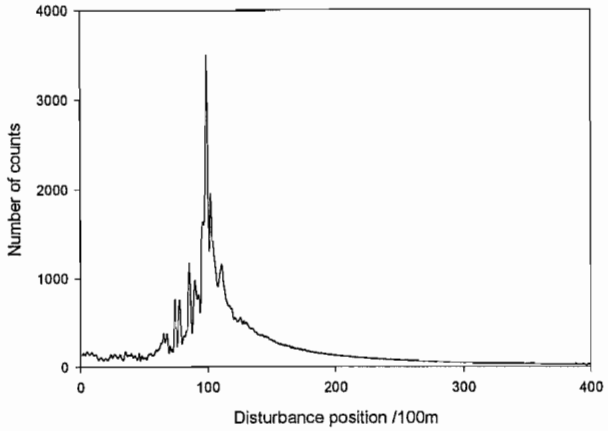

Figure 1.3.8 Theoretical Positional Histogram, Different frequency disturbances. *Disturbance 1, 0.1 radians, 100Hz at z = 5km, Disturbance 2, 0.2 radians, 50Hz at z = 15km.*

As has been shown this signal-processing method can be easily fooled, positioning multiple disturbances at their weighted average position. However, if additional information is known about the disturbance that is to be located then it maybe possible to extract the disturbance from others present on the sensor loop.

For example consider the case as shown above. We have two disturbances acting on the sensor loop of a phase biased dual-Sagnac interferometer. The first acts at 5km, with an amplitude of 0.1 radians. Let us assume that the frequency of the disturbance is now known to be 100Hz, but its amplitude and position are still unknown. A second disturbance acts at 15km, with a frequency of 50Hz and an amplitude of 0.2 radians. By bandpass filtering the output obtained after dual-sideband demodulation, it is possible to locate a disturbance of known frequency. This assumes that during the sample time, there is only a single disturbance acting on the sensor loop, which is of the correct frequency, selected by the filter.

Figure 1.3.9 shows the simulated results for the above situation. The data was bandpass filtered, with a pass-band of 10Hz and centre frequency 100Hz. The simulation was then run again but with the filter centred at 50Hz. The results obtained for each of the simulations were then plotted on the same axis. As can be easily seen the two disturbances are separated and located correctly. Also, the broadening of the histogram peak is significantly reduced.

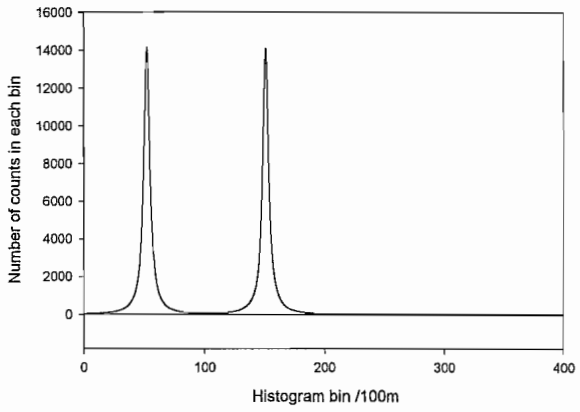

Figure 1.3.9 Graph showing separation of multiply disturbances of different frequencies. *The first disturbance, (100Hz), acts at 5km with an amplitude of 0.1 rads, the second disturbance, (50Hz), acts at 15km, with a 0.2 rads amplitude.*

The principle of superposition of the disturbance signals has now been presented and the ability, with correct processing to separate the disturbances digitally has been demonstrated.

1.3.4.3 Effects of acoustic noise

As defined previously, such a dual-wavelength dual-Sagnac interferometer is likely to be employed in an uncontrolled environment. It is therefore possible that several disturbances may act on the sensor loop simultaneously. This being the case, what effect would this have on the positional sensitivity of the sensor?

Any disturbance to be located accurately, must be assumed to be (or arranged to be, e.g. by filtering), dominant over other disturbances present on the sensor loop. However, any distributed acoustic noise present will still have a cumulative effect on the position at

which a disturbance is located. If we consider the situation where we have only acoustic noise present on the sensor loop. Acoustic noise can be assumed to be several disturbances of random nature acting at random positions. This being the case, we now have enough information about the predicted operation of the Sagnac to make an estimate of the effect. Since all the noise sources are uncorrelated, then they can be considered to beating together, as with multiple frequency disturbances, sometimes reinforcing or cancelling each other. Since we assume a broad spectrum of acoustic noise, the positional peak generated will therefore be broadened as for multiply frequency disturbances and disturbances out of phase. The position at which the noise is to be located is dependent on the distribution of the acoustic noise around the sensor loop. The position will be the amplitude-weighted average of the disturbances separate positions, (i.e. two disturbances of equal frequency and phase with be located midway between their two locations but weighted towards the stronger of the two disturbances). In the case where we have a long sensor loop laid underground in a rural area then we may assume that the acoustic noise amplitude will be constant along its length. The noise peak will therefore be at the loop centre. If, however, the loop were to pass under a larger source of acoustic disturbance, such as a road or railway then the peak would accordingly be moved towards the noise source. Any disturbance that is now to be located will average with the acoustic noise peak. The overall effect of acoustic noise is to "pull" the positional results in a direction towards the centre of the sensor loop and broaden the sensor positional sensitivity.

1.3.5 Summary and conclusions

The response of a dual-Sagnac interferometer to a time varying strain disturbance has been previously presented in chapter 1.1. However, throughout previous chapters it was assumed that only a single arbitrary disturbance acted on the sensor loop of the Sagnac at any given time.

For the application of interest, there will often be very little knowledge of the characteristics of the disturbance acting on the sensor loop. A disturbance, may at any given time, have an unknown frequency, phase and or amplitude. Also, due to the nature of the sensor, there will often be no direct contact between the source of acoustic disturbance and the fibre sensing cable. Inevitably the acoustic wave generated by the

disturbance will disperse and thus act on a finite section of fibre and not act as a point source, as was modelled by the ideal theory. In practice however, even an interaction length of 10-20m will be traversed almost instantaneously, (45-90nsec). Over this time period the disturbance can be assumed to be a constant. A further complication is the distributed nature of the application. A long length of fibre, typically several tens of kilometres, will be laid along a reasonably direct path. It is very probable therefore that more than one acoustic disturbance would be acting on the sensor loop at any given time. This leads to the assumption that there will inevitably be some acoustic noise background level present in the system. Attempts have been made to investigate the effects these situations will have on the location capabilities of the dual-Sagnac and the effects expected for each of the previous arguments have been separated and quantified for simple simulated cases.

A model has been written to simulate the operation of the dual-wavelength, dual-Sagnac interferometer, including the function of the signal processing electronics and algorithms applied to the sampled data. The only assumption made about the disturbance characteristics was that the relative phase shift it generates was small enough, ($\Delta\phi < 0.1rads$), as not to move the biased interferometer outside of its linear response region. The signal processing method chosen was a Taylor approximation, [Eq 1.3.13]. In this way, each sampled data point could be used to calculate a related position and could then be used to update a histogram showing the calculated disturbance position versus the relative number of counts for which that position was found.

The response of the sensor has been modelled firstly for an ideal situation, that of a single ideal point disturbance acting at a specific location, time varying at a fixed frequency. It was found that the modelled response fitted the theoretically expected situation. A time varying signal was recovered which was directly related to the first time derivative of the disturbance and its position on the loop. It was found that the positional dependence of the first harmonic demodulated amplitude at an instant in time was linear, offset for each Sagnac by the delay length of 4km. The effects of cross-talk could also be seen in this simulation. The effect of crosstalk was to preferentially alter the amplitude of the demodulated response, which itself was dependant of the sensor loop, delay loop length and the frequency at which the interferometer was biased. The positional histogram was

found to give a well-defined positional indication, with a sharp peak at the disturbances position.

The effects of statistical noise of the positional results obtained from the sensor have been considered. Due to the nature of the Sagnac it was found, as expected, that there was an increase in acoustic sensitivity towards the ends of the sensor loop and a corresponding decrease towards the centre. The effect of noise was to broaden the peak observed on the positional histogram, but the centre of the observed peak remained at the disturbance position. In contrast to the acoustic sensitivity, the positional sensitivity increased towards the centre of the sensor loop. This was due to the fact that the estimate ratio changed sharply towards the loop centre, therefore a larger tolerance was possible before the positional result was severely affected.

The effects of multiple disturbances were then considered, the simplest of which were twin disturbances of the same frequency acting in phase, but at different positions around the sensor loop. It was found that each disturbance would "add" constructively to "fool" the positional algorithm, locating the disturbance at a position, which was the average of their individual positions, weighted with respect to their individual amplitudes. Following from this investigation the effect of a constant relative phase shift between the two disturbances was then investigated. This situation yielded an unsuspected result. Each of the disturbances indeed added constructively together, however, the combined disturbance generated an estimate ratio, which had a time varying component. The result of which was to broaden the observed histogram peak to a point where when the two disturbances were acting in anti-phase that all positional data was lost and the histogram became flat.

Finally disturbances of different frequencies were investigated. Following the argument that disturbances of different frequencies beat together, reinforcing and cancelling each other, at a rate which was directly related to their difference frequency. It was unsurprising that the result was a single broadened peak at the average of the two disturbance positions, weighted with respect not only to their amplitude but also to their rate of change.

The effects of an acoustic background noise level were then considered. Combining each of the above observations, the expected result of an acoustic background would be to effectively generate a false disturbance signal at the centre of the loop. This when

averaged with the actual disturbance acting on the sensor loop would broaden and move the positional result towards the centre of the loop, giving an incorrect positional result. However, it was also shown that with correct processing a disturbance signal could be separated, and correctly positioned. In conclusion it has proved possible to show that even under a wide variety of situations the Sagnac interferometer can still be used as a location sensor for a time varying disturbance. Also that effects such as background noise, with correct processing should prove possible to calibrate out of the sensor's response.

Chapter 1.4 Realisation and Experimental Results

The following chapter presents experimental details of the dual-wavelength, dual-Sagnac interferometer, which has so far only been discussed theoretically. The experimental apparatus is firstly presented and then confirmation of its ability to locate a tone disturbance. First trials, then improvements made to the initial set up in the light of these results are highlighted and the final results presented.

1.4.1 Experimental Setup

For ease of construction and use, the apparatus for the investigation of this novel dual-Sagnac interferometer was divided into three separate sections, as shown in (Fig 1.4.1).

1) The interrogation optics
2) The sensing fibre loop
3) The signal processing electronics and data acquisition hardware.

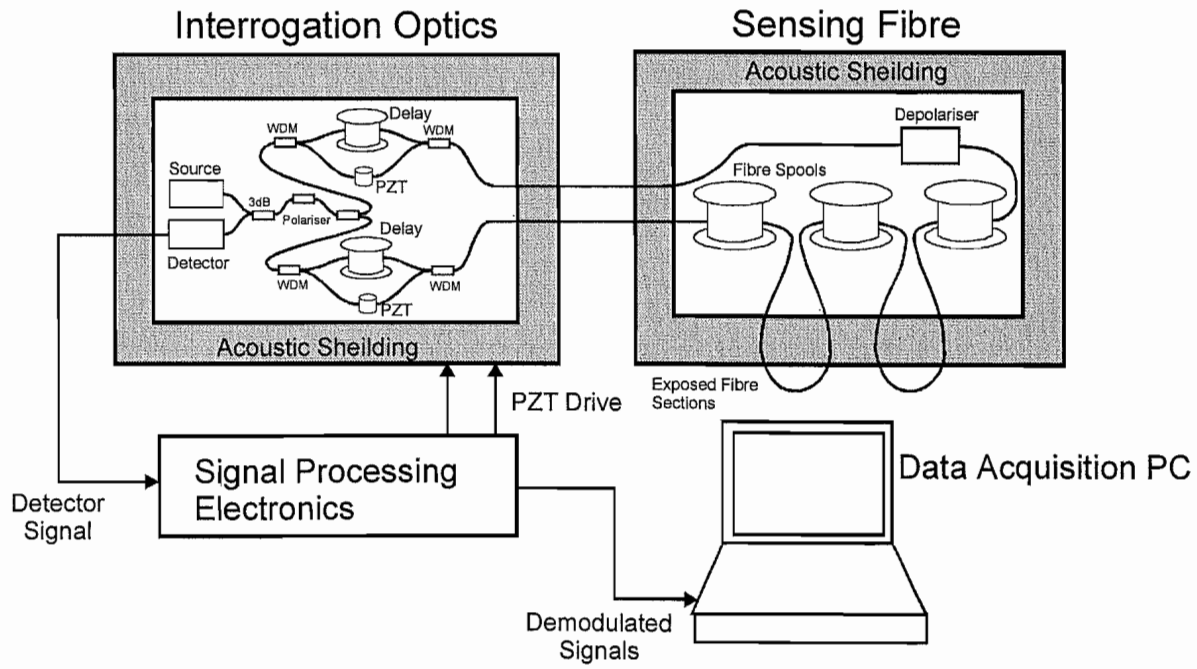

Figure 1.4.1 Schematic of experimental set-up for the dual-wavelength, dual-Sagnac interferometer. *The system was constructed in three separate parts, the interrogation optics, the sensor loop and the signal processing electronics. The acoustically sensitive interrogation optics and the simulated sensor cable (on reels of fibre for convenience) were placed in two separate acoustically shielded and sealed containers, reducing background laboratory noise.*

1.4.1.1 The interrogation optics

The optical network and its principle of operation have already been described in section 1.2.1. However, the actual experimental apparatus built for the investigation of this novel architecture has not yet been described. A specialised broadband superluminescent source was constructed, giving a 40nm wide spectral output centred at 1550nm, with a power variable between 0.2mW and 1mW. This was then spectrally sliced and routed to form two Sagnac loops, (Fig 1.2.1). The 3dB couplers used were Sifam, (SC155050/50), biconically-fused-taper devices. The WDM's first chosen were similarly biconically-fused-taper devices from IRE-polus, (IRE-W1540-1570). These devices had sinusoidal spectral transmission characteristics, with peaks at 1540nm and 1570nm respectively for each output arm. The fibre based polariser used was a Sifam product, (SP15), giving a 25dB polarisation extinction ratio. Fibre delay coils, each measuring approximately 4km in length, were wound onto heavy, machined aluminium fibre bobbins, designed such that the rigid bobbin was decoupled from its central supporting bush by an acoustically damping material, in our case, plastic sealing compound (GEC Plastic). Piezo-electrically-driven, fibre phase modulators were also constructed, using fibre wound around hollow PZT cylinders. These were incorporated into the system along with variable gain amplifiers so that they could be driven by a tone generated by filtering a TTL square wave. The gain adjustment was done manually. These components were then mounted and sealed in an acoustically shielded container, (800×600×600mm), with sound absorbing layers of mono-cellular foam and rock-wool (150mm thick). In addition to these layers of acoustic shielding, the exterior of the container was layered with a specialist acoustic damping sheet material consisting of a composite of mastic and foil (3mm thick, form Ainsley, acoustic damping mat). These layers of acoustic shielding helped reduce laboratory noise between 20-40dB depending on the noise frequency and direction. The detector used was an Indium Gallium Arsenide (InGaAs) pin diode device, (Nortel DPR2SB-43T2), used in conjunction with a Theoptics transimpedance amplifier (LAD40) with a 10Mohm gain.

1.4.1.2 The optical source

It was decided that the ideal source for this system was a broadband superluminescent ASE source. A 980nm, 80mW laser diode (Nortel LC91A-20) was used to single-end pump a 30m length of Er/Al-doped fibre (the fibre was made in-house and had a pump absorption of approximately $3dBm^{-1}$) via a biconically fused fibre WDM (ETEK SWDMC10095A10), (Fig 1.4.2). The forward ASE provided a 1mW source, having a centre wavelength of 1550nm and a 40nm FWHM bandwidth. However, the spectrum of this source was not exactly flat over the desired band, with the emission at 1532nm being dominant over that at 1550nm. A more balanced spectrum could, however, be achieved with a pump-laser drive current of 67mA, giving an ASE power output of 200μW, (Fig 1.4.3). As seen later, this becomes important, in order to approximately balance the optical power in each of the Sagnac interferometers. In addition to the optical components, a laser driver and cooler are required. An SDL800M laser driver and an ILX lightwave LDT-5412 Peltier cooler controller were used to drive and control the temperature of the 980nm pump diode.

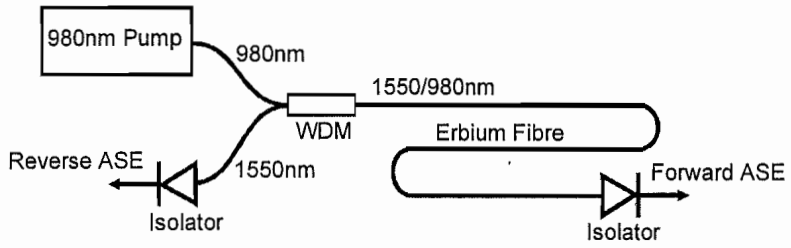

Figure 1.4.2 The Super-luminescent source. *30m of $3dBm^{-1}$ (absorption at 980nm) Erbium / Aluminium doped fibre is pumped at 980nm by a diode laser. The ASE spectrum is then used as a broadband source.*

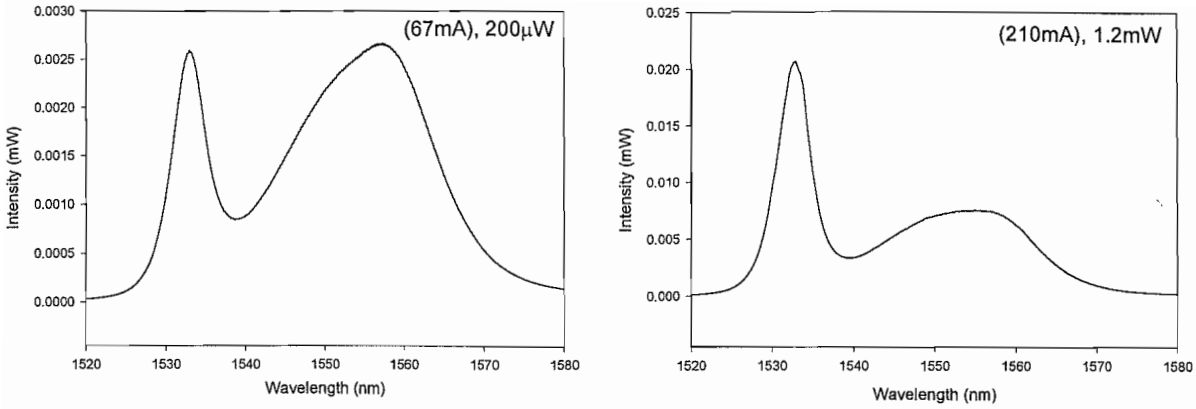

Figure 1.4.3 Optical spectrum of forward ASE SLS. *A balanced optical spectrum is achieved with a 980nm pump-laser drive current of 67mA, giving a fibre output power of 200μW. When more strongly pumped (210mA) an optical power of 1.2mW is achieved, but the optical spectrum becomes highly non-symmetric, (Note resolution of OSA was 0.5nm).*

1.4.1.3 Characterisation of WDMs

The WDMs initially chosen to demonstrate the dual-wavelength, dual-Sagnac interferometer were biconically-fused-tapered devices, giving a sinusoidal spectral transmission response. When the peak transmission is selected for each desired WDM channel, there is still significant overlap between the spectra emitted in each of the output arms. The WDM's purchased were specified to have spectral transmission peaks at 1540nm and 1570nm for each output arm respectively. To investigate this and calculate the expected optical crosstalk in the resulting optical sensor system, a broadband ELED source was initially used for experimental measurement of the WDMs transmission as it had a relatively clean Gaussian profile. This allowed the spectral transmission peaks for each of the WDM's to be found experimentally, for example the spectral transmission in each arm of WDM W115 and the optical source used are shown in (Fig 1.4.4).

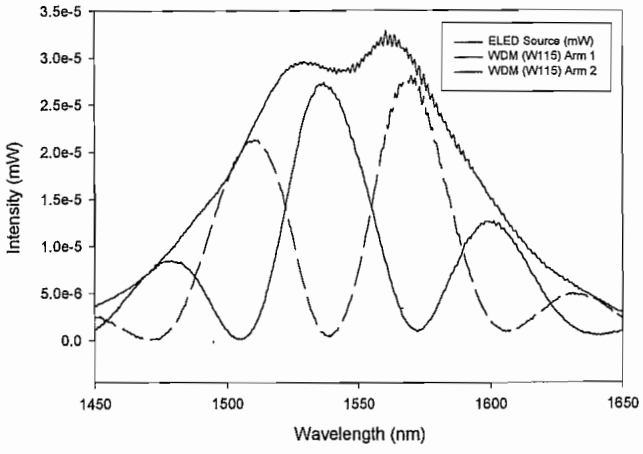

Figure 1.4.4 Measured spectral transmission of fused biconical WDM (IRE-Polus W115). *The spectral transmission of the WDM's used in the dual-Sagnac interferometer were measured using an ANDO optical spectrum analyser (Serial No 48320803).*

This was done for all four WDMs and their characteristics were found to be as follows.

Serial Number of WDM	Max-Min Arm 1 (nm)	Max-Min Arm 2 (nm)
W113	1570.0-1541.2	1541.6-1572.2
W114	1570.0-1545.6	1545.2-1570.2
W115	1570.0-1538.6	1536.2-1572.4
W452	1567.0-1545.0	1544.4-1568.2

These spectral transmission curves were then used to calculate the crosstalk in the system when using the previously defined ASE source. For example, if we compare the measured spectra profile of W115 with the modelled response we can see good agreement.

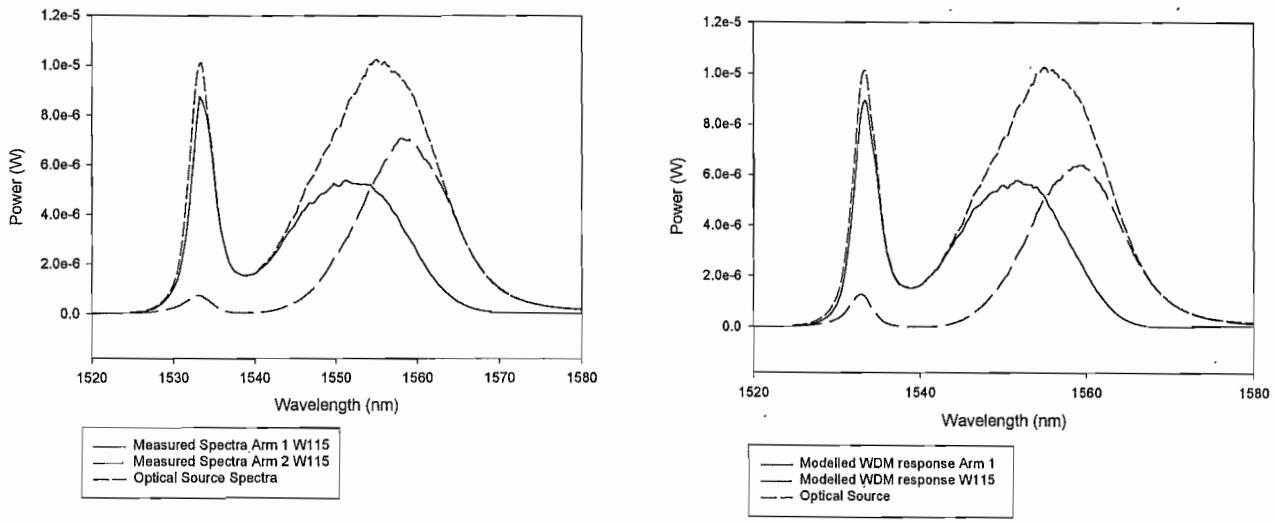

Figure 1.4.5 Measured and modelled WDM W115 spectra transmission profiles. *The left hand plot shows the experimentally observed spectra transmission profile for W115 and the right hand plot shows the modelled response*

Using this model, it is possible to calculate the expected optical crosstalk in the system. Fig 1.4.6 depicts the modelled response of the system. However, this model assumes that the loss for each of the wavelength defined Sagnacs is the same. This is not necessarily the case, as each of the PZT phase modulators is likely to have a different insertion loss and the fibre splice losses in each Sagnac may not be identical. It is expected, therefore, that the actual crosstalk in the final system may prove to be different than this calculated value

for our simple model. However, it does give a useful value for the expected order of magnitude of the crosstalk; vis: 17.4% for Sagnac 1 and 10.7% for Sagnac 2. Also it shows that the Sagnacs will still not be balanced in terms of optical power and that Sagnac 2 with have approximately 1.6 times higher received light power than Sagnac 1. This is due to the unfortunate dip in the source spectrum at 1540nm. Ideally WDM's with transmission peaks at 1532nm and 1555nm would be used. However, at the time of investigation they were not available. (Note: As better WDM components were subsequently used, these rather poor crosstalk figures have been greatly improved upon; now they are effectively insignificant, see section 1.4.3).

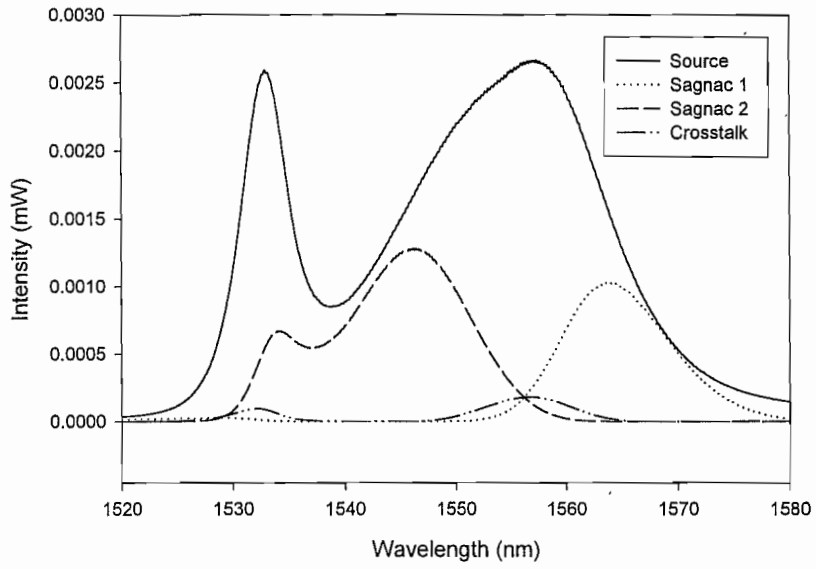

Figure 1.4.6 Calculated spectra for Sagnac 1, Sagnac 2 and optical crosstalk. *Integrating this spectra we find that Sagnac 2 has approximately 1.6 times the light transmitted around it when compared to Sagnac 1. The optical crosstalk figure for Sagnac 2 is 10.7% and 17.4% for Sagnac 1.*

1.4.1.4 The sensor loop

The sensor loop was built to attempt to simulate 40km of buried optical fibre. Six fibre bobbins were wound, (Fig 1.4.7), and placed in an acoustically shielded container identical to that used for the interrogation optics. However, a short test length of fibre between each of these bobbins was brought outside of the acoustic shielding to allow disturbances to be applied to the loop. A Lyot depolariser was constructed from two lengths, (3m and 6m of 2.93mm beat length), of elliptical core HIBI fibre joined with their polarisation axes

aligned at 45 degrees relative to each other. This was then spliced into the sensor loop near to its centre were acoustic disturbances would effect its action the least. As shown in figure 1.4.7, the positions along the loop at which disturbances could be applied, were measured, using an OTDR (Anritsu MW98A), to be at 0km, 12.83km, 25.66km, 26.15km, 26.67km, 27.17km and 40km respectively.

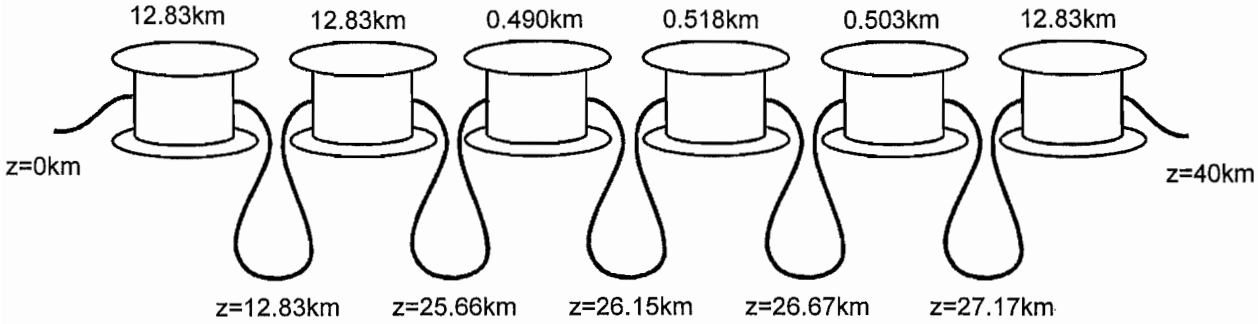

Figure 1.4.7 The sensor loop and disturbance locations. A sensor loop was constructed using 6 fibre wound bobbins.

The irregular spacings of these initially selected disturbance test positions were due to the lengths of fibre available at the time of construction. As will be shown later, once it was proved that the sensor operated as expected, this loop was rebuilt with evenly spaced test positions.

1.4.1.5 The Piezo Electric Phase modulators

As previously described, it was necessary to provide a phase bias to the Sagnac interferometer in order to 1) improve the sensitivity of the sensor, 2) allow the two Sagnac's to share the same detector, by virtue of different phase-bias frequencies foe each WDM channel. The first-order fundamental biasing modulation frequency necessary for a Sagnac interferometer having a total loop length of 44.0Km is of the order of 5kHz. The most effective solution was to build piezoelectric fibre stretchers to modulate the optical path length for light propagating along the fibre, as they have low polarisation dependence and low insertion loss when compared to integrated optics types. Piezoelectric cylinder's having the following characteristics were obtained from Morgan Martoc LTD.

Piezo cylinder specifications *(Length L = 38.1 ± 0.381mm, Outer Diameter OD = 50.8 ± 1.27mm, Wall thickness T = 5.08 ± 0.508mm, material PZT-5H,* $N_{3t} = 2000 H_{z\text{-}m}$, $T_c = 195\,℃$, $d_{33} = 593 \times 10^{-13} m/V$, $K^T_{33} = 3400$, $Na = 2290\ H_{z\text{-}m}$*).*

The performance of cylindrical piezoelectric fibre wound phase modulators has been investigated by G Martini[1.4.1], who showed that the phase efficiency of a cylindrical piezoelectric phase modulator, defined as the phase shift induced per turn of fibre per volt, can be expressed by;

$$\eta_{\phi l} = \frac{\Delta\phi_l}{NV} = \left[\frac{(2\pi)^2 C}{\lambda}\right] \cdot \left[n + (1+\nu)\frac{n^3}{2}\left[(p_{11} + p_{12})\left(\frac{r}{2R}\right) - p_{12}\right]\right] \qquad [1.4.1]$$

λ, is the wavelength of the radiation in the fibre, N, is the number of fibre turns, V, is the applied voltage, n, is the fibre core refractive index, ν, is the Poisson ratio for the fibre, p_{11}, is the longitudinal strain optical coefficient for the optical fibre, p_{12}, is the transverse strain optical coefficient for the fibre, r, is the outer fibre radius, R, is the outer cylinder radius and, C, is a constant dependant on the cylinder geometry and material and can be found from (Fig 1.4.8).

Values shown below were used for modelling,

Constant	Symbol	Value Used
Possion ratio	ν	0.17
Longitudinal strain/optic coefficient	p_{11}	0.121
Transverse strain/optic coefficient	p_{12}	0.270
Refractive index of fibre	n	1.46
Wavelength	λ	1550nm
Cylinder Constant	C	See (Fig 1.4.5), 0.5×10^{-9}

Using these values, it is possible to calculate that the expected phase modulation efficiency of our PZT modulators should be 16 mrads V^{-1} $Turn^{-1}$

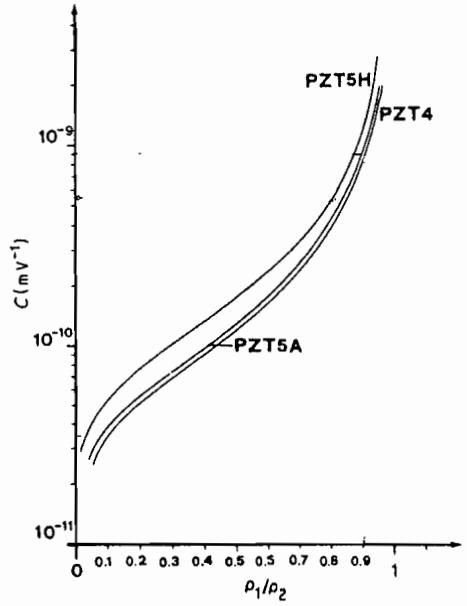

Figure 1.4.8, Graph showing variation of C against the ratio of the inner/outer cylinder radius for various piezo electric materials.

A 100 turn phase modulator was constructed with a ±15V variable gain amplifier (Fig 1.4.9). This allowed a theoretical maximum phase modulation depth of 48 radians, more than enough for the π/4 phase modulation depth required for the Sagnac interferometer. For example, (Fig 1.4.10), shows the detected signal for the dual-Sagnac, when biased with a sinusoidal tone at 40.6kHz. This figure shows that the required π/4 modulation depth is easily achieved and that the modulator is capable of over driving the interferometer. Note that this figure does not show the maximum modulation depth and that many more fringes were actually observed when the drive to the modulator was increased further.

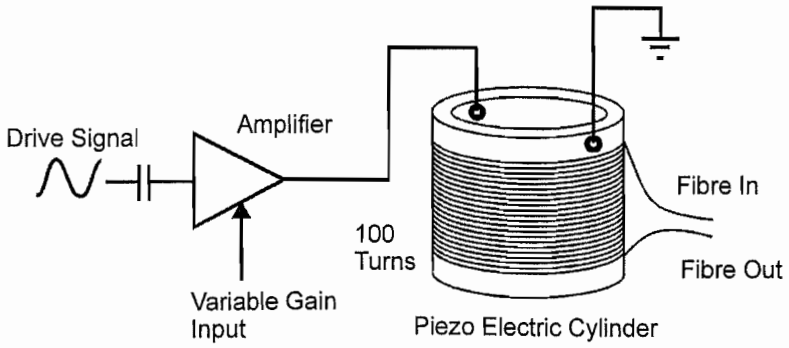

Figure 1.4.9 Piezoelectric Phase Modulator. *Schematic of piezoelectric fibre stretcher.*

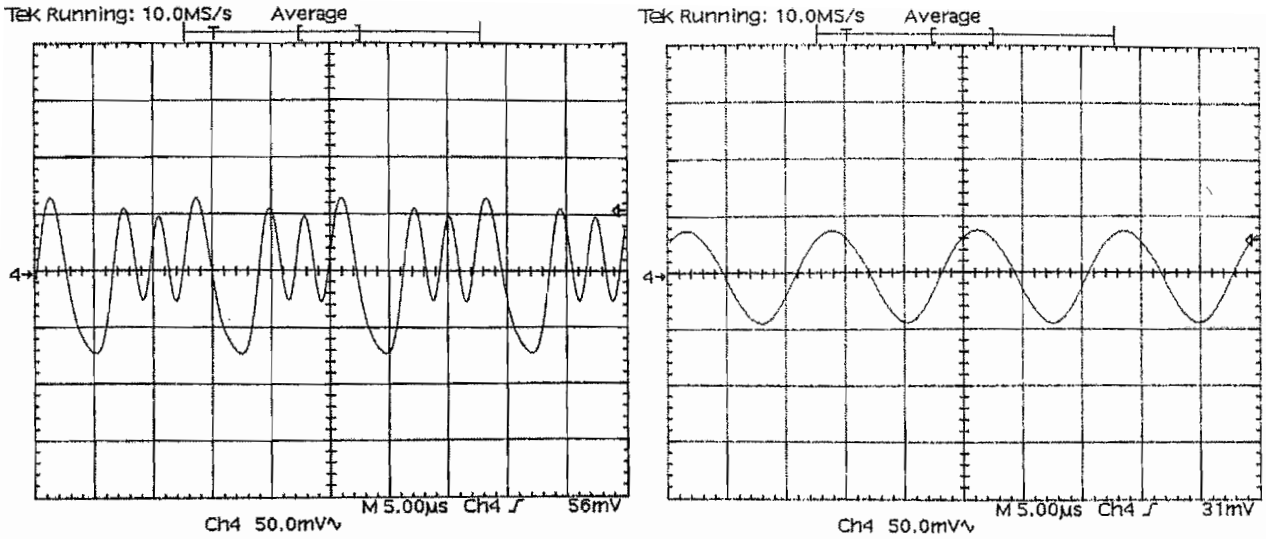

Figure 1.4.10 Detector traces, PZT1 being driven at 40.6kHz. *The first of the two graphs shows that the PZT phase modulator is capable of driving the interferometer past its quadrature point, when multiple fringes are observed. The second graph shows the desired waveform observed when the Sagnac is biased at quadrature, i.e. modulation amplitude of $\pi/4$. The relative phase shift generated at the interferometer output is $\pi/2$.*

1.4.1.6 The Signal Processing and data acquisition electronics

The electronics required for the dual Sagnac performs several functions. As stated each of the Sagnac interferometers require to be phase biased at Eigenfrequencies of their loop lengths. These phase-bias signals then result in generation of amplitude modulated carriers of the information corresponding to any disturbance acting on the loop. The signal received by the optical detection system has then to be coherently demodulated at two frequencies corresponding to the first and the other the second harmonic of the biasing frequency for each Sagnac. However, due to optical propagation delays, electronic delays and mechanical response delays, there is an unknown phase shift between the applied bias and the final detected signal, which must be allowed for when decoding.

The signal processing electronics is therefore required to firstly generate a sinusoidal waveform of variable frequency that can be employed as a PZT drive signal. This has then to be used as a phase reference and the electronics has to generate two waveforms, at frequencies f and $2f$. These reference signals must be phase shifted to match the observed phase difference between the applied bias and the detected signal. These waveforms can then be used to drive twin lock-in amplifiers which demodulate each separate bias signal from the optically detected signal.

A simplified schematic of the electronics operation is shown in, (Fig 1.4.11).

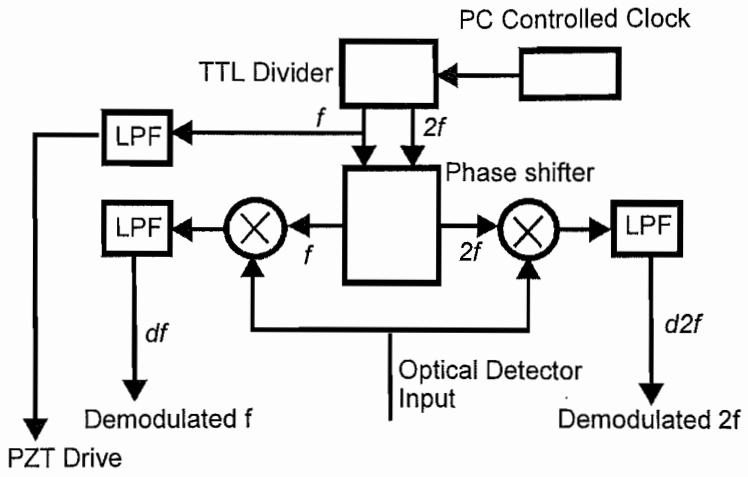

Figure 1.4.11 Schematic of signal processing electronics.

A single "master" clock is used to provide all bias and reference signals. This clock is computer controlled and is set at eight times the required phase bias frequency, *8f*. It is then divided, using a series of D type flip-flops, and a reference at a frequency *f* is generated. This is then filtered to its fundamental sine wave using a low pass filter and is then employed as the PZT phase bias drive signal. The higher order harmonics, *2f*,*4f* and *8f* generated by the divider are used to drive a 3bit digital phase shifter, generating phase shifted reference waveforms at *f* and *2f*. The digital phase shifter has a step size of $\pi/4$ and a range of $\pm\pi$.

These phase-shifted reference waveforms are then used to drive the twin lock-ins, operating at *f* and *2f*, producing demodulated waveforms *df* and *d2f* after low pass filtering. The base bandwidth of these lock-in amplifiers was initially set to 800Hz. Finally, a 16bit analogue data acquisition card (AT-A2150) was used to simultaneously sample the four output signals df_1, $d2f_1$, df_2 and $d2f_2$. These correspond to the demodulated signals at the first and second harmonics of the phase bias frequency for the two Sagnacs respectively. The data was sampled at a rate of 24kHz and stored as a "comma-separated-variable" data file, so that it could be further processed at the operators discretion. The digital and analogue sections of the electronics were built on separate boards and screened from each other to prevent pickup of the digital switching noise. A full circuit diagram of the lock-ins is given in appendix 1.4.

1.4.1.7 Frequency response and linearity of decoding electronics

Each of the wavelength-defined Sagnac interferometers needs to be biased at different frequencies. Each of the lock-in amplifiers are therefore driven at different frequencies. They will inevitably have a non-linear frequency response, which will effectively alter the observed estimate ratio, $df_1 d2f_2 / d2f_1 df_2$, which determines the position of the disturbance. The transimpedance amplifier used with the pin diode also has a frequency response, which has to be calibrated as it also effects the estimate ratio. Using a bench top signal generator as a test signal, the gain of the lock-ins were measured as a function of the bias frequency (Fig 1.4.12).

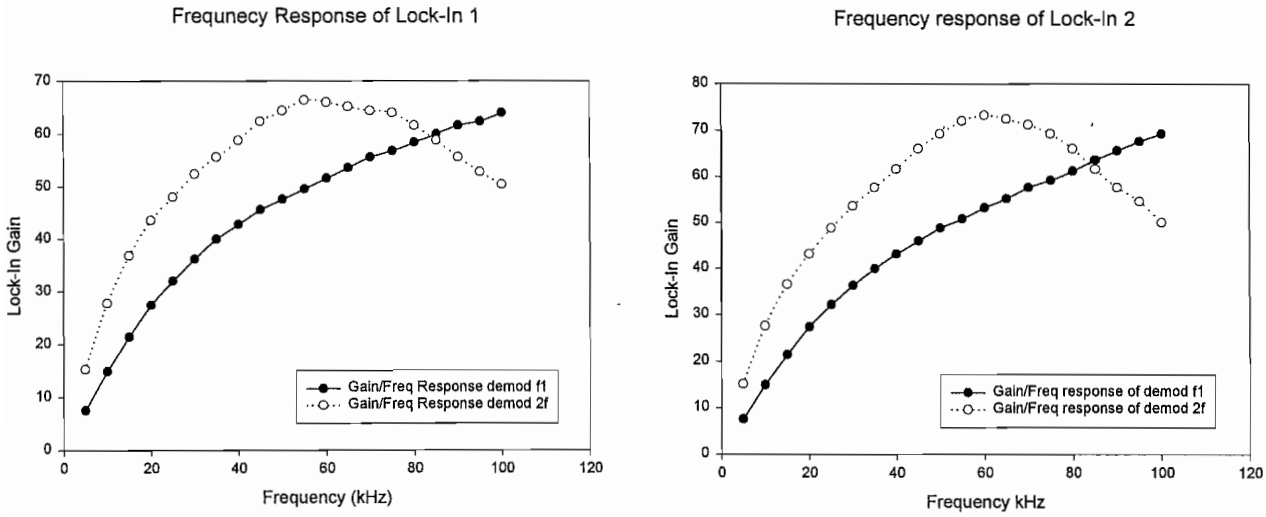

Figure 1.4.12. Frequency response of Lock-in Amplifiers. *Using a signal generator the gain of each lock-in was measured. This was done by inputing, in turn a signal at very close +0.1Hz f and 2f and measuring the amplitude of the sinusoid generated at each demodulated output.*

Although each of the lock-in amplifiers have very similar form of frequency response, the change in gain between the two Sagnacs bias frequencies can lead to a required correction factor of between 1 and 1.5, depending on the bias frequencies used. The linearity of the lock-ins was also investigated, to ensure that the variations in amplitude of the input signal did not adversely effect the lock-in gain (Fig 1.4.13).

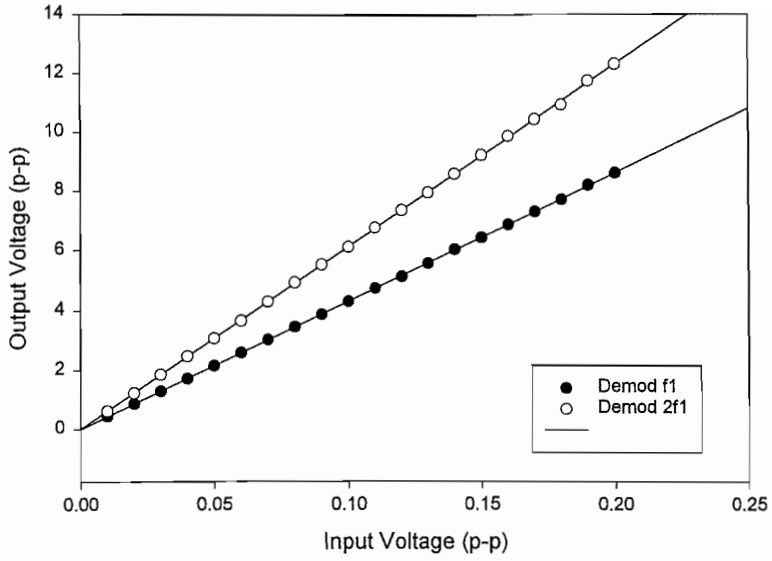

Figure 1.4.13. Linearity of Lock-in amplifers. The linearity of the Lock-in amplifiers confirmed as a function of the input signal peak to peak voltage. The above graph shows the response of Lock-in 1 at 40kHz.

In order to measure the frequency response of the optical detector we measured the peak-peak voltage observed when the Sagnac was biased to a known modulation depth, i.e. $\pi/2$ radians at loop Eigenfrequencies, (π phase shift generated at the interferometer output). This depth was set by observing the shape of the detected signal waveform. In this way, as shown in Fig 1.4.14, we were able to plot the frequency response of the detector module up to 500kHz.

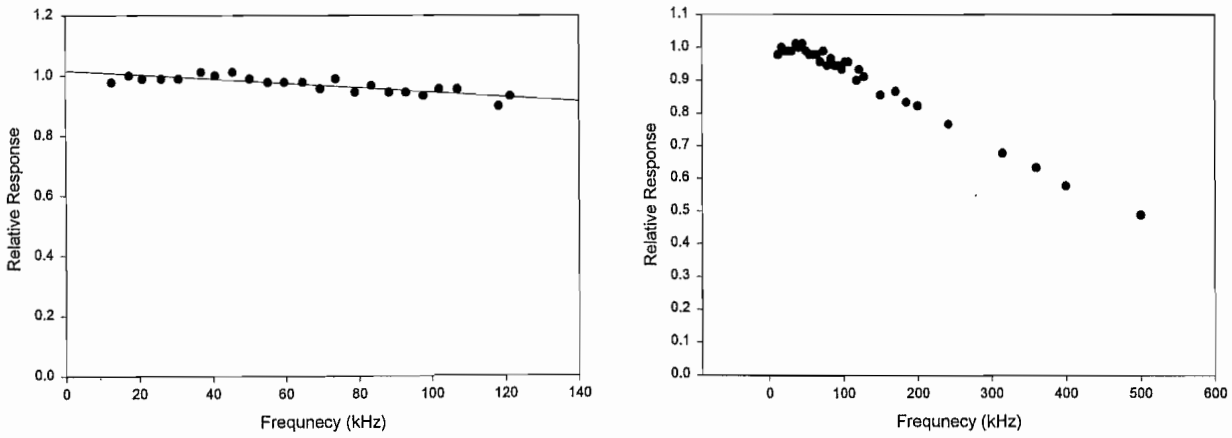

Figure 1.4.14. Frequency response of optical detector/ receiver module. *Theoptics LAD40, 10Mohm gain transimpedance amplifier. The frequency response of this optical detector was measured by observing the p-p voltage of the signal observed when the Sagnac was biased to $\pm\pi/2$ amplitude at varying frequencies. Its 3dB Bandwidth was approximately 450kHz and its "flat" region of response extends to approximately 130kHz.*

(Fig 1.4.14), shows the measured frequency response of the LAD40 (10MΩ) transimpedance amplifier from Theoptics. The response is relatively flat up to approximately 130kHz. Falling to –3dB at a frequency of 450kHz. This allows easy use of bias modulation frequencies in the range 5-100kHz. However, as with the frequency response of the lock-in amplifiers, the frequency response of the detector will require a correction factor to the observed estimate ratio to allow the disturbance position to be determined.

Fig 1.4.15, shows a photograph of the apparatus being tested, in the laboratory. Note that the interrogation optics and the 40km long sensor loop are in large acoustically shielded containers, as described earlier.

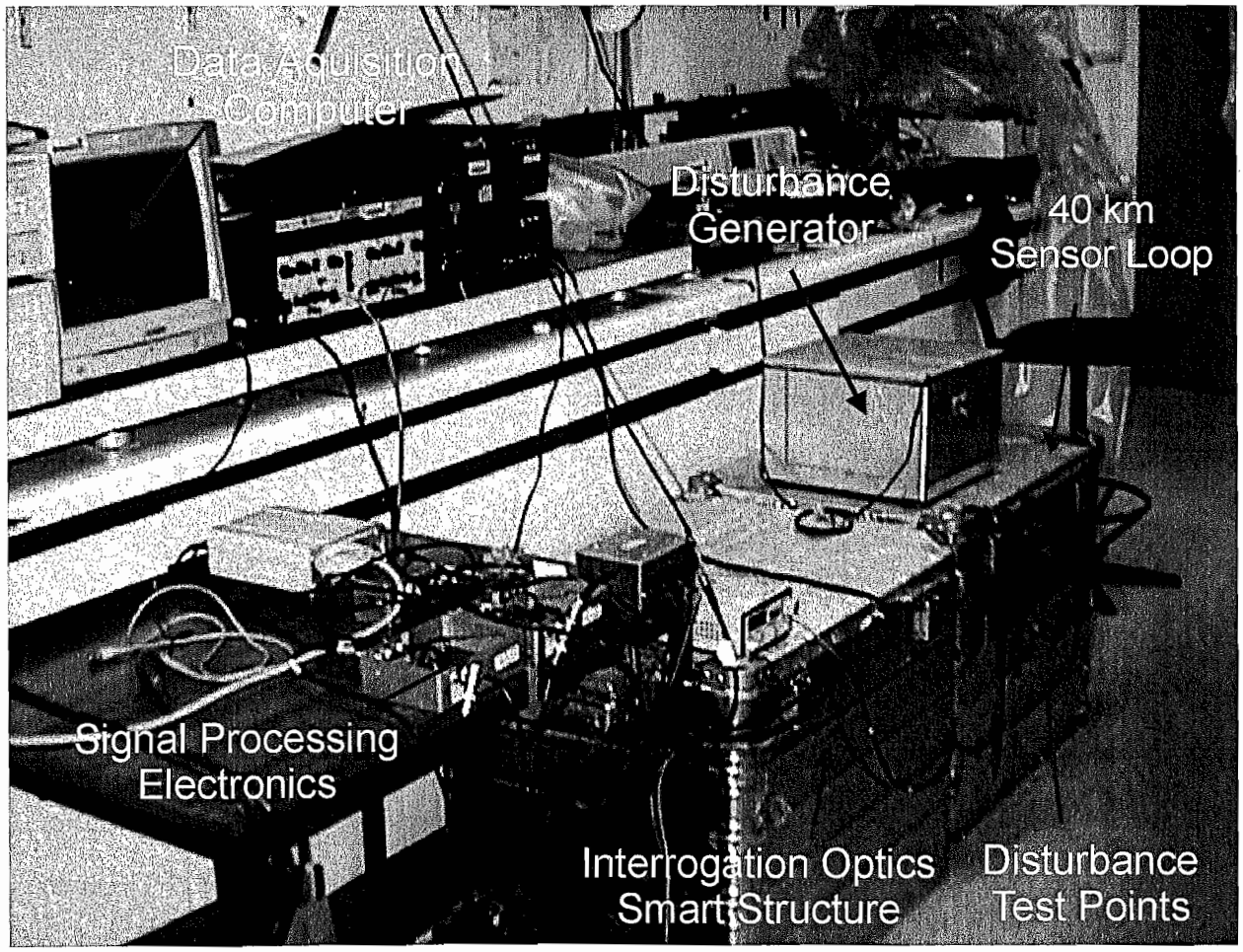

Figure 1.4.15 Photograph of experimental set up.

1.4.2 Experimental location of a tone disturbance

1.4.2.1 Calibration procedure for optical apparatus

In order for the system to respond as described by the theory several key variables must be set to known values. These include the bias-modulation frequency, the bias-modulation depth and the phase of the demodulation reference. The lengths of both the delay coils and the sensor loop must also be known. The lengths of the delay coils were measured to be 4.0 ± 0.1km during winding. The sensor loop length was measured using an OTDR (Anritsu MW98A) and was found to be 40 ± 0.2Km. Finally, the value of the modulation depth and frequency are not independent and optical cross-talk complicates the situation. To prevent optical cross-talk from affecting the calibration procedure each Sagnac must be set-up individually.

With only one piezo-modulator running, the procedure to set the modulation depth and frequency is simple. The amplitude of the drive signal to the PZT modulator is set to an arbitrary value, where changes in the modulation depth are easily observed, either by observing the DC level of the 2nd harmonic demodulated output *d2f*, or by observing the peak to peak voltage of the waveform generated at the detector. The modulation frequency may then be set to an Eigen-frequency of the loop by maximising this observed modulation depth, without altering the output level of the piezo drive amplifier. When this is the case, the drive signal to the modulator must be increased, until the interferometer is biased to a depth where the DC offset of the second harmonic demodulation term, *d2f*, just approaches its maximum offset (This corresponds to twice the normally desired bias level, i.e. $x = \pi/2$). The modulation depth should then be reduced to half of this observed maximum, i.e. $x = \pi/4$. This ensures that the Sagnac is operated at its most sensitive position, i.e. at the quadrature point of its phase response.

The Eigen-frequencies of each of the Sagnacs were measured as described above and are shown in Fig 1.4.16. As can be seen, each of the Sagnacs show approximately the same Eigen-frequency spacing of 4.64kHz, corresponding to a total loop length value of 44.2km, close to the value expected (44 ± 0.2km) from the actual measured loop lengths.

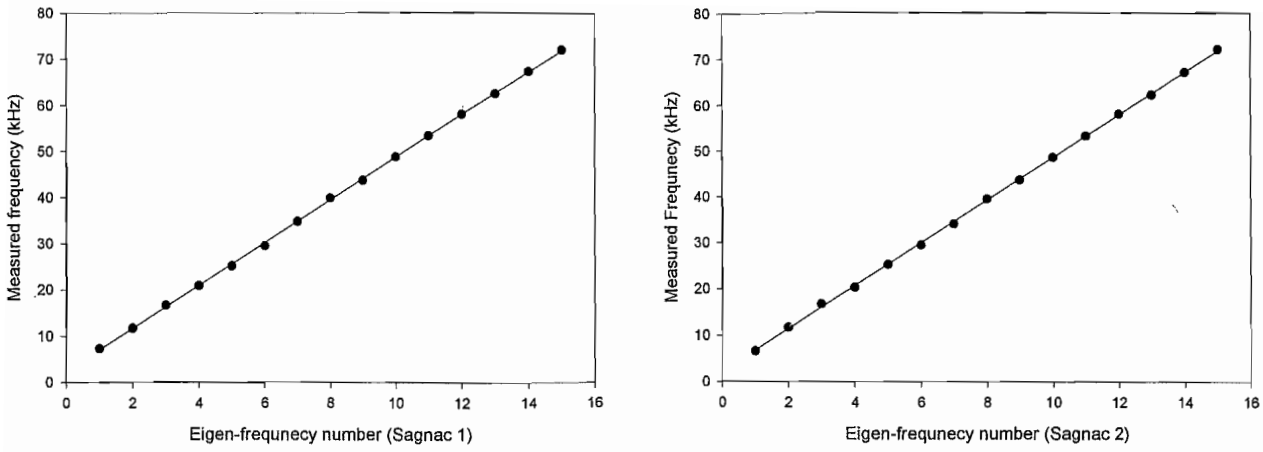

Figure 1.4.16 Eigen-frequency index, versus measured bias frequencies for each wavelength defined Sagnac. *The eigen-frequencies for each of the Sagnacs were measured as described previously and found to be 4.64kHz, implying a loop length of 44.2km.*

The optimum phase offsets for the lock-in demodulator references may then be set. To set the phase reference for the second-harmonic demodulator, the DC offset of the demodulated signal, *d2f*, should be maximised when the sensor loop is unperturbed. Similarly to set the phase reference for the first harmonic demodulator, the amplitude of the demodulated signal when a disturbance acts on the sensor loop should be maximised. When these procedure have been followed the system should obey the theory as previously described.

1.4.2.2 Experimental procedure

The equipment was constructed and set up as previously described. The dual wavelength dual-Sagnac was calibrated so that it operated at the 13^{th} and 10^{th} Eigenfrequencies. This corresponds to modulation frequencies of f_1 = 62.497kHz and f_2 = 48.561kHz. The modulation depth was then set to the quadrature point, i.e. $x = \pi/4$ modulation amplitude.

As described, the sensor loop was constructed such that there were a possible seven positions where a disturbance could be applied. A simple disturbance generator was constructed. This consisted of a loudspeaker which was mounted such that it vibrated an thin aluminium sheet, 20cm's square. A fibre could then be held against this plate allowing a time dependant strain to be applied to the fibre. The entire loudspeaker assembly was placed in a separate acoustically shielded box to prevent the remaining sections of the sensor loop from being perturbed. A sinusoidal disturbance was applied to

the sensor loop at these seven positions. The first selected disturbance was at 283Hz and its amplitude was set to produce a relative phase shift of approximately 0.1 radians, at the ends of the sensor loop, determined from optical response signal. The resulting signals obtained at the demodulators were then sampled into the computer at 24kHz with a sensitivity of 5V = Hex7fff and saved as ASCII text files. An example of the fringe patterns observed is shown in (Fig 1.4.17).

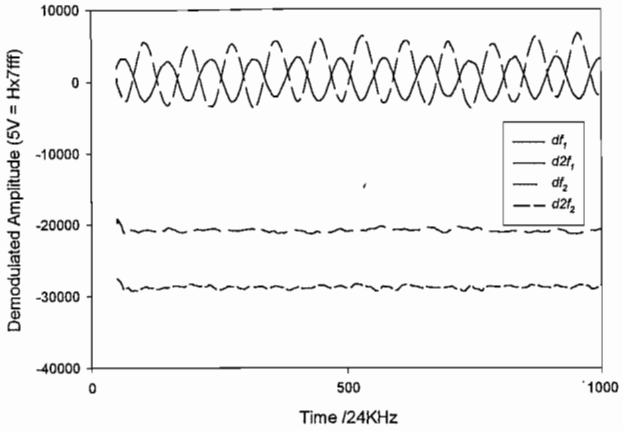

Figure 1.4.17 Experimentally observed fringe pattern generated by a sinusoidal disturbance acting at z = 40km *disturbance frequency f =283Hz, amplitude ≅0.1 radians. (Note: required correction factor is –1.15).*

As can been seen from this fringe pattern, there is undesirable frequency component at approximately 50Hz. There is also a DC offset present on the first harmonic signals. This 50Hz was later found to be due to intensity variations imparted to the source via changes in the pump drive current. In addition to this there was significant acoustic noise present on the demodulated signals. This acoustic noise acts on the entire sensor loop simultaneously. The position result obtained by taking the direct ratio between the four demodulated channels when no disturbance acts is therefore in the centre of the sensor loop. The positional histogram obtained by directly processing these results was very noisy and showed little positional sensitivity, an example of the unprocessed histogram is shown in figure 1.4.18. As with the simulations, the acoustic noise tended to "pull" the positional results towards the centre of the sensor loop. From these results we can make an estimate of the acoustic background level. The 283Hz disturbance inducing a relative phase shift of $\Delta\phi \approx 0.1$ radians at 0km into the sensor loop is positioned at approximately 13km. Similarly the 283Hz disturbance acting at 40km is positioned at 27km. As the

weighted average position of the disturbance and the acoustic background pulls the result 13km closer to the sensor loop centre, this is turn implies that the integrated acoustic background is likely to be approximately 10 times larger in magnitude of phase disturbance than the disturbance to be located.

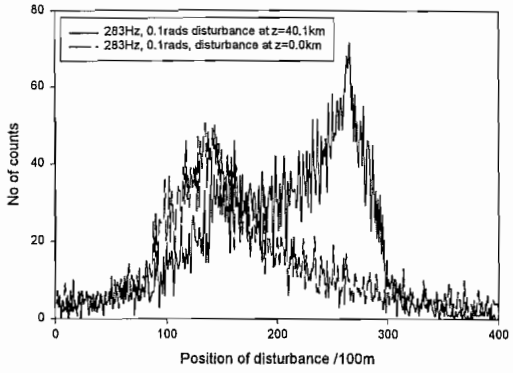

Figure 1.4.18 Experimentally observed positional histogram for a single disturbance of 283Hz and 0.1 radians amplitude acting at 0km and 40km respectively. *The above graphs shows the directly processed results for a disturbance acting at 0km and 40km respectively. As can be seen the position algorithm incorrectly positions these disturbances, averaging them with the acoustic background.*

As described in chapter 1.3 section 1.3.4.2, disturbances of different frequencies may be separated by band-pass filtering the data at the disturbance frequency. To accomplish this the data was digitally filtered with a pass band of 10Hz around the known disturbance frequency of 283Hz. The fringe pattern recovered was far cleaner than that obtained directly. This is shown in figure 1.4.19.

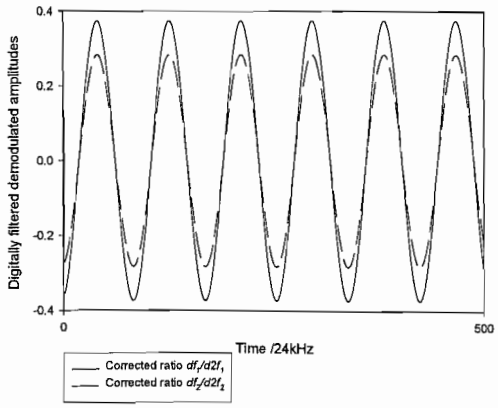

Figure 1.4.19 Experimentally observed fringe pattern after digital filtering with 10Hz pass band around 283Hz.

The same disturbance was then applied to each of test positions and the results were processed in the same manner. The estimate ratio, df_1d2f_2 / df_2d2f_1, was then calculated for each of the test positions and was plotted as a function of the test positions location along the sensor loop. Figure 1.4.20 shows the results obtained for each of the seven test positions, located at 0km, 12.83km, 25.66km, 26.15km, 26.67km, 27.17km and 40km respectively. Since the data card is only capable of producing a data set lasting a fraction of a second, (0.416s), then the results obtained are necessarily the average of several samples taken consecutively. The theoretical model for the dual wavelength Sagnac interferometer biased at 62.50kHz and 48.56kHz is also shown for the two following cases,

1) Zero optical cross-talk and
2) The measured modelled value of optical cross-talk previously presented in section 1.4.1.3.

Please note, also that as previously explained, a correction factor of -1.15 was used to account for the frequency response of the optical detection system and the signal processing electronics. The negative sign indicates that the phase of the frequency reference was 180 degrees from the normal in-phase condition. Good agreement between the theory and experimentally observed values can be seen.

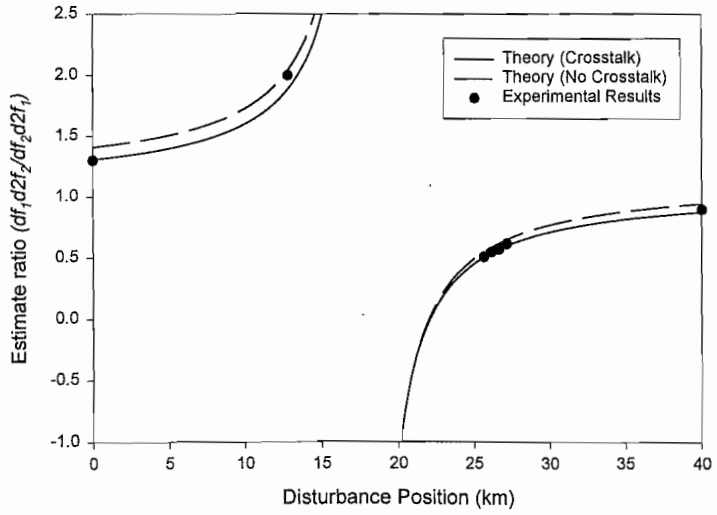

Figure 1.4.20 Experimental observed "estimate ratio" results *Also plotted is the theoretical response of the dual wavelength Sagnac both including and excluding the effects of optical cross-talk.*

The position, as calculated from the recovered estimate ratio was then determined for each of the test positions. The measured disturbance position was then plotted versus the calculated disturbance position. The predicted straight line, $y = x$, is also plotted

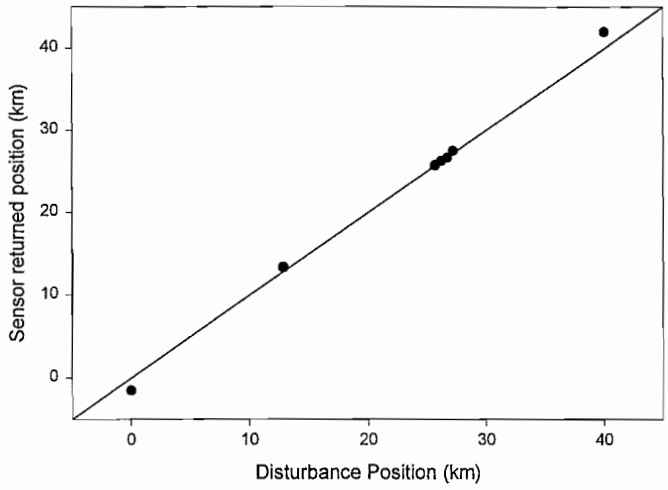

Figure 1.4.21 Experimental Positional Results Measured disturbance position versus calculated positional results

As shown in Figure 1.4.20 and 1.4.21, the theory that describes dual-sideband demodulation of the biasing frequencies gives positional results which agree well with the observed experimental results, providing account is taken the effect of optical cross-talk.

1.4.2.3 Discussion

We have shown that the initial dual-wavelength, dual-Sagnac interferometer performed as expected, exhibiting the characteristics predicted by the theoretical analysis presented in chapter 1.2. The position-dependent results obtained from the sensor agreed well with the theoretical response, but this first system suffered from several unfortunate problems. The first, and most obvious was the excessive acoustic noise "pickup", as evidenced by (Fig 1.4.18). Although we were able to reduce the effects of this noise, by reducing the bandwidth of the sensor by digitally filtering the results, this noise remained a problem for all early testing of the system. Also, due to the low power of the source, (200μW), and the excessive loss in the system due to non-ideal components, the theoretical signal / noise limit predicted by fibre thermal phase noise is not approached also leading to a poor

system performance. Fortunately, there was considerable room for improvement in several areas, including the optical source and loss in optical components.

Another disadvantage of this system is that at present the data acquisition hardware is limited in its capabilities. The data acquisition used to capture these results was capable of gathering a data set lasting only a fraction of a second (0.416s). This was then saved as a data file for later processing. The speed of the data-processing PC was also a factor. Although it was able to simply calculate the estimate ratio ($df_1 d2f_2 / df_2 d2f_1$) and then, in turn plot, (in histogram form), the calculated position, it was not able to perform any higher level signal processing functions such as digital filtering and frequency analysis. This meant that the results could not initially be processed in real-time, leading to difficulties in the calibration and analysis of the sensor.

The results obtained using this first system were nonetheless encouraging. Although, as can be seen in (Fig 1.4.21), the position determined for disturbances acting towards the ends of the loop tended to drift away from the ideal $y = x$ response, we still see very good, repeatable position dependent results. Since the system was not calibrated in real-time, by observing the position of the disturbance as it was calculated, any number of effects could have caused this very slight drift. These may have included the bias-modulation depth set slightly away from quadrature or similarly the bias frequency, not quite at an Eigenfrequency of the loop. To quantify how small a miscalibration is required to account for these observations, the change required in estimate ratio for a position error of 1m towards the end of the sensor loop is only 10^{-5}. Therefore in order for the disturbance at 0km to be positioned at –1.5km, the estimate ratio needed only to be 1.5% away from the predicted value. A miscalibration in either the modulation depth of $\Delta x = 0.012$ rads or the bias frequency of, $\Delta f = 69$Hz would have caused such a position error. It is easy to see how a 0.012 miscalibration in the modulation depth could have resulted.

Before further investigations of this initial sensor system were to take place it was decided that the obvious system deficiencies should be addressed. The system was therefore examined critically and each part improved where possible. It was found that the 50Hz pickup noted previously on the lock-in outputs was in fact due to intensity fluctuations imparted to the super-luminescent source by variations in the current supply to the 980nm

pump diode, via the SDL laser driver. It was decided that a new source should be constructed not only to reduce this 50Hz noise but also to achieve higher output intensity. The optical loss and crosstalk in the system was also addressed. The WDMs initially chosen for the dual-Sagnac set up exhibited sinusoidal transfer functions, leading to high crosstalk, (10.7% and 17.4%) and, when averaged over the wavelength band of interest, high insertion loss. However, the most important factor is the data-acquisition hardware and its ability to process, in real-time, the sampled data and display the results. The following section describes the improved optical set up now incorporating;

1) a new higher power optical source,
2) new WDMs exhibiting spectral transmission profiles much closer to the ideal "Top-hat" shape required, resulting in an optical system with far lower optical crosstalk, (-50dB),
3) a significantly reduced optical loss.

A final signal processing improvement in the use of an improved data-acquisition card and PC, allowing for the first time, real-time disturbance location over a 40km long dual-wavelength, dual-Sagnac interferometer.

1.4.3 An improved Dual-Wavelength, Dual-Sagnac sensor system

1.4.3.1 Improvements to the optics structure

One of the problems observed in the original investigation of the dual-wavelength, dual-Sagnac interferometer was an excessive acoustic noise source, present in the laboratory. In an attempt to reduce the pickup of this noise by the 40km long sensor loop, the acoustic shielding built into the sensor loop housing was investigated and improved. The housing itself, which was 800×600×600mm, aluminium flight trunk, with a hinged lid, was mounted on acoustic absorbing plastic compound in an attempt to decouple it from the laboratory floor. Also additional layers of acoustic damping matt, (Ainsley, acoustic damping mat), were used to cover all faces of the container. In addition to this, a 120mm thick layer of compressed fibre-glass was used to build a separate acoustically shielded compartment within the outer container. This reduced the laboratory noise significantly to a level where experimentation was possible. However, we still see a noise level limited by acoustic pickup in the laboratory. Figure 1.4.22 shows the noise-induced frequency

spectrum of the demodulated output df_1, firstly when the lid of the sensor housing is closed and then when the lid is open. It is easy to see that, above frequencies of 60Hz, the acoustic shielding reduces the effect of acoustic noise from the laboratory by at least 20dB. However, noise sources of frequency less than this still appears to penetrate the acoustic shielding. Since acoustic noise sources are highly directed, it is estimated that without this shield the noise floor would be at least 35dB higher than with the container sealed.

Calibrating the noise response against a known applied disturbance, (A single-tone disturbance seen to give a detected voltage of -14dBV, producing a relative phase shift of 8mrads) we can plot this noise as an equivalent phase modulation. We find that the minimum noise level is approximately 16μrads $Hz^{-1/2}$ at 120Hz. The amplitude of the applied sinusoidal-tone disturbance was measured by comparing the amplitude of demodulated signals $d2f_1$ and df_1 at both the applied disturbance frequency and that at twice the disturbance frequency respectively. It may be shown that for this ratio to be $d2f_1(2f_{dist})/df_1(f_{dist}) = 2\%$ then the relative phase amplitude $\Delta\phi$ is 0.1rads.

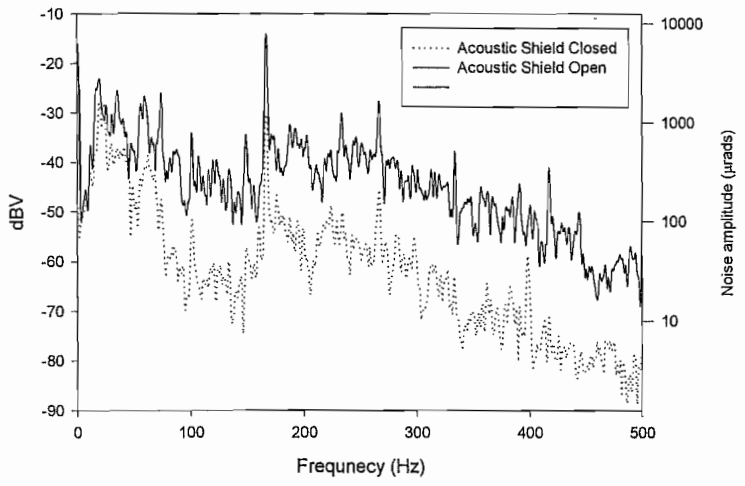

Figure 1.4.22 Measurement of laboratory noise, frequency spectra of 1st harmonic demodulated output df_1. *The frequency noise spectrum of the first demodulated output for Sagnac 1 was measured with 1) The lid of the sensor-loop housing closed 2) The lid open. As can be seen, the additional air-coupled noise increases system noise by typically 20dB. Also, please note that the low frequency noise <60Hz still penetrates the acoustic shield. (Note the FFT bin-width was 2Hz and the 3dB bandwidth of lock-ins was 200Hz.*

Once the improvements to the acoustic shielding of the sensor were complete, attention was turned to the optics components of the dual-Sagnac system. The fused-taper WDM's were replaced with dichroic-filter based WDM's, from Dicon optics (FWC-28.0). The spectral transmission profiles for these devices were measured using an ANDO, OSA (Fig 1.4.23). These exhibit a spectral transmission profile approaching the ideal "Top-hat" response, superior to the sinusoidal response of the fused-taper ones, (improved average transmission loss and far lower crosstalk). The crosstalk between the channels in each individual WDM was specified to be approximately -10dB, and the excess insertion loss approximately only 0.7dB over the pass band (1552-1565nm) and 0.5dB over the reflected band (1528-1544nm). When compared to the biconically fused fibre devices, these new WDMs offer an expected improvement in the spectrally averaged insertion loss of 0.8dB per WDM, i.e. a loss reduction of 3.2dB for the complete dual-Sagnac system. The crosstalk of the resulting dual-Sagnac sensor system is also reduced to a negligible theoretical value of –40dB. Later measured to be –50dB.

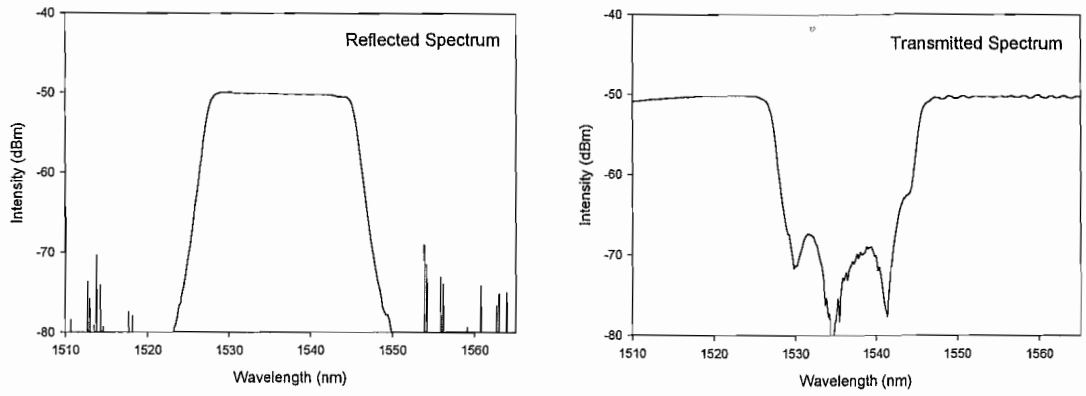

Figure 1.4.23 Transmitted and reflected spectral profiles for dichroic based WDMs used in the improved dual-Sagnac system.

The delay coils used initially appeared to have excessive microbend losses so they were rewound. Due to an unfortunate winding accident, however, one of the delay coils ended up being 500 meters shorter than its original length. The new lengths were now measured as L_1= 3550m and L_2 = 4050m. As before, these were mounted on acoustically decoupled collars. One of the most important improvements was in the optical source. An extra 10m of Erbium doped fibre was added, (Fibercore DF1500F with a pump absorption of 5.2dBm^{-1} at 980nm), to the source, giving a total source fibre length of 40m. This allowed the pump power to be increased whilst keeping the ASE spectra shape reasonably

balanced, Fig 1.4.24. With these changes, an ASE output power of 4.2mW was achieved, whilst still enabling a balanced spectrum. The 50Hz intensity modulation due to main-frequency signals in the current driver to the 980nm pump was solved by using a new driver from Theoptics (ATLAS 60). Since this driver is powered by a filtered 6V DC supply, no 50Hz pickup is seen.

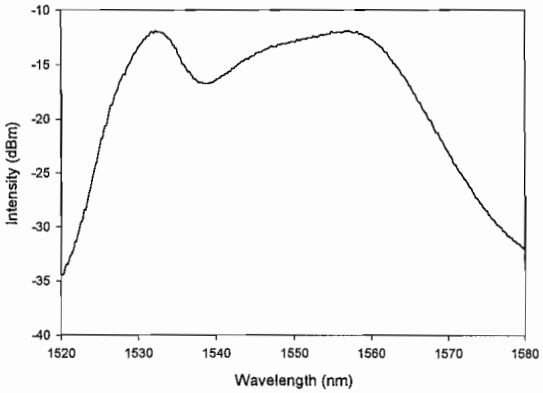

Figure 1.4.24 The improved ASE source. *An extra 10m of Erbium doped fibre (Fibercore DF1500F), was added to the length already in the source, giving a total fibre length of 40m. This allowed the pump power to be increased without making the 1532nm emission dominant.*

The average total transmission loss of the optical network over both wavelength bands was measured to be 33.8dB, compared to a minimum theoretical loss of 24.2dB. The laboratory constructed components, such as the delay coils, sensor loop etc will inevitably suffer from additional losses, i.e. from microbending and splice loss. Breaking this down:-

40km single mode fibre, sensor loop @1550nm 0.21dBkm^{-1}	8.4dB
4km delay coil @1550nm 0.21dBkm^{-1}	Measured average 2.4dB
PZT phase modulator	Measured average 1.0dB
Lyot Depolariser	Measured 1.6dB
Polarising Filter	Measured 1.6 + 6dB
WDMs	Calculated average over wavelength band 3.2dB
3dB Couplers	Measured 0.5dB
Intrinsic architectural loss, from 3dB couplers and spectral slicing.	Calculated 9.0dB
Total loss	**33.7dB**

As can be seen, several of the components built have additional loss. The polarising filter has an excessive loss of 1.6dB. Similarly the delay coils, due to the winding tension, suffer from microbending loss and exhibit a loss 1.6dB higher than their fundamental limit of intrinsic fibre loss. The PZT modulators also show an insertion loss of 1dB again, due to bend losses. However, even with losses as high as 33.8dB, the light incident on the detector was now adequate, being approximately 2μW. (Fig 1.4.25) shows a spectrum of the detected light when the source was set to an optical power of 1.2mW. As can be seen the intensity changes as a function of wavelength with a periodic structure. This is the action of the Lyot depolariser and is evidence that it is performing its function well.

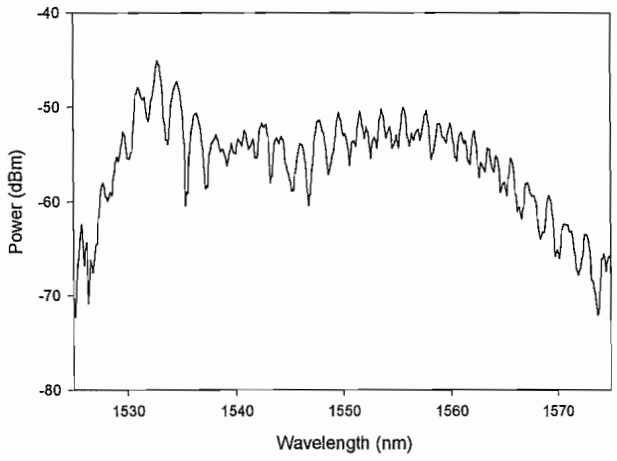

Figure 1.4.25 Detected optical spectrum, Ando spectrometer. *The source was set to an optical power of 1.2mW and a received power of 500nW was detected. Note the fine structure in this spectrum, likely to be evidence of the Lyot depolariser.*

Due to the significant increase in received optical power an improved transimpedance amplifier was required. A new 512kΩ transimpedance amplifier was constructed using a Burr Brown device (OPA655) FET-input amplifier (GBP 400MHz). The saturation voltage of this amplifier was 15V and so the expected signal level of 1V was well below this. The –3dB frequency response was 2MHz and was essentially flat up to 400kHz.

The optical network was rebuilt into a more suitable container for laboratory and field trials. A photo of the interrogation structure, outside of its acoustic shielding is shown in (Fig 1.4.26). As can be seen, the two delay coils are mounted on acoustically decoupled

collars towards the back of the unit. The PZT modulators are mounted on either side of the container in separate boxes, which also contain the variable gain amplifiers required to drive them. The routing and spectral slicing components are mounted in number of smaller boxes in the centre of the container. Also labelled are the source and detector units. The interrogation optics structure was then placed within its acoustic shield in order to investigate its properties.

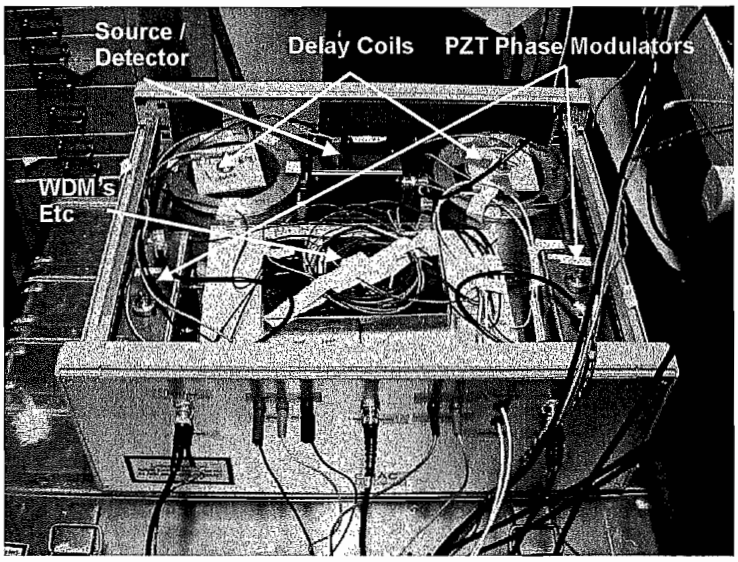

Figure 1.4.26 Photograph of optics interrogation structure forming a dual-wavelength, dual-Sagnac interferometer. *Note each delay coil is wound on acoustically damped and decoupled bobbins, The PZT phase modulators are in small boxes on either side of the box. The source and detector are mounted towards the back of the rack and the spectral slicing and routing components are in the centre.*

To investigate more thoroughly the positional sensitivity of the dual-wavelength, dual-Sagnac interferometer, the sensor loop was rebuilt to provide more evenly spaced test positions. Each of the fibre bobbins were rewound in lengths approximately 6.5km in length. (Fig 1.4.27), shows the new sensor loop with the distances between test positions marked. 0km, 6.4km, 12.84km, 19.28km, 25.78km, 32.2km and 38.67km respectively.

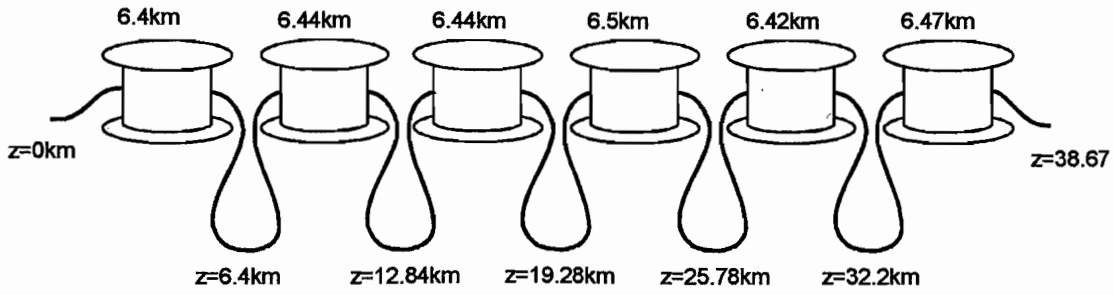

Figure 1.4.27 The rebuilt sensor loop. *The spacing of the test positions were more evenly spaced, however the total loop length was reduced slightly to 38.7km.*

1.4.3.2 Improvements to the data-acquisition hardware and signal-processing

Data-acquisition hardware

The data-acquisition hardware used originally for the dual-wavelength, dual-Sagnac interferometer system was capable of simultaneously sampling data with 16bit resolution from 4 analogue channels at a rate of 24kHz. However, due to the memory buffer size on the card and the DOS memory limit, the continuous sampling time was limited to a fraction of a second, (0.416s), i.e. 10000 data points. As a result real-time signal processing of these data sets would be difficult, and also limited by the CPU speed of the computer used, (Cyrix 486DX-50).

An improved data-acquisition card was bought from National-Instruments (PCI 6023E). This card, although now having only a 12bit resolution, was capable of simultaneously sampling up to 16 channels with a combined sampling rate of 200kHz. So for 4 simultaneously sampled channels, sample rates of 50kHz could be achieved. Unlike the other card, this allowed direct memory access and was supported under windows. This allowed continuous sampling of all four channels at 50kHz into a memory buffer up to 96MB in size.

Signal-processing scheme

The initial investigation of the dual-wavelength, dual-Sagnac interferometer showed that the unprocessed data generated by the lock-in amplifiers required some amount of signal processing in order for the position of the disturbance to be recovered. This was accomplished by applying a narrow band digital filter to the signals generated by the lock-ins around a frequency corresponding to the disturbance to be positioned. As was predicted by the theoretical modelling of the system presented in chapter 1.3 this allowed the disturbance to be located. As part of a supervised third year student project a new data-acquisition and signal processing control software was written using Borland Builder C++.

This signal processing software samples the four demodulated outputs df_1, $d2f_1$, df_2 and $d2f_1$ simultaneously at an individual rate of up to 48kHz. The data obtained is then converted to the frequency domain by applying a Fast Fourier Transform (FFT). Both the

frequency power spectrum and the phase spectrum can then be displayed on screen or saved as comma separated data files. The software can then be instructed to perform several tasks.

1) Locate a disturbance with a specific frequency
2) Locate the largest observed disturbance
3) Locate up to 3 user defined disturbances simultaneously

The sampled demodulated signals, df_1 and df_2, corresponding to the first harmonics of the bias frequencies are then bandpass filtered at the disturbance frequency. This is done in the Fourier domain by applying a Blackmann data window routine. Similarly the sampled demodulated signals, $d2f_1$ and $d2f_2$, corresponding to the 2nd harmonic of the bias frequency are low pass filtered to recover the DC component. The resulting estimate ratio is then calculated by taking the ratio of these 4 digitally filtered signals, and the corresponding disturbance position displayed on screen. These results may, as before, be saved as comma separated data files. Also the ratio of the Fourier components $d2f(2f_{dist})$ and $df(f_{dist})$ is then calculated and displayed as a percentage, where f_{dist} is the disturbance frequency. This gives a measure of the relative phase shift, $\Delta\phi$, generated by the disturbance. A ratio of 2 percent corresponds to a relative phase shift of $\Delta\phi = 0.1$ radians. The system therefore prompts a non-linear alert when this ratio increases past 2%. (Note position error from using the small-signal approximation is approximately 100m over a 40km loop for 0.1 radian disturbance, towards the sensor loop ends).

Using methods presented in chapter 1.3, it should be possible to separate several disturbances acting on the simultaneously on the loop, providing they are of different frequencies. This new processing scheme has now been implemented, and allows for the first time, multiple disturbances to be separately positioned using a Sagnac architecture. This method will be published shortly [1.4.3]. The software samples the data, just as it would for a single disturbance, but it then processes the same data set (up to 3 times) at different disturbance frequencies, (input by the user, or the three largest peaks observed in the FFT spectrum of the demodulated output), and plots not only each of the calculated disturbance positions but also their corresponding frequencies. Figure 1.4.28 shows a screen capture of the Sagnac data acquisition and signal processing software.

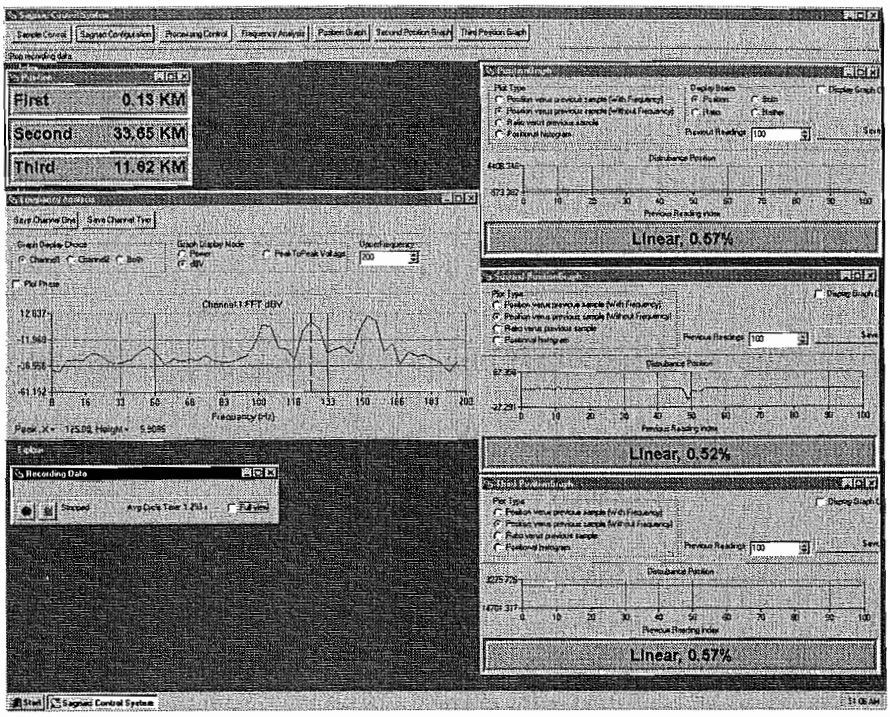

Figure 1.4.28. Screen capture of Sagnac data-acquisition and signal processing control software.

1.4.4 Initial set up and testing of the improved dual-Sagnac

Since the lengths of the delay coils have been changed the Eigenfrequencies of the Sagnac have now also altered slightly. Figure 1.4.29 shows the new Eigenfrequency-plots for the improved Sagnac.

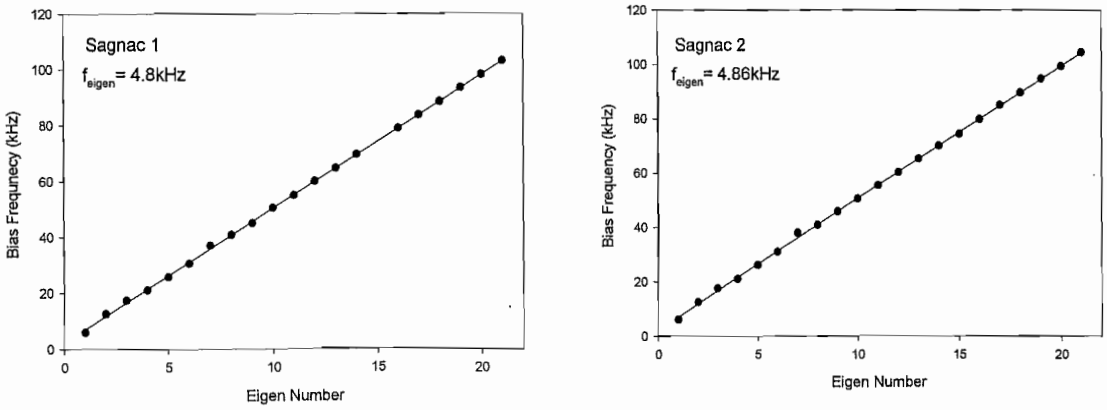

Figure 1.4.29 Eigen-plots for improved dual-wavelength, dual-Sagnac Interferometer. *The eigen-frequencies measured for the new improved dual-Sagnac interferometer correspond to calculated loop lengths of 42.808km for Sagnac 1 and 42.279km for Sagnac 2.*

Sagnac 1 showed an Eigenfrequency of 4.8kHz, implying a total loop length of 42.8km. The second Sagnac an Eigenfrequency of 4.86kHz, implying a total loop length of 42.279km. Knowing the delay loop lengths of L_1= 4050m and L_2= 3050m, then the sensor loop length is calculated to be 38.7km in good agreement with that measured by the OTDR (Anritsu MW98A). The two Sagnac interferometers were biased at 40.59kHz and 50.73kHz, respectively. Figure 1.4.30 shows the frequency spectrum of the signal detected at the output of the dual Sagnac sensor.

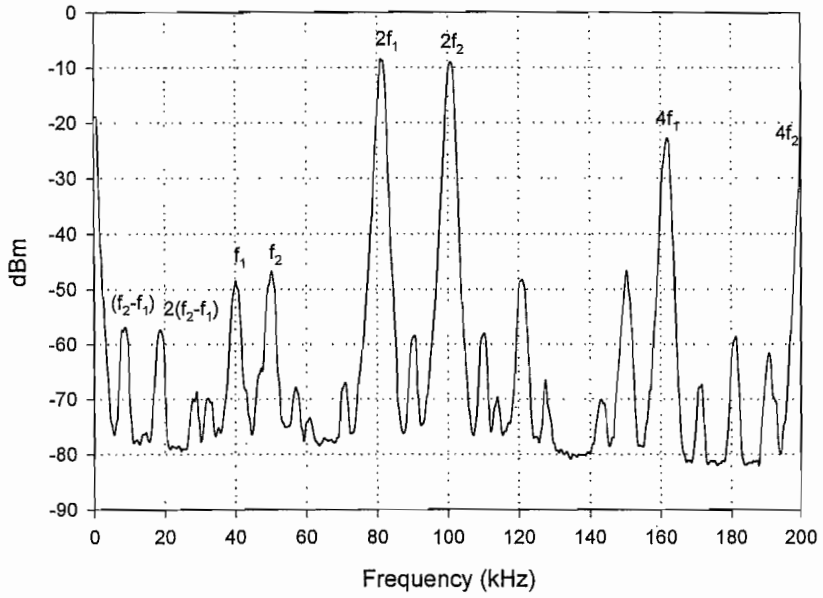

Figure 1.4.30 Frequency Spectrum of detected signal at the output of the <u>unperturbed</u> dual-wavelength, dual-Sagnac interferometer. *The Sagnac is biased at 40.6kHz and 50.7kHz respectively. The components at 2f are easily observable, but components at f also appear due to an acoustic background in the laboratory. Other beat components are also present, but are much lower in intensity than even the f components induced by the acoustic background in the laboratory. Optical crosstalk is approximately –50dB. (Spectrum analyser settings, Res BW 1kHz, Vid BW 22Hz, scan 5s/div, Avg 6, attenuator 30dB).*

We see the expected signals at $2f_1$ and $2f_2$ expected from the theoretical frequency spectrum modelled in chapter 1.2 (Fig 1.2.4). Also, the higher order components at $4f_1$ and $4f_2$ appear at a level approximately 13dB lower than at $2f$. However, since there is a certain amount of acoustic noise in the laboratory, the f components also appear, they are approximately 40dB below the $2f$ components. There are also expected to be components created by optical crosstalk but, due to the improved WDM components, the optical crosstalk level is at least –50dB and its effects can therefore be neglected.

1.4.4.1 Improved location of a point tone disturbance

We shall now investigate the ability of this sensor system to locate a tone disturbance. The narrow-band signal processing software described previously was instructed to locate a disturbance at a frequency of 125Hz. A disturbance generator was constructed using a loudspeaker driver to deform a thin plastic beam to which the fibre could be attached. A tone disturbance was applied in turn to each of the seven test positions described previously in figure 1.4.27. The amplitude of this disturbance was adjusted at each test position to give the same RMS relative phase modulation amplitude of 25mrads. This level corresponded to a ratio of 0.5% between the signals generated at f_{dist} and $2f_{dist}$ on the first and second harmonic demodulated signals respectively. The lock-in demodulated outputs df_1, $d2f_1$, df_2 and $d2f_2$ were then sampled simultaneously, at a rate of 16kHz, and the results processed in the manner described in section 1.4.3.2. The effective signal processing bandwidth used was 8Hz. The position results were then calculated and displayed. Fig 1.4.31 shows the results from 100 consecutive sample trials for this type of disturbance at each test position.

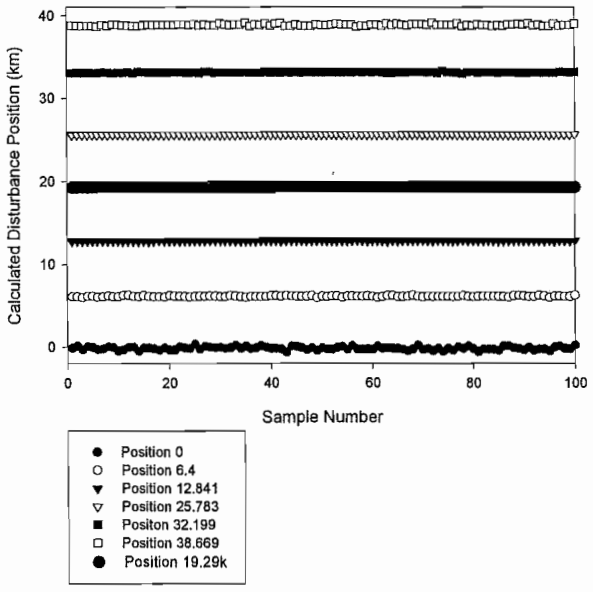

Figure 1.4.31 Results of point tone disturbance using improved Sagnac sensor. *A tone disturbance of 125Hz was applied to each of the seven test positions 0km, 6.4km, 12.84km, 19.28km, 25.78km, 32.2km and 38.67km. The amplitude of the disturbance was adjusted to give the same 25mrad RMS amplitude relative phase shift at each position.*

This figure highlights the change in positional sensitivity as a function of the disturbance position. Towards the ends of the sensor loop, the error in the results generated by the sensor increases, but even here the standard deviation of the position results is still only 20m and reduces to a few meters towards the loop centre. More sensitive results are also possible by further reducing the bandwidth of the digital signal processing. However, in any real application, the bandwidth possible will be limited by the length of time for which a disturbance is expected to be present. For any real threat to the cable to occur, the disturbance will have to be present for quite some time. A detection bandwidth of 10Hz should be the lowest that could probably be used in practice. The positional response of the sensor is plotted in (Fig 1.4.32).

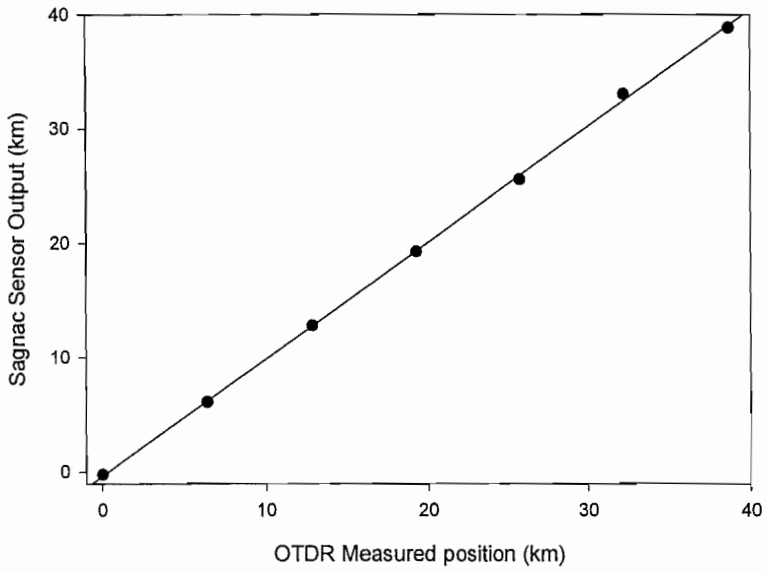

Figure 1.4.32 Positional response of the improved Sagnac disturbance sensor. *The average of the previous 100 results were plotted against the applied disturbance position, as measured by an OTDR.*

As expected, this improved Sagnac sensor system shows much more reliable positional results. The sixth position, however, exhibits greater variation from the predicted ideal $y = x$, response. This is thought to be probably due to a systematic error when measuring the distances using the OTDR, as the signal / noise above 30km degraded significantly. It is intended to measure the loop from both ends, when the system is next dismantled.

1.4.4.2 Discussion

We have shown that the improvements made acoustically shielding housing for the dual-wavelength, dual-Sagnac interferometer has reduced the effects of the laboratory acoustic background on system noise significantly, typically reducing this by 20dB. This allowed investigation of the system response in a relatively narrow window between 80-160Hz where the acoustic background seen by the penetrating the acoustic shield was low (16μrads $Hz^{-1/2}$). However, this acoustic background below approximately 60Hz is virtually unaffected by the acoustic shielding and increases the system noise by approximately 20dB.

Improvements were also made to the optics structure. The most significant of these were the WDMs improving the interrogation optic network loss by 3.2dB and also decreased optical crosstalk to a negligible level of –50dB. The optical ASE source was also improved to give a 4mW balanced spectrum, some 20 times more powerful than before. A 20m resolution was achieved and good agreement between experimental results and theory was observed. Due to the fact that the sensor could now be calibrated in real-time, using the two end test positions as references, there was no longer a large error from the expected $y = x$ response towards the ends of the sensor loop, (Fig 1.4.32).

1.4.5 Simultaneous location of multiply disturbances

1.4.5.1 Disturbances of different frequencies

We now investigate the possibility of simultaneously locating several separate disturbances acting on the sensor loop. The theory presented in chapter 1.3 predicted that disturbances of different frequencies could be separated in the Fourier domain and individually located. We have so far put this to use in order to separate and locate a tone disturbance of known frequency from background noise present in the laboratory. The sensor was calibrated using a disturbance of known frequency at each end of the loop and the calibration factor found. There is a complication if we now wish to locate several disturbances of different frequencies. Due to very slight differences in the frequency response for each of the lock-in amplifiers, the calibration factor needed will be a function

of the disturbance frequency. Remember that a factor of 10^{-5} in the frequency response calibration factor results in a position error of 1 meter towards the ends of the sensor loop. It is easy to see how the low-pass filters required at the df_1 and df_2 outputs could easily have responses which vary by this amount in the disturbance frequency range 100-150Hz. The system was calibrated for a tone disturbance of 140Hz. This disturbance was then applied at the first test position, i.e. 0km. The frequency of the disturbance was then tuned, but the amplitude of the phase shift, $\Delta\phi$, created by the disturbance was kept constant. Figure 1.4.33 shows the variation in the calculated position and the disturbance frequency used. As this shows a positional error as high as 5km could be observed when the disturbance frequency was 100Hz.

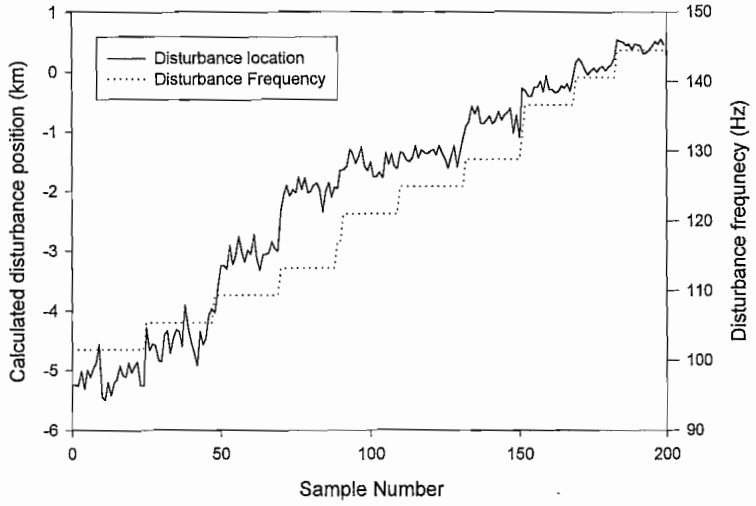

Figure 1.4.33 Variation in calculated position as a function of the disturbance frequency. *Due to differences in the frequency response of each lock-in the calibration constant for the Sagnac sensor becomes a function of the disturbance position. As is shown, a positioning error of ~5km results for a 100Hz disturbance when the system was calibrated at 140Hz.*

Discussion

The lock-in amplifiers in the dual-wavelength, dual-Sagnac system were followed by a two pole Sallen-key low pass filter stage of the demodulated outputs, *df* and *d2f*. The observed position error of approximately 1km / 10Hz, implies a frequency response difference of only 10^{-3} Hz^{-1}. Engineering a system where the frequency response of each of the four lock-in outputs is identical would be extremely difficult. However, there are

several potential ways to avoid these problems and these will be presented in the further work section in the following chapter.

Given the limitations of even the improved system, it is important to investigate the feasibility of whether multiple disturbances can be separated and positioned, independent of other perturbations on the loop.

The system was set up with a signal processing bandwidth of 2Hz and instructed to locate a disturbance of 145Hz. A 145Hz tone disturbance with an RMS amplitude of 12mrad was applied to the first test position (z = 0km), a second disturbance of 25mrads was applied to the seventh test position (z = 38.67km). The frequency of this second disturbance was then tuned over the range, 100Hz to 160Hz whilst the position for the first disturbance was calculated and plotted. Fig 1.4.34 shows the position results for the 145Hz disturbance. As can be seen, until the 2nd frequency falls within the pass-band of the detection system the this disturbance has little or no effect on the calculated position of the first. At this point, the system is "fooled" and the disturbance is located outside of the sensor loop.

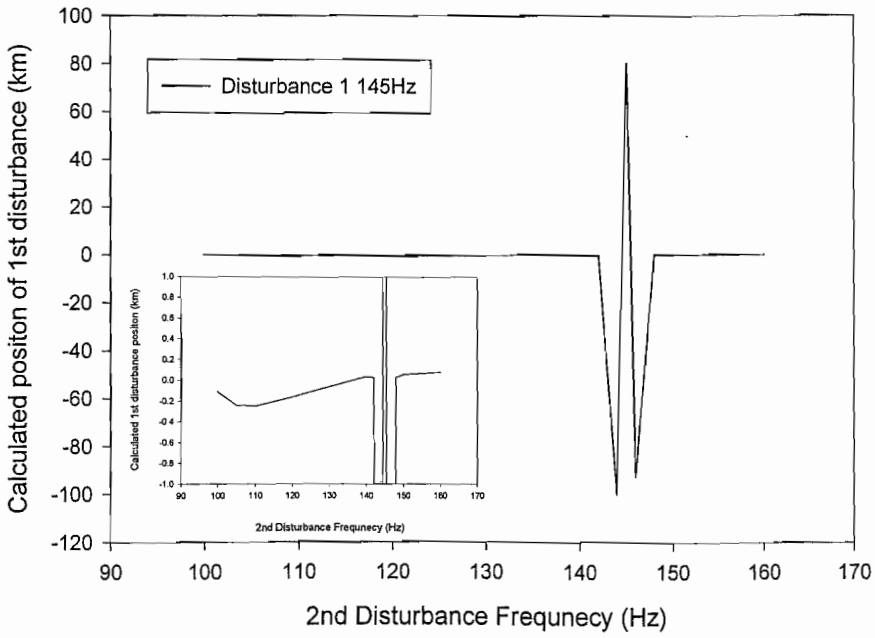

Figure 1.4.34 Graph showing calculated position for a 12mrad rms tone disturbance of 145H, as the frequency of a second tone disturbance of 25mrads acting on the same sensor loop is swept.

As an example of the capabilities of the signal processing software, we shall now demonstrate the desired ability to simultaneously separate and locate three applied disturbances. Disturbances of 105Hz, 125Hz and 155Hz were applied simultaneously to the sensor loop, at 12.2km, 0km and 32.2km, respectively and their amplitudes adjusted to give an RMS phase shift of 25mrads. Each of the disturbances were determined to lie at 11.62km, 0.13km and 33.65km respectively. A screen capture of these results was shown earlier in figure 1.4.28. The disturbances have been located slightly away from their true positions, as was discussed earlier. This is believed to be due to the frequency response fo the lock-ins. The important result of this experiment is that, for the first time in a Sagnac location system, each disturbance has been positioned independently from the other two. If the any one disturbance is removed then the calculated position of the other two is essentially unaffected. Any real application of the sensor could easily get around the residual positional error problems in a number of ways. The simplest of course to have a complete characterisation procedure and look-up table that the software would refer to, in order to correct the location of a disturbance. However, there is a convenient future way of removing this problem and further reducing the complexity of the system which will be presented in the next chapter on proposed future work.

References Chapter 1.4

[1.4.1] G.Martini, "Analysis of a single mode optical fibre piezoceramic phase modulator", Optical and Quantum electronics, Vol 19, 1987, pp 179-190

[1.4.2] V.J. Tejippe, "Passive fibre optic components made by fused biconical taper process." Proceedings of SPIE, Optical fibres and their applications, 1989, vol 1085.

[1.4.3] S.J.Russell, K.R.C.Brady, J.P.Dakin, "An improved 40km dual-wavelength, dual-Sagnac sensor, with enhanced signal processing, allowing real-time location of multiple time-varying strain disturbances", OFS-2000, Venice, Italy, October 2000.

Chapter 1.5 Conclusions and Further Work

1.5.1 The Sagnac Interferometer

The research work presented in the first section of this thesis was instigated by a need to solve real operational problems faced by the telecommunications industry. The main aim of the work undertaken, was to design and build an acoustic strain sensor, capable of locating the position at which the time-varying strain perturbs the sensor. The intended application of this sensor is for the protection of telecoms services, determining threats to the cable and raising an alarm before damage to the service can occur. The Sagnac interferometer was presented as our solution to this problem. The response of the Sagnac was derived and discussed and its ability to determine the position of the disturbance presented. Unfortunately it was shown that a single Sagnac interferometer gives a response related to both the disturbances distance from the loop centre, and its rate of change. Previously published research has presented several different optical structures for the location of disturbances using Sagnac interferometers, which have in one way or an other solved the response generated by the Sagnac and determined the disturbance position. We investigated these previous structures and have presented a novel dual-wavelength, dual-Sagnac as an improved solution to the disturbance location problem. This novel sensor architecture spectrally sliced a broadband ASE source using WDM components and routed the light in two wavelength bands to form two essentially separate interferometers. The response form each could then be solved simultaneously and the disturbance position found.

This novel structure exhibited several improvements over previously published designs. These included a low intrinsic loss of 9dB, the use of only a single high power source and the need for only a single optical detector. This significantly reduced the complexity and cost of the system. However, this novel architecture had one potential disadvantage. Due to imperfect WDM components there was the possibility for optical crosstalk to occur when spectrally slicing the single optical source. This effect was, for the first time, fully modelled and it was found that it was a predictable effect that could be calibrated in the sensor response. It was also found that given certain conditions of phase biasing frequency, i.e. if the two different phase-biasing frequencies were both an integral factor

of the natural frequency of the sensor loop length, then the effects of optical crosstalk could be completely cancelled and therefore ignored.

The expected signal to noise ratio of the resulting sensing system was then investigated. It was found that there are three main contributions to the theoretical system noise. These included the thermal phase noise inherent to the fibre from which the sensor was constructed. This noise source was found to be the dominant contribution to the final systems noise. However, at very low frequencies, (<50Hz) and when low optical powers, (<1μW) are detected, shot-noise becomes relevant. But, the system designed should in theory be largely dominated by the thermal noise contribution from the fibre.

When considering short loop lengths, when the thermal noise contribution is far lower, shot noise will generally dominate. In these situations there is another source of noise which would limit the minimum noise achievable in the system. This contribution arises from ASE-ASE beat noise generated in the source. As the received intensity increases, this noise source also increases. Eventually this noise will dominate the shot-noise contribution and limit the performance of the sensor.

However, even in the case where we have a 40km loop at room temperature we expect thermal phase noises of the order of 1μrad $Hz^{-1/2}$ allowing a signal to noise ratio of 100dB before we reach the non linear disturbance limit of 0.1rads.

Following the theoretical analysis of the sensor system we turned our attention to modelling the signal processing of the sensor output. Throughout this thesis, we have assumed that the disturbance generates a small relative phase modulation signal amplitude and we have therefore been able to make the approximation that the biased Sagnac interferometer remains within its linear response regime. This processing method limits the applications of such a sensor and makes it vulnerable to high acoustic background interference. Since the effects of background interference and multiple disturbances were unclear, chapter 1.3 presented a model of the Sagnac system. It was determined that it should be possible to separate multiple disturbances in the Fourier domain. In this way, we are able to separate disturbances from background noise and more accurately locate them. This method also allows us to separate many disturbances acting on the loop

simultaneously and locate them individually. One problem highlighted by the theoretical modelling was that if, multiple disturbances act on the loop with similar frequencies, then the location algorithm used can be fooled, locating the disturbances as a single disturbance at their amplitude-weighted average position. In any real situation, however, it is unlikely that two disturbances, remote from each other would be correlated, and so effects of this nature would be unlikely.

The sensor described in theory was then constructed for laboratory trials and we showed experimental confirmation of its ability to locate a tone disturbance acting on its sensor loop. These initial experiments also confirmed the effect of optical crosstalk and showed that the modelled sensor response is a valuable tool when accurately calibrating the sensor. This initial set up did, however, suffer from several problems. The first and most important was that despite layers of acoustic shielding, protecting the sensor and delay loops. This is unsurprising as we have 40km of fibre in an environment which, when compared to the ground, is very noisy. This 40km loop acts as a continuous microphone which integrates the disturbance and therefore positions the acoustic background at the loop centre. A further disadvantage was the use of high-loss, high crosstalk WDM's. These WDM's significantly complicated the calibration of the system, as predicted by the theoretical analysis, making it difficult to choose suitable eigenfrequencies at which each Sagnac could be biased without effecting the positional response of the sensor. Also the initial source built for initial investigations of this sensor architecture was limited to 200μW. This meant that the signal / noise achievable with this first set up was far lower than the maximum predicted.

It was decided that before investigating this sensor further these problems should be addressed. An improved sensor was constructed with much lower losses, (4dB), greatly reduced optical crosstalk, (-50dB), and a far more powerful optical source. (4mW). The signal processing was also greatly improved, allowing for the first time, real-time Fourier domain analysis of the disturbances acing on the sensor loop and the ability to locate simultaneously up to 3 disturbances, provided they were of different frequencies.

In conclusion we have shown that a 40km long Sagnac disturbance sensor can be realised with a signal to noise large enough to allow positioning of 20mrads disturbances with a

positional sensitivity of 20m. We have also shown that with suitable post-processing it is possible to actually simultaneously locate multiple disturbances acting on the same Sagnac sensor loop. This is a very important new result because in any real situation where we have a 40km length of buried fibre there are almost definitely locations which will be constantly perturbed, i.e. where the fibre route runs under a busy road or runs parallel to a railway. This enhanced signal processing method points to the possibility of accounting for such effects and positioning a disturbance despite railways and roads etc. Despite these encouraging results the sensor system realised could still be further improved and it is this which will be discussed in the following section. Clearly the sophistication of the processor could be enhanced considerably.

1.5.2 Suggested future improvements to the dual-Sagnac interferometer

The theoretical loss of the dual-wavelength, dual-Sagnac interferometer is 9dB. However, the measured loss of the optical system built was at best 33.8dB. 22.8dB higher than the theoretical minimum. The majority of these additional losses, however, are unavoidable. For example the 44km of fibre used to form the sensing and delay loop has an intrinsic loss of 9.24dB. Also, due to the need for the polarising filter and Lyot depolariser, an additional 6dB occurs from using a non-polarised source. The total loss could, in principle, be decreased to a value of 24.24dB, to gain a potential improvement of approximately 9dB in the required power of the source. The WDM's used in the construction of the Sagnac were, and still are state of the art. The loss caused by microbending in the delay coils and PZT modulators could, however, be addressed. Although it would increase the overall loss by increasing the lengths of the delay coils, the positional sensitivity of the sensor could be improved significantly, particularly towards the ends of the sensor loop and errors in output signal ratios would have less effect on the calculated position.

The most important single improvement that could be investigated is a way in which the previously-highlighted frequency response problem of the lock-ins could be removed, whilst simultaneously reducing the complexity and cost of the system. Since each lock-in has a slightly different frequency response, the calibration factor becomes a function of the

frequency of the disturbance to be located. This is an undesirable situation if the frequency of the disturbance to be located is unknown.

An excellent solution would be to allow each lock-in to effectively share the same filtering components. Using traditional analogue electronics, this would be difficult. However, using a fast analogue data-acquisition card and digitally processing the detected signal directly, would be far more simple. As was done in the numerical simulations of the dual-Sagnac system, a computer could be used to sample the signal generated by the optical detector directly. The required amplitude resolution and sample rate would need to be 12bit and at least 200kHz (Nyquist of *2f*). The multiplication action of the lock-in amplifiers could then be simulated in software and the demodulated signals digitally generated and processed in the usual manner. The only frequency dependant component, i.e. the optical receiver, is shared by both interferometers. If the detector is engineered to give a reasonably flat frequency response over the range *f* to *4f*, then each of the software-simulated lock-ins would have identical frequency responses and the required calibration factor would now be independent of the disturbance frequency.

1.5.3 Alternative sensor systems

Perhaps the greatest disadvantage presented by the Sagnac interferometer is that the response it generates is related to the integral of the effects on the entire loop. The positional sensitivity of the sensor is based on the break in symmetry that a disturbance creates. This can therefore be complicated when considering multiply disturbances. Ideally we would like a system which can discriminate a certain section of its sensing fibre length and "listen" for disturbances unambiguously from that defined section only.

1.5.3.1 Dual wavelength OTDR distributed strain sensor

OTDR systems are widely used to characterise optical fibres[1.5.1]. OTDR's can characterise fibre back-scatter and attenuation, splice losses and locate fibre breaks and faults. Such sensors generally rely on Rayleigh scattering from scatter sites present in single mode fibres.

OTDR in distributed sensor applications generally take advantage of inelastic scattering processes such as Raman[1.5.2] and Brillouin[1.5.3] scattering

1.5.3.1.1 Principle of OTDR operation

An OTDR system recovers positional information by measuring the time delay between emitted and received radiation. A Rayleigh based OTDR operates by sending a single optical pulse of length l along a long length of fibre. As the pulse propagates along the fibre, radiation will be scattered by scattering sites inherent to the fibre. Each scattering site acts as a point source of radiation. Some of this scattered radiation will be "captured" by the fibre and guided back towards the source.

For example consider a power, P_0, incident at a position $z = 0$ along a fibre. The transmitted power P_t at a distance z will thus be related to the fibres loss or attenuation;

$$P_t = P_0 e^{\alpha z} \qquad [1.5.1]$$

Where the attenuation coefficient α is the sum of the scattering and absorption coefficients. I.e. $\alpha = \alpha_a + \alpha_s$. The loss is the difference between the transmitted power P_t and the incident power P_0.

$$P_d = P_0\left(e^{(\alpha_a+\alpha_s)z} - 1\right) \qquad [1.5.2]$$

This assumes an optical pulse width of zero, which is not the actual case. Consider a pulse of length l. The loss attributed to a pulse can be found by differentiating equation 1.5.2 with respect to z. The loss $P_{d,l}$ which a pulse of length l at a position x incurs can be shown to be;

$$P_{d,l} = (\alpha_a + \alpha_s)P_0 e^{\alpha z} l \qquad [1.5.3]$$

The total scattered power $P_{s,l}$ from a pulse of length l at a distance z may then be shown to be,

$$P_{s,l} = -\alpha_s l P_0 e^{\alpha z} \qquad [1.5.4]$$

The amount of scattered light that is captured and guided back towards the source is dependant on the capture fraction b, this depends on the numerical aperture NA, the core index and the type of fibre, and may be shown to be,

$$P_{bs} = -b\alpha_s l P_0 e^{\alpha 2z} \qquad [1.5.5]$$

For single mode fibre $b = \frac{1}{4.55}\left(\frac{NA}{n_1}\right)^2$ where NA $\cong$ 0.1

Thus by measuring the intensity of light received versus time it is possible to retrieve the loss of the fibre at a position z. Where $z = ct/2n$, where n is the refractive index, c is the speed of light in a vacuum and t is the time.

In addition to back-scattered radiation, there may be sites in the fibre that act as reflectors. For example bad splices and the end of the fibre. Following a similar logical derivation it may be shown that the back-reflected power can be expressed as follows;

$$P_{br} = -r\alpha l P_0 e^{\alpha 2z} \qquad [1.5.6]$$

where r is the reflectivity of the reflective point.

A typical Rayleigh back-scatter plot for a standard fibre is shown in figure 1.5.1

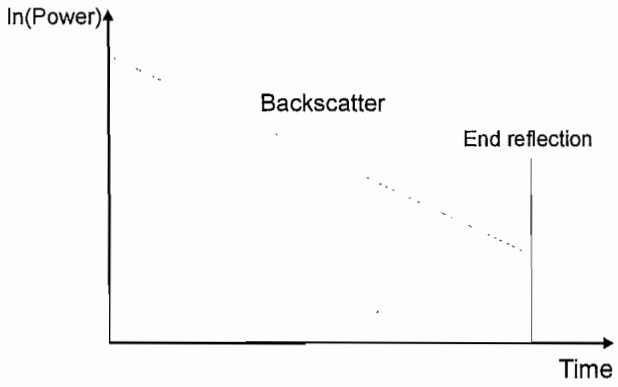

Figure 1.5.1 Typical OTDR trace for standard fibre *The ln plot of received radiation shows a linear response with time indicating a constant loss along the fibre. The trace peaks up again at the end due to the end reflection from the fibre's end. Splice losses show themselves as steps in the linear loss region.*

1.5.3.1.2 The dual wavelength COTDR system

The dual wavelength coherent OTDR is an adaptation of the simple single frequency Rayleigh scatter method. Consider the following optics structure.

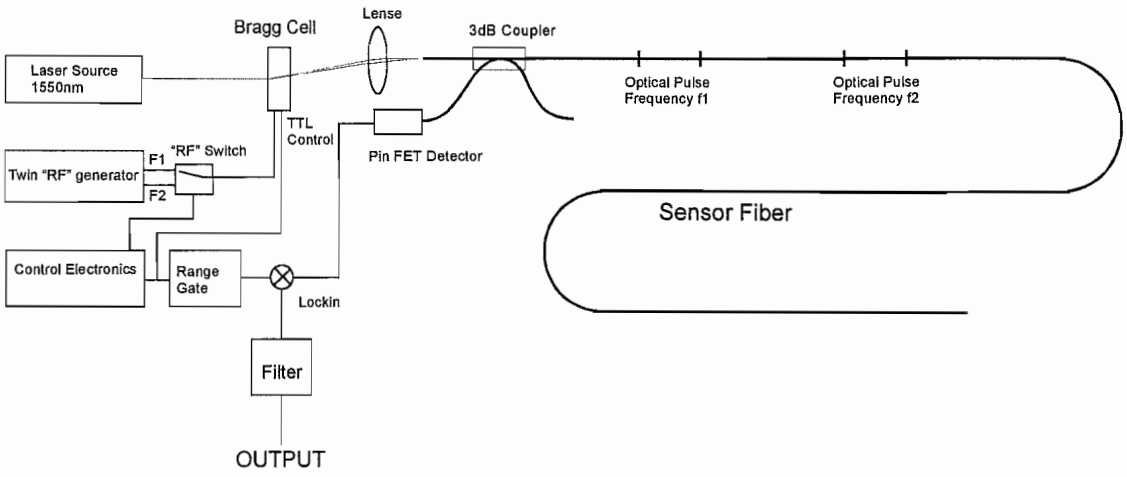

Figure 1.5.2 The Dual Wavelength COTDR. *Twin RF pulses are sent down a length of fibre. The back-scattered radiation interferes coherently at the detector. Any strain disturbance then phase modulates the back-scattered signal. Positional information is recovered as in the standard OTDR.*

The Bragg cell is a device that produces an optical grating of varying pitch related to the frequency of the exciting RF signal applied to it. In this manner it is possible to use such a device not only as an optical switch but also as a wavelength selective switch. The proposed dual wavelength COTDR operates by using such a device to send two closely spaced optical pulses along a length of single mode fibre. The frequency of each pulse will be separated by approximately 10MHz. As each pulse propagates along the fibre light will be scattered from scattering sites inherent to the fibre, randomly distributed along its length. Some of this scattered light will be captured and guided back toward the detector. In the ideal system each of the optical pulses can be regarded as a travelling coherently radiating point source. This being the case the scattered light from each of the pulses interferes coherently at the detector and cause's a beat signal at a frequency equal to the difference between the optical frequencies of the two pulses. Any time varying disturbance acting on the sensor fibre will cause both a length and a refractive index modulation of the fibre. Both of these effects will in turn modulate the distance between the two optical pulses propagating along the sensor fibre. This will have the effect of frequency modulating the beat signal obtained at the detector. By range gating the signal

received it is then possible to choose a single point in the fibre to be observed and then extract the strain modulation signal acting on the fibre at that point.

1.5.3.1.3 Implementation of the novel OTDR

There are several things that have to be considered for good operation of such a coherent dual wavelength OTDR system. The drive signals to the Bragg cell must be of a known continuous phase in order for phase demodulation of the received signal to yield correct results. This is easily accomplished by having two independent oscillators that output at a constant difference frequency. The drive to the Bragg cell may then be switched between these two oscillators as needed.

Two pulses are obtained by a separate control signal that actually turns the Bragg cell on and off at the correct time intervals. These control logic signals may then be used for coherent detection of signals obtained at the detector by range gating the phase demodulator.

The signal obtained at the output will not be a continuous signal but will be portions of the disturbance signal obtained as each pulse pair propagated past the position in the fibre that has been range gated for observation. For example if the fibre were 50km in length then the propagation time for a pulse to travel to the end and any scattered light to travel back toward the detector would be t = 500μs. The repetition rate of pulse pairs therefore must be less than this time to prevent overlap between the pulse's and the returning signal. I.e. Rep rates of the order of 1kHz are expected. This in turn limits the maximum frequency of disturbance that can be retrieved by this method. The signal recovered by range gating and phase demodulation must therefore be filtered to obtained a continuous signal. This signal may then be fed into a frequency spectrum analyser and any discrete frequencies corresponding to expected disturbances can be observed.

1.5.3.1.4 Possible problems

The most significant problem is phase noise incurred by the back-scattered radiation from each of the optical pulses. The source of the phase noise is inherent to the fibre itself. Light is scattered by scatter sites along the fibre which are pseudo randomly distributed

along the fibre. Such scatter sites are frozen in during the glass manufacture stage. Its is the random nature of these scatter sites which creates the problem. Consider the situation shown in figure 1.5.3.

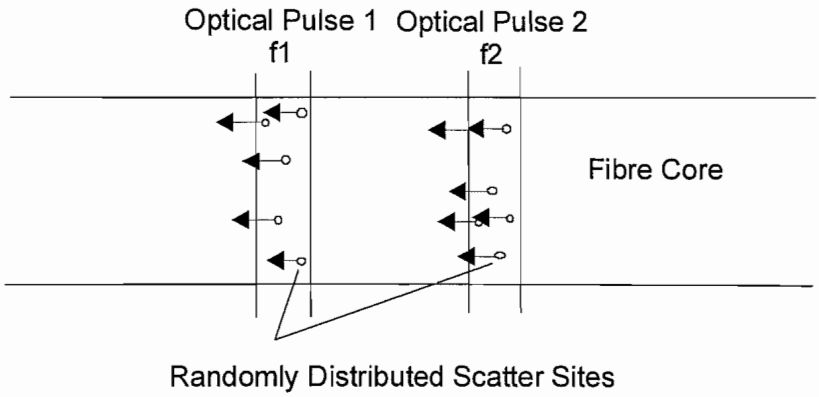

Figure 1.5.3 Coherent Rayleigh Back-scatter, Origin of phase Noise. *Randomly distributed scattering sites scatter radiation as a pulse passes. There will be many sites within a pulse, each scattering coherent radiation. The phase of the scattered radiation is random and thus for any part in the fibre the back-scattered intensity is also random.*

In figure 1.5.3 a close up section of the core of an optical fibre is shown. Consider the intensity of the light scattered from the first optical pulse. Light is scattered from each of the scatter sites. Each of these scatter sites acts as a point source radiator. The scattered light from each of these sites interferes constructively, since the phase of the light scattered from each of these sites is random then the resulting intensity of scattered light may take a value anywhere between zero, up to the maximum possible. As the pulse propagates along the fibre this scattered intensity will change randomly. The randomness of the distribution of these sites occurs on a scale much smaller than that of the optical pulse width. The scattered intensity from each pulse may therefore be very different. The overall effect of this is to add phase noise to the beat signal obtained at the detector. Figure 1.5.4 shows as expected scatter intensity versus distance profile.

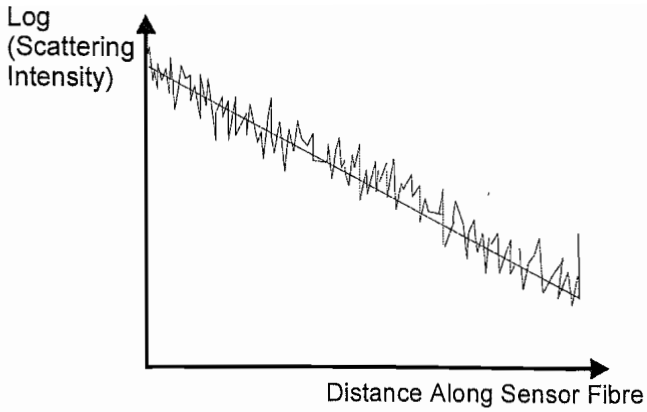

Figure 1.5.4 Expected Scatter Intensity Vs Distance along a standard telecoms Fibre

1.5.3.1.5 Summary Dual-Wavelength OTDR system

The general scheme for the research into a novel dual wavelength OTDR has been set out. The most significant problem expected to cause problems with the initial construction of such a device is the expected high phase noise present on the acoustic signal which we are attempting to recover. However, with correct phase or frequency demodulation is should be possible to at least obtained an audio frequency spectrum of the recovered signal and observe discrete peaks corresponding to the disturbance acting at the position of the fibre under observation.

References Chapter 1.5

[1.5.1] P.Healy, "Review of long wavelength single-mode optical fiber reflectometry techniques", Journal of lightwave technology, Vol LT-3, No 4, August, 1985.

[1.5.2] J.P.Dakin, D.J.Pratt, "Distributed optical fibre Raman temperature sensor using a semiconductor light source and detector", Electronics letters, Vol 21, No 13, June, 1985.

[1.5.3] P.C.Wait, K.De Souza, T.P.Newson, "A theoretical comparison of Raman and Brillouin based fibre optic distributed temperature sensors", Optical communications, Vol 144, pp 17-23, 1997.

SECTION 2 : (EMO)

Electro-Magnetic / Optical

Cable Location System

An Optical Sensor For The Location Of Buried Dielectrically Sheathed Fibre Cables.

Chapter 2.1 Buried Dielectric Cable Location System, Theoretical Background

2.1.1 Introduction

Fibre optic technology is now essential to the modern telecommunications industry. Protection of these fibre services is therefore an important factor in the operation of any telecommunications network. Generally, optical fibres in steel reinforced cable bundles of up to a hundred or so are used. One disadvantage in using this type of cable is that steel is a conductor, and a nearby lightning strike can induce electrical currents in this protective steel sheath, damaging it along with the fibres it is intended to protect. As you might expect, the loss of a fibre bundle can deprive the network operator of substantial revenue and the speed of locating and fixing the fault is crucial.

When a cable is damaged, the distance along the fibre to the fault can be easily found using automated OTDR's. This gives a rough position along the cable route for the repair technicians to locate and fix the fault. However, the buried position (including depth) of the fibre must be determined, before it can be safely dug up, without causing further damage to the cable or surrounding services. This stage of the repair procedure creates the largest "bottle neck" and so several technologies have been developed to aid in this task. Unfortunately, most cable location systems in use today can, in general, locate only cables reinforced with a conducting sheath. Such systems operate by applying, (typically from an accessible end of the fibre sheath, in a signal regeneration hut maybe 50miles from the fault), an alternating current to this sheath, which in turn generates a magnetic field which emanates from the cable. This field can then be detected, from above ground, using a handheld portable magnetic field detector in proximity to the cable. The lateral location of the cable is then inferred by observing the maximum response as the field detector is traversed across the cable's buried position.

This method however, suffers from some serious drawbacks. Maintenance of the protective sheath becomes important as it is relied upon for cable location. Also the application of an AC tone to this sheath may, given time, degrade it. Electrical conductors

running parallel to, or nearby the fibre bundle being located, can also cause problems. The AC tone applied to the conducting sheath can inductively couple to these other conductors, which in turn generate their own magnetic fields, creating errors in the location of the fibre cable. Methods have been developed to minimise these effects, such as current direction measurement (CD), absolute current ID (ACID) and local probes that are pushed into the ground to measure the near field pattern generated by the sheath, (e.g. Radiodetection PDL4, Smart probe). However, in certain situations these effects can still create problems and require considerable experience with the location equipment to be able to accurately locate the buried cable.

Due to the vulnerability of conducting cables to lightning strikes, and the costs of the cable and its maintenance, many network operators wish to move to non-conducting dielectric sheaths, such as Kevlar-reinforced cables. Such cables offer reduced costs, easier installation, primarily due to their lighter weight, and have much lower lightning strike vulnerability. These cables unfortunately render all of the above location systems ineffective. A new method of locating buried fibre cables is needed that is not reliant on the conducting sheath, but uses some other measurable property presented by the fibre.

2.1.2 The Faraday location system (EMO)

It is proposed that the linear magneto-optical or Faraday effect could be used to locate the position of a buried Kevlar reinforced cable, (Fig 2.1.1). An alternating magnetic field, applied from above ground, above the cable, induces a rotation in the polarisation azimuth of the light guided by the buried fibre. The amplitude of this polarisation modulation can then be measured using a suitable polarisation source and polarisation sensitive detection system, situated at the other end of the fibre cable. The results can be relayed to the operator of the magnetic field generator, via a radio link or other communications system. The amplitude of this response, as the field generator is traversed across the cable, can then be directly used to infer the fibres position. This new magneto-optical location method has been termed **EMO** (**E**lectromagnetic **M**agneto-**O**ptical location system).

This system does not suffer from the same disadvantages as the previous current-based cable detection schemes. Since the signal of interest is the optical signal carried by the

fibre, it is impossible for the "tone" carried by the light to couple to or from another fibre, or to other services which would lead to positioning problems. This then allows the operator to get an unambiguous confirmation that it is their service that they are locating. Also, the presence of secondary conductors nearby the buried fibre, have no effect on the location, since any induced currents would generate magnetic fields with the incorrect symmetry to create an effect. The required field symmetries will be discussed in detail in a following section.

The following chapter discusses research undertaken into the initial realisation and testing of this sensor system. The physical effects we wish to exploit in order to design this cable location system are explained and the expected experimental problems / complications discussed.

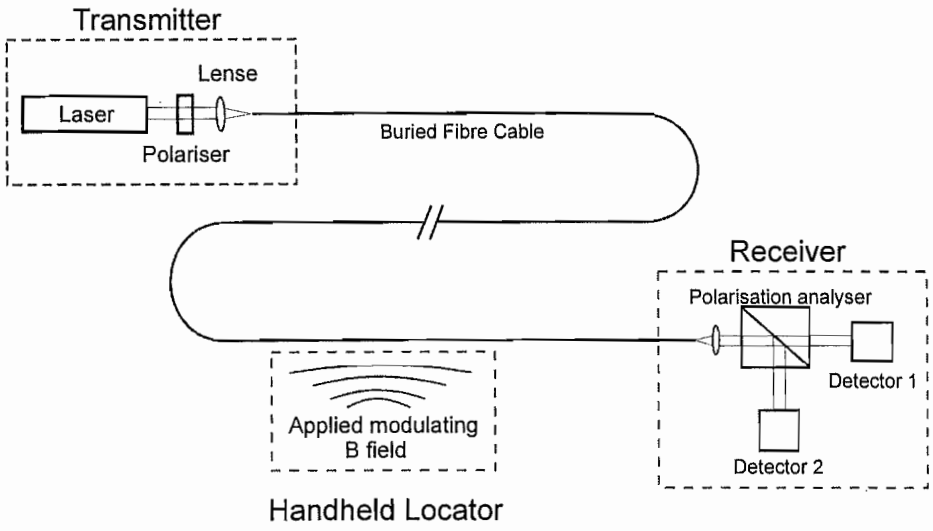

Figure 2.1.1, Schematic of the Faraday cable location system. *A polarised laser source is launched into a standard single mode fibre and propagates until reaching a polarisation sensitive detection system. A magnetic field applied part way along the cable and above the ground modulates the polarisation azimuth of this light, which reveals itself as a time dependent intensity change at the detection system, at a frequency equal to the modulator. From the lateral position of the handheld modulator and amplitude of the optical response, the position of the buried cable can be inferred*

2.1.2.1 The Faraday effect

Michael Faraday discovered that the state of polarisation (SOP) of light propagating through a material could be influenced by the application of an external magnetic field. In

particular, the polarisation azimuth of the light, β, can be rotated by an amount proportional to both the magnitude of the magnetic flux density, $\boldsymbol{B}$, and the materials interaction length with this field, $\boldsymbol{l}$. Since these two quantities are vectors, the amplitude of rotation is proportional to their dot-product. This linear magneto-optical effect has since been known as the Faraday effect [2.1.1].

$$\beta = V \cdot \int_{-L/2}^{L/2} \mathbf{B}(\mathbf{l}) \cdot d\mathbf{l} \qquad [2.1.1]$$

Similarly, the effect can be expressed in terms of the magnetic field strength, $\boldsymbol{H}$, where, μ_0, is the permitivity of free space ($4\pi \times 10^{-7}$ Henrys).

$$\beta = V \cdot \mu \cdot \int_{-L/2}^{L/2} H(l) \cdot dl \qquad [2.1.2]$$

The constant of proportionality, V, is referred to as the Verdet constant, which for silica (suprasil W2) is approximately 3.2 rads $(Tm)^{-1}$ @1550nm [2.1.1]. The relationship between the magnetic field strength and the flux density is shown in equation 2.1.3 [2.1.2].

$$H = \frac{B}{\mu} - M \qquad [2.1.3]$$

For the following chapter we are conserned with the Faraday effect in silica optical fibre. Silica is a paramagnetic material and it is therefore possible to assume that its magnetisation, M, is approximately zero.

2.1.2.2 Effects of birefringence on the Faraday effect in optical fibres

The above definition of the Faraday effect assumed that the material through which the light was propagating exhibited no intrinsic birefringence. This however, will not generally be the case. The SOP of light emitted from the end of a length of fibre will, in general, be different to its launch SOP. Although we can assume that the circular birefringence of the fibre can be neglected (assuming that the fibre is not twisted), single mode optical fibre does however exhibit a small linear birefringence. A linear birefringent material exhibits a different refractive index for light polarised in each of two orthogonal directions. If plane polarised light is incident on a fibre with its polarisation azimuth at an angle, θ, to one of the principle axes of the fibre, then its polarisation state may be

resolved into two orthogonal components parallel to the birefringent axes. It can further be shown that, after a distance z, a phase shift, δ [2.1.3] [2.1.4] occurs between these two components. This is related to the difference in the refractive indices for each orthogonal component. Using Jones calculus, the effect of this retardation on the SOP of the launched light can be represented by the matrix shown in [2.1.5].

$$\delta = \frac{2\pi(n_x - n_y)\cdot z}{\lambda} \qquad [2.1.4]$$

$$\begin{bmatrix} E_{xt} \\ E_{yt} \end{bmatrix} = \begin{bmatrix} \exp(j\delta/2) & 0 \\ 0 & \exp(-j\delta/2) \end{bmatrix} \cdot \begin{bmatrix} E_{xi} \\ E_{yi} \end{bmatrix} \qquad [2.1.5]$$

Where, E_{xi}, and, E_{yi}, are the incident electric field components of the light and, E_{xt}, and E_{yt}, are the modified transmitted field components.

Considering the situation shown in figure 2.1.1, if we launch linearly polarised light along a standard single mode fibre, then its SOP will change as it propagates and it cannot be assured that it will be linearly polarised when it encounters the modulation field generated by the locator. In the worst case, if the light encounters the modulating field when it is circularly polarised, no effect will be seen by the polarisation sensitive detection system. A second concern is that, if the light arrives at the polarisation sensitive detection system with its polarisation azimuth perpendicular to that of the polariser, again no signal with be observed. We therefore need a system, which can dynamically control the SOP of the light to achieve the optimal operating position. For the laboratory system, the SOP is conditioned using two manually operated polarisation controllers at either end of the fibre. However, a fully automated system would be required for any realistic commercial system. Ways in which this may be done are discussed later in this section of this thesis.

Another complication is the fact that the light propagating along the fibre interacts with the magnetic field over a finite length. Typically this will be of the order of only a few metres or so. The SOP of the light as it propagates over this length can therefore no longer be considered to be constant. In turn the Faraday shift incurred by the light can no longer be assumed to be simply a rotation of its polarisation azimuth, proportional to the line integral of the magnetic field along its propagation path. The presence of birefringence

drastically alters the characteristics of the change in the SOP of the light when a magnetic field is present. Equation 1.2.6 shows the Jones matrix for a birefringent fibre in a parallel magnetic field [2.1.4,-2.1.7].

$$\begin{bmatrix} \cos\left(\frac{\phi \cdot z}{2}\right) - j\frac{\delta}{\phi}\cos\left(\frac{\phi \cdot z}{2}\right) & -\frac{2F}{\phi}\sin\left(\frac{\phi \cdot z}{2}\right) \\ \frac{2F}{\phi}\sin\left(\frac{\varphi \cdot z}{2}\right) & \cos\left(\frac{\phi \cdot z}{2}\right) + j\frac{\delta}{\phi}\cos\left(\frac{\phi \cdot z}{2}\right) \end{bmatrix} \qquad [2.1.6]$$

Where, F, is the Faraday rotation per unit length and $\phi^2 = \delta^2 + (2F)^2$.

Upon closer investigation of the matrix shown in [2.1.6], it can been seen that, in the limiting case of zero birefringence, ($\delta = 0$), it reduces to a simply rotation matrix. This rotates the co-ordinate system by an amount equal to the Faraday rotation $2F$. Similarly in the limiting case of zero Faraday rotation ($F=0$), this matrix [2.1.6] reduces to that of a linear retarder, as previously shown in [2.1.5].

2.1.2.3 The effective Verdet constant

To simplify the understanding of the effect birefringence has on the Faraday response of materials, Cruz et al [2.1.8] defined an effective Verdet constant.

$$\begin{pmatrix} E_x(0) \\ E_y(0) \end{pmatrix} = {E_0}^2 \begin{pmatrix} \sqrt{P} \\ \sqrt{1-P}\exp(j\gamma) \end{pmatrix} \qquad \begin{matrix} P = 0 \rightarrow 1 \\ \gamma = 0 \rightarrow 2\pi \end{matrix} \qquad [2.1.7]$$

We shall assume that light is launched into a length of fibre, z, with an arbitrary polarisation state defined as in equation [2.1.7], and that the emitted radiation is viewed through a polarisation analyser parallel to the x-axis. Determining the slope, $m = d|E_x(z)|^2/dF$, [2.1.8] of the detected light intensity, $|E_x(z)|^2$, with respect to the Faraday shift, and taking the limit as F tends to zero, gives us the relative response of the system to the action of a magnetic field and allows determination of its sensitivity [2.1.8] [2.1.8].

$$m = 4\sqrt{P}\sqrt{1-P}\frac{1}{\delta \cdot z}\sin\left(\frac{\delta \cdot z}{2}\right)\cos\left(\frac{\delta \cdot z}{2} + \gamma\right) \qquad [2.1.8]$$

As can be seen from this equation, if there is no birefringence, the optimal response of such a sensor occurs when we have linearly polarised light launched into the fibre with its polarisation azimuth oriented at an angle of 45° to the output analyser, $P = 0.5$, $\gamma = 0$. However, the presence of birefringence causes this slope to be reduced, an effect often referred to as "quenching" of the Faraday effect [2.1.8]. However, Cruz also showed that by varying the input SOP it was possible to obtain an optimal input state which substantially reduced this quenching effect. Using these results it was possible to define an effective Verdet constant;

$$V_{ef} = V\frac{2}{\delta \cdot z}\sin\left(\frac{\delta \cdot z}{2}\right) \qquad [2.1.9]$$

For low residual birefringence, the effective Verdet constant is almost equal to the bulk Verdet constant. However, over interaction lengths of several meters this effect is likely to become more significant and this possibility should not be ignored. Cruz measured a value of $V_{eff} = 0.54\ rads\ Tm^{-1}$, some six times lower than the Verdet constant exhibited by bulk Silica.

2.1.3 Generation of the modulating magnetic field

Now that we know, how we expect the optical system to react to the action of a magnetic field, we turn our attention to the generation of an appropriate field. The field generator to be used in this system has to be located above ground and must generate a Faraday shift in light propagating along an optical fibre running beneath ground, between separated points, usually two regeneration stations on a long cable link. In order for this to occur, the line integral of the field in a direction along the cables path, must be non zero. The line integral of a magnetic field may be expressed by Maxwells equations [2.1.8];

$$\oint \mathbf{B} \cdot d\mathbf{l} = \mu_0 \cdot \int_A \left(\mathbf{J}_f + \frac{\partial \mathbf{P}}{\partial t} + \nabla \times \mathbf{M} + \epsilon_0 \frac{\partial \mathbf{E}}{\partial t} \right) \cdot d\mathbf{A} \qquad [2.1.9]$$

where, J_f, is the free current density, P, is the electronic polarisation of the material supporting the magnetic field and, E, is the electric field. As previously stated, we shall assume, M, is zero. So in order for the line integral of the magnetic field to be non-zero

over any path, then it must either be a continuous loop enclosing a current or have a changing electric field perpendicular to its direction.

2.1.3.1 The field generated by a solenoid

Perhaps the most commonly used magnetic field generator is the solenoid. A solenoid is a cylindrical coil of wire wound around common axis. When current flows around the coil, a magnetic field is generated. The field generated within the winding of the solenoid is a well-known quantity. It can be shown to generate a Faraday rotation in light guided by a fibre passing along the axis of the solenoid [2.1.2]. However, in order for this solenoid to be used to locate the buried fibre, the line integral of the field along a path external to the winding must also be non-zero. The external magnetic field generated by a solenoid is a less well known quantity, but can be calculated using the Biot-Savart Law [2.1.2]. Equations 2.1.10 – 2.1.12 show the calculated field components for a single winding of radius, *a*, centred at co-ordinates (0,0,0), lying in the xz plane.

$$B_x(x,y,z)=\frac{\mu\cdot I}{4\pi}\int_0^{2\pi}\frac{a-z\cdot\sin(\theta)-y\cdot\cos(\theta)}{\left[x^2+y^2+z^2+a^2-2\cdot a\cdot\left(y\cdot\cos(\theta)+z\cdot\sin(\theta)\right)\right]^{\frac{3}{2}}}d\theta \qquad [2.1.10]$$

$$B_y(x,y,z)=\frac{\mu\cdot I}{4\pi}\int_0^{2\pi}\frac{x\cdot\cos(\theta)}{\left[x^2+y^2+z^2+a^2-2\cdot a\cdot\left(y\cdot\cos(\theta)+z\cdot\sin(\theta)\right)\right]^{\frac{3}{2}}}d\theta \qquad [2.1.11]$$

$$B_z(x,y,z)=\frac{\mu\cdot I}{4\pi}\int_0^{2\pi}\frac{-x\cdot\sin(\theta)}{\left[x^2+y^2+z^2+a^2-2\cdot a\cdot\left(y\cdot\cos(\theta)+z\cdot\sin(\theta)\right)\right]^{\frac{3}{2}}}d\theta \qquad [2.1.12]$$

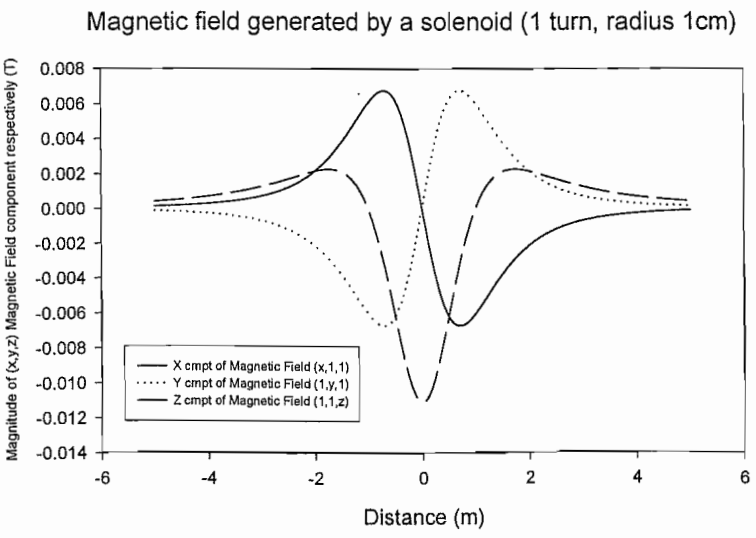

Figure 2.1.2 The magnetic field generated by a solenoid. *Shown above are several graphs that together give an image of the magnetic field that a coil of wire generates external to itself. The magnitudes of the x,y and z field components are plotted versus the displacement along their respective axis at a distance of 1m on the remaining two axis'*

Figure 2.1.2 shows the variation of each of the magnetic field components generated by a coil of wire, (1cm radius carrying a current of 1A), as a function of the displacement along each axis. As is shown by Fig 2.1.2 the symmetry of the field is such that its integral along an unclosed path outside the coil is zero. This assumes that the integration path is much longer than the coil length. This makes the solenoid an unsuitable magnetic field generator for our application as the only way in which it could generate a Faraday rotation in the guided light would be to wrap it around the buried fibre, which is impossible. However, it may prove useful as a known magnetic field generator for laboratory based experiments. Please note however, that this argument has assumed that the magnetic field solutions, derived for the solenoid have not taken into account the time-varying solution, but the static. It may prove possible to modulate the signal to the solenoid and generate a magnetic field with a non-zero line integral along a path external to the coil winding.

2.1.3.2 The field generated by an electric dipole

A more suitable time-varying, travelling EM field solution would be that of a dipole, of which there are two types, the electric and magnetic dipoles. In its simplest form the electric dipole consists of two charges of equal and opposite magnitudes separated by a distance *d*. When this charge distribution is modulated. I.e. charge flows from one end of the dipole to the other, then an equivalent representation would be an element of time varying current ***J(t)***, as shown in figure 2.1.3

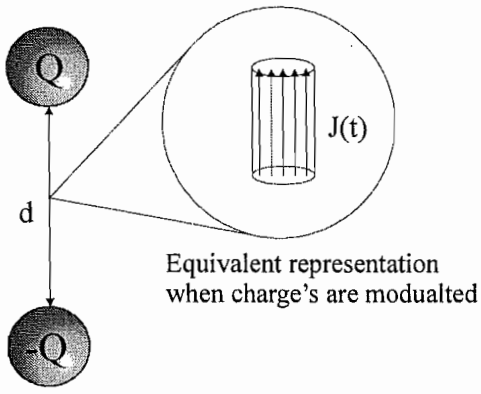

Figure 2.1.3 The electric dipole. *This diagram shows the simplest model for an electric dipole. Two equal and opposite charges separated by a distance d. When this charge distribution is modulated, i.e current flows between the two charges, then an equivalent representation is that an inifitesimally small current element changing in time, J(t).*

Consider the field generated by a current element of length d and area A. We shall assume that the time dependence of this current element is $\boldsymbol{J}(t) = \boldsymbol{Re}(\boldsymbol{J}e^{i\omega t})$. It is assumed that the current $\boldsymbol{J} = \mathbf{i}_z J_0$ is constant over the length of the element and that it is aligned with the z axis. It can be shown that the vector potential A_p set-up by this current element is given by eq 2.1.13, [2.1.9 pp 640, 2.1.10]

$$\boldsymbol{A}_p = \boldsymbol{i}_z \cdot \left(\frac{\mu \cdot \boldsymbol{J}_0}{4\pi} \cdot \int_{-\infty}^{\infty} \frac{e^{-j\beta_0 r_{QP}}}{r_{QP}} dA_Q \right) \qquad [2.1.13]$$

Where the curl of, $\boldsymbol{A}$, is defined as the magnetic flux density $\boldsymbol{B} = \nabla \times \boldsymbol{A}$ and $\beta_0 = \omega/c$, where ω is the EM field frequency and c is the speed of light in a vacuum. However, we have assumed that the elemental length of the current is infinitesimally small and are therefore interested in the limiting case, when this length reduces to zero. The vector potential of the field then becomes that shown in [Eq 2.1.14].

$$\boldsymbol{A}_p = \boldsymbol{i}_z \cdot \left(\frac{\mu \cdot I_0 \cdot d}{4\pi} \cdot \frac{e^{-j\beta_0 r}}{r} \right) \qquad [2.1.14]$$

$$\boldsymbol{H} = \frac{1}{\mu} \cdot (\nabla \times \boldsymbol{A}) \qquad [2.1.15]$$

Here, $\boldsymbol{I_0}$ is the total complex current and $\boldsymbol{r}$ is the displacement vector from the dipole centre. Converting to spherical polar co-ordinates (SPC's) and applying the relationship, 2.1.15, it can be shown that the magnetic field component H_ϕ is defined by 2.1.16 [2.1.9,2.1.10];

$$\boldsymbol{H}_\varphi(t) = \mathrm{Re}\left[\frac{-I_0 d}{4\pi} \cdot \beta_0{}^2 \cdot \sin\theta \cdot \left[\frac{1}{j\beta_0 \boldsymbol{r}} + \frac{1}{(j\beta_0 \boldsymbol{r})^2} \right] \cdot e^{j(\omega t - \beta_0 \cdot \boldsymbol{r})} \right] \qquad [2.1.16]$$

Similarly the electric field components may be found from their relationship to the, $\boldsymbol{H}$, field by; $\boldsymbol{E} = \frac{1}{j\omega\varepsilon}(\nabla \times \boldsymbol{H})$

$$\boldsymbol{E}_r(t) = \mathrm{Re}\left[\frac{-I_0 d}{4\pi} \cdot \beta_0{}^2 \cdot \eta \cdot 2\cos\theta \left[\frac{1}{(j\beta_0 \boldsymbol{r})^2} + \frac{1}{(j\beta_0 \boldsymbol{r})^3} \right] \cdot e^{j(\omega t - \beta_0 \cdot \boldsymbol{r})} \right] \qquad [2.1.17]$$

$$\boldsymbol{E}_\theta(t) = \mathrm{Re}\left[\frac{-I_0 d}{4\pi} \cdot \beta_0{}^2 \cdot \eta \cdot \sin\theta \left[\frac{1}{j\beta_0 \boldsymbol{r}} + \frac{1}{(j\beta_0 \boldsymbol{r})^2} + \frac{1}{(j\beta_0 \boldsymbol{r})^3} \right] \cdot e^{j(\omega t - \beta_0 \cdot \boldsymbol{r})} \right] \qquad [2.1.18]$$

There is only a single component of magnetic field generated and it lies along the SPC unit vector, i_ϕ. As can be seen from (Fig 2.1.4), if the electric dipole is aligned such that it is along the z axis, then the field at a position (x,y,z) away from the dipole will in general always contain both x and y components of the field which, when on the same side of the dipole, always point in the same direction. This asymmetry in the magnetic field leads to our desired non-zero line integral of the field along an unclosed path remote from the dipole. We shall now consider the situation shown in (Fig 2.1.5), where we have such an electric dipole above the ground aligned along the z axis, and the ground lying in the yz plane. A buried fibre runs beneath the ground a buried distance *d* from the dipole. The dipole is aligned such that the fibre runs parallel with the y axis. As can now be seen from the dipole field symmetry, there is a component of the H field that always lies along the path taken by the fibre. It would appear that calculating the field integral along the fibre's path would now be a simple task. However, there is an additional effect to consider. Since the field emitted from the dipole has to travel a finite distance to arrive at the fibre, and that the light has a finite propagation velocity along the fibre, we have to take into account the field that the light will encounter as it propagates along the fibre and not the field at any given instant in time.

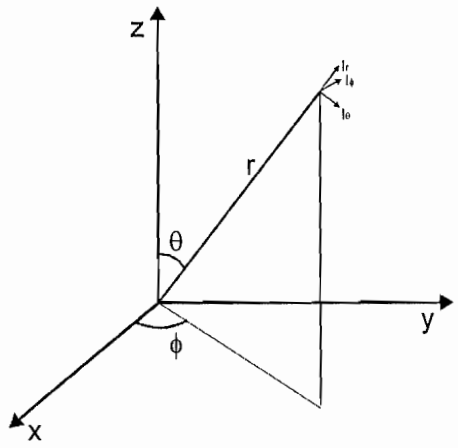

Figure 2.1.4 Spherical polar co-ordinates

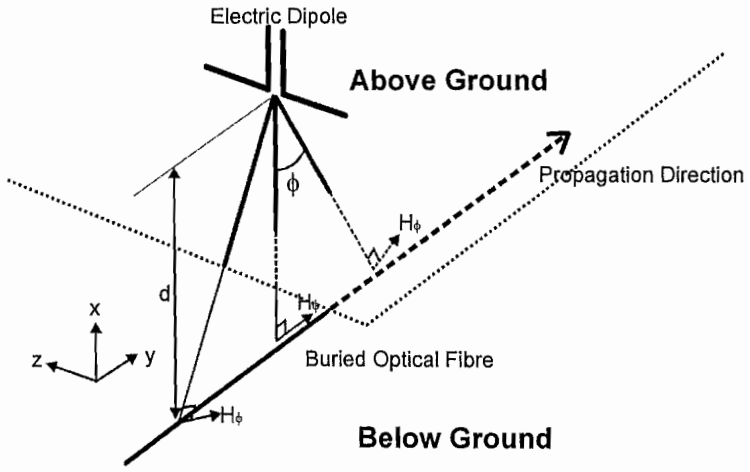

Figure 2.1.5 Orientation of dipole in relation with buried optical fibre. *We have an electric dipole situated above ground. We choose a co-ordinate system such that the dipole lies along the z axis and that the ground lies in the zy plane. The dipole is aligned such that the fibre runs along the y axis. The field generated by the electric dipole has only a $i\phi$ component which given this co-ordinate system ensures that there will always be a component of this field along the direction of the buried fibre.*

If we consider the simplest case, i.e. that for a single photon travelling along the fibre with a phase velocity of, *c/n*, where *c* is the speed of light in a vacuum and, *n*, is the refractive index of glass. We will assume for now that the Radio frequency waves emitted by the dipole, propagate from the dipole through a loss-less medium towards the buried fibre at a speed equal to the vacuum speed of light. This will in general of course not be the case and the Radio waves will travel at a somewhat lower velocity and will experience some attenuation in the lossy soil. This, however, will be discussed latter. Fig 2.1.6 depicts this situation. We shall assume that the instance at which the photon is directly below the dipole is defined as time zero (t = 0). This diagram, (Fig 2.1.6), shows that the field at each point along the fibre must be calculated for the arrival time corresponding to when the photon is at that position. For future reference we shall define this propagation-modified field as the photon-observed field. This was done using a computer maths package Mathcad 8.0 plus and shown in, (Fig 2.1.7), is the variation of the magnetic field component in the direction of the fibre, as a function of the photons displacement along the fibre.

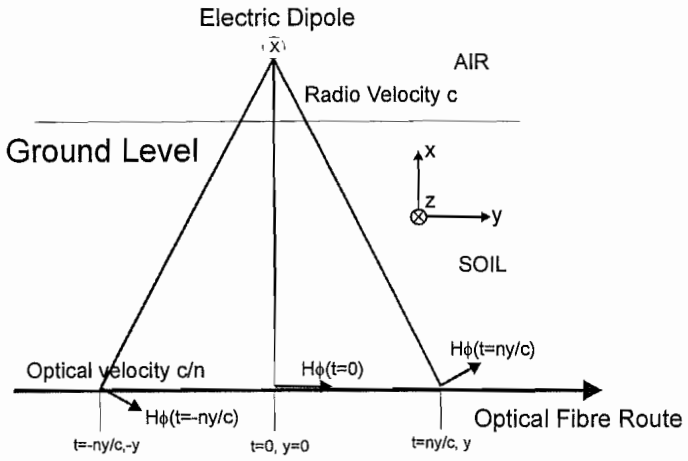

Figure 2.1.6. 2-D diagram showing time dependence of magnetic field "observed" by the photon. *Since the light propagates along the fibre with a slower velocity than the Radio-waves emitted by the dipole, the field "seen" by a photon as it propagates along the fibre will be a function of the time it took the photon to reach a position along the fibre and the distance of that position from the dipole at that instant in time.*

Fig 2.1.7 shows the magnetic field "observed" by a photon propagating along a fibre, situated 1m below and 0.5m to the left of a dipole emitting radio frequency radiation. The four plots, show this effect for several different radiation frequencies, ranging from 1MHz to 100MHz. The "3D" surface plot shows the progression of this field shape with increasing radiation frequency. As can be seen from these plots, the expected result of this

mismatch in propagation velocities is analogous to "Doppler shifting" in acoustic waves as an observer travels past a sound source. Upon approaching the dipole emitting radio-waves, the frequency of the photon-observed field appears to increase and as you pass and recede from the object the converse is true.

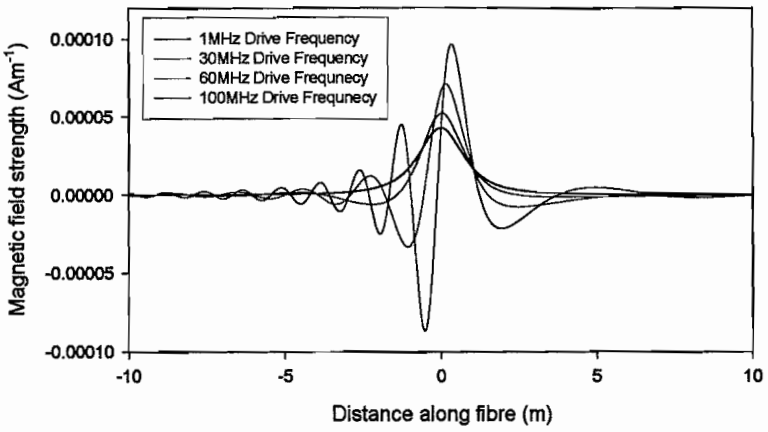

Figure 2.1.7 Magnetic field "observed" by a propagating photon. *A photon propagates along an optical fibre at a speed of c/n. The field it "observes" emitted by an electric dipole 1m above and 0.5 laterally offset is dependent on the emitted radiation frequency.*

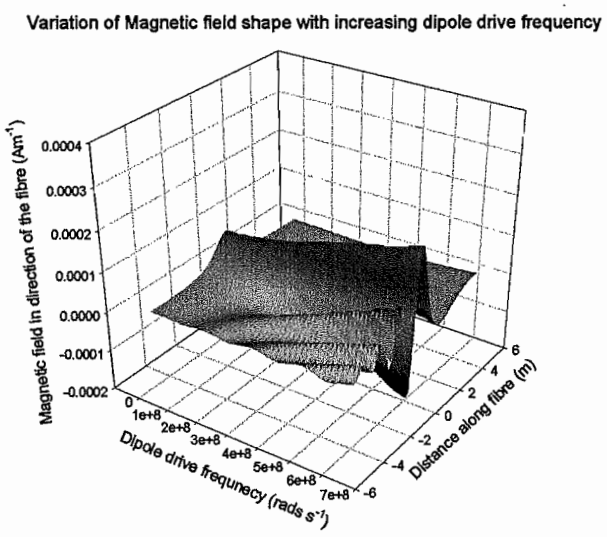

How does the field generated by an electric dipole enable us to find the lateral position and depth of a buried optical fibre. The field generated by the dipole and "observed" by the light can be shown to have a non-zero line integral along the fibres path. In order for this field to enable cable location, the magnitude of the line integral of the field observed by the light must show a variation as a function of the relative position of the dipole and cable. Figure 2.1.8 shows how the line integral of the field changes with both the depth of the buried fibre and the lateral displacement of the dipole from the fibre. A clear peak is observed as the dipole is laterally traversed across the buried fibre, as was originally predicted. A complication to this, however, is that the "Doppler shifting" effect can change this response. Shown in figures 2.1.9-2.1.11 are

similar plots for different radiation frequencies. The model presented predicts that if the wavelength of the radiation emitted by the dipole becomes of the order of the dipole to fibre distance, then we get a periodic response of the field line integral magnitude as the dipole is traversed across the buried fibre. Also that this "Doppler shifting" of the photon-observed field can generate nulls in the line integral of the field leading to a decreased sensitivity with increasing radiation frequency.

Figure 2.1.8 Positional sensitivity of field integral. *Shown above is the variation of the "observed" field integral with respect to the position of the emitting dipole. The radiation frequency of this plot was 10MHz.*

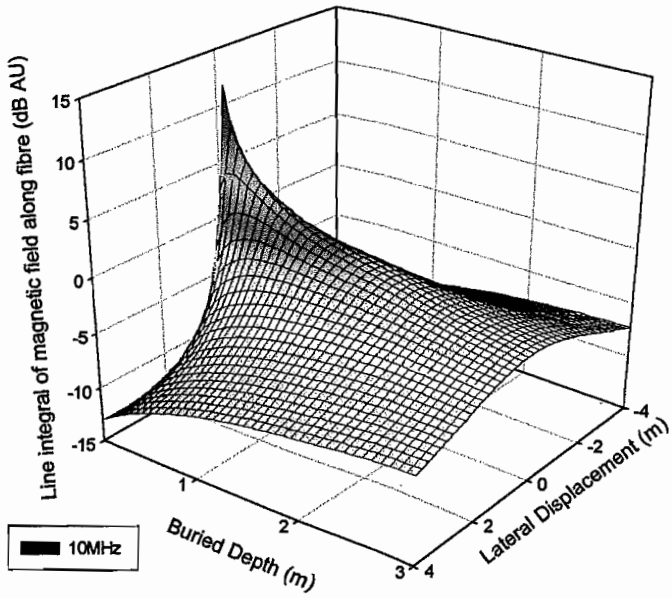

Figure 2.1.9 Positional sensitivity of field integral. *Shown above is the variation of the "observed" field integral with respect to the position of the emitting dipole. The radiation frequency of this plot was 30 MHz.*

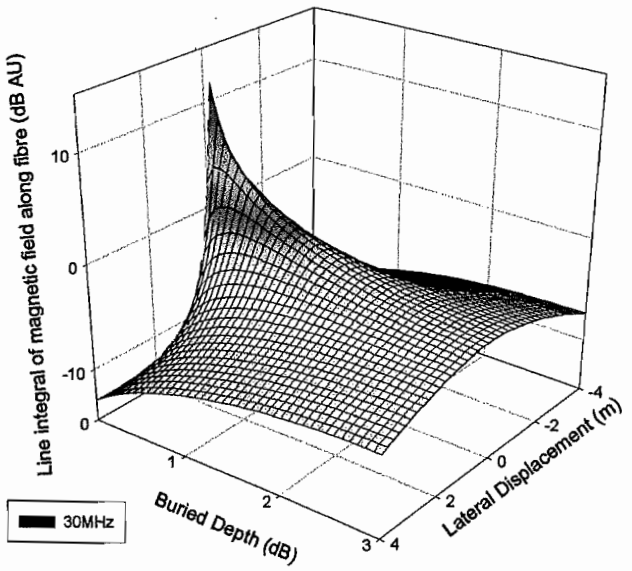

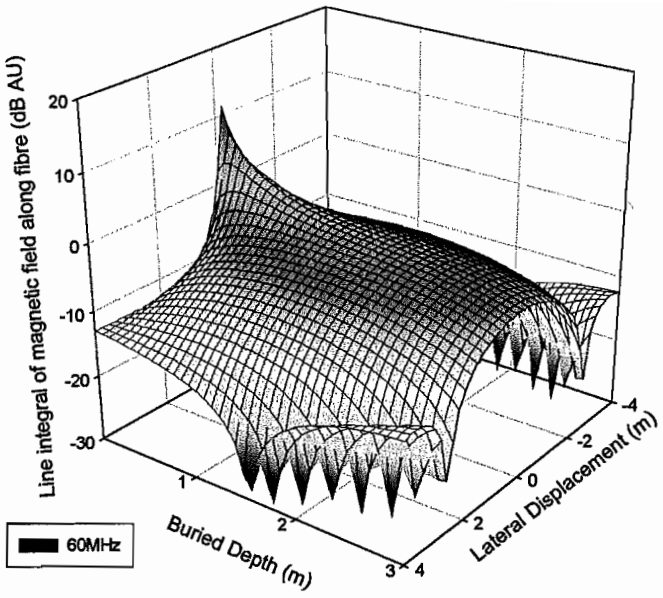

Figure 2.1.10 Positional sensitivity of field integral. *Shown above is the variation of the "observed" field integral with respect to the position of the emitting dipole. The radiation frequency of this plot was 60 MHz.*

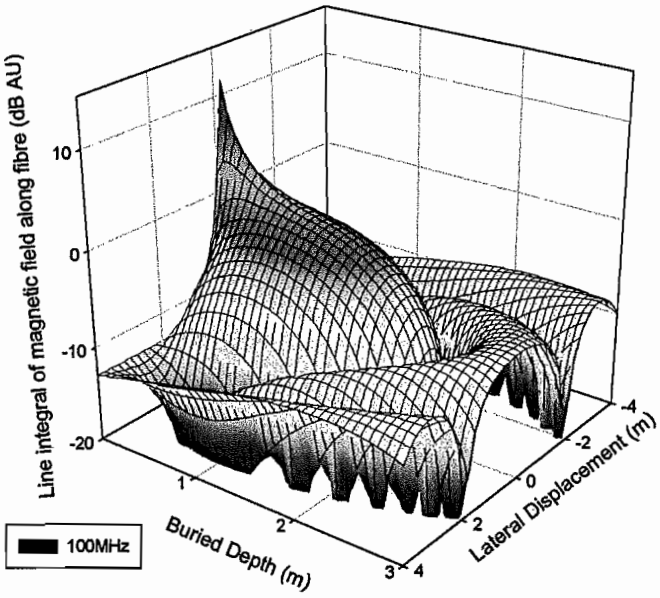

Figure 2.1.11 Positional sensitivity of field integral. *Shown above is the variation of the "observed" field integral with respect to the position of the emitting dipole. The radiation frequency of this plot was 100 MHz.*

2.1.4 Signal processing schemes and noise considerations

2.1.4.1 Derivation of signal to noise ratio of polarimetric optical system

To gain a better understanding of the expected performance and system requirements of the previously presented cable location system, we need to derive a formula that predicts the optical signal strength and the inherent noise of the system. This can then be used to predict the signal to noise ratio, expected in the final system. Consider the following situation. Light is launched from a linearly polarised source with an optical power of, P_0, and propagates along an optical fibre assumed to have a residually low birefringence, (i.e. beat length of approximately 10m). The SOP of this light is then modulated by an electromagnetic field with a radiation frequency of the order of MHz. This light is then incident on a linear polarisation analyser, before its intensity is observed by a photodiode. The photodiode produces a current I, expressed by $I = R_s P_{det}$, where R_s is the photodiode responsivity (usually 0.8A/W for an InGaAs photodiode) and P_{det} is the optical power incident on the photodiode.

The optical power incident on the photodiode can however, be expressed in terms of the launched power and the transmission function of the optical system. This can be shown to give the following result [2.1.19].

$$I_s = P_0 \cdot T_{opt} \cdot R_s \cdot \sin^2\left(\frac{\pi}{4} + V \int_{-\infty}^{\infty} \boldsymbol{B}(l).dl\right) \qquad [2.1.19]$$

where, T_{opt} is the linear optical loss of the system and the trigonometric term represents the action of the linear polarisation-state analyser. As defined previously, V is the Verdet constant of the fibre and $\boldsymbol{B(l)dl}$ is the dot product of the magnetic field along the fibres path. Since we are interested only in the AC component of the detected signal, we split the above, Eq [2.1.19], into AC and DC terms, yielding;

DC component : $\dfrac{R_s \cdot P_0 \cdot T_{opt}}{2}$

AC component : $\dfrac{R_s \cdot P_0 \cdot T_{opt}}{2} \cdot \sin(2\phi)$

where the optical polarisation rotation has been abbreviated to the symbol, ϕ.

There are two main noise sources which should be considered. These are the shot noise of the photodiode and the thermal noise of the transimpedance preamplifier used to convert the photo-current to an observable voltage. These noise components are fundamental limitations and cannot be avoided. All one can do is to choose one of these components to dominate the other in order, to achieve a maximum signal to noise.

1) **Photon (shot) noise** [2.1.11]. This noise source represents the fundamental limitation which dominates at high input optical power. It can be shown that their exists a photon noise current of i_{sn};

$$i_{sn} = \sqrt{2 \cdot q \cdot I_s \cdot BW} \qquad [2.1.20]$$

where q is the electron charge, and BW is the bandwidth of the employed detection scheme.

2) **Thermal (Johnson) noise** This noise is generated by thermally-generated currents in the transimpedance resistor [2.1.12] and can be shown to be, i_{tn};

$$i_{tn} = \sqrt{\frac{4 \cdot k_B \cdot T \cdot BW}{R}} \qquad [2.1.21]$$

where, k_B, is Boltzmanns constant, T, is the absolute temperature and, R, is the transimpedance gain.

As described later, we have chosen two different RF detectors for the high frequency experiments. The first of these devices has an integral transimpedance amplifier with a 5kohm transfer function. We can then calculate that the system will become shot noise limited with a received optical power of 15.6μW. However, there is an additional noise source which we must consider. At high frequencies, (>10MHz), detector preamplifiers have the potential to exhibit higher noise than this fundamental Johnson noise limit. This detector / preamplifier module was quoted to have a digital sensitivity of –33.5dBm in a 420MHz bandwidth, (this assumes a BER of 10^{-10}). This equates to an average, amplifier generated noise, of 3.6pWHz$^{-1/2}$, i.e 2.9pAHz$^{-1/2}$ current noise. This is slightly higher than the fundamental Johnson noise and therefore raises the shot noise limited threshold to

33μW. We can therefore engineer the system such that the received optical power exceeds this threshold (33μW) and ensures shot noise limitation.

Assuming that the dominant noise source is shot noise, we can therefore show that the signal to noise ratio is given by;

$$\frac{signal}{noise} = \frac{1}{2}\sqrt{\frac{R_s P_0 T_{opt}}{qBW}} \cdot \sin 2\phi \qquad [2.1.23]$$

As this equation shows, the signal to noise ratio is proportional to the polarisation rotation, the square root of the received power and the inverse square root of the detection bandwidth.

2.1.4.2 Detection processing schemes

In the previous section, we derived an equation predicting the signal to noise of a polarimetric optical system, detecting an RMS polarisation rotation of, ϕ. This shows us that, as expected the signal to noise will increase as the detection bandwidth is reduced. There are several ways in which this could be achieved

1) Simple passive filtered detection

The simplest way to increase the signal-to-noise ratio of a detection scheme would be to band-pass filter the output of the pre-amplified optical receiver signal to extract a narrow band. This would reduce the effective bandwidth of the detection system expending from near DC to somewhat greater than, $f_{mod,}$ to a much reduced value, equivalent to that of the bandwidth of the filter, where, $f_{mod,}$ is the frequency of the magnetic field modulation.

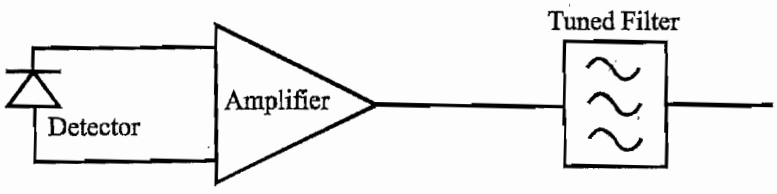

Figure 2.1.12 Filtered detection scheme. *The above detection system reduces the detection bandwidth by simply bandpass filtering the detected signal. The bandwidth of the detection system is reduced to the bandwidth of the filter. Reduced bandwidth = Filter Pass-Bandwidth*

2) Coherent electronic detection

A signal reference can be, extracted from the originally applied magnetic field signal and used to provide a frequency reference for the post-detection filtering system. This allows coherent detection of the signal using a lock-in amplifier. This would reduce the effective bandwidth to 1/ ($2\pi \times$ time constant of base-band filter.)

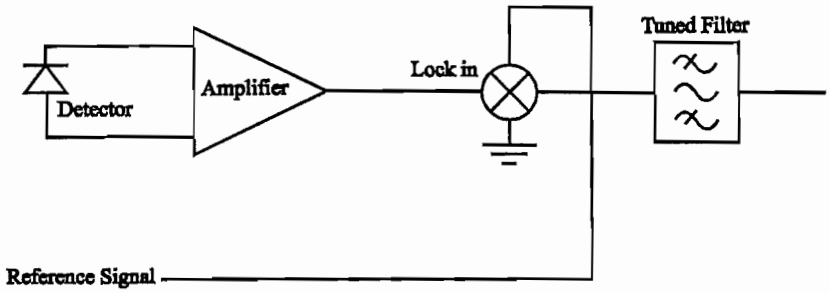

Figure 2.1.13 Electronic Coherent Detection scheme. *The detected signal is multiplied with a reference at the same frequency as the applied disturbance. This generates a baseband signal in which can then be low-pass filtered and then averaged. The detection scheme shown above reduces the effective bandwidth to = $1/2\pi \times$ time constant of low-pass filter. A 1 minute time-constant, (coherent averaging time), decreases the bandwidth to 2.6mHz.*

3) Phase lock loop (PLL).

This is similar to the previous detection scheme. The difference is that the reference is derived from the output of the pre-amplifier and used to phase lock an oscillator to the desired frequency component in the detector output. This has the effect of deriving a coherent reference signal from the received signal. It is however, significantly more complicated to implement and could easily lose lock, or fail to lock under poor signal / noise conditions.

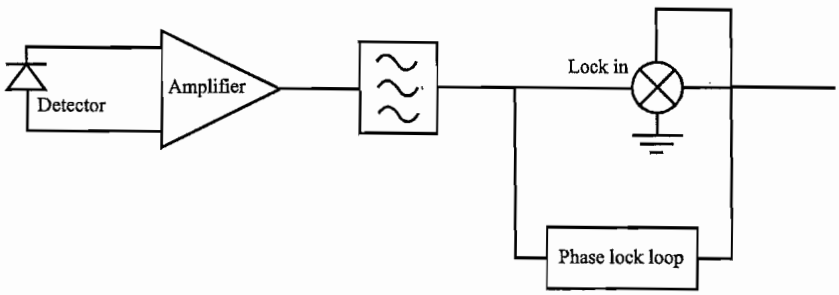

Figure 2.1.14 Generated reference, PLL detection scheme. *The detection scheme shown above uses the signal as a reference and then phase locks to itself. This generates a signal in baseband which can be averaged. This reduces the effective bandwidth to = $1/2\pi \times$ Sample time. So a 1 minute average time decreases the bandwidth to 2.6mHz.*

4) Heterodyne detection system.

A final alternative, with advantages of simplicity of construction and reliability, is to use a heterodyne detection system. In such a system a crystal would be used to control the magnetic field modulation at a frequency f_1. Another crystal oscillator f_2 at the receiver would act as a reference. However, there would be a slight difference in the frequencies at which each of the crystals would oscillate (f_2 - f_1). This would produce a beat frequency of the order of Hertz which could be easily detected.

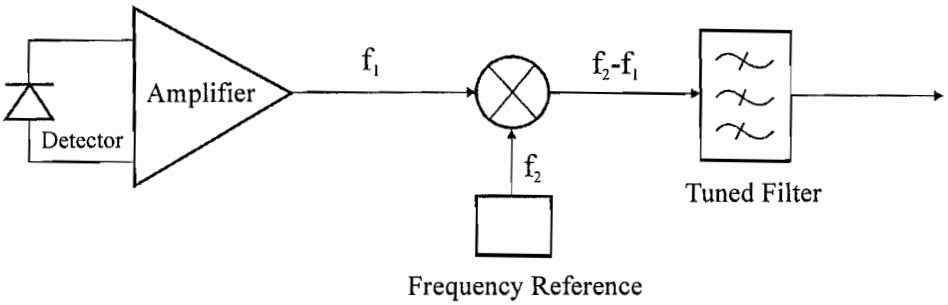

Figure 2.1.15 Reference heterodyne detection processing scheme. *The optically detected signal, of frequency f_1 is multiplied with a fixed reference at a frequency f_2, producing a beat signal at a frequency $f_2 - f_1$. It can be arranged such that this beat signal lies in the baseband. This baseband signal can then be filtered reducing the effective bandwidth of the detection system to that of the post-filter. The baseband signal can then further be coherently averaged, again reducing the effective bandwitdh to $1 / 2\pi \times$ Sample time.*

In fact as is presented later an adaptation of this method was actually used in the final system.

2.1.4.3 Estimate of achievable signal to noise ratio.

Now that we have a formula to predict the signal to noise ratio, expected for the Faraday cable location system, we need to make an estimate of the systems performance. For a first estimate let us assume that we have a 1550nm source, emitting 2mW of light (A typical specification for a telecoms source). Subject to non-linear thresholds of the optical fibre this could easily be increased if necessary, but we would like to use a standard telecoms source if possible. Secondly the averaging time for each interrogation point during the location of a fibre should be no longer than a minute. The length of optical fibre on which this cable location system may be used is around 60km, the normal maximum distance between regeneration stations. Standard telecoms cable has an optical attenuation

0.21dBkm^{-1}, so 60km will exhibit a typical loss of 12 dB. Including an additional 6dB for the interrogation optics, then we get a total optical loss of 18dB. This equates to a linear attenuation of $T_{opt}=10^{-1.8} = 1.6\times10^{-2}$. Using a value of $V_{eff} = 0.54\ rads\ Tm^{-1}$ [2.1.8] as observed by Cruz et al.

Fig 2.1.16 shows the modelled signal / noise ratio generated by a 1m long dipole radiating 50W of RF power at the four radiation frequencies noted in the legend.

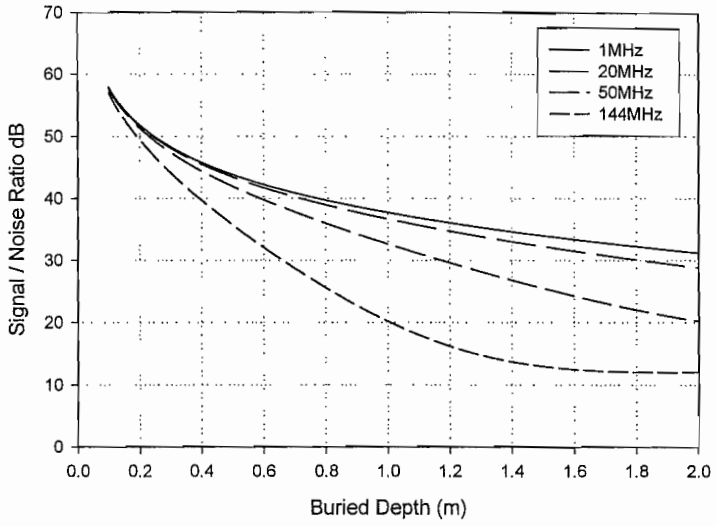

Figure 2.1.16 Modelled signal / noise ratio for the Faraday cable location system. *Plotted above is the expected variation in the observed signal / noise ratio for the Faraday location system as a function of the fibres buried depth. This simulation assumed a loss-less medium, which will not be the case in any real situation and the use of an antenna 1m long driven at 50W. This simulation assumed shot noise limited operation and a detection bandwidth of 2.6mHz.*

As can be seen in Fig 2.1.16 the signal to noise ratio for a standard dipole decreases, as expected, as the dipole is taken further away from the fibre. Also, as the frequency of the EM field is increased the sensitivity of the system decreases, degrading the observed signal / noise ratio. Also we have assumed a loss less medium between the dipole and the fibre. We expect in a real situation that the attenuation of the ground would vary between 5dBm^{-1} to 15dBm^{-1}, and maybe increase beyond this in extreme cases.

The response as the cable locator is traversed across the buried position of the fibre is also of interest. A modelled response for this situation is shown in Fig 2.1.17. We have

assumed that the cable is buried 1m below the magnetic field generator and that the dipole is again 1m long and driven with an RF power of 50W.

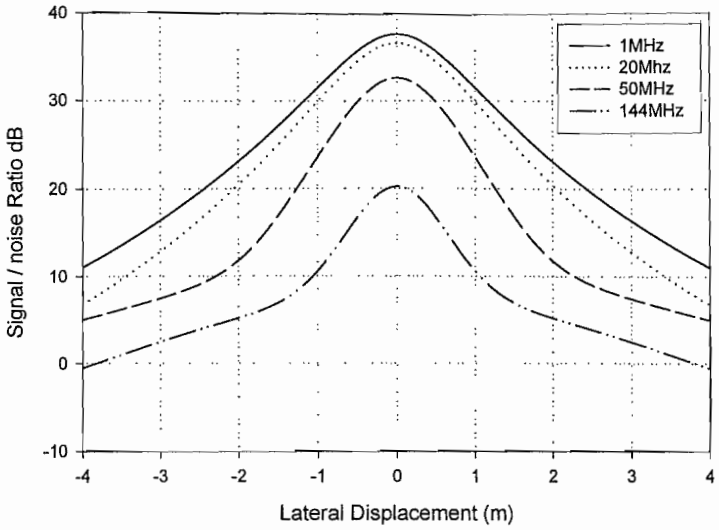

Figure 2.1.17 Modelled signal / noise ratio versus the lateral position of the magnetic field generator. *Plotted above is the expected signal / noise ratio for the Faraday cable location system as a function of the magnetic field generators lateral displacement from the fibre. We have assumed a fibre buried 1m deep and a dipole 1m driven at 50W. The simulations for EM fields at 1MHz, 20MHz, 50MHz and 144MHz are shown. Detection bandwidth was assumed to be 2.6mHz.*

As this figure shows, a peak is observed in the response of the sensor, as the magnetic field generator is traversed across the location of the buried fibre. A theoretical signal to noise ratio of 38dB should be possible at 1MHz and even at 144MHz a signal / noise ratio of 20dB should be easily achievable.

Limitations of this model

The simulations of the expected response of the Faraday cable location system do have some limitations. The most important thing to note is that the model assumes that the current density $\boldsymbol{J}(t)$ is constant over the dipole length. This is turn implies that any physical dipole is much shorter than the wavelength of radiation it emits, (a Hertzian Dipole). If this were not the case then additional retarded potentials would need to be considered, altering the field shape and hence the line integral of the field. The modelled response above assumed a 1m long dipole, an approximation that holds true for low

frequencies <10MHz but becomes increasingly invalid approaching 100MHz. However, in order for a real dipole to radiate efficiently its length must be half that of the radiation wavelength. This does, however, give an approximation for the expected field shape and response from a tuned Hertzian dipole. Since the half-wave length at 50MHz is 3m then, due to size constraints, it is likely that Hertzian dipoles would be used in a finished device. These shorter dipoles will require an electrical matching network to ensure efficient radiation from a 50Ω source.

A further note is that these simulations have so far assumed the use of a single, straight, electric dipole, with no field directivity. However, antennae with directive gains of >10dB can be easily realised, (i.e. log-periodic or YAGI arrays). A 10dB gain in the RF energy would result in a 3.16 times larger rotation in the SOP of the light guided by the fibre and thus would result in a 10dB increase in the signal to noise modelled previously. However, the effect of directed antennae in the near field is extremely complicated to accurately model and so this needs to be experimentally investigated.

2.1.5 Summary and Conclusions

This chapter has dealt with the theoretical analysis of using the Faraday effect for the location of a buried fibre optic cable. By generating a magnetic field above the buried cable, the SOP of the guided light is modulated. This modulation is then detected at the far end of the cable and the results relayed to the location equipment operator. The location of the fibre can then be inferred by observing the peak in this response as the magnetic field generator is traversed across the buried fibre.

Firstly the response of the fibre to an external magnetic field was investigated. It was found, as expected from prior work in polarimetric based sensors, that residual birefringence in the fibre can quench the Faraday effect, reducing the sensitivity of the sensor. However, this is expected to usually be a small effect for likely degrees of birefringence in straight cables and the sensor will remain sensitive to an external field.

The generation of an appropriate magnetic field was then discussed. In order for a magnetic field to effect the SOP of the light guided by the fibre, its line integral along the

path that the light propagates, must be non-zero. It was found that time-varying, travelling-wave solutions to Maxwell's equations solved this problem. The electric dipole was then presented as a suitable magnetic field generator and analysed. Since the EM radiation emitted by the dipole has to travel a different distance from the dipole to arrive at each different position on the optical fibre and the photons are travelling along the fibre, there is an added complication due to the time varying nature of the magnetic field. It was found that, when the wavelength of the radiation emitted by the dipole has a value close to the distance between the dipole and the fibre, then an effect similar to Doppler shifting is observed in the field "seen" by the light as it propagates past the dipole. It was shown that this could, in turn, lead to a reduction in the induced polarisation rotation, and a periodic response as the locator is traversed across the fibre.

Finally, several signal processing methods, designed to improve the signal / noise ratio by reducing the bandwidth of the detection system were discussed. The system was then modelled and it was found that at a depth of 1m we can expect to achieve a signal / noise ratio of 35dB within a 2.6mHz bandwidth (1 minute sampling time). However, it is expected that this would be 1) reduced by the attenuation of the ground which tends to increase with increasing frequency and 2) increased by the use of a magnetic field generator with superior field directivity. It was decided that size constraints may limit the use of large / highly directive antennas.

To summarise we have shown that it is possible to induce a Faraday shift in the SOP of light guided by an optical fibre without enclosing the fibre with a conducing element, as would be required when using a solenoid, and that the calculated signal / noise for realistic sample times should be sufficient to construct a practical cable location system.

References Chapter 2.1

[2.1.1] C.Z.Tan, J Arndt, "Faraday effect in silica glasses." Physica B, Vol 233 (1997) 1-7

[2.1.2] Lorrain, Corson, Lorrain, "Electromagnetic fields and waves." (*Freeman).*

[2.1.3] Hecht "Optics". Pub Addison Wesley.

[2.1.4] W.J.Tabor, F.S.Chen, "Electromagnetic Propagation through Materials Possessing Both Faraday Rotation and Birefringence", Journal of Applied Physics, Vol 40, No 7, pg 2760-2765, 1969.

[2.1.5] A.M.Smith, "Polarisation and magneto-optical properties of single mode fiber.", Applied Optics, Vol 17, No 1, pg52-56, 1978.

[2.1.6] G.W.Day, D.N.Payne, A.J. Barlow, J.J.Ramskov-Hansen, "Faraday rotation in coiled, monomode optical fibers: isolation filters, and magnetic sensors.", Optics letters, Vol 7, No 5, pg 238-240, 1982.

[2.1.7] R.Ulrich, S.C.Rashleigh, W.Eickhoff, "Bending-induced birefringence in single mode fibers." Optics letters, Vol 5, No 6, pg 273-275, 1980.

[2.1.8] J.L.Cruz, M.V.Andres, M.A.Hernandez, "Faraday effect in standard optical fibers: dispersion of the effective Verdet constant", Applied Optics, Vol 35, No 6, pg 922-927, 1996.

[2.1.9] Magid, "Electromagnetic fields, energy and waves." (Wiley).

[2.1.10] Solymar, "Lectures on electromagnetic theory." (Oxford Science).

[2.1.11] P.Horowitz, W. Hill, "The art of electronics-second edition," (Cambridge University Press), Ch 7, pp 453, 1996.

[2.1.12] P.Horowitz, W. Hill, "The art of electronics-second edition," (Cambridge University Press), Ch 7, pp 450, 1996.

[2.1.13] A.W.Rudge,K.Milne, A.D.Olver, P.Knight. "The handbook of antenna design Vol 2", Pub Peter Peregrinus London.

Chapter 2.2 Practical Evaluation of the Faraday Effect Cable Location System

This chapter describes the experimental apparatus built to investigate the feasibility of the Faraday effect cable location system. A system using a solenoid driven at relatively low audio frequencies, to induce a Faraday shift in light propagating along an optical fibre along its axis, is firstly presented. This system is then used to investigate whether a single mode fibre could successfully support a polarised optical signal over several tens of kilometres, and transmit the Faraday induced modulation over these lengths. An initial laboratory experimental structure is then introduced, to investigate the possibility for inducing the Faraday shift, using the magnetic field generated by an electric dipole held in proximity, (<2m away), to the optical fibre. Several antenna types are investigated and the variation of the response of the fibre as a function of the distance from the dipole is measured. The results of initial field trials are then presented and plans for future work and further improvements are outlined.

2.2.1 Laboratory Based Experiments

The system for our initial experiments is shown in figure 2.2.1. A 2mW, fibre coupled 1550nm semiconductor diode DFB laser, (Nortel LC111F-18), was used as the source for our initial tests, which was then coupled through an optical isolator (Oykoden labs 1550nm single stage AMS-1550-R-S), having a return-loss of 48dB. This ensured that any back-scattered light did not adversely effect the stability of the source. This light was then coupled through a bulk Polarcor dichroic polariser, (Newport optics), with a polarisation extinction ratio of approximately 20dB. This linearly polarised light was then passed through a fibre based polarisation controller, before being launched into a 100m length of standard single mode optical fibre. The transmitted light was then coupled from the fibre into a balanced quadrature, polarisation sensitive detection system, (Fig 2.2.1). This was constructed from a bulk polarising beam splitter, (Newport), and two fibre- pigtailed optical detectors with responsivities of $0.9AW^{-1}$, (Epitaxx ETX75FJ-SLR). Simple transimpedance amplifiers were constructed using a FET input TLO72, (GBW 3MHz), with gains of 10kΩ.The signals generated by these detectors were then separated into AC

and DC components. The AC component was amplified by 40dB and band-pass filtered with a 3dB passband of 1kHz centred at 10kHz. A solenoid was constructed using 400 turns of Litz wire, wound in 25 turn sections, as to reduce its capacitance, around a former 20cm in length and radius of 1cm. This served as a magnetic field generator and the fibre was passed along its axis. The signals generated at the output of the quadrature detection system were then sampled by a PC allowing the amplitude of the Faraday induced modulation to be measured. The directly observed signal (before filtering and 40dB gain) was also observed using an RF spectrum analyser, (Marconi 2382).

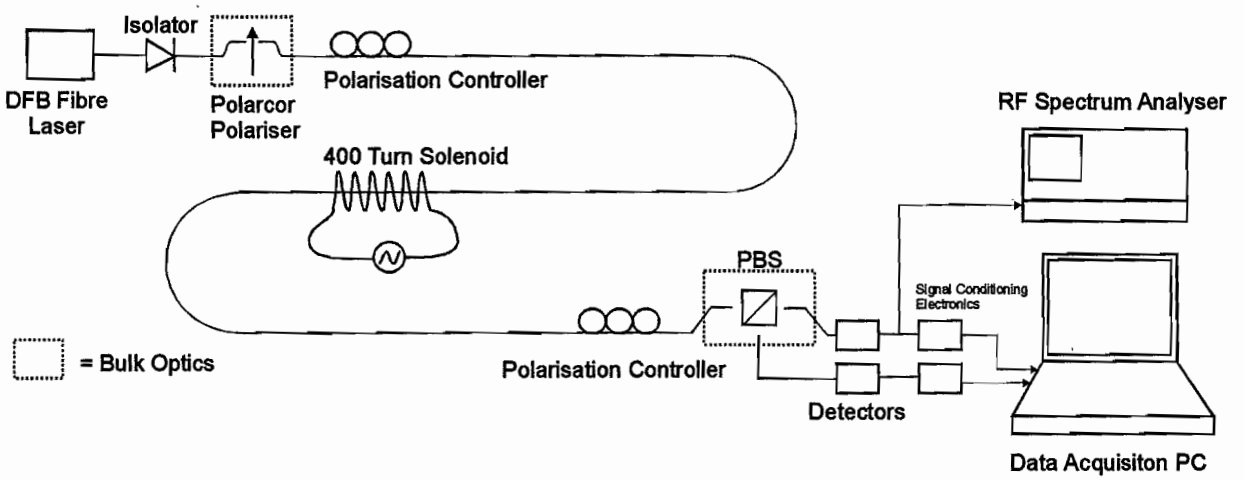

Figure 2.2.1 Experimental structure of initial laboratory test set up. *A telecoms specification fibre coupled 1550nm DFB laser was coupled through a 40dB isolator before passing through a 40dB extinction ratio bulk polariser. This polarised light was then coupled into a 100m length of single mode fibre. At the approximate midpoint of the fibre a 400 turn solenoid was wrapped around the fibre and was driven with a 10kHz tone. This solenoid modulated the SOP of the light guided by the fibre, and was detected by a polarisation sensitive detection system, constructed from bulk components. The detected signals were then observed on a spectrum analyser and also, after amplification and filtering, sampled by a PC. Knowing the drive to the solenoid and its characteristics allowed us to measure the Verdet constant of the optical fibre.*

Figure 2.2.2 Initial laboratory experimental set up for the Faraday location system. *A fibre coupled DFB fibre laser was coupled through an optical isolator before passing through a bulk optics polariser. The light then propagated along a 100m length of single mode fibre before it was incident on a quadrature polarisation sensitive detection system. Also constructed from bulk optic components. A magnetic field was applied part way along the optical fibre by a 400turn solenoid, wrapped around the fibre.*

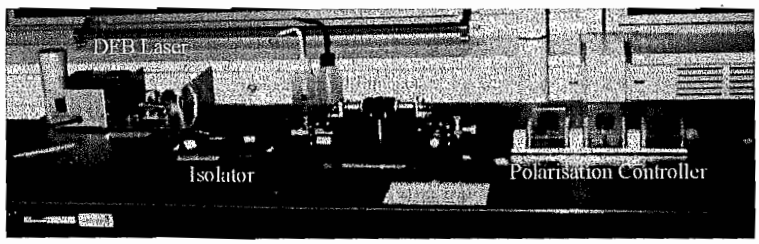

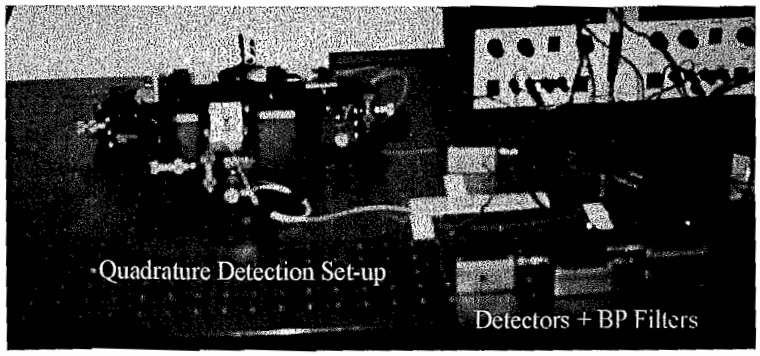

The return loss of the 400 turn solenoid, (radius 1cm, length 20cm), was measured, (Fig 2.2.3), using a network analyser. From this it was found that the coil had the following characteristics: DC resistance 0.75Ω, and a self-inductance of 0.43mH the self capacitance was known to be small <1nF and can therefore be neglected. This gave a self-resonance of approximately 115MHz (dip in figure 2.2.2). Its radius was 1cm and its length was 20cm.

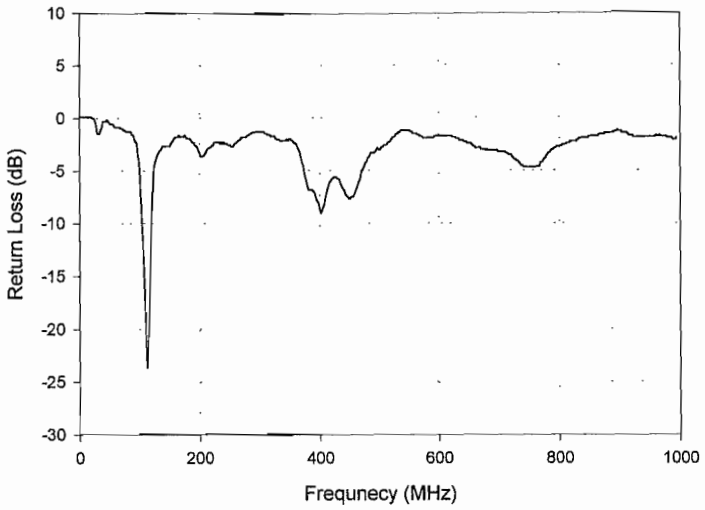

Figure 2.2.3 Return loss plot for 400 turn Litz wire wound solenoid. *This solenoid was wound using Litz wire in sections of 25 turns around a coil former of 1cm radius and 20cm in length. The return loss plot above shows a self resonance of 115.39MHz. When modelled the solenoid is found to have an inductance of 0. Its DC resistance was measured to be 0.75Ω*

The solenoid was driven with a 10kHz sinusoidal tone, with an RMS amplitude of 18.4V. The solenoid was then used to modulate the polarisation of the light in the fibre, using the system described in figure 1.2.1. Observing the detected signal on a frequency spectrum analyser yielded the result shown in figure 2.2.3. This gave a detected RMS amplitude of –70dBm at 10kHz and the measured DC component of the detected signal was 128mV when biased at quadrature. Using the equation given by Cruz et al [2.2.1] we can calculate the field generated by a solenoid carrying 677mA RMS to be 6.795×10^{-4} Tm. This infers a Verdet constant for our silica fibre of approximately 0.42 rads $(Tm)^{-1}$, approximately that measured by Cruz [2.2.1]. Also, previous experiments have yielded similar results to Cruz, i.e. Rose et al [2.2.2] measured a Verdet constant of 3.6rad $T^{-1}m^{-1}$ (@ λ = 633nm) compared to Cruz who measured 3.25rad $T^{-1}m^{-1}$(@ λ = 633nm). Zhangbing et al also measured similar values [2.2.3]. Noda et al also measured a value of 0.8 rads $(Tm)^{-1}$@ 1550nm.

Since we have this uncertainty in the response of any particular fibre, it was decided to design and build a portable system which could be taken to several different buried telecommunications, active cables, allowing a number of different cable types, with different sheathings and fibre composition to be tested.

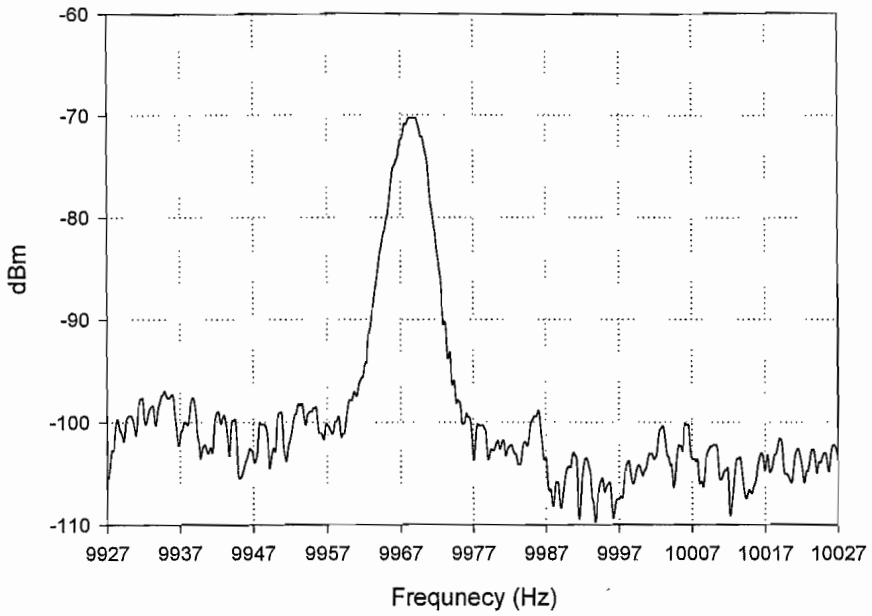

Figure 2.2.4 Results for a 9.987kHz magnetic field disturbance acting on single mode (9μm, 125μm) silica fibre. *A 400 turn solenoid generating a field integral of 6.8×10^{-4} Tm modulated at 9.987kHz shows a dynamic modulation in the SOP of the light guided by the fibre passed along its axis.*

2.2.2 Audio-Band Field Trial

It was decided to design and build a portable (solenoid-excitation) test unit, (Fig 2.2.5), which could be taken to a remote location and tested on a "live" cable route. The bulk optic components in fig 2.2.1 were replaced with fibre coupled devices. The polariser used was a fibre pigtailed Lamipol device, (LP-15-A, with a 55dB extinction ratio), and the fibre-coupled, polarisation sensitive beam splitter was a device from Laser 2000, (L2KPDM-1-1-21-11) with an extinction ratio of approximately 30dB and a nominal insertion loss of 0.6dB.

To generate the magnetic field, a 96turn solenoid with an approximate radius of 6cm and 1.5cm length was used. This could be driven with an RMS current of up to 4amps, at

10kHz, 50kHz and 180kHz. With the aid of a multi-way connector this solenoid could also be split along a diametric plane, allowing it to be wrapped around a live optical cable without interrupting the communications traffic.

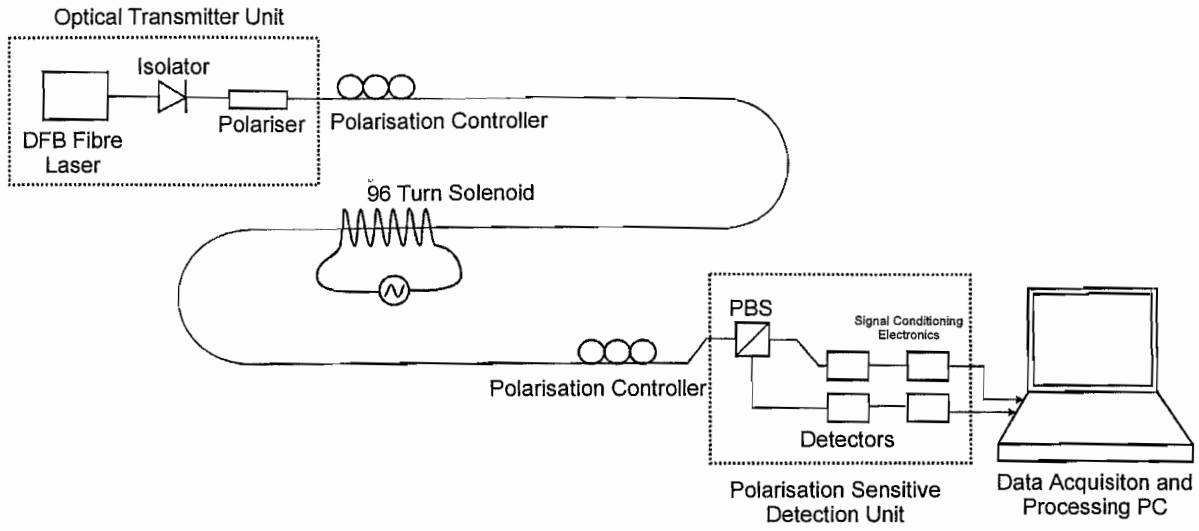

Figure 2.2.5 Field portable, solenoid excitation, Faraday cable location system. *In order to investigate the properties of real buried fibre optic cables a portable polarised source and polarisation sensitive detection unit were built. The major improvement was a narrow bandwidth signal processor, capable of bandwidths 0.68Hz at frequencies of up to 255kHz.*

The Faraday shift signal was detected at the far end of the fibre and sampled at 450kHz, with a 12bit resolution using a National Instruments data acquisition card (DAQCard-AI-16E-4). The sampled data was then digitally processed. By converting to the Fourier domain and applying a Blackman data window, a frequency spectra was generated with a minimum FFT bin-width of 0.4Hz, (with the chosen Blackmann window, due to its profile in the frequency domain, this equates to an effective noise bandwidth of 0.68Hz), and a dynamic range of –120dBV. Note: the design and programming of this FFT and filter section of the data-acquisition and processing was performed by the industrial sponsors of the project. The centre of the selected filter channel could be chosen by the user to lie between 0-255kHz

In order to investigate the properties of real buried cables, it was proposed that this test unit would utilise a single unused "dead" fibre in a bundle containing several other fibres, which still carry active telecoms services. Before testing on live cables was attempted, the Faraday rotation equipment was first tested in a communications laboratory, to verify that the induced polarisation rotation did not effect communications traffic in other adjacent

optical fibres, which must, of course be exposed to the same field. To verify this, two fibres were passed along the axis of the 96 turn solenoid. A communications test unit was used to measure the bit error rate in a standard communications, 2.2Mbits s^{-1}, signal in the first fibre. Our test equipment was attached to the second fibre. It was found that, even with magnetic field strengths, temporarily increased by 20dB than that used in the normal trials, the bit error rate of the communications system was unaffected. This was as expected, since communications systems in current use, are virtually polarisation insensitive and the polarisation rotation induced is only of the order of, at most, milli-radians. (Fig 2.2.6) shows the portable field test equipment being used.

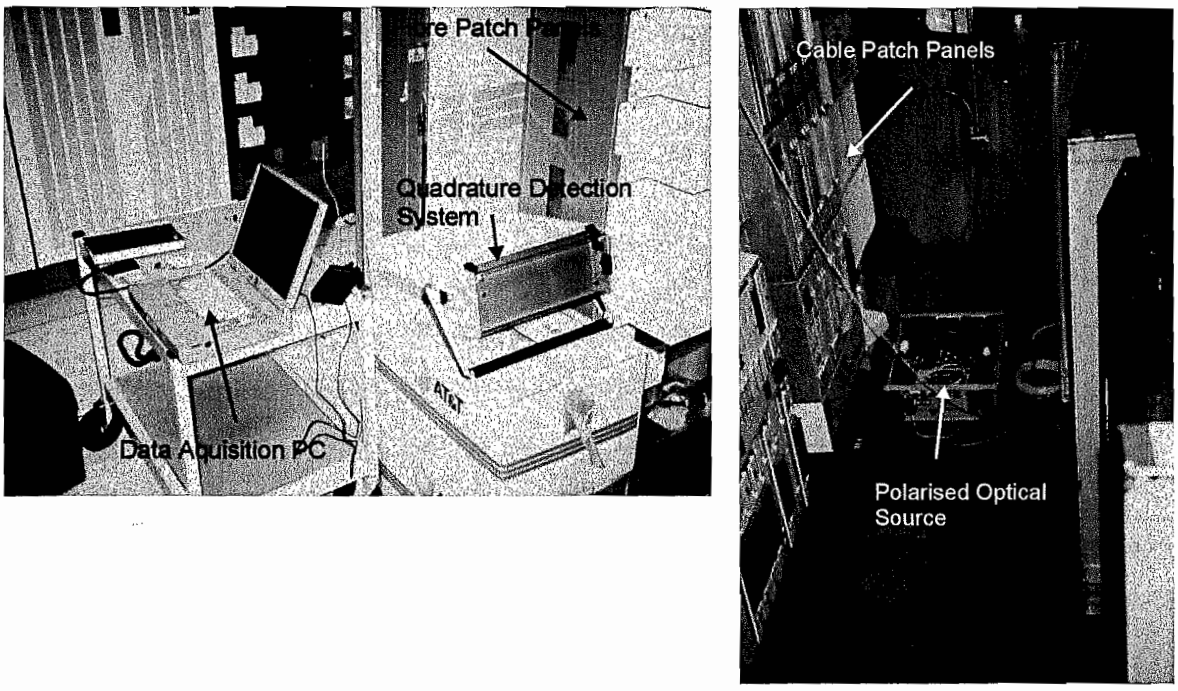

Figure 2.2.6 Photographs of audio-band field portable equipment. *This system was used to test over long lengths of active cable whether the fibre could support a polarised optical signal for 50km and that the effective Verdet constants exhibited by different cables were similar.*

Using the Audio-frequency solenoid test equipment we were able to gather results from several locations and for several different cable and cladding types. We carried out field tests on three separate fibre sections. Figure 2.2.7 shows results for a 10kHz disturbance, acting at the midpoint of, firstly, a 100m length of fibre in the laboratory and then a buried 50km length in active service. This shows that single mode fibre can support light, with a high degree of polarisation, with very little scrambling over several tens of kilometres and that, provided a polarisation controller is used to correct for birefringence, the single to

noise ratio is not significantly effected. A 39dB signal / noise ratio, within a 0.7Hz FFT-filter bin-width, was observed for the short 100m fibre section and a 34dB signal / noise within a 0.4Hz FFT bin-width was seen over 50km's. This degree of signal to noise degradation can be attributed solely to the signal attenuation due to the 10dB additional optical loss in the 50km fibre.

Several of these simple test units were built and given to the cable operators to test the suitability of their different types of fibre and fibre cable to this new location technique. They found that all of the cables they tested could support a propagation mode with a high degree of polarisation, even after propagation through ≈ 50km of installed cables. Also they found that the signal / noise ratios that they observed varied only slightly from fibre to fibre. Even in the worst cases, the signal was only degraded by approximately 10dB. We had no precise feedback of the results of these tests. However, the network operators were confident that this method was suitable for a wide range of fibre and cable types, presently in service. This system was also tested on cables with metal foil moisture protective layers and conducting strength members. Even on cables of this type, signals were observed, albeit with up to 10dB additional attenuation of the induced polarisation modulation. However, when considering higher frequency magnetic fields the attenuation of a conducting cable will become a significant problem, limiting this systems use to non-conducting, non-metallic cables, as was first predicted.

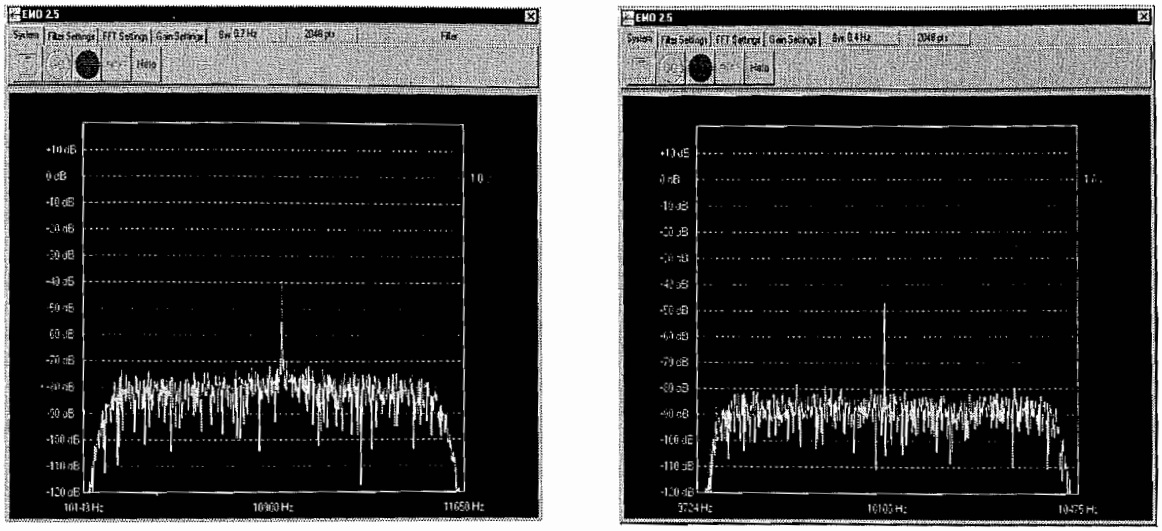

Figure 2.2.7 Detected polarisation rotation for 10kHz disturbance generated by a 96 turn solenoid. *Plot 1 shows the laboratory results when transmitter and receiver are connected via only 100m of fibre. Plot 2 shows the field results obtained when the transmit and receive ends of the system are linked via a 50km length of buried Kevlar sheathed optical cable. The fibre was accessed through a manhole at approximately 20km from the transmit end of the system, where the solenoid was used to modulate the SOP of the light. A signal / noise ratio of 39dB and 34dB is observed within a 0.7Hz and 0.4Hz FFT bin-width respectively.*

Discussion

A novel test set has been designed and constructed to test for Faraday modulation of polarised light in fibre and fibre cables. A number of these relatively simply tests have been carried out, primarily to investigate whether there might be any unforeseen problems when considering the modulation and detection of modulation of polarised light propagating over long lengths of standard single mode fibre. It was found that, on all of the fibres and cables tested, a detectable Faraday shift could be observed and that for all types, the signal / noise ratios varied very little. However, some cables were reported by our collaborator to have shown a reduced sensitivity to the applied magnetic field, but even in these cases the signal / noise ratio was degraded by at worst 10dB. Initial results are highly encouraging, giving confidence in the practicality of the method.

2.2.3 Laboratory experiments using a radio frequency dipole system

2.2.3.1 Initial Laboratory trials

In order for the Faraday system to be practical for cable location, the modulating magnetic field has to be applied form above the ground over the fibre route. Also, (as previously explained in chapter 2.1.), in order for the field to generate a Faraday shift, its line integral along the path of the fibre must be non-zero. The simplest way to generate a field with the required characteristics is to use a simple electric dipole. We are limited however, to the frequencies at which we are allowed to operate, in accordance with the permissable radio band allocation. The frequency bands in which we were able to transmit were 50-52MHz, 70-72MHz, 144-146MHz and 430-434MHz. Although we previously predicted that the magnetic field line integral would decrease with increasing frequency, we have nonetheless chosen to construct a resonant dipole at 144.01Mhz. This is due to the fact that a dipole of 1m is of the maximum convenient length, and so is more representative of the final size likely to be used in practice. A half-wave dipole of 96cm length was constructed and its return loss measured, as a function of frequency, using a network analyser, shown in (Fig 2.2.8).

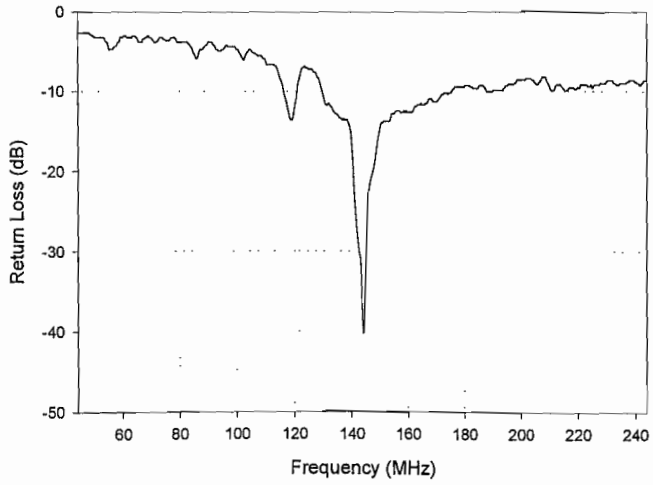

Figure 2.2.8 Return loss plot for balanced dipole of length 0.96m. *The above plot shows the return loss of a 0.96m long balanced dipole. As can be clearly seen there is a -40dB resonance at 144Mhz as is needed.*

The optical arrangement used for these experiments was the same as that used in the previous audio-band experiments, (Fig 2.2.9), with one major difference. The detector now being replaced with a choice of two wideband detector modules, the first made by Epitaxx (ERM535FJ-S) and the second by analogue devices (AD713A-7). Their specifications are shown in table 2.2.1. The first detector, although specified to generate lower noise, has the added complication of having an integral AGC amplifier which reduces the detectors gain when optical powers greater than 50μW are detected. The analogue devices module, however, has a normal linear transimpedance amplifier with no gain suppression.

Detector Model	Transimpedance	Response	Bandwidth	Noise $Hz^{-1/2}$	Sensitivity
Epitaxx ERM535FJ-S	5kΩ	4V/mW	420MHz	3.6pW	-33.5dBm
Analogue Devices AD713A-7	20kΩ	18V/mW	200MHz	8pW	-39.5dBm

Table 2.2.1 RF Detector Specifications.

The experiment was set up such that the polarised optical source, "the transmitter", was situated in the laboratory. A Kevlar reinforced cable then exited the lab and was laid along the service ducts and routed, such that it went up four floors across the metal-skinned roof and back down the opposite side of the building, before re-entering the lab, (Fig 2.2.9). The polarisation sensitive receiver was positioned at the opposite end of the fibre, again in the laboratory. Having a closed-loop integration path along the fibre path should not be a problem as the "skin" of the building is metal, which is expected to have adequately shielded the fibre exiting and returning to the laboratory. Due to the extremely high sensitivity of our narrowband detection system, the transmitter and detection hardware had to be placed in an EM-screened cabinet, (Electrospeed EMC 19inch rack, the quoted isolation was -70dB at 144MHz). This prevented direct pickup of the, albeit greatly attenuated, residual RF field generated by the electric dipole on the roof. The initial signal processing scheme employed for detection, was simply an RF spectrum analyser, (Marconi 2382) after the RF optical receiver.

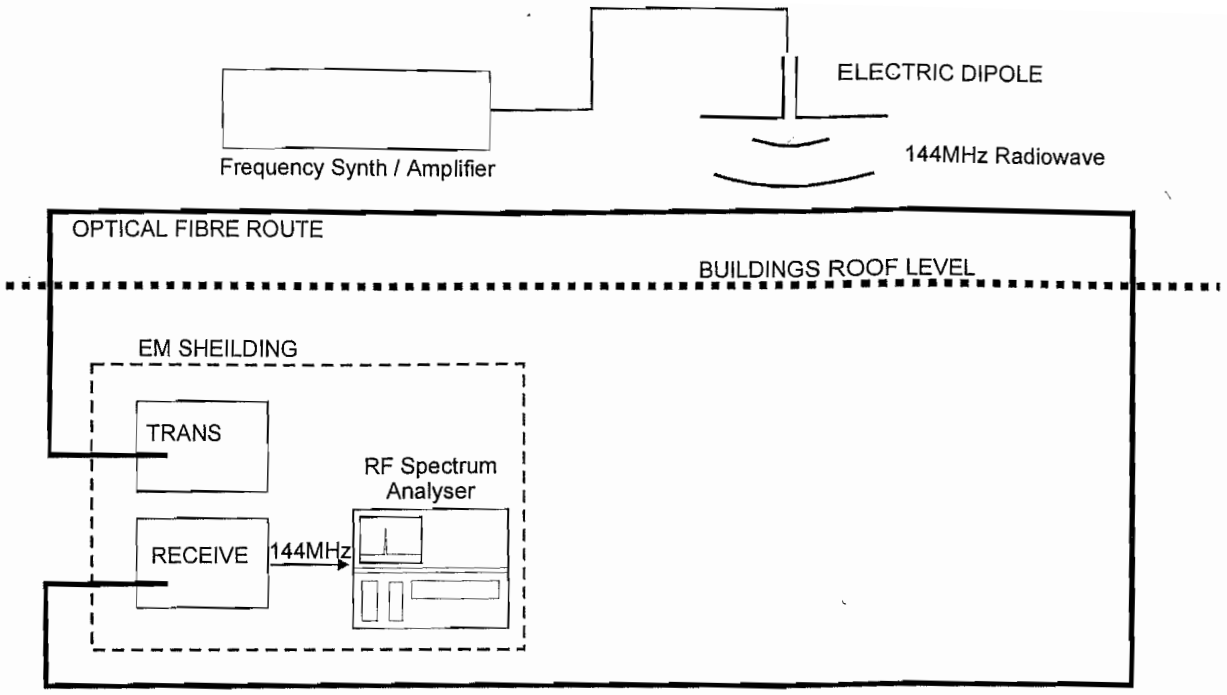

Figure 2.2.9 Initial RF dipole laboratory experimental set up. *The optical transmitted launches light into an optical fibre in a Kevlar reinforced cable bundle. This cable then exits the laboratory and is laid in service duct where it exits the building and runs across the metal skinned roof, where a dipole driven at RF frequencies modulates the SOP of the light guided by the cable. The cable then re-enters the building and is routed back to the laboratory. The polarisation sensitive detection system measures the modulation. The signal amplitude is measured using an RF spectrum analyser. The transmitter, receiver and spectrum analyser are shielded, to prevent pickup of the residual EM field.*

A 144.01MHz signal was generated, (Marconi 3021), and amplifier to 50W (AR amplifiers 75AP250), and used to drive the electric dipole, (the reflected RF power was measured using a SWR meter and found to be only 200mW), which was placed in proximity to the fibre, a distance of 15cm away. The spectrum shown in figure 2.2.10 was obtained, showing a weak, but observable detected signal at a low level of –130dBm. The signal to noise was only 7dB in a 3Hz detection bandwidth. To ensure that the signal observed, was an actual Faraday shift and not direct pickup, the polarisation sensitivity of the optics was removed, by bypassing the polarising beam splitter and observing the optical signal directly on the detector module, so that only amplitude changes were revealed. The signal at 144.01MHz was found to vanish as expected. As a second check the dipole was rotated through 90 degrees, in the ZY plane and the signal again vanished. It should be noted that such checks were necessary for all such experiments, as otherwise low-level RF "pickup" could easily be confused with the desired signal. This problem became ever more severe as the sensitivity of the reciever systems improved.

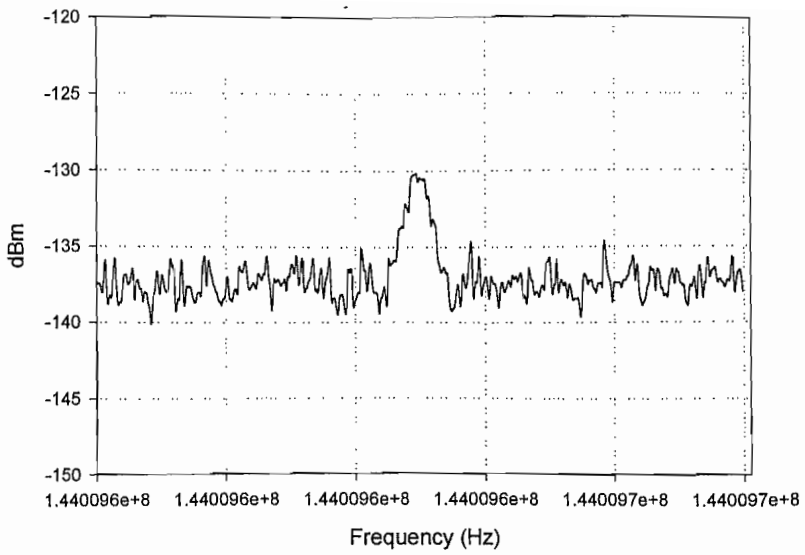

Figure 2.2.10 Initial results for detected response (using Epitaxx detector) with an electric dipole antenna driven with 50W at 144.01MHz, held 15cm away from the fibre. *Light from a polarised semiconductor DFB diode source was guided via a 200m length of Kevlar sheathed fibre, to a remote location where the fibre could be irradiated. There was a metallic RF screen between the excited fibre section and the launch/receiver ends in the laboratory below. The signal generated on the photodiode was then observed using an RF spectrum analyser. with a 3Hz bandwidth.*

2.2.3.2 Noise considerations over long lengths of fibre (>30km)

The initial results above showed that we could obtain a Faraday shift in a standard single mode optical fibre, by exciting it with a time varying magnetic field, generated by an electric dipole. However, these first results highlighted two main problems. The first being that the noise floor observed was some 12dB higher than that expected, and that in order to gain further insight into the effects we wish to investigate, that we would require a detection system with a much lower detection bandwidths. Due to the fact that the Epitaxx detector module had a non-linear gain. the noise floor of the experiment was compared to theory using the other detector module from analogue modules. Light was guided through 200m of signal mode fibre. The launched optical power was adjusted such that the detected power was always 970μWs. When the light was observed directly by the detector module, with no polarisation sensitivity, a flat noise floor of –111dBm was observed, (comparing exactly with the theoretical shot noise floor of –111dBm), in a 3Hz bandwidth. When the light first passed though a polarising filter and then observed by the detector module, (the optical power was again increased to give a detected power of 970μWs), the noise floor increased to –99dBm. 12dB higher than the predicted shot noise floor, (Fig 2.2.10).

The possible sources of optical noise were relatively limited.

1) Source intensity noise
2) Noise in the RF field generated by the dipole field and any external RF radio sources
3) Source frequency fluctuations, causing phase noise
4) Strain-induced polarisation changes, causing noise as a result of high frequency mechanical disturbances.

Several of these possibilities were ruled out by simple experiments. The noise of the optical receiver was measured and it was found to be dominated by photon noise. Phase noise in the RF signal to the dipole was also ruled out. Although the frequency of the tone generated by the signal generator (which drove the dipole via an amplifier) was found to drift slowly, (±100mHz), there was no evidence of any high frequency noise in the MHz range. Any strain-induced birefringence would effect the polarisation state of the light guided by the fibre. However, for this effect to alter the observed noise level at 144MHz the strain would have to be modulated at this rate. Strain induced birefringence changes might be expected to effect the baseband noise level, but they are expected to be insignificant at RF frequencies.

The remaining, most likely, possibility was that the frequency fluctuations (phase noise) of the optical source were, in some way, being translated into polarisation noise in the SOP of the guided light. The possibility of noise in coherent polarimetric systems has been noted previously [2.2.4]. The optical fibre will inevitably have a degree of residual birefringence. This can be modelled and approximated as a linear retarder, where for single mode fibre there is a finite beat length l_b. Typical values of the intrinsic l_b for high quality telecoms fibre is of the order of 10m. If linearly polarised light is initially incident at an angle to one of these eigenaxes, then as it propagates along the fibre, the two eigen-components will phase shift relative to each other, as was previously shown, [Eq 2.1.4]. This causes a time delay between when the two orthogonally polarised components arrive at the detector. If the phase noise spectrum of the source, (i.e. the spectrum of the intensity detected at the output of a dual-path interferometer, when the source frequency fluctuates), extends out to this RF band, then a modulation component at 144MHz will be observed at the far end of the fibre, when the two polarised components are mixed in a polarisation sensitive element. Over very long fibre lengths the path differences in any polarimetric

interferometer can increase significantly, and even a very small difference in optical frequency can result in a significant noise signal. It is therefore important to measure the linewidth and phase noise of the semiconductor diode used in these experiments.

2.2.3.3 Measurement of optical source linewidth / phase noise

The line width of the source was measured using a self-heterodyne technique [2.2.5]. In this method, as shown in (Fig 2.2.11), light from the source under investigation is, essentially split equally into two unequal length paths, then recombined. The first half of the light is delayed, by passing it through a length of fibre (12km). The other half, however, is up-shifted in frequency by 110MHz using an acoustic optic modulator (AOM). These two beams are then combined and a beat signal, centred at 110MHz, may then be observed using an RF spectrum analyser. The phase noise present on this 110MHz carrier is then a measure of the optical phase noise of the source. Similarly, without the AOM, this method is termed self Homodyne and the signal generated becomes biased at DC and not 110MHz.

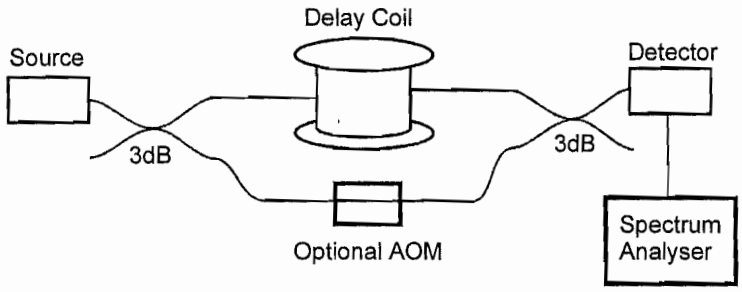

Figure 2.2.11 Optical set up for source linewidth measurement using a self-heterodyne technique. *Light from a DFB laser (Nortel LC111F-18) source is passed through a Mach-Zehnder interferometer which is unbalanced 10km. The light in one arm is shifted in frequency by 110Mhz, using an AOM. The light is combined on an RF detector, where the heterodyne signal generated gives a direct measure of the source linewidth.*

An analysis of this method was performed by Gallion et al [2.2.5]. In their analysis they examine many possibilities. Both self-heterodyne and self-homodyne arrangements are examined and the different ways in which a delay may be introduced discussed. These included delays caused by birefringent elements in coherent polarimatric interferometers and delays in interferometric sensor and delays. The complete analysis is complicated and we are interested only in the case where we have a self homodyne system.

Consider first the quantum phase noise inherent to a laser. Consider the situation where we have an amplitude stabilised, single frequency wave, $E(t)$ undergoing a phase fluctuation $\phi(t)$;

$$E(t) = E_0 \exp i[\omega_0 + \phi(t)] \qquad [2.2.1]$$

where ω_0 is the average optical frequency, and the time dependence of E_0 is an amplitude noise and can be neglected. By taking the autocorrelation function of this field we get;

$$G_E(\tau) = \left\langle E^*(t)E(t+\tau)\right\rangle = \left\langle \exp[j\Delta\phi(t,\tau)]\right\rangle \exp(j\omega_0\tau) \qquad [2.2.2]$$

where $\Delta\phi(t, \tau)$ is the phase jitter, i.e. the random phase change between times t and τ, where τ is the delay time. This phase jitter can usually be assumed to be a zero-mean Gaussian process with an associated probability distributed. Working through this we find the result that for a laser operated far above threshold the mean square phase jitter increases linearly with time, giving $<\Delta\phi^2(\tau)> = 2\gamma\tau$, where 2γ is the full linewidth of the laser at half maximum (FWHM) of the Lorentzian laser field. The coherence time of the laser is given by the inverse of this linewidth.

If we now consider the situation shown in figure 2.2.11, without the AOM, i.e. the self-homodyne system. We now have two optical waves interfering at the output of an unbalanced interferometer.

$$E_T(t) = E(t) + \alpha E(t+\tau_0) \qquad [2.2.3]$$

where τ is now the time delay caused by the imbalance in the interferometer and α is a term which accounts for the different amplitudes of the two waves interfering at the output of the interferometer. We will assume a perfect case, i.e. that $\alpha = 0$.

It maybe shown that the autocorrelation function of the detected photocurrent, $R_I(t)$ is now given by;

$$R_I(\tau) = e\sigma G^{(2)}{}_{E_T}(0)\delta(\tau) + \sigma^2 G^{(2)}{}_{E_T}(\tau) \qquad [2.2.4]$$

where $G^2{}_{ET}$ is the second order autocorrelation function of the total detected field, e is the electron charge, σ is the detector responsivity and δ is the Dirac function.

I will not derive the result as Gallion has already shown a full derivation. However, it may be shown that the spectrum $S(\varpi)$ of the photocurrent detected by the photodiode should obey the following theory;

$$\frac{S(\varpi)}{4\sigma^2 E_0^4} = \left[1+\exp\left(\frac{-\bar{\tau}_0}{2}\right)\right]^2 \delta(\varpi) + \exp\left(-\bar{\tau}_0\right)\frac{1/\pi}{1+\varpi^2}\left[sh\bar{\tau}_0 - \frac{\sin\varpi\bar{\tau}_0}{\varpi}\right] \qquad [2.2.5]$$

where $\varpi = \omega/2\gamma$ and $\bar{\tau} = 2\gamma\tau$. For further details please refer to Gallion et al [2.2.5].

Results for the DFB semiconductor diode laser, (Fig 2.2.12), indicated that its –3dBc phase noise varied between 10-20MHz. Also that the phase noise of the source 144MHz away from its central frequency was -30dBc. The delay in this experiment was 12km, corresponding to a time delay of 60μs. When this source is coupled into 200m of single mode fibre, the time delay between the orthogonally polarised components is expected to be of the order of 10^{-13} seconds. Since the amplitude of the phase noise is related linearly to the delay time, the phase noise at 144MHz is therefore expected to be 85dB down on the level detected in this self-homodyne experiment, i.e. at approximately –125dBm, (not very far from the observed value of –138dBm). Note, that this assumes that the frequency fluctuations in the source output are generated by the quantum fluctuations and that the self-homodyne experiment represented the fundamental linewidth of the source, and not some externally modulating phase term. However, in fig 2.2.12 we see structure in the laser phase noise which appears to increase the noise at 144MHz. This may account for the difference seen in the expected noise floor of the polarimatric interferometer.

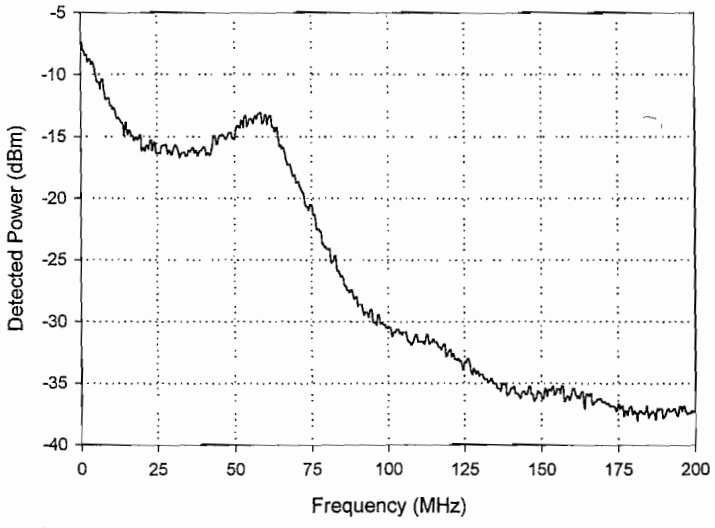

Figure 2.2.12 Measurement of source linewidth. *The linewidth of the semiconductor DFB diode was measured using a self-Heterodyne technique. As is shown above the –3dB linewidth is of the order of 20MHz and there is evidence of frequency changes of 40MHz in the optical source. The phase noise at 144MHz however is at –30dBc.*

In order to reduce this source of noise in our polarimetric system an external-cavity laser source, (Nano-tunics, Photonetics), was used. When measured by the above method it was found to have a phase-noise linewidth of approximately 100kHz. This source was then used in further evaluation of the Faraday cable location system and gave a 12dB decrease in the noise of the system. This will be discussed in more detail later.

2.2.4 Improved laboratory dipole experimental set up

As previously stated, in order to investigate the Faraday cable location system more effectively, we require a lower bandwidth detection system, (ideally of the order of a few mHz or less). This may sound a trivial matter, as that it could simply be achieved by averaging the signal coherently with the known signal as a reference in a lock-in with an output time constant of a minute or so. This, however, becomes a problem in our long-distance cable location system as we will not normally have access to the transmitted signal at the far end of the fibre where the modulation is detected. We shall therefore need an extremely stable RF transmitter and a similarly stable frequency reference. If the signal frequency were to drift during the sampling period then the detected signal amplitude would be spectrally spread and thus attenuated. With a detected signal frequency of the order of 144MHz, we would require a frequency stability of the order of 10^{-11} to achieve a detection bandwidth of 1mHz. This is not easily achievable using temperature-controlled crystal oscillators and so it was decided to use clock oscillators based on Rubidium standards, which can give an accuracy of 10^{-13} over a period of about a minute. This would allow a minimum bandwidth of 0.01mHz even using two oscillators.

As a result of the above results, a new detection and signal processing system was constructed, as shown in figure 2.2.13. In this experimental set up, the 144.01MHz signal generated on the optical detector was converted to a baseband signal using a communications receiver (IRC8500). The 30.2MHz local oscillator of this standard communications receiver was replaced by a 30.2MHz digitally synthesised waveform, generated by a 10MHz Rubidium locked signal generator. The signal generator used to produce the modulating magnetic field was also locked to a separate Rubidium standard. The IF frequency of 450kHz was taken from the comms receiver and sampled (at either 20kHz, 50kHz, 400kHz or 455KHz) by a laptop computer with a 12bit resolution

(DAQCard-AI-16E-4). An improved FFT program, capable of producing FFT bin-widths between, selectable between 3Hz and 0.1mHz, was used as a narrow bandwidth spectrum analyser, (The FFT programme was written by our industrial sponsors). The amplitude of the alias signal produced (i.e. at a frequency equal to the difference between Nyquist and 450kHz), then gives a measure of the Faraday rotation induced in the fibre. This improved system now allowed both the signal and detection system to be frequency stabilised to within 0.2mHz, so that coherent averaging times of up to 13 minutes could be used if necessary. However, our experiments were limited to detection bandwidths of 2.6mHz, (1 minute averaging times).

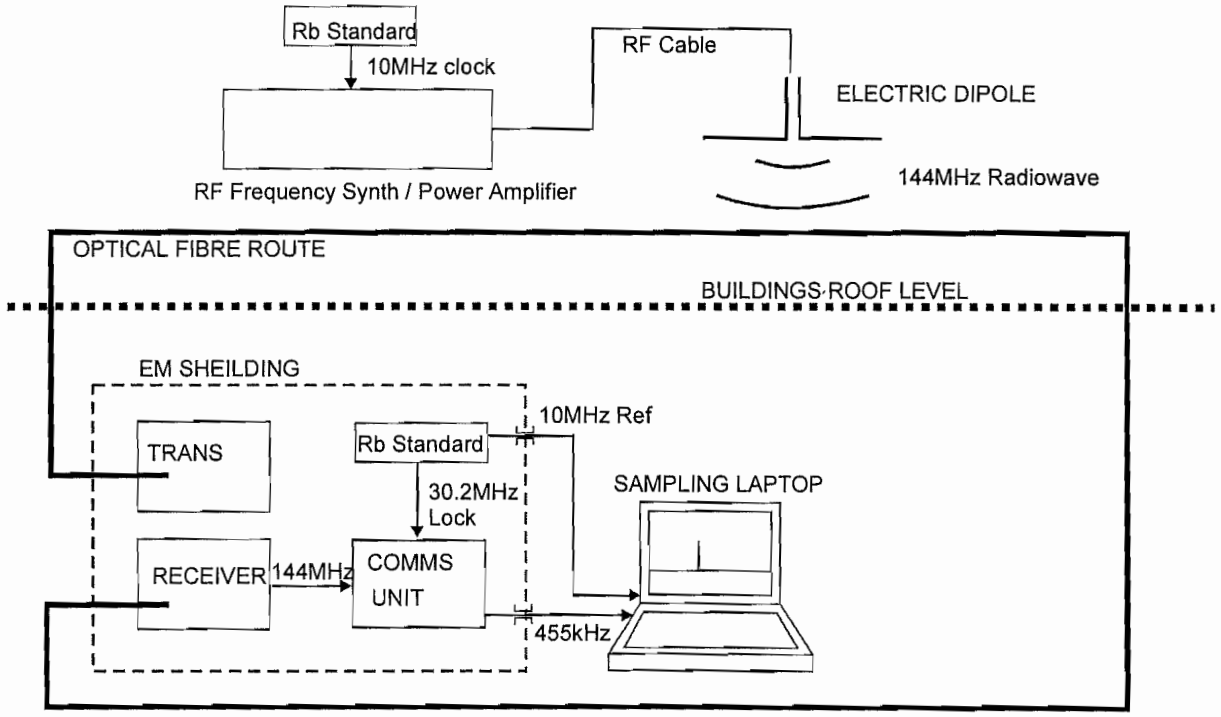

Figure 2.2.13 Schematic of laboratory based ultra-low bandwidth detection system for Faraday location experiment. *Both the field emitter and the detection system are locked to Rubidium standards to reduce frequency drift. It is then possible to achieve coherent detection bandwidths below 1mHz.*

Figure 2.2.14 shows pictures taken of the Kevlar sheathed cable running, supported on tressels, across the roof of the building of the laboratory and the transmit and receive ends of the experiment, housed in their EM screened cabinet.

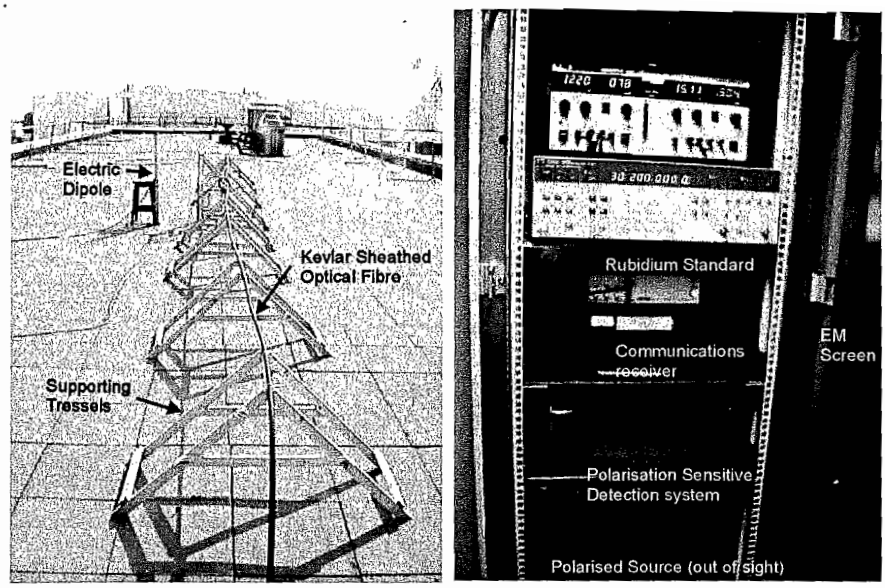

Figure 2.2.14 Photographs of the Kevlar sheathed cable laid across the buildings roof and the laboratory set up. *Note that the fibre is supporting by non-conducting tressels to hold the fibre away from the conducting roof. The electric dipole was packaged in a dielectric case and held in proximity to the fibre cable. The second photograph shows the optical source and narrow-bandwidth detection systems in the laboratory. Note that the sensitive apparatus is screened in a commercial RF-screened 19inch rack unit, giving 70dB RF isolation at 144MHz.*

2.2.3.5 Results and discussion

This new optical architecture was used to investigate the signals generated by several different dipoles at varying distances from the optical fibre (summary of results shown in table 2.2.2). Using a semiconductor diode light source we initially observed a signal of –74dBV, using a standard electric dipole, (at 144MHz and 50W), held 10cm away from the fibre. This dropped to –88dBV at 1.2m. The noise floor within a bandwidth of 2.8.mHz was approximately –110dBV. The observed signal to noise ratio was therefore 36dB an 22dB for each distance respectively. The modelled signal to noise predicted a signal to noise of 55dB and 18dB respectively. The experimental results obviously don't agree with this modelled response. However, this is not surprising due to the fact that the model made several assumptions which are not true in any real situation. The first was that it assumed a Hertzian dipole, whereas a half-wave dipole was used in experiments. Secondly the model assumed a loss-less medium between the dipole and the fibre.

As discussed previously, there was an additional noise source related to the source linewidth. Using the improved narrow linewidth source, (Nanotunics), we showed that over this relatively short length of fibre, (200m), the noise floor dropped by approximately

12dB. However, due to the fact that the communications receiver used an AGC amplifier built into its IF frequency section, this improvement was revealed as an increase in the observed peak signal and not a reduction in the measured noise floor. The previous experiment was repeated giving a signal of -61dBV (at 144MHz and 50W) when the dipole was positioned 10cm away from the fibre and -77dBV (at 144MHz and 50W) when 1.2m away. This corresponds to signal to noise ratios of 49dB and 33dB within a 2.8mHz bandwidth respectively. Further experiments investigated the possibility of increasing the induced Faraday rotation by using directed antennas. A 12 element YAGI array, with a far field gain of 10dB, was used and it was found that this increased the observed signal / noise ratio by 30dB when the tip of the dipole was at a distance of 1.2m away from the fibre, (i.e. –47dBV at 1.2m giving a signal / noise of 63dB). A wide-band antenna was also tested, (Log-periodic with a 6dB far field gain), and found to give a signal level of –57dBV at a distance of 1.2m (i.e. a 53dB signal /noise ratio in a 2.8mHz bandwidth).

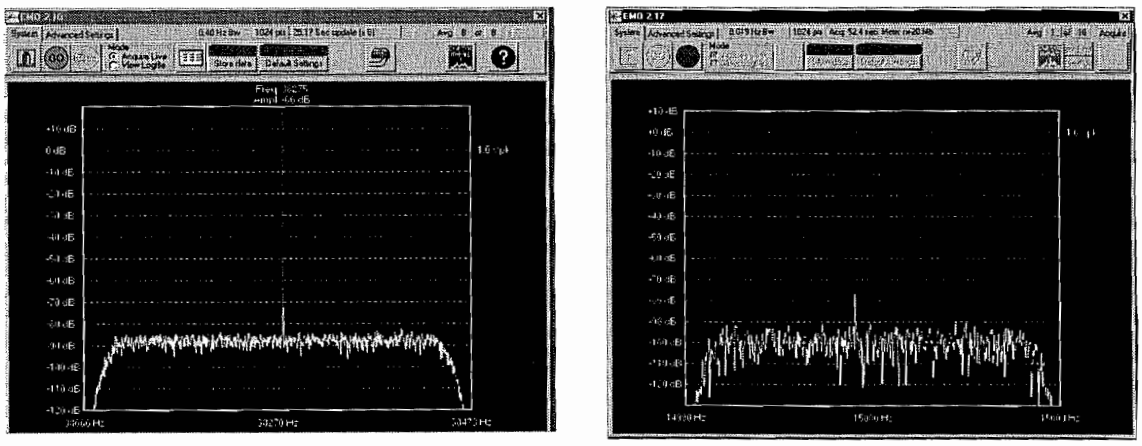

Figure 2.2.15 Results for an electric dipole driven with 50W held 10cm and 1m away from the fibre respectively.

Description	Distance from fibre	Observed Signal Peak (dBV) With two different light sources	
		DFB semiconductor diode	Nano-tunics External Cavity
0.96m Standard Dipole $\perp r$	10cm	-74	-61
0.96m Standard Dipole $\perp r$	120cm	-88	-77
0.96m Standard Dipole ll'	10cm	-87	
12 element, 10dB, YAGI $\perp r$	10cm	-77	
12 element, 10dB, YAGI $\perp r$	120cm	-88	
12 element, 10dB, YAGI ll'	10cm	-60	
12 element, 10dB YAGI ll'	120cm	-82	-47
Folded Dipole ll'	10cm	-68	
Folded Dipole ll'	120cm	-88	
Folded Dipole $\perp r$	10cm	-84	
50MHz-1GHz, 6dB, Log periodic	120cm		-57

Table 2.2.2 Results achieved in laboratory based trials. *Please note that all tests were carried out at 144.01MHz and that within a detection BW of 3.4mHz the noise level was observed to be –110dBV.*

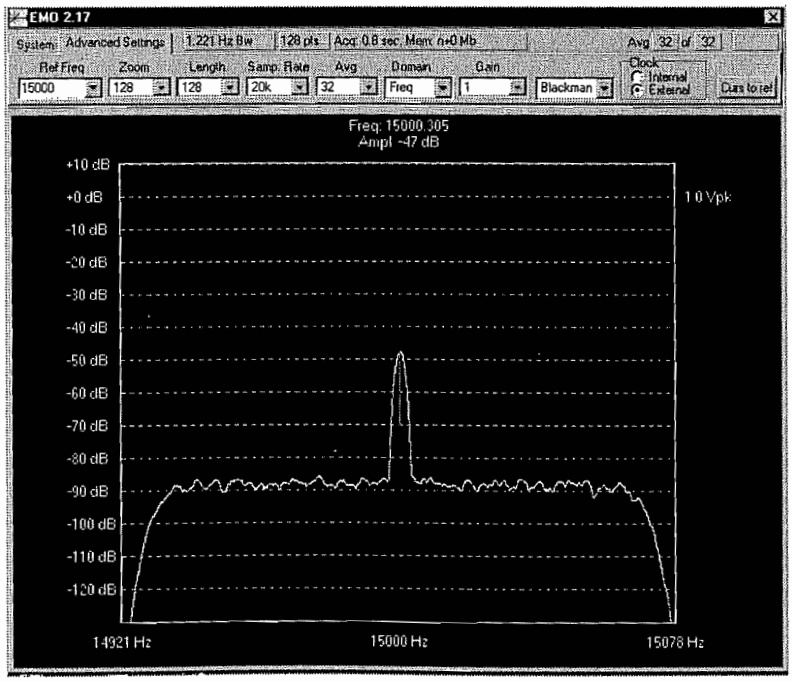

Figure 2.2.16 Results for an YAGI array driven at 50W, 144.01MHz at a distance of 1.2m from the fibre.

Using this apparatus, it was also possible to measure the variation in the observed signal, as a function of the distance between the dipole and the optical fibre. This was done using the standard electric dipole. This dipole was driven with 50W at 144.01Mhz and held at varying distances from the optical fibre. The amplitude of the observed Faraday induced modulation was then measured as previously described. Fig 2.2.17 shows the relative response of the system as a function of the dipole -> cable separation.

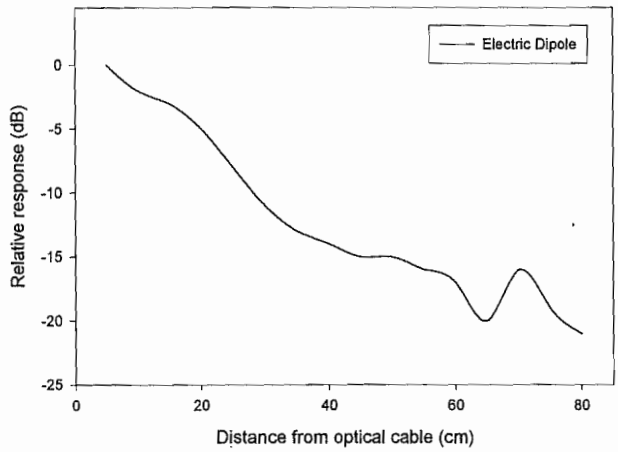

Figure 2.2.17 Variation in the observed Faraday induced signal amplitude as a function of the distance between the dipole and the optical cable.

As expected, the amplitude of the observed signal reduces as a function of distance. There will therefore be a peak in the observed signal amplitude as the dipole is traversed laterally across the buried location of the fibre. It is believed that the peaks and troughs observed at around 70cm separation are probably due to reflections from the metallic roof interfering with and altering the shape of the magnetic field emitted directly by the dipole.

2.2.5 Field test of Faraday cable location system

In order to determine whether we could observe a Faraday shift in the light guided by a fibre **buried** in the ground, the equipment was tested on an semi-metallic sheathed cable (Lucent RL-Sheath) buried 5ft deep in clay soil. The cable was an active telecoms link, running between Birmingham and Leeds, (both in Alabama, USA). It was predicted that this type of soil would be one of the most lossy types for RF signals and hence, if a signal could be observed in these conditions, the system should work in most other soils or to

greater depths in good conditions. Unfortunately, there were no installed dielectrically-sheathed cables available for testing and so an older RL-sheathed cable was used. This cable is not dielectrically reinforced and has parallel metal wire which act as strength members. It was expected that these conductors would reduce the sensitivity of the system. However, when compared to other conductive sheathed cables this RL-sheath is expected to be the least attenuating. This was predicted from the small amount of metallic strength members and the observed attenuation at 50kHz and 180kHz in previous solenoid based experiments.

The polarised source was coupled into the fibre at the regeneration station in Birmingham, USA. The polarisation-sensitive detection system was placed 50km away, in a regeneration station at Leeds. The signal generator and RF amplifier used to drive the dipole were powered by a portable generator and taken to an approximately midway position, where the fibre could be excited. The fibre was excited with a 50W field generated by a log-periodic, (50MHz-1GHz), dipole driven at 50MHz. The average directive gain of the antenna at was 6dB. The polarisation state of the light was adjusted and a signal was observed. The result is shown in Fig 2.2.18. As can be seen, a signal level of –87dBV was observed with a detection bandwidth of 17mHz.

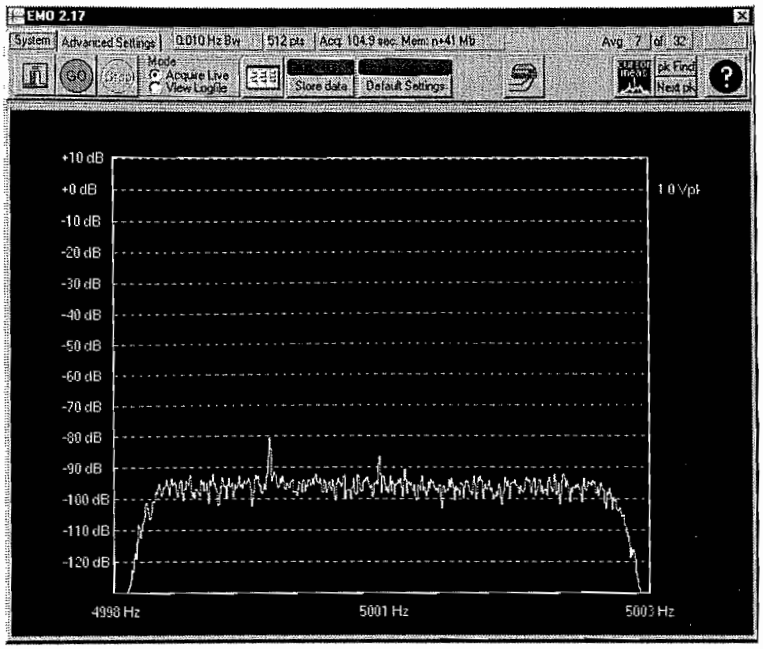

Figure 2.2.18 Signal observed (at 5001Hz) when exciting a semi-metallic RL-sheathed cable with 50MHz RF field. *The cable was buried 5ft deep in clay soil and the dipole used was a log-periodic with a 6dB far field gain driven at 50MHz with 50W. (Please note that the signal at 4999.5Hz is not the optically carried signal. When the dipole is not switched on the 4999.5Hz signal remains but the 5001Hz signal vanshes).*

A signal was observed at –87dBV. In a bandwidth of 1.7mHz this would give a signal / noise of 23dB. This would be enough to locate the cable. Unfortunately, in order for the signal to be observed, we had to reduce the dipole field frequency to 50MHz and use a wideband directed antenna, (log-periodic 6dB gain). This then allowed the magnetic field to penetrate both the soil and partially conducting fibre sheath. This was expected, due to the fact that the soil was predicted to give a high loss and that the conducting sheath of the cable bundle would also attenuate the field reaching the optical fibre within the bundle.

2.2.4 Summary and conclusions

This chapter has dealt extensively with an experimental feasibility study into using the Faraday effect for locating of buried fibre and cables. Firstly, using a simple solenoid around the fibre it was confirmed that, as expected, a single mode fibre could support light with a high degree of polarisation over lengths of up to at least 50km and that modulations in this polarisation state could be induced and effectively transmitted over these distances.

Perhaps the most important confirmation, was that the time-varying magnetic field generated by a standard electric dipole at a distance from the fibre cable could be used to induce a polarisation modulation of the light guided by the fibre.

Several experiments were carried out, in order to investigate the signal / noise ratio generated by several different dipole types at different distances from the fibre. It was found that a useful polarisation modulation could be induced and that, using post-detection filter bandwidths of the order of mHz, signal to noise ratios approaching 60dB could be achieved using a 10dB gain directed antenna at a distance of 1 meter.

This system was field-tested on a 50km length of installed buried RL-sheathed cable. Although not an ideal test situation, due to the conducting cable sheath and clay type soil, we were still able to observe a signal, with a 20dB signal to noise. Although these are very encouraging results, there are several ways in which the system sensitivity could be further increased. This is discussed in the following chapter.

References Chapter 2.2

[2.2.1] J.L.Cruz, M.V.Andres, M.A.Hernandez, "Faraday effect in standard optical fibers: dispersion of the effective Verdet constant", Applied Optics, Vol 35, No 6, pg 922-927, 1996.

[2.2.2] R.Zhanbing, W.Yu, R.Philippe-Alain, Journal of lightwave technology, Vol 7, No 8, 1989.

[2.2.3] A.H.Rose, S.M.Etzel, C.M.Wang, Journal of lightwave technology, Vol 15, No 5, 1997.

[2.2.4] Y.Yamamoto, T.Mukia, S.Saito, "Quantum phase noise and linewidth of semiconductor lasers", Electronics letters, Vol 17, pp-327-329, 1981.

[2.2.5] P.Gallion, G.Degarge, "Quantum phase noise and field correlation in single frequency semiconductor lasers systems," Journal of lightwave technology, Vol QE-20, No 4, April 1984.

Chapter 2.3 Further improvements to the Faraday effect cable location system.

This chapter describes further evolution of the optical arrangement used for the Faraday effect cable location system to improve the signal to noise. In addition, further improvements to the electronic signal conditioning, acquisition and processing electronics are described.

2.3.1 The optical source

The first problem observed in previous experiments, was that over long lengths of optical fibre, (>20km), the line-width of the source was a problem. Frequency fluctuations of the source manifest themselves as polarisation related noise, which exceeds the detector photon-noise and hence reduces the observed signal to noise. It was found that, even using a source of 100kHz line-width, this noise source again became relevant, when using optical fibre lengths of 50km. There is therefore still some room for improvement of the optical system in the choice of source used.

In an attempt to generate a source with a lower phase noise, a 980nm FBG stabilised laser was used to pump an Erbium-doped, distributed feedback (DFB), fibre-Bragg grating (Ionas IW-HP series laser). This gave a laser with a wavelength of 1550.5nm. The pump power could be varied between 1 and 12mW. However, when measuring its phase-noise it was found that it was highly sensitive to acoustic pickup from the laboratory environment, explaining why original tests seemed to show that it degraded the signal to noise of the system more than the Nanotunics alternative source. However, this fibre DFB laser has now been packaged in an acoustically shielded unit, and its –3dBc phase-noise with a 40km delay has been measured to be extremely low at 8kHz. It is expected that this source will improve the observed signal / noise ratios over long lengths of fibre. There is, however, an potential disadvantage in using a source with such a narrow line-width. As the line-width reduces, the threshold for non-linear effects, (particularly stimulated Brillouin), in the optical fibre reduces. As shown in (Fig 2.3.1), the backscattered power from an acoustically shielded 40km section of fibre was measured, as a function of the

launched optical power. This shows that Brillouin scattering becomes relevant when considering launched optical powers of the order of 4mW. Fortunately, we expect to operate at powers of 2mW or so.

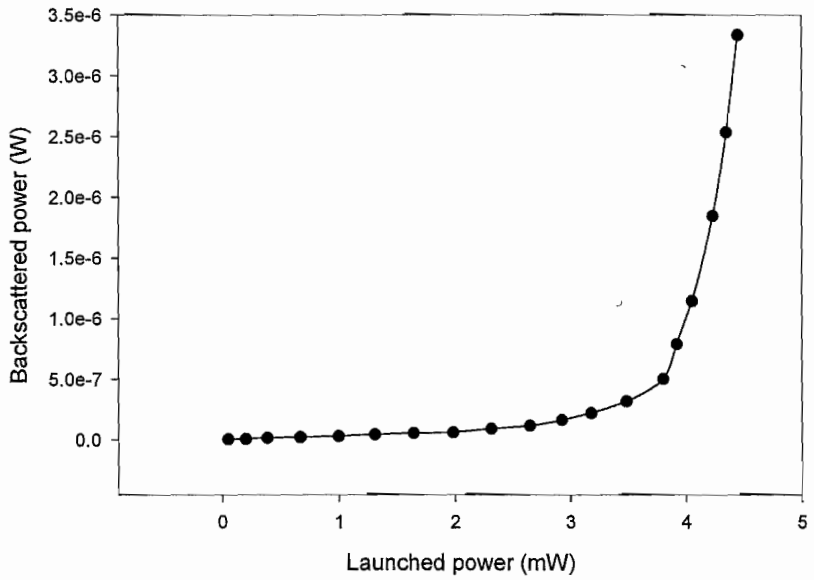

Figure 2.3.1 Back-scattered power as a function of launched power in a 40km length of single mode fibre. *Light was launched from a DFB fibre laser, with an 8kHz line-width, into a 40km length of standard single mode fibre, via a 90/10 coupler. The backscattered power was then measured as a function of the launched optical power.*

2.3.2 Novel optical structures

2.3.2.1 The dual-pass configuration

Until now all the experiments have been carried out using a single pass configuration. Light from a polarised source is launched into a length of fibre. Part way along this length of fibre, a magnetic field induces a time-varying Faraday shift in the SOP of the light guided by the fibre. This light is then detected at the far end of the fibre where the polarisation modulation imparted to the light can be measured, using a narrow bandwidth detection system.

In order to improve this situation, we can as already discussed, decrease the detection bandwidth, or increase the amplitude of the Faraday modulation imparted to the light by

the magnetic field. We now present another novel optical arrangement, which takes advantage of the non-reciprocal nature of the Faraday effect to induce a larger modulation than possible with a single pass system. In this way, we are able to increase the pre-processor signal to noise ratio. Figure 2.3.2 shows a simple optical structure which has the potential to increase the observed signal by up to 6dB.

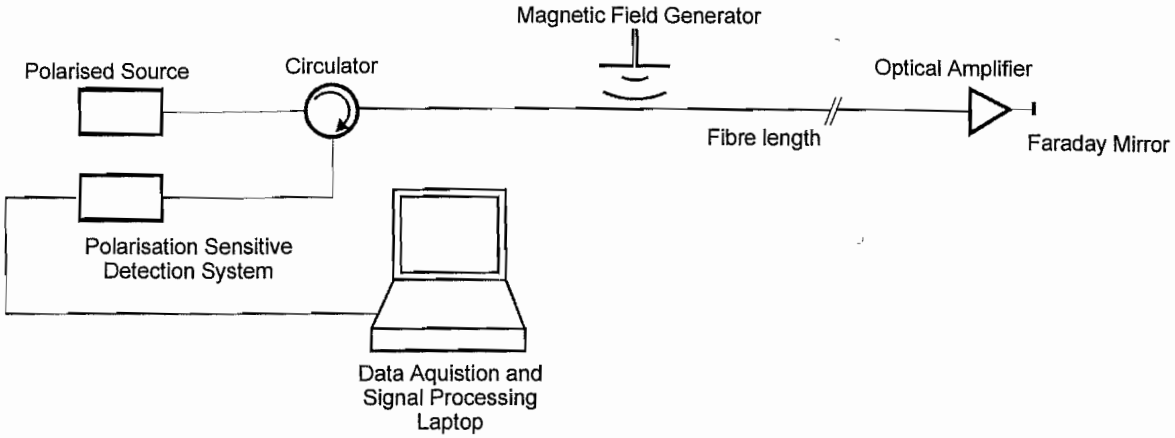

Figure 2.3.2 Dual-pass optical configuration for Faraday effect cable location system. *Light form a polarised source is launched, via a fibre circulator, along a length of single mode fibre. The light propagates along the fibre until, at the far end, it is reflected by a Faraday mirror. This ensures that the polarisation state of the reverse travelling light is the conjugate of the forward travelling light at any given position. The backward travelling light is then detected at the same end of the fibre from which it was launched allowing the polarisation modulation to be observed.*

Light is launched from a polarised source, via a fibre circulator, into a section of standard single mode fibre. The light propagates along this fibre and, part way along its path, is perturbed by the action of a magnetic field. When the light reaches the end of the fibre it is reflected by a Faraday mirror. This device alters the polarisation state of the incident light such that the SOP of the reflected light is always its exact conjugate. By tuning the frequency of the dipole to be resonant with a delay period related to its distance from the end of the fibre, the polarisation modulation induced on the second pass will add in phase with the modulation induced on the first pass. The amplitude of the resulting polarisation modulation is then measured from the same end of the fibre as that from which the light was originally launched. This optical set up was constructed using the fibre across the roof of the building. For convenience, a tuned solenoid was used as the magnetic field generator and was wrapped around the fibre running across the metallic roof. This solenoid was then driven with 10W at 144.01MHz. The induced polarisation modulation was measured, firstly in a single pass configuration and secondly, in the dual pass configuration. In both cases the optical power incident on the detector was adjusted to be

200μW. Also, since we were limited to only a few frequencies at which we were allowed to radiate, the coil had to be moved until it became resonant with its distance from the fibres end, rather than changing the frequency at which it was driven. The results from both tests are shown in figure 2.3.3. As can be seen, by observing the peak amplitude of the detected signal, the dual-pass configuration increases the observed signal from –67dBV by 6dB to give a signal level of –61dBV, as expected. Over longer fibre lengths an optical amplifier would be required to account for the optical loss.

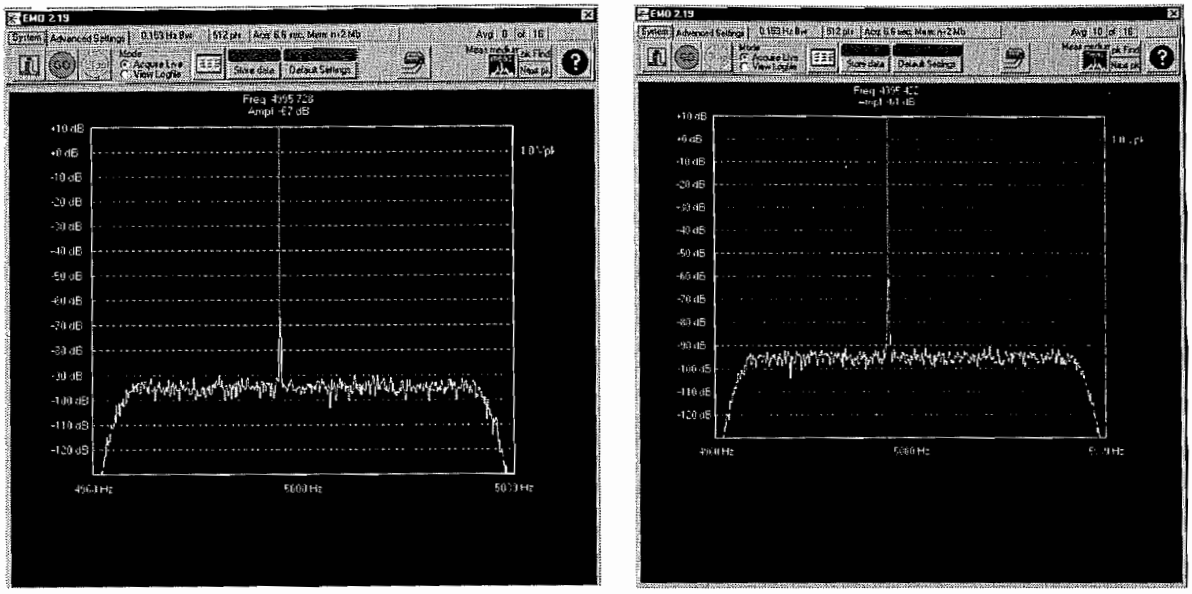

Figure 2.3.3 Experimental results, comparing single pass and dual-pass EMO optical configurations. *The first of the two plots shows the signal generated by a 20 turn Litz wire solenoid driven at 144.01MHz with 10W, using a single pass configuration. The second plot shows the signal generated, using the same magnetic field but using the dual-pass optical configuration. As can be seen there is an increase of 6dB in the observed signal using dual-pass configuration.*

2.3.2.2 The multi-pass configuration

The dual-pass optical system was shown to double the induced polarisation modulation and hence increase the signal to noise ratio of the observed signal by 6dB, within the same detection bandwidth. A further possible improvement to this structure is shown in (Fig 2.3.4). In this system, light is optically switched into the optical fibre to be located. This fibre is then arranged to be a loss less cavity, by inclusion of an amplifier, where the light is left to propagate back and forth up and down the cavity. Each time the light passes the magnetic field modulator, it can be arranged that the modulation imparted to the light coherently adds to that previously induced. In this way, it is expected that the signal to

noise could potentially increase by 20dB after 10 passes, 40db after 100 passes etc. Even over 50km, it takes only 0.05 seconds for light to propagate 100 times past the modulator. To achieve a similar improvement by increasing the averaging time would require 10000 minutes. Obviously this is impractical and would require a frequency standard with a 10^{-17} accuracy, which is not possible at present.

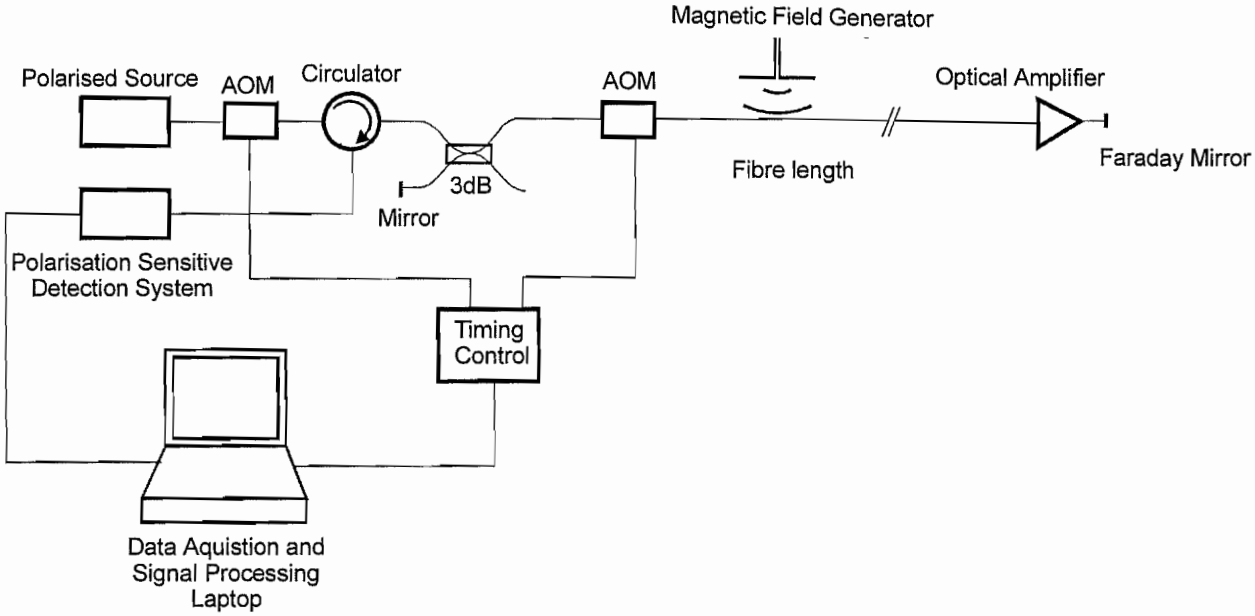

Figure 2.3.4 The multi-pass optical configuration. *Light from a polarised source is switched into an optical cavity. The light then propagates up and down the fibre, each time incurring an increased polarisation modulation when passing the magnetic field modulator. The light is allowed to travel back and forth in the cavity for a fixed time before being switched out and onto a polarisation sensitive detection system where the amplitude of the polarisation state modulation can be measured.*

This optical configuration, has not yet been experimentally demonstrated and there are likely to be a few problems in its implementation. The gain of the amplifier will have to compensate for the loss in the cavity yet keep the net gain just less than 1. Engineering this system is expected to be difficult but not impossible. Also, if the initial optical input powers are high, then non-linearly scattered light may cause a problem when setting the gain of the cavity. However, it may prove possible to reduce these effects by scrambling the coherence of the source using a high-frequency phase modulator.

2.3.3 Improved RF Down-converter system

This section of the improvements were carried out, directly by the industrial sponsors of this work. However, since this equipment will form the basis for future work it is worth describing. In the experiments described in section 2.2.4 another limitation of the detection system used was found, when comparing the noise between the input signal and the sampled IF frequency, there appeared to be an additional noise source. This was found to have been introduced by the local oscillator, synthesised by the communications receiver. A unit was built by our sponsors, and this incorporated several improvements. The most notable, was improved digital-down-conversion and signal-processing software. The communications receiver used in previous experiments was replaced with a custom designed direct-digital-down-converter (DDC). It is expected that this should decrease the system noise by approximately 8dB. Also, the signal processing software was improved. A new FFT algorithm, capable of sampling new data, whilst simultaneously processing and displaying the results was coded. This effectively improves the measurement duty cycle, allowing the theoretical sampling time required for a specific detection bandwidth to be approached. Figure 2.3.5 shows a picture of the improved detection system and signal processing hardware that was built by our sponsors.

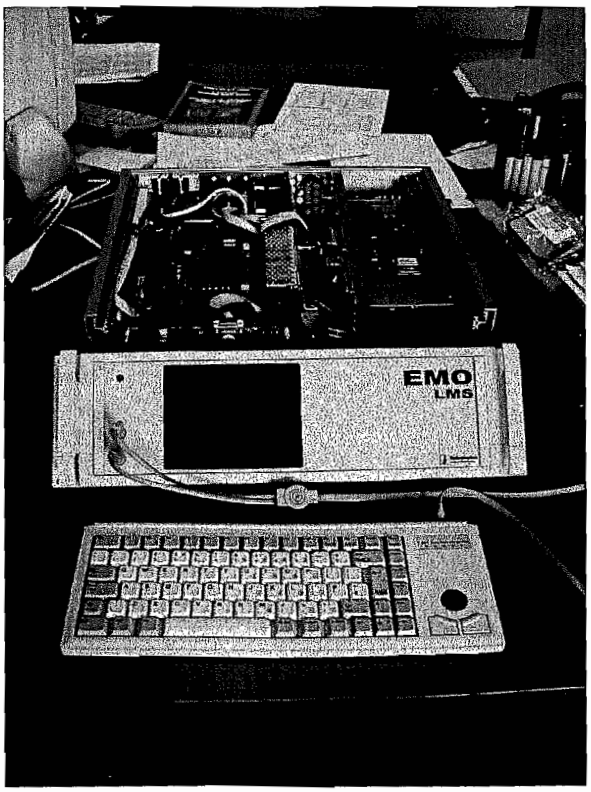

Figure 2.3.5 Improved detection system and signal processing unit, (Built by industrial sponsors). *Shown above is a picture of the improved EMO detection unit, built by the industrial sponsors of the work presented in this thesis. This unit incorporates a DDC unit. The output is then sampled by a PC also included in the unit. The data is then processed and displayed simultaneously on the screen on the front of the unit. A frequency reference is recovered from a GPS signal. This unit also has satellite phone capabilities to communicate with the mobile magnetic field generator.*

2.3.4 Summary and conclusions

We have shown that, although the initial results obtained with the Faraday cable location system have been very encouraging, there are still many improvements possible for this cable location system. The optical source used in previous experiments exhibited a phase noise of approximately 100kHz. Over long lengths of fibre >30km, this phase noise was shown to increase the noise floor of the system above the fundamental photon-noise floor. A new fibre DFB source was constructed and its phase-noise was measured to be as little as 8kHz. Although not yet tested in the actual system over long lengths of cable, it is expected that this new source will improve the signal / noise of the system by at least 6dB. This new source also offers the added advantage of being some 6 times more powerful than the previously used Nanotunics. However, due to the narrow linewidth of these sources, necessary for the experiment, it was shown that we are limited to optical powers of less than 4mW before non-linear optical effects, such as stimulated-Brillouin become a problem.

Perhaps the most valuable improvement is an improved optical arrangement that takes advantage of the non-reciprocal nature of the Faraday effect. At the far end of the fibre the light is no longer detected but reflected back down the same fibre from which it came. In this way, with correct choice of EM-field frequency, the induced Faraday modulation can be coherently doubled. This may then be detected from the same end from which it was launched by virtue of a circulator. This system was demonstrated in laboratory and shown to give the expected 6dB increase in signal / noise. A second improvement to this optical arrangement was then discussed, whereby the fibre route is arranged to be a virtually loss less cavity. The light is then left in the cavity, travelling back and forth, past the magnetic field generator. After a set time the light could be optically switched out of the cavity and the modulation induced by the magnetic field measured. This system has the potential to significantly increase the signal / noise of the resulting cable location system. Although this has not yet been demonstrated experimentally it is a topic suitable for further work.

Finally, another limitation of the system was the noise figure of the down-converting electronics. In the original laboratory set-up the induced polarisation modulation at 144MHz was detected and then down converted to 455kHz to allow it to be sampled by a

PC. It was latter found that this down conversion raised the noise floor by approximately 6dB. However, this did not become apparent for quite some time due to the fact that the IF section of the down-converting electronics had an integral AGC amplifier that continuously normalised the noise floor. An improved digital-down-converter, (DDC), has been built by the industrial sponsors of the project, which it is expected to improve the signal / noise ratio of the system by approximately 6dB. With these improvements, a cable location system using a dual-pass optical configuration, is expected to have an improved signal / noise of 18dB. This is quite a significant improvement that would mean that on the previously field-tested cable running between Birmingham and Leeds (USA) we expect to see a signal / noise ratio of 41dB within a minutes averaging time. This would easily allow cable location.

Chapter 2.4 Conclusions and Further Work

The work presented in the second section of this thesis has been involved with the research and development of a novel cable location system. Cable location systems in use today can, in general only locate cables with a conducting sheath. However, these conducting sheaths make the fibre cables, expensive, difficult to install and vulnerable to damage caused by lightning strike. Network operators therefore wish to install new, cheaper, cables that use a dielectric strengthening sheath, such as Kevlar. Such cables will have a greatly reduced risk of damage from lightning strike, making the resulting telecoms network much more robust and reduce the operational costs, by virtue of lower installation, maintenance and repair costs. The one disadvantage of using such cables is that they render the present location technology ineffective.

Since cable operators have to locate their cables almost on a daily basis, such a disadvantage would greatly increase the operational cost, due to the fact that the cable would have to be physically dug up to find its position. This work has investigated the possibility of locating the buried position of a buried cable using the Faraday effect.

A magnetic field, generated above ground, above the cable, radiates through the ground where it modulates the SOP of the light guided by the fibre. This modulation can then be measured at the far end of the cable and the results relayed to the operator of the magnetic field generator. The position of the buried cable can then be inferred by observing the peak in the detected response as the magnetic field generator is traversed laterally over the buried position of the cable bundle.

This problem was first investigated theoretically. In order for a magnetic field to induced a Faraday modulation its line integral along the lights path must be non-zero. It was found that although the solenoid did not meet these criteria (unless the fibre passed along its axis) the electric dipole did. The magnetic field generated by a dipole was shown to exhibit a non-zero line integral along a path perpendicular to its direction. However, there was an added complication. Since both the field and the position of a photon travelling along the fibre are time varying, the field at any given instant in time, as a function of distance, is not the field observed by the photon as it propagates along the fibre. The field

"observed" by the photon was therefore calculated and it was shown that despite this modification to the field the line integral did not vanish. However, it was shown that as the wavelength of the EM-radiation generated by the dipole becomes of the order of the dipole-cable separation then the line integral could be reduced, leading to a reduced sensitivity of the polarised light to the field. The response of the system was then modelled and it was found that a signal / noise ratio of the order of 35dB could be expected for a normal electric dipole held 1m from the fibre, in air.

The feasibility of such a cable location system was then investigated experimentally. Firstly the ability of a normal single mode fibre to support a polarised mode over several tens of kilometres, and for this mode to carry a tiny polarisation modulation was investigated. Using a simple optical arrangement and a solenoid, wrapped around the cable, as a magnetic field generator several active cables were tested. These results showed that the Faraday modulation induced by the solenoid could be detected at the far end of the fibre (50km) with very little degradation in the observed signal / noise when compared to laboratory results over short fibre lengths (200m).

The ability for the magnetic field generated by a dipole to induce a Faraday modulation was then investigated. We initially found that a half-wave balanced electric dipole driven with 50W at 144.01MHz, held 15cm from a Kevlar sheathed cable induced a Faraday modulation in the SOP of the light guided by the fibre. When, photon-noise limited and detected in a 3Hz bandwidth this gave a 7dB signal / noise ratio. Improvements to this initial laboratory set up were then developed. An ultra-narrow bandwidth detection system was constructed. This consisted of an RF-down-converter which converted the detected signal at 144MHz to 455kHz, allowing it to be sampled by a PC. Using digital signal processing we were then able to generate a frequency spectra of the detected signal with a minimum noise effective bandwidth of 1mHz. To achieve these bandwidths both the signal generator driving the RF amplifier for the dipole and the detection system had to be locked to separate Rubidium standards (frequency accuracy of 10^{-13} over a time of 1 minute). Using this improved detection system several antenna types were investigated at varying distances from the fibre. It was found that as expected the amplitude of the induced polarisation modulation reduced as the dipole was moved further from the cable. The initial results also highlighted some drawbacks of the optical system. It was found that phase-noise of the optical signal generated by the source was being converted to

polarisation noise at the polarisation-sensitive detection system. An improved narrow-linewidth laser was used and shown to give a signal / noise improvement of 12dB over a 200m length of fibre. The results obtained in laboratory conditions showed that using a standard electric dipole, (driven at 50W and 144MHz), a signal / noise of 33dB was achieved at a distance of 1.2m in a 2.8mHz detection bandwidth. It was shown however, that directive gain antennae could be used to increase the induced polarisation modulation. A 12 element, 10dB far field gain YAGI array was shown to give a signal / noise of 63dB (an increase of 30dB) again at a distance of 1.2m in a detection, bandwidth of 2.8mHz. For a full listing of the results of these experiments please see table 2.2.2. It is not yet well understood why directed antennas improve the observed signal / noise as much as they do, as they are difficult to model in the near field. However, the investigation of multiple antennae and phased arrays is worth noting and should be considered for further work.

This system was then field tested on a 50km length of RL-sheathed fibre cable buried 5ft deep in clay soil. Using a 6dB gain log-periodic (50MHz-1GHz) array to modulate the SOP of the light guided by this fibre a signal was observed with a signal to noise of 23dB in a 2.8mHz detection bandwidth. However, since RL-sheathed cable is a partially metallic cable we expect that when tested on Kevlar cables that this signal / noise will be increased. Also the soil type, clay, was also expected to be one of the most attenuating soil types due to its high water content and high density. Several further improvements to the system were then introduced. Including the demonstration of a novel dual-pass optical configuration which doubles the induced polarisation modulation and hence increases the signal / noise by 6dB. We also discussed a multi-pass system which has the potential to increase the systems sensitivity by several tens of dBs. A final note is that the possibility of determining the depth of the cable by relating the observed signal from two dipoles a known distance apart should also be investigated as part of the further work.

In conclusion we have shown that the Faraday effect and the EM-field generated by an electric dipole (50W at 144MHz) can be used to induce a modulation in the SOP of light guided by a fibre and has a definite potential for the location of buried cables. With further improvements, waiting to be experimentally confirmed it should be possible to construct a cable location system with a signal / noise ratio of 40dB through 5ft of clay soil with only 1 minute sampling and cable positioning times.

Appendix 1 Derivation of demodulation terms

This Appendix will derive the separate frequency components present in the detected signal for the dual wavelength Sagnac interferometer. These frequency components are the demodulation terms for a dual wavelength interferometer.

If we consider the following set-up.

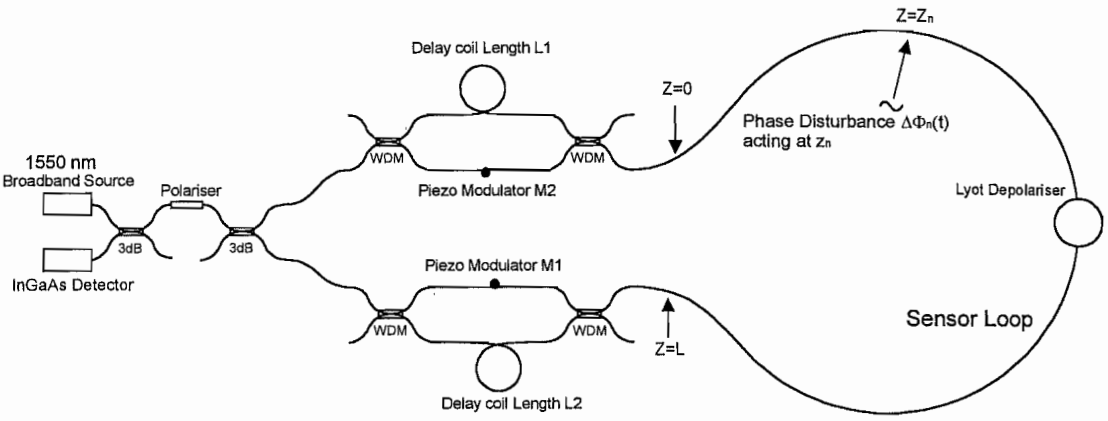

Figure Appendix 2.1 The dual wavelength Sagnac Interferometer. *Each Sagnac interferometer is formed by paths defined by the WDMs. The dual wavelength Sagnac interferometers formed are phase biased by Piezo modulators m_1 and m_2. The sensor loop for each interferometer is also offset by a delay loop of length L_1 and L_2 respectively.*

1 Assume tone modulations

i.e. $\Phi_{m1}(t,\lambda) = \beta_{m1}(\lambda) \cdot \cos(\omega_1 t)$ and

$\Phi_{m2}(t, \lambda) = \beta_{m2}(\lambda) \cdot \cos(\omega_2 t)$

It can therefore be shown, as presented in chapter 3 that the intensity received at the detector of the Saganc interferometer varies with time in the following manner.

DC Component
$$I = I_0\left[T_1^4(\lambda)+T_2^4(\lambda)+2T_1^2(\lambda)T_2^2(\lambda)+T_1^2(\lambda)T_2^2(\lambda)\cos\left(\sum_n \Delta\phi_{n00}\right)+\right.$$

Signal 1
$$T_1^4(\lambda)\cdot\cos\left[\beta_{m1}(\lambda)\left\{\cos(\omega_{m1}t)-\cos\left(\omega_{m1}\left(t-\frac{n}{c}(L+L_1)\right)\right)\right\}+\sum_n \Delta\phi_{n1}\right]$$

Signal 2
$$T_2^4(\lambda)\cdot\cos\left[\beta_{m2}(\lambda)\left\{\cos\left(\omega_{m2}\left(t-\frac{n}{c}(L+L_2)\right)\right)-\cos(\omega_{m2}t)\right\}+\sum_n \Delta\phi_{n2}\right]$$

Cross-talk Term

$$T_1^2(\lambda)T_2^2(\lambda)\cdot\cos\left[\beta_{m1}(\lambda)\left(\cos(\omega_{m1}t)-\cos\left(\omega_{m1}\left(t-\frac{n}{c}(L_1)\right)\right)\right)+\beta_{m2}(\lambda)\left(\cos\left(\omega_{m2}\left(t-\frac{n}{c}(L_1)\right)\right)-\cos\omega_{m2}t\right)+\sum_n\Delta\phi_{n11}\right]$$

[A3.1]

Firstly consider the signal terms separately

Defining the time delays $T_n = nL_n/c$, the first signal term becomes.

$$T_1^4(\lambda)\cdot\cos\left[\left\{\beta_{m1}(\lambda)\cdot\left(\cos\omega_1 t-\cos\omega_1(t-(T_L+T_2))\right)\right\}+\sum_n\Delta\phi_{n1}(t)\right] \qquad [A3.2]$$

Using Cos(A-B) - Cos(A+B) = 2sinAsinB we can simplify equation A.2

$$T_1^4(\lambda)\cdot\cos\left[2\cdot\beta_{m1}(\lambda)\cdot\sin\left(\omega_1\left(t-\frac{T_L+T_2}{2}\right)\right)\sin\left(-\frac{\omega_1}{2}\cdot(T_L+T_2)\right)+\sum_n\Delta\phi_{n1}(t)\right] \qquad [A3.3]$$

Introducing the following constants. Then we get

$$a_1=-2\sin\omega_1\left(\frac{T_L+T_2}{2}\right)\qquad\theta_1=\frac{\omega_1}{2}\cdot(T_L+T_2)\qquad\psi_1=\omega_1\cdot t-\theta_1$$

So this now becomes

$$T_1^4(\lambda)\cdot\cos\left[\beta_{m1}(\lambda)\cdot a_1\sin(\psi_1)+\sum_n\Delta\phi_{n1}(t)\right] \qquad [A3.4]$$

Now using cos(A+B) = cosAcosB - sinAsinB, equation A.4 becomes

$$T_1^4(\lambda)\cdot\left[\cos(\beta_{m1}(\lambda)a_1\sin\psi_1)\cos\left(\sum_n\Delta\phi_{n1}(t)\right)-\sin(\beta_{m1}(\lambda)a_1\sin\psi_1)\sin\left(\sum_n\Delta\phi_{n1}(t)\right)\right] \qquad [A3.5]$$

In order to further simplify this equation we must use a mathematical expansion known as the Jacobian expansion. Defined as

$$\cos(x\sin\omega)=J_0(x)+2\sum_{n=1}^{\infty}J_{2n}(x)\cdot\cos(2n\omega)$$

$$\sin(x\sin\omega)=2\sum_{n=1}^{\infty}J_{2n-1}(x)\sin((2n-1)\omega)$$

Applying these expansions and taking terms only in ψ_1 and $2\psi_1$ then we get

terms in ψ_1 : $-2T_1^4(\lambda)\cdot J_1(\beta_{m1}(\lambda)a_1)\sin(\psi_1)\sin\left(\sum_n\Delta\phi_{n1}(t)\right)$

terms in $2\psi_1$: $2T_1^4(\lambda)\cdot J_2(\beta_{m1}(\lambda)a_1)\cos(2\psi_1)\cos\left(\sum_n\Delta\phi_{n1}(t)\right)$

Similarly following the same procedure for the second signal term, then defining the constants

$$a_2 = 2\sin\left(\omega_2 \cdot \frac{(T_1 + T_L)}{2}\right) \quad \theta_2 = \frac{\omega_{21}}{2} \cdot (T_L + T_1) \quad \psi_{21} = \omega_2 \cdot t - \theta_2$$

Then we get the terms as follows.

$$\psi_2 = -2T_2^4(\lambda) \cdot J_1(\beta_{m2}(\lambda)a_2) \cdot \sin(\psi_2) \cdot \sin\left(\sum_n \Delta\phi_{n2}(t)\right)$$

$$2\Psi_2 = 2T_2^4(\lambda) \cdot J_2(\beta_{m2}(\lambda)a_2) \cdot \cos(2\psi_2) \cdot \cos\left(\sum_n \Delta\phi_{n2}(t)\right)$$

The crosstalk term is more complicated.

Again assuming tone modulations then substituting in we get.

$$T_1^2(\lambda)T_2^2(\lambda)\cos\left[\beta_{m1}(\lambda)\{\cos(\omega_1 \cdot t) - \cos(\omega_1 \cdot (t - T_L))\} + \beta_{m2}(\lambda)\{\cos(\omega_2 \cdot (t - T_L)) - \cos(\omega_2 \cdot t)\} + \sum_n \Delta\phi_{n11}(t)\right]$$

Using the difference relation cos(A-B) - cos(A+B) = 2sinAsinB on the two difference terms within this equation we get

$$T_1^2(\lambda)T_2^2(\lambda)\cos\left[2\beta_{m1}(\lambda)\sin\left(\omega_1 \cdot \left(t - \frac{T_L}{2}\right)\right)\sin\left(-\frac{\omega_1 \cdot T_L}{2}\right) + 2\beta_{m2}(\lambda)\sin\left(\omega_2 \cdot \left(t - \frac{T_L}{2}\right)\right)\sin\left(\frac{\omega_2 \cdot T_L}{2}\right) + \sum_n \Delta\phi_{n11}(t)\right]$$

defining constants

$$a_{1c} = -\sin\left(\omega_1 \frac{T_L}{2}\right), \quad \theta_{1c} = \omega_1 \frac{T_L}{2}, \quad \psi_{1c} = \omega_1 t - \theta_{1c}.$$

$$a_{2c} = -\sin\left(\omega_2 \frac{T_L}{2}\right), \quad \theta_{2c} = \omega_2 \frac{T_L}{2}, \quad \psi_{2c} = \omega_2 t - \theta_{2c}$$

The previous equation then becomes

$$T_1^2(\lambda)T_2^2(\lambda) \cdot \cos\left[a_{1c}\beta_{m1}(\lambda)\sin\psi_{1c} + a_{2c}\beta_{m2}(\lambda)\sin\psi_{2c} + \sum_n \Delta\phi_{n11}(t)\right]$$

[A3.6]

Now using cos(A+B) = cosAcosB - sinAsinB then equation 7 becomes

$$T_1^2(\lambda)T_2^2(\lambda)\left[\cos(a_{1c}\beta_{m1}(\lambda)\sin\psi_{1c} + a_{2c}\beta_{m2}(\lambda)\sin\psi_{2c})\cos\left(\sum_n \Delta\phi_{n11}(t)\right) - \sin(a_{1c}\beta_{m1}(\lambda)\sin\psi_{1c} + a_{2c}\beta_{m2}(\lambda)\sin\psi_{2c})\sin\left(\sum_n \Delta\phi_{n11}(t)\right)\right]$$

[A3.7]

Further simplifying with the identities cos(A+B) = cosAcosB - sinAsinB

sin(A+B) = sinAcosB + cosAsinB

Then equation A.7 becomes:

$$T_1^2(\lambda)T_2^2(\lambda)\begin{bmatrix}\cos(a_{1c}\beta_{m1}\sin\psi_{1c})\cos(a_{2c}\beta_{m2}\sin\psi_{2c})\cos\left(\sum_n\Delta\phi_{n11}(t)\right)-\sin(a_{1c}\beta_{m1}\sin\psi_{1c})\sin(a_{2c}\beta_{m2}\sin\psi_{2c})\cos\left(\sum_n\Delta\phi_{n11}(t)\right)\\-\sin(a_{1c}\beta_{m1}\sin\psi_{1c})\cos(a_{2c}\beta_{m2}\sin\psi_{2c})\sin\left(\sum_n\Delta\phi_{n11}(t)\right)+\cos(a_{1c}\beta_{m1}\sin\psi_{1c})\sin(a_{2c}\beta_{m2}\sin\psi_{2c})\sin\left(\sum_n\Delta\phi_{n11}(t)\right)\end{bmatrix}$$

Cross-talk terms in;

$$\psi_{1c} = -2T_1^2(\lambda)T_2^2(\lambda)J_0(a_{2c}\beta_{m2})J_1(a_{1c}\beta_{m1})\sin\psi_{1c}\sin\left(\sum_n\Delta\phi_{n11}(t)\right)$$

$$2\psi_{1c} = 2T_1^2(\lambda)T_2^2(\lambda)J_0(a_{2c}\beta_{m2})J_2(a_{1c}\beta_{m1})\cos 2\psi_{1c}\cos\left(\sum_n\Delta\phi_{n11}(t)\right)$$

$$\psi_{2c} = -2T_1^2(\lambda)T_2^2(\lambda)J_0(a_{1c}\beta_{m1})J_1(a_{2c}\beta_{m2})\sin\psi_{2c}\sin\left(\sum_n\Delta\phi_{n11}(t)\right)$$

$$2\psi_{2c} = 2T_1^2(\lambda)T_2^2(\lambda)J_0(a_{1c}\beta_{m1})J_2(a_{2c}\beta_{m2})\cos 2\psi_{2c}\cos\left(\sum_n\Delta\phi_{n11}(t)\right)$$

Collecting terms we get the following for the demodulated signals:

Demod f1 $-2T_1^4(\lambda)\cdot J_1(\beta_{m1}a_1)\sin(\psi_1)\sin\left(\sum_n\Delta\phi_{n1}(t)\right)-2T_1^2(\lambda)T_2^2(\lambda)J_0(a_{2c}\beta_{m2})J_1(a_{1c}\beta_{m1})\sin\psi_{1c}\sin\left(\sum_n\Delta\phi_{n11}(t)\right)$

Demod 2f1 $2T_1^4(\lambda)\cdot J_2(\beta_{m1}a_1)\cos(2\psi_1)\cos\left(\sum_n\Delta\phi_{n1}(t)\right)+2T_1^2(\lambda)T_2^2(\lambda)J_0(a_{2c}\beta_{m2})J_2(a_{1c}\beta_{m1})\cos 2\psi_{1c}\cos\left(\sum_n\Delta\phi_{n11}(t)\right)$

Demod f2 $-2T_2^4(\lambda)\cdot J_1(\beta_{m2}a_2)\cdot\sin(\psi_2)\cdot\sin\left(\sum_n\Delta\phi_{n2}(t)\right)-2T_1^2(\lambda)T_2^2(\lambda)J_0(a_{1c}\beta_{m1})J_1(a_{2c}\beta_{m2})\sin\psi_{2c}\sin\left(\sum_n\Delta\phi_{n11}(t)\right)$

Demod 2f2 $2T_2^4(\lambda)\cdot J_2(\beta_{m2}a_2)\cdot\cos(2\psi_2)\cdot\cos\left(\sum_n\Delta\phi_{n2}(t)\right)+2T_1^2(\lambda)T_2^2(\lambda)J_0(a_{1c}\beta_{m1})J_2(a_{2c}\beta_{m2})\cos 2\psi_{2c}\cos\left(\sum_n\Delta\phi_{n11}(t)\right)$

Appendix 2 The Lyot Depolariser

This appendix describes the operation of a device known as the Lyot depolariser. Such a device rapidly scrambles the polarisation azimuth of the incident light in the wavelength domain. If a polarised broadband source is incident on such a device the net effect is an output beam of light with an average polarisation state of r = 0, completely depolarised.

Birefringence, the retarder

A birefringent fibre has two optical axes, oriented perpendicularly to each other. Each of which has a different refractive index. Along the "fast axis" the light "sees" the lowest refractive index n_{min}, and along the "slow" axis the larger index, n_{max}. Light which is incident on such a fibre with a linear polarisation state parallel to one of these axes is unaffected. However, if light is incident with its polarisation azimuth at an angle θ relative to one of the optical axes then a polarisation mode with be excited along both optical axes. Due to the fact that light propagates along each of the axes at different velocities, a phase shift δ will occur between these two modes. Where;

$$\delta = \left(\frac{2\pi n_{\max}}{\lambda} - \frac{2\pi n_{\min}}{\lambda} \right) l \qquad \text{[A2.1]}$$

λ = The wavelength of the light, l is the propagation length

The Jones matrix which represents the two rectangular electric field components of the excited polarisation modes along each axis is,

$$\boldsymbol{J} = \begin{pmatrix} \sin\theta e^{j\frac{\delta}{2}} \\ \sin\theta e^{j\frac{\delta}{2}} \end{pmatrix} \qquad \text{[A2.2]}$$

Where we have assumed that the co-ordinate axis' co-inside with the optical axis of the birefringent fibre.

When recombined the polarisation state of the resulting beam may not be a simple linear state. For example if the light is launched with its polarisation azimuth at θ = π/4 to the

fast optical axes then after a propagation distance equivalent to a phase shift of $\delta = \pi/2$, we get circularly polarised light and for $\delta = \pi$ we get linear again but rotated through 180°.

The length corresponding to a phase shift of $\delta = 2\pi$ is called the beat length of the fibre and defined as, $l_b = \dfrac{\lambda}{n_{\max} - n_{\min}}$.

Depolarisation of a broadband source

Depolarisation of a source maybe achieved by launching light into a high-birefringent fibre from a broad range of angles. For each angle a different output polarisation state will be achieved. If the source spectrum is broad then for each wavelength the path length will also change through the retarder, also altering the output polarisation state.

If the source spectrum varies from λ_{min} to λ_{max} then it may be shown that the range of relative phase shifts that occur through a retarder of length l is,

$$\delta_{\max} = \frac{2\pi l(n_{\max} - n_{\min})}{\lambda_{\min}} \quad \text{and} \quad \delta_{\min} = \frac{2\pi l(n_{\max} - n_{\min})}{\lambda_{\max}} \qquad \text{[A2.3]}$$

Defining the beat length l_{b0} of the retarder at the central wavelength λ_0, and the relative wavelengths $\lambda_{r\_min} = \lambda_{max}/\lambda_0$ and $\lambda_{r\_max} = \lambda_{min}/\lambda_0$. Then we may define,

$$\Delta\delta = 2\pi \frac{1}{l_{b0}} \left(\frac{1}{\lambda_{r\_\min}} - \frac{1}{\lambda_{r\_\max}} \right) \qquad \text{[A2.4]}$$

If the range of relative phase shifts is greater than 2π then a unique polarisation state exists for the light at each wavelength between λ_{min} and λ_{max}. However, since in the Sagnac interferometer we do not know the initial polarisation state, we cannot ensure complete depolarisation of the source, using only a single retarder. A second high birefringent fibre is therefore included, orientated at 45 degrees relative to the first. This is shown in figure appendix 1.1. It is this type of depolariser that is known as the Lyot depolariser.

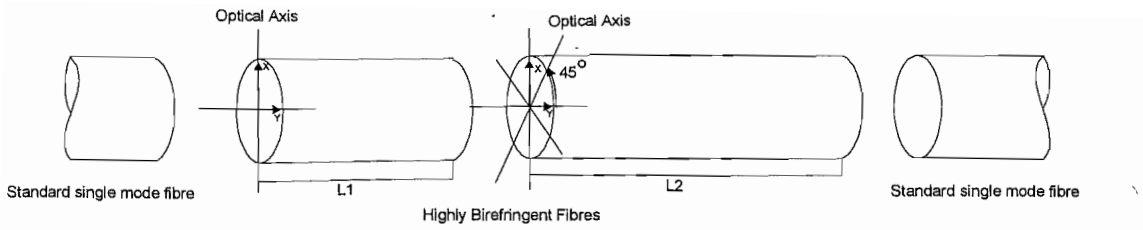

Figure Appendix 1.1 The Lyot Depolariser. *Two highly birefringence fibres orientated with the optical axes at 45 degrees relative to each other.*

In this way if light is incident with a polarisation state parallel to one of the optical axis in the first fibre then it will be unaffected, until it reaches the second fibre. Since this fibre is rotated through 45 degrees the polarisation azimuth of the light will no longer be parallel to the optical axis. The second HI-BI fibre will therefore depolarise the light.

This type of depolariser is only suitable when the source spectrum is "wide" enough to provide a large range of relative phase shifts between the two polarisation modes in the first section of the Lyot depolariser.

In order to understand the operation of such a passive device it is helpful to describe the system in terms of a matrix that describes the propagation of light through the two sections of HI-BI fibre. The Jones matrix **M** gives a relationship between the incident lights electric field vectors and the corresponding output.

I.e.
$$\begin{pmatrix} E_{x1} \\ E_{y1} \end{pmatrix} = \boldsymbol{J}_1 = \boldsymbol{M}\boldsymbol{J}_0 = \boldsymbol{M}\begin{pmatrix} E_{x0} \\ E_{y0} \end{pmatrix} \qquad \text{[A2.5]}$$

E_x and E_y are the electric field amplitudes in the x and y directions.

The Jones matrix that describes a retarder with two optical axes, with refractive indices n_{min} and n_{max} respectively, orientated with its fast optical axes ρ degrees relative to the x co-ordinate axis may be shown to be;

$$\boldsymbol{M}_{\delta}(\rho) = \begin{pmatrix} \cos^2\rho e^{j\delta/2} + \sin^2\rho e^{-j\delta/2} & 2j\sin\rho\cos\rho\sin(\delta/2) \\ 2j\sin\rho\cos\rho\sin(\delta/2) & \cos^2\rho e^{-j\delta/2} + \sin^2\rho e^{j\delta/2} \end{pmatrix} \cdot \exp\left(-j\frac{2\pi}{\lambda}\frac{n_{max}+n_{min}}{2}\right) \qquad \text{[A2.6]}$$

The complete matrix that describe the entire Lyot depolariser is the product of the matrices $\mathbf{M}_{\delta 1}(45°)$ and $\mathbf{M}_{\delta 2}(0°)$.

The Lyot depolariser Jones matrix may therefore be shown to be;

$$\boldsymbol{M}_{Lyot} = \frac{1}{\sqrt{2}}\begin{pmatrix} e^{j\frac{\delta_1+\delta_2}{2}} & e^{j\frac{\delta_1+\delta_2}{2}} \\ e^{-j\frac{\delta_1+\delta_2}{2}} & e^{-j\frac{\delta_1+\delta_2}{2}} \end{pmatrix} \qquad [A2.7]$$

In the case of the Sagnac there is a further effect to consider. The source used is broadband (70nm FWHM), with a central wavelength of 1555nm. However, we use WDM technology to define two separate channels. 1) With a 15nm bandwidth, centred at 1540nm and 2) a 15nm bandwidth centred at 1570nm. We must therefore ensure that the lengths of the highly birefringent fibre in the Lyot depolariser are such that within the range of wavelengths defined by the WDMs for each of the optical channels used, there exists a full range of polarisation modes. If this were not the case then the combined polarisation mode for all the light each of the optical channels would be different. The single mode fibre polariser would therefore "filter" each channel differently, making the interferometer unbalanced, reducing its performance.

If it is ensured that the relative phase shift produced between light of wavelength λ_{min} and that at λ_{max} is $\delta = 10\pi$ then this should be ample to ensure complete depolarisation of the light within the range defined for each optical channel.

Reference

P.R.Cooper, "All fibre Lyot deplosriser" ***Optics and laser technology, vol 18, No 2, April 1986***

N.J.Frigo, A.Dandbridge, A.B.Tveten, "Technique for elimination of polarisation fading in fibre interferometers." ***Electronics letters, April 12 1984, vol 20, No 8, pp 319-320***

Appendix 3 Mathcad Simulation Worksheet

Defining Constants

$L := 40 \cdot 10^3$ Sensor loop length $\quad x = 1.1$ Biasing modulation depth

$L2 := 4 \cdot 10^3$ Delay coil lengths $\quad c = 3 \cdot 10^8$ Speed of light

$L1 := 4 \cdot 10^3$ $\quad n = 1.46$ Refractive index

$h1 = 10$

$h2 := 13$

$\omega mod1 := \frac{2 \cdot \pi \cdot c}{n} \cdot \frac{(2 \cdot h1 + 1)}{2 \cdot (L + L2)}$ Modulation frequency 1 $\quad \frac{\omega mod1}{2 \cdot \pi} = 4.9034869240348691 \cdot 10^4$

$\omega mod2 := \frac{2 \cdot \pi \cdot c}{n} \cdot \frac{(2 \cdot h2 + 1)}{2 \cdot (L + L1)}$ Modulation frequency 2 $\quad \frac{\omega mod2}{2 \cdot \pi} = 6.3044831880448321 \cdot 10^4$

Define the terms that act as disturbances on the loop

Amplitudes $A_0 = 0.2$ $\quad m := 1$

Positions $p_0 := 15 \cdot 10^3$

Phase $\phi_0 := 0$

Frequencies $\omega_0 = 2 \cdot \pi \cdot 100$

$$NOISE1(t) = \sum_{i=0}^{m-1} A_i \cdot \left[\cos\left[\omega_i \cdot \left(t - \frac{n}{c} \cdot p_i \right) + \phi_i \right] - \cos\left[\omega_i \cdot \left[t - \frac{n}{c} \cdot (L + L2 - p_i) \right] + \phi_i \right] \right]$$

$$NOISE2(t) = \sum_{i=0}^{m-1} A_i \cdot \left[\cos\left[\omega_i \cdot \left[t - \frac{n}{c} \cdot (p_i + L1) \right] + \phi_i \right] - \cos\left[\omega_i \cdot \left[t - \frac{n}{c} \cdot (L - p_i) \right] + \phi_i \right] \right]$$

$$NOISE11(t) = \sum_{i=0}^{m-1} A_i \cdot \left[\cos\left[\omega_i \cdot \left(t - \frac{n}{c} \cdot p_i \right) + \phi_i \right] - \cos\left[\omega_i \cdot \left[t - \frac{n}{c} \cdot (L - p_i) \right] + \phi_i \right] \right]$$

$$NOISE00(t) := \sum_{i=0}^{m-1} A_i \cdot \left[\cos\left[\omega_i \cdot \left[t - \frac{n}{c} \cdot (p_i) \right] + \phi_i \right] - \cos\left[\omega_i \cdot \left[t - \frac{n}{c} \cdot (L + L2 + L1 - p_i) \right] + \phi_i \right] \right]$$

Define expected intensity at detector

$$I(t, CT) = \frac{1}{2} + \frac{CT}{8} \cdot \cos((NOISE00(t))) \ldots$$
$$+ \left(\frac{1}{8} + \frac{1 - CT}{8} \right) \cdot \cos\left[\left[\left[x \cdot \cos(\omega mod1 \cdot t) - x \cdot \cos\left[\omega mod1 \cdot \left[t - \frac{n}{c} \cdot (L + L2) \right] \right] \right] + NOISE1(t) \right] \right] \ldots$$
$$+ \left(\frac{1}{8} + \frac{1 - CT}{8} \right) \cdot \cos\left[\left[\left[x \cdot \cos\left[\omega mod2 \cdot \left[t - \frac{n}{c} \cdot (L + L1) \right] \right] - x \cdot \cos(\omega mod2 \cdot t) \right] + NOISE2(t) \right] \right] \ldots$$
$$+ \frac{CT}{8} \cdot \left[\cos\left[\left[x \cdot \cos(\omega mod1 \cdot t) - x \cdot \cos\left[\omega mod1 \cdot \left[t - \frac{n}{c} \cdot (L) \right] \right] \right] + \left[x \cdot \cos\left[\omega mod2 \cdot \left[t - \frac{n}{c} \cdot (L) \right] \right] - x \cdot \cos(\omega mod2 \right. \right. \right.$$

$tmax := 0.0002$ $\quad div = 1000$

$t := 0, \frac{tmax}{div} .. tmax$

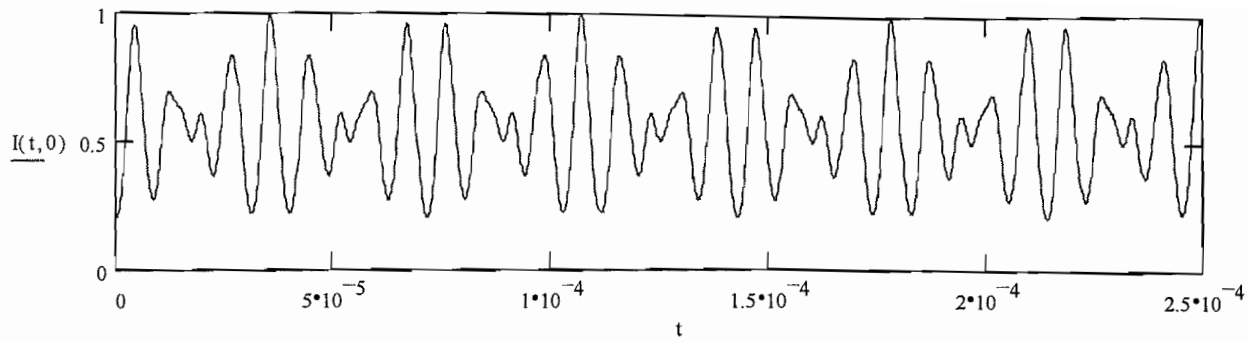

Now we need a procedure to generate a square wave at a certain frequency oscillating between +/- 1.

$$\text{Square}(\text{ang\_freq}, t, \text{phase}) := \left| \begin{array}{l} T \leftarrow \dfrac{2\cdot\pi}{\text{ang\_freq}} \\ t \leftarrow t + \dfrac{T}{360}\cdot\text{phase} \\ \text{no\_periods} \leftarrow \dfrac{t}{T} \\ x \leftarrow \text{no\_periods} - \text{floor}(\text{no\_periods}) \\ -1 \text{ if } 0<x<0.5 \\ 1 \text{ if } 0.5 \le x \le 1 \end{array} \right.$$

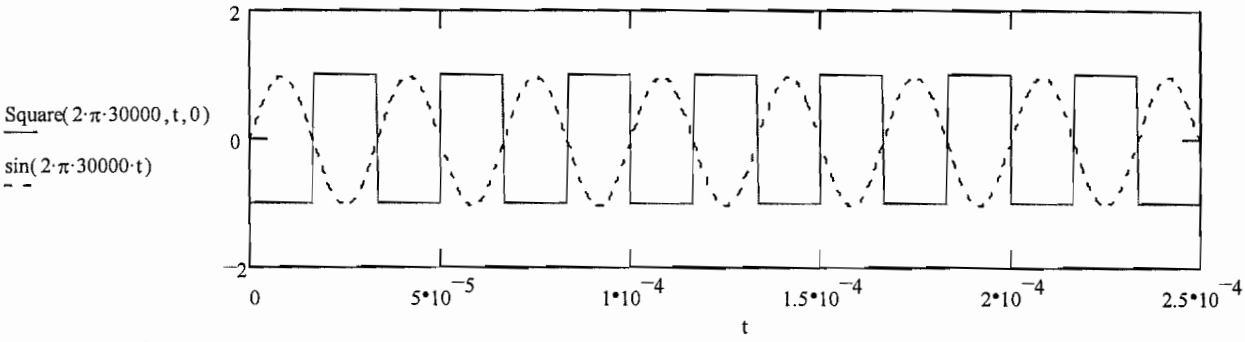

Define Demodulated terms

$\text{demod\_f1}(t, CT) := I(t, CT)\cdot\text{Square}(\omega\text{mod1}, t, 245)$

$\text{demod\_f2}(t, CT) := I(t, CT)\cdot\text{Square}(\omega\text{mod2}, t, 245)$

First need to sample data into arrays

$k := 17$

$\text{no\_data\_points} := 2^k - 1$

$\text{Samples} := \text{no\_data\_points} + 1$

Defines number of data points taken

$\text{smin} := 0 \quad \text{smax} := 0.1$ Sample start and end

$\text{element} := 0..\text{no\_data\_points} \qquad \text{Samples} = 1.3107210^5$

Sample Data into arrays

$$\text{Data\_f1}_{\text{element}} := \text{demod\_f1}\left(\text{element}\cdot\frac{\text{smax} - \text{smin}}{\text{no\_data\_points}}, 0\right)$$

$$\text{Data\_f2}_{\text{element}} := \text{demod\_f2}\left(\text{element}\cdot\frac{\text{smax} - \text{smin}}{\text{no\_data\_points}}, 0\right)$$

Low Pass Filter procedure (filters data with a LP 3dB point of flp)

$$\text{filter}(data, flp) = \left| \begin{array}{l} e \leftarrow 0 \\ j \leftarrow \sqrt{-1} \\ \omega n \leftarrow 2 \cdot \pi \cdot flp \\ \gamma \leftarrow 0.5 \\ \text{for } loop \in 1..\dfrac{no\_data\_points}{2} \\ \quad \left| \begin{array}{l} data\_f_e \leftarrow data_e \cdot \dfrac{\omega n^2}{\left[j \cdot \left(2 \cdot \pi \cdot \dfrac{e}{smax - smin} \right) \right]^2 + 2 \cdot \gamma \cdot \omega n \cdot \left(j \cdot 2 \cdot \pi \cdot \dfrac{e}{smax - smin} \right) + \omega n^2} \\ e \leftarrow e + 1 \end{array} \right. \\ data\_f \end{array} \right.$$

Conversion to and from frequency domain

$$e := 0..\frac{Samples}{2}$$

$$Data\_freq\_f1 := fft(Data\_f1)$$

$$Data\_freq\_f2 := fft(Data\_f2)$$

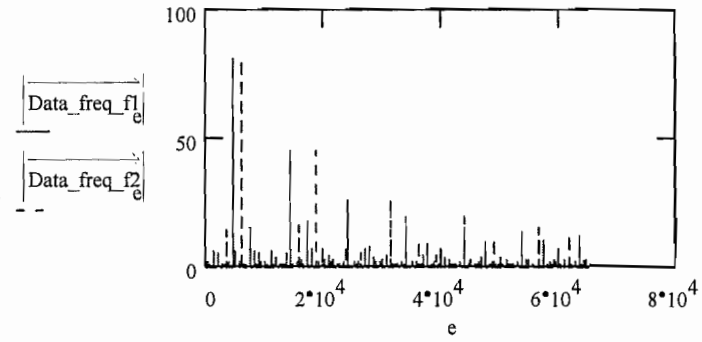

$$Data\_filtered\_f1 := filter(Data\_freq\_f1, 100) \quad Data\_filtered\_f2_{\frac{Samples}{2}} := 0$$

$$Data\_filtered\_f2 := filter(Data\_freq\_f2, 100) \quad Data\_filtered\_f1_{\frac{Samples}{2}} := 0$$

$$Data\_filtered\_time\_f1 := ifft(Data\_filtered\_f1)$$

$$Data\_filtered\_time\_f2 := ifft(Data\_filtered\_f2)$$

$$el := 0..\frac{Samples - 1}{2}$$

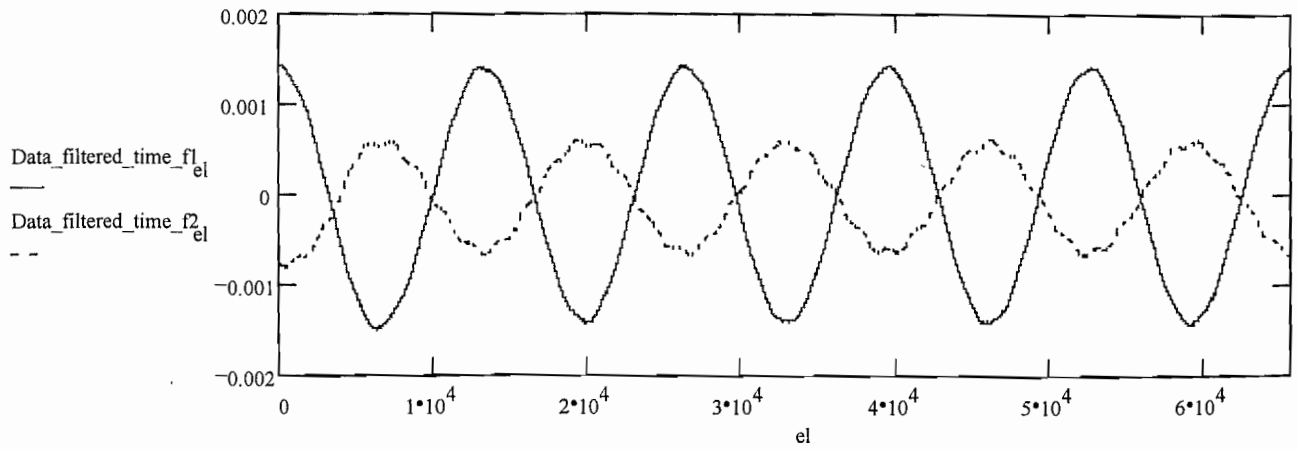

Define estimate ratio

$$ratio_{element} = \frac{Data\_filtered\_time\_f1_{element}}{Data\_filtered\_time\_f2_{element}}$$

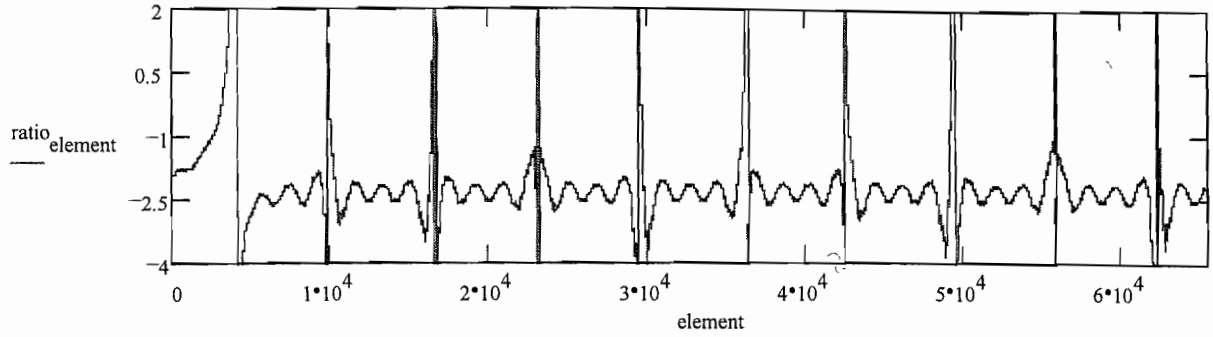

$Data\_filtered\_f2_{\frac{Samples}{2}} := 0$ $Data\_filtered\_2f1_{\frac{Samples}{2}} := 0$ $Data\_filtered\_2f2_{\frac{Samples}{2}} := 0$

$Data\_filtered\_f1_{\frac{Samples}{2}} = 0$

$$Average := \frac{\sum_{n=0}^{Samples-1} ratio_n}{Samples - 1} \qquad Average = -3.441566028121434$$

Note there is also a beat frequency interfering with the results from the f2 term

$a_1 := 2 \cdot \sin\left(\omega mod1 \cdot \frac{n}{c} \cdot \frac{L + L2}{2}\right)$ $a_{11} := -2 \cdot \sin\left(\omega mod1 \cdot \frac{n}{c} \cdot \frac{L}{2}\right)$ $CT := 0$

$a_2 = 2 \cdot \sin\left(\omega mod2 \cdot \frac{n}{c} \cdot \frac{L + L1}{2}\right)$ $a_{21} := 2 \cdot \sin\left(\omega mod2 \cdot \frac{n}{c} \cdot \frac{L}{2}\right)$

Calculate position for each data element

$round(x) := if(x - floor(x) < 0.5, floor(x), ceil(x))$

$$position\_round\_100m_{element} := round\left(\frac{10 \cdot position_{element}}{10^3}\right)$$

$drw(data, size) :=$
- $e \leftarrow 0$
- for $loop \in 0..500$
  - $b_{loop} \leftarrow 0$
- for $loop \in 0..size$
  - $no\_of\_bin \leftarrow data_e$
  - $b_{no\_of\_bin} \leftarrow b_{no\_of\_bin} + 1$ if $0 \le no\_of\_bin \le 500$
  - $e \leftarrow e + 1$
- b

$res := drw(position\_round\_100m, no\_data\_points)$

$range = 0..500$

Positional Histogram

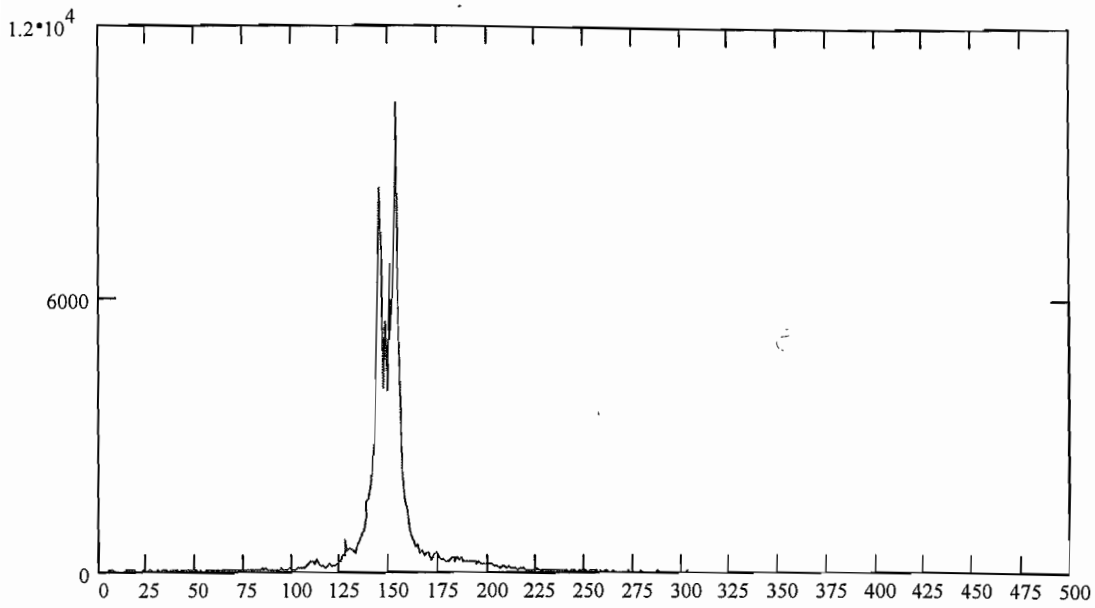
1.2•10^4
6000
0
0 25 50 75 100 125 150 175 200 225 250 275 300 325 350 375 400 425 450 475 500

Appendix 4 Circuit diagrams

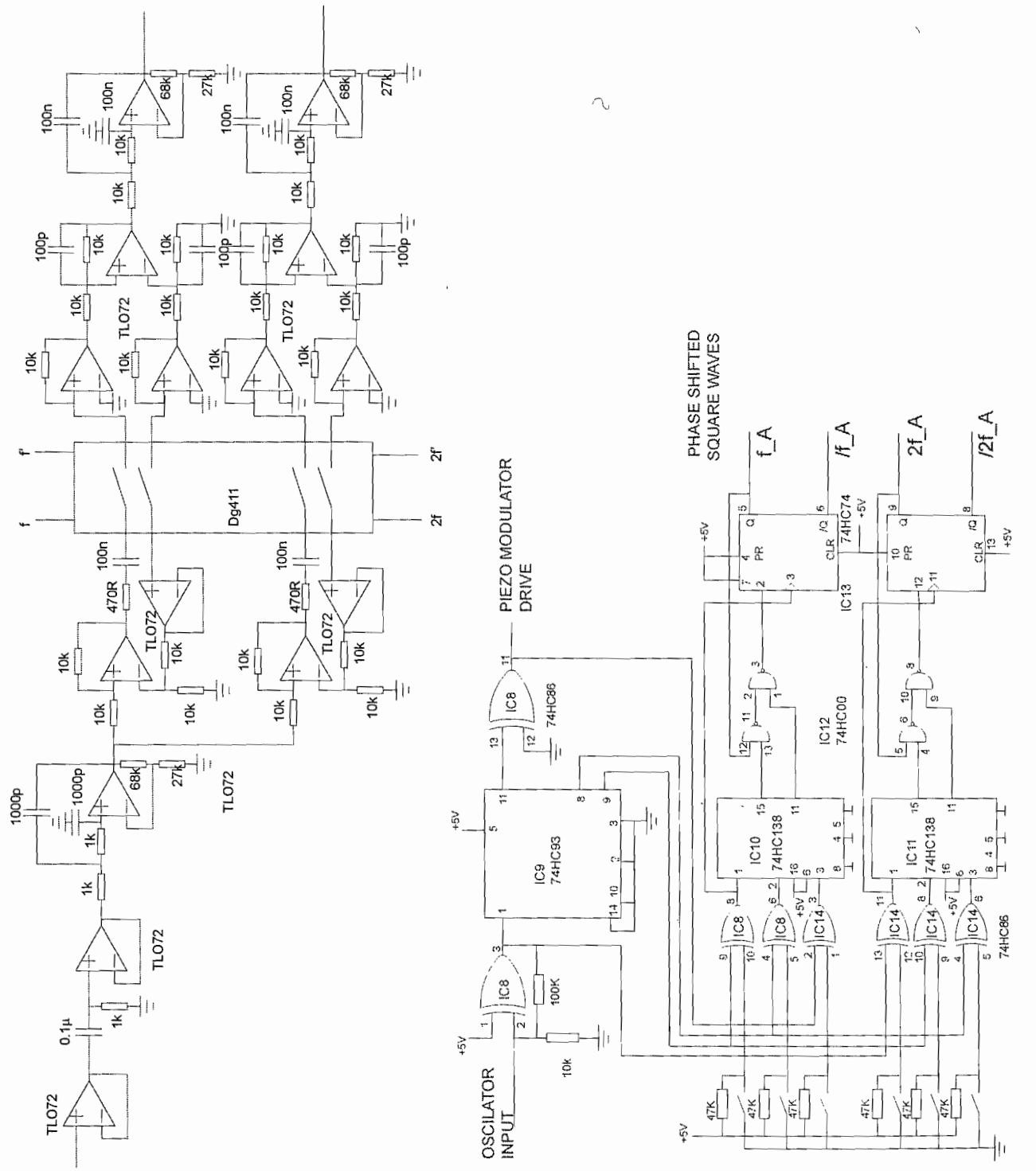

Analogue and digital sections for AM demodulator built for Sagnac system.

Appendix 5 Derivation of magnetic field sensitivity in the presence of birefringence

Assuming that the input SOP of light entering a length of fibre (z) is given by;

$$\begin{bmatrix} Ex(0) \\ Ey(0) \end{bmatrix} = E_0^{\,2} \begin{pmatrix} \sqrt{P} \\ \sqrt{1-P}\exp(j\delta) \end{pmatrix}$$

and that the light emitted from the fibres end is viewed through a polarisation analyser parallel to the x-axis then the change of the emitted light intensity $|E_x(z)|^2$ with respect to the Faraday rotation (F) can be found. Determining the slope (m) of $|E_x(z)|^2$ with respect to F at F = 0, then gives us the relative response of the system to the action of a magnetic field and hence its sensitivity. Using the birefringent Faraday rotation matrix;

$$\begin{bmatrix} \cos\left(\frac{\phi \cdot z}{2}\right) - j\frac{\delta}{\phi}\cos\left(\frac{\phi \cdot z}{2}\right) & -\frac{2F}{\phi}\sin\left(\frac{\phi \cdot z}{2}\right) \\ \frac{2F}{\phi}\sin\left(\frac{\varphi \cdot z}{2}\right) & \cos\left(\frac{\phi \cdot z}{2}\right) + j\frac{\delta}{\phi}\cos\left(\frac{\phi \cdot z}{2}\right) \end{bmatrix}$$

We can see that the emitted electric field component of the light in the x direction relates to the input SOP as below.

$$E_x(z) = \cos\left(\frac{\phi z}{2}\right)E_x(0) - \frac{2F}{\phi}\sin\left(\frac{\phi z}{2}\right)E_y(0) - j\cdot\frac{\Delta\beta}{\phi}\sin\left(\frac{\phi z}{2}\right)E_x(0)$$

The normalised response of the system per unit length is then given by;

$$m = \lim_{F\to 0}\left[\frac{1}{zE_0^{\,2}}\frac{\partial\left|E_x(z)^2\right|}{\partial F}\right]$$

It can be shown that;

$$m = \lim_{F\to 0}\left[\frac{1}{zE_0^{\,2}}\left(-z\sin\left(\frac{\phi z}{2}\right)E_x^{\,2}(0)\frac{\partial\phi}{\partial F} + \frac{4F^2z}{\phi^2}\cos\left(\frac{\phi z}{2}\right)\frac{\partial\phi}{\partial F}E_y^{\,2}(0) + \left(\frac{8F}{\phi^2} - \frac{4F^2}{\phi^3}\right)\sin^2\left(\frac{\phi z}{2}\right)E_y^{\,2}(0)\right.\right.$$

$$-2\frac{\Delta\beta^2}{\phi^3}\frac{\partial\phi}{\partial F}\sin^2\left(\frac{\phi z}{2}\right)E_x^{\,2}(0) + \frac{\Delta\beta^2 z}{\phi^2}\cos^2\left(\frac{\phi z}{2}\right)\frac{\partial\phi}{\partial F} - \left(\frac{2Fz}{\phi}\cos\left(\frac{\phi z}{2}\right)\frac{\partial\phi}{\partial F} + \frac{4}{\phi}\sin\left(\frac{\phi z}{2}\right)\right)\cos\left(\frac{\phi z}{2}\right)E_x(0)E_y(0)$$

$$\left.\left.\left(\frac{2Fz}{\phi}\sin\left(\frac{\phi z}{2}\right)\right)\frac{z}{2}\sin\left(\frac{\phi z}{2}\right)E_x(0)E_y(0)\right)\right]$$

Since $\phi^2 = \Delta\beta^2 + (2F)^2$ then its differential with respect to F vanishes as F approaches zero. Applying this to the above equation for m, all terms except one vanish leaving a simply expression;

$$m = 4\sqrt{P}\sqrt{1-P}\frac{1}{\Delta\beta \cdot z}\sin\left(\frac{\Delta\beta \cdot z}{2}\right)\cos\left(\frac{\Delta\beta \cdot z}{2} + \gamma\right)$$